Scale-bridging of Elasto-Plastic Microstructures using Statistically Similar Representative Volume Elements

Von der Fakultät für Ingenieurwissenschaften,
Abteilung Bauwissenschaften
der Universität Duisburg-Essen
zur Erlangung des akademischen Grades

Doktor-Ingenieur

genehmigte Dissertation

von

Lisa Scheunemann, M.Sc.

Hauptberichter:	Prof. Dr.-Ing. habil. J. Schröder
Korreferenten:	Prof. Dr.-Ing. habil. D. Balzani

Tag der Einreichung:	12. April 2017
Tag der mündlichen Prüfung:	21. Juli 2017

Fakultät für Ingenieurwissenschaften,
Abteilung Bauwissenschaften
der Universität Duisburg-Essen
Institut für Mechanik
Prof. Dr.-Ing. habil. J. Schröder

Herausgeber:

Prof. Dr.-Ing. habil. J. Schröder

Organisation und Verwaltung:

Prof. Dr.-Ing. habil. J. Schröder
Institut für Mechanik
Fakultät für Ingenieurwissenschaften
Abteilung Bauwissenschaften
Universität Duisburg-Essen
Universitätsstraße 15
45141 Essen
Tel.: 0201 / 183 - 2682
Fax.: 0201 / 183 - 2680

ISBN-10 3-9818074-2-1
ISBN-13 978-3-9818074-2-4
EAN 9783981807424

Vorwort

Die vorliegende Arbeit entstand während meiner Tätigkeit als wissenschaftliche Mitarbeiterin am Institut für Mechanik (Abt. Bauwissenschaften, Fak. Ingenieurwissenschaften) an der Universität Duisburg-Essen im Rahmen der durch die Deutsche Forschungsgemeinschaft (DFG) geförderten Forschungsprojekte SCHR 570/8-2 (Forschergruppe FOR797 „Microplast“), SCHR 570/19-2 sowie BA 2823/8-2 (Schwerpunktprogramm SPP1648 „Exasteel II“). An dieser Stelle möchte ich der DFG für die finanzielle Unterstützung danken und einigen Menschen meinen persönlichen Dank aussprechen, die zum Gelingen dieser Arbeit ihren jeweiligen Anteil beigetragen haben.

An erster Stelle gilt mein Dank meinem geschätzten Doktorvater Professor Jörg Schröder, der mir die Möglichkeit gab unter seiner Leitung zu promovieren. Für seine intensive Förderung während meiner gesamten Promotionszeit und das mir entgegengebrachte Vertrauen bedanke ich mich sehr. Ein großer Dank gilt auch Professor Daniel Balzani für die Übernahme des Korreferates sowie für die gute Zusammenarbeit während meiner Promotionszeit. In gemeinsamen Diskussionen habe ich viel von ihm gelernt und konnte jederzeit auf seine Unterstützung bauen. Ich danke Professor Joachim Bluhm, mit dem ich in gemeinsamen Lehrveranstaltungen mein Wissen im Bereich der Kontinuumsmechanik festigen konnte und der sich darüber hinaus immer Zeit für Fragen und Diskussionen nahm. Ein weiterer Dank gilt Dominik Brands für die gute Zusammenarbeit in Forschung und Lehre, den technischen Support und das gewissenhafte Korrekturlesen meiner Dissertation. Bedanken möchte ich mich auch bei meinen ehemaligen und derzeitigen Kollegen am Institut für Mechanik, Solveigh Averweg, Julia Bergmann, Moritz Bloßfeld, Sarah Brinkhues, Bernhard Eidel, Simon Fausten, Ashutosh Gandhi, Markus von Hoegen, Maximilian Igelbüscher, Veronika Jorisch, Marc-André Keip, Simon Kugai, Matthias Labusch, Veronica Lemke, Petra Lindner-Roullé, Sascha Maassen, Simon Maike, Rainer Niekamp, Carina Nisters, Yasemin Özmen, Mangesh Pise, Sabine Ressel, Thomas Schmidt, Alexander Schwarz, Serdar Serdaş, Steffen Specht, Karl Steeger, Huy Ngoc Thai, Vera Vetrov und Nils Viebahn, für die gute Atmosphäre und die zielführenden Diskussionen. Darüber hinaus richtet sich ein besonderer Dank an den „Mechanik Stammtisch”, der für die notwendige Zerstreuung nach getaner Arbeit gesorgt hat. Meinen derzeitigen und ehemaligen studentischen Hilfskräften, Tobias Strohmann und Kavitha Sundu, danke ich für die gute Zusammenarbeit und ihre Unterstützung.

Meinen Eltern Ude und Johanna Scheunemann, meiner Schwester Anne und meiner gesamten Familie gilt ein großer Dank für ihre Unterstützung in jeglicher Lebenslage. Ihr Rat hat für mich sehr hohen Wert. Dani Rüdel danke ich für ihr offenes Ohr und ihre humorvolle Art. Abschließend danke ich meinem Freund Christoph für seinen bedingungslosen Rückhalt, seine Geduld und seinen ingenieurtechnischen Sachverstand, mit denen er mich auf dem Weg zur Promotion begleitet hat.

Essen, im Juli 2017 Lisa Scheunemann

Abstract

The present work deals with the numerical modeling of the mechanical behavior of microheterogeneous materials, with a focus on dual-phase steel. The macroscopic behavior of this material is largely influenced by an interaction of the microstructural constituents. The influence of the morphology of a real microstructure can be included in the material modeling by the application of a suitable representative volume element (RVE) in a direct micro-macro homogenization scheme (also known as FE^2-method). However, the use of sections of a real microstructure as an RVE can lead to huge computational costs. A cost reduction can be achieved by the application of statistically similar RVEs (SSRVEs). They are governed by similarities of selected statistical measures with respect to a real microstructure and show a comparable mechanical behavior. The different aspects in the construction method are a main focus of this work. It is shown that SSRVEs can resemble the mechanical behavior of a real DP steel microstructure appropriately, which permits their use in FE^2-simulations instead of real microstructures. Aiming for a description of polycrystalline materials governed by texture, the simulation of macroscopic properties based on polycrystalline RVEs is shown.

Zusammenfassung

Die vorliegende Arbeit behandelt die numerische Modellierung des mechanischen Verhaltens mikroheterogener Materialien, wobei das Hauptaugenmerk auf Dualphasenstähle gelegt wird. Ihr makroskopisches Verhalten wird durch die Interaktion der Einzelphasen auf mikrostruktureller Ebene geprägt. Der Einfluss der Morphologie einer realistischen Mikrostruktur kann durch die Verwendung von repräsentativen Volumenelementen (RVEs) unter Anwendung der FE^2-Methode direkt in die Materialmodellierung einbezogen werden. Dabei entsteht für RVEs, die als Ausschnitte einer realen Mikrostruktur konstruiert werden, ein enormer Rechenaufwand. Eine Reduzierung des Aufwands ist durch die Verwendung von statistisch ähnlichen RVEs (SSRVEs) möglich. Diese sind durch Ähnlichkeit in Bezug auf bestimmte statistische Maße definiert und liefern gleichzeitig Gleichartigkeit des mechanischen Verhaltens. Die verschiedenen Aspekte der Konstruktion von SSRVEs sind ein Schwerpunkt dieser Arbeit. Es wird gezeigt, dass SSRVEs die mechanischen Eigenschaften der realen Mikrostruktur widerspiegeln und damit ihre Verwendung im Rahmen der FE^2-Methode ermöglicht wird. Die Simulation makroskopischer Eigenschaften basierend auf polykristallinen RVEs wird gezeigt. Diese ermöglichen die Beschreibung polykristalliner Materialien, welche von ihrer mikrostrukturellen Textur geprägt werden.

Contents

1 State of the Art and Motivation

Numerical simulation techniques have become a regularly used tool in the design and analysis of structures in many engineering disciplines. Simulation provides insight into areas which cannot be described by standard experimental procedures, for example distribution of stress or strain inside a construction part. Furthermore, it offers the opportunity to design and optimize a production process at a low effort compared to experimental tryout. The recent advances in computational power have created the possibility to increase the detail in which a simulation can be modeled, which poses new challenges to the scientific community to provide reliable techniques for this purpose. With the approximation and idealization of a material's behavior by phenomenological material laws being today's standard, the incorporation of a realistic description of the heterogeneous material's structure, often only visible on a very small scale, is a major aim of recent development in this field. For example, dual-phase steel (DP steel) offers excellent material properties, combining high strength and good formability, for modern engineering applications in, e.g., the automotive industry. These material properties originate in the microheterogeneous composition of the material: martensitic inclusions embedded in a ferritic matrix material are created through special production processes which involve heating the alloy material to the austenitic temperature regime followed by rapid cooling causing the formation of martensite. The interaction of the two-phase microstructure results in the above mentioned material behavior which can improve part design especially in sheet metal forming applications. The description of this material behavior is challenging and the formulation of a pure macroscopic material law, i.e., a material law describing the behavior on the scale of a construction part, is cumbersome. The direct incorporation of the microstructure as an important contributor to the behavior is a promising technique to obtain a realistic description of the material behavior. Furthermore, the description of the material behavior solely on the macroscale cannot capture critical states in the microscale, for example regions of high stress concentration which can lead to the initiation of damage and failure.

For the incorporation of microstructural effects in the description of material behavior, analytical models exist. They go back to Eshelby [37; 38] and Hill [56]. Various semi-analytical approximation schemes were proposed based on these findings, such as the dilute distribution approach, Christensen [30], the Mori-Tanaka approach, Tanaka and Mori [156], the self-consistent method, Hill [57], and the differential scheme, Gross and Seelig [48]. For further details, see e.g. Hashin [52], Suquet [153], Zohdi and Wriggers [182], Gross and Seelig [48]. The latter approaches only allow the consideration of microstructures with very specific inclusion morphologies. Numerical approaches, such as the finite element method (FE-method), can describe arbitrary microstructure morphologies, however, a full discretization of the microstructure in a macroscopic problem could not be handled computationally due to the large number of elements needed. Numerical homogenization schemes are a senseful tool to overcome this obstacle. Therein, the microscopic material is considered using a representative volume element (RVE), capturing the vital microstructural features. Upscaling techniques are then used to calculate the homogenized microscale material response which is transferred to the material point on the macroscale. This approach is known as direct micro-macro transition approach, also often referred to as FE^2-method or multilevel FE-

method, see e.g. Smit et al. [143], Moulinec and Suquet [99], Miehe et al. [96], Miehe and Schröder [93], Feyel [40], Schröder [130], Terada et al. [162], Feyel and Chaboche [41], Geers et al. [43], Schröder [131]. Classically, a macroscopic boundary value problem (bvp) in the framework the FE-method is defined. In the one-scale FE-method, in every Gauss point, a material law would be evaluated to compute, e.g., the stress response under the given loading state. Here, a microscopic bvp is attached in every Gauss point, representing the microstructure of the material using an RVE. The boundary conditions on the microscale result from the known deformation state on the macroscale under consideration of energy consistency in the transition between the two scales. The different materials in the microscopic bvp are described using appropriate phenomenological laws. With the solution of the microscopic bvp, volume averaging techniques are used to compute the counterparts on the macroscale. The dominating role of the RVE in terms of computational effort becomes obvious here. Depending on the size and complexity captured, the ability to describe the material's microstructure properly rises as well as the computational costs. For a suitable RVE, there is no unique definition of its size. Generally, it should contain a subsection of the material's microstructure, which is representative of the overall properties of the material. Hashin [52] postulates that an RVE should be large enough to contain enough microstructural information, however it should be much smaller than the macroscopic body. Drugan and Willis [35] state that the smallest subvolume of a microstructure which provides a sufficient accuracy comparing the mean constitutive response and the macroscopic constitutive response, can be considered as an RVE. While Ostoja-Starzewski [104] only defines an RVE in very special cases of periodic or statistically homogeneous and ergodic microstructures, Stroeven et al. [151] relates the RVE size to the considered physical quantity which shall be represented. This is also found by Kanit et al. [66] and Gitman et al. [44], where an RVE size is sought for a specific property or physical quantity under observation. Here, the RVE size is found to differ vastly. Kanit et al. [66] present an approach based on the evaluation of the integral range of a physical property to determine either the sufficient volume of an RVE for one realization or a number of samples needed for a fixed volume of an RVE for a given error in the measured value in the microstructure. This approach has been used for defining a minimum RVE for elastic cortical bone tissue by Grimal et al. [47]. Pelissou et al. [108] extend the method to save computational costs by using uncertainty quantities to evaluate the stopping criterion. The method is tested for linear and nonlinear properties, which results in a larger required size for the latter ones. Furthermore, the definition of a suitable RVE is restricted by the limitations of measuring techniques for the microstructural information. Even though microscopy techniques have advanced and can capture various microstructural effects and properties in DP steel using Electron backscatter diffraction (EBSD), Calcagnotto et al. [26], the techniques cannot capture regions of limitless size.

Due to the high complexity, which is most likely to determine the microstructure morphology in an RVE, the computational effort is a major drawback of the FE^2-method. In order to reduce this effort, Moulinec and Suquet [99] have proposed an FE-FFT framework, where the microscopic boundary value problem is solved with the help of fast fourier transformation, providing a potential speedup under certain conditions. The issue of high complexity of the RVE can be overcome by using statistically similar RVEs

(SSRVEs), as proposed in Schröder et al. [132] for 2D and Balzani et al. [11] for 3D. These artificial microstructures offer an enormous reduction of complexity by resembling the statistical properties of the real microstructure using a simplified inclusion morphology consisting of, e.g., a limited number of ellipsoidal inclusions. Therefore, selected statistical descriptors are measured in the real microstructure and the SSRVE's morphology is then adjusted in an optimization process such that it resembles the statistical properties of the real microstructure. It is assumed that the real microstructure can be described as a periodic one, such that the SSRVE only needs to model a periodic unitcell. By reproducing the morphological properties of the real microstructure, the SSRVE is able to describe the effects related to the microheterogeneity. In Scheunemann et al. [128], different types of SSRVEs are constructed, showing the similarity in the mechanical response of the SSRVEs and the real microstructure. Other authors adapted the concept of SSRVEs for the simulation of dual-phase steel simulations with SSRVEs based on shape coefficients, Rauch et al. [117], Ambrozinski et al. [2], Rauch et al. [118]. The utilized statistical measures play a crucial role for the construction of SSRVEs regarding their performance and the efficiency of the construction process. An overview of available statistical descriptors can be found in e.g. Yeong and Torquato [176], Ohser and Mücklich [103] and Torquato [165]. Among the different descriptors, one can distinguish between scalar measures and measures of higher order. While the computational effort increases with the use of higher order statistical measures, such as n-point probability functions or the lineal-path function, they also drastically increase the information which is captured. It has been shown in Yeong and Torquato [176] that hybrid approaches which incorporate more than one statistical measure perform better in the reconstruction process of real microstructures than methods where only one measure is used. For the use in the construction of SSRVEs, several measures are compared, see Balzani et al. [8] and Scheunemann et al. [128].

While the consideration of the phase contrast is inevitable to describe many properties of microheterogeneous materials accurately, this approach is not sufficient when the plastic anisotropy of a material is considered, see e.g. Pagenkopf et al. [105]. The degree of plastic anisotropy in sheet metal is often described using the *Lankford coefficient*, also known as *r-value* or *plastic strain ratio*. This measure is experimentally determined using tensile tests with respect to different directions to rolling direction of the sheet metal (0°, 45°, 90°). A suitable average of the ratio of plastic strains in width and thickness direction of the specimen is then calculated to obtain the Lankford coefficient. Pagenkopf et al. [105] compare stress-strain curves and the plastic strain ratio for DP steel microstructural models incorporating the martensite inclusion shape as well as the texture properties of the ferrite phase. They show, using a full-field homogenization approach, that in order to describe the plastic anisotropy in DP steel, one needs to consider the crystallographic texture properties of the ferrite phase. While stress-strain curves of DP steel can be predicted well for simulations not considering the crystallographic texture of the ferrite phase, they fail in characterizing the Lankford coefficient.

The fundamental characterization of the deformation mechanisms in single crystals was early investigated by Taylor [159], Taylor [160], while the first finite element simulations were carried out decades later by e.g Asaro and Rice [4], Peirce et al. [107], Hutchinson [63], Cuitiño and Ortiz [32]. For the consideration of polycrystalline

structures based on the behavior of the underlying single grains, an isostress approach was first proposed by Sachs [123], assuming the resolved shear stress on all slip systems in the polycrystal to be equal to the highest resolved shear stress in the compound. The isostrain assumption, Taylor [158], Bishop and Hill [20], also called Taylor or Taylor-Bishop-Hill (TBH) model, in which all grains undergo the same state of deformation, shows good results in the prediction of deformation textures, however violates the equilibrium condition between individual grains. While no grain interaction is considered in the latter approaches, grain cluster models, see e.g. Van Houtte et al. [168], or grain interaction models, see e.g. Raabe [113], include some grain interaction and relax the rigid isostrain assumption set up in the TBH models. Self-consistent models, first developed by Kröner [77] and later extended by Budiansky and Wu [25], Hill [57], consider each grain as an inclusion embedded in a homogeneous effective medium. Thereby grain interaction is considered as well, however most models treat the grain itself using simplified geometries. Full-field models, which enable a consideration of morphological information of the polycrystal as well as local grain interaction and intra-grain inhomogeneities of the micromechanical fields, can be described using FEM models, also called crystal plasticity (CP) FEM models in this case, see e.g. Roters et al. [120]. As mentioned earlier, these methods require a sufficiently high resolution of the considered polycrystalline RVE and due to their multiscale nature result in large computational costs. A crystal plasticity implementation within a finite-strain continuum mechanical framework which utilizes a spectral solver has been developed at Max-Planck Institut für Eisenforschung, Düsseldorf, see, e.g., Roters et al. [122].

For a long time the direct modeling of microstructural effects was not possible due to the lack of computational power and has only just become available to some extent due to large supercomputers and suitable algorithms. In the past, and still today, macroscopic material laws describing the underlying effects are used. Phenomenological descriptions of plastic anisotropy have been defined in the form of yield functions, see e.g. Hill [55; 58; 59; 60], Barlat and Lian [14], Barlat et al. [15], Karafillis and Boyce [69]. For an overview on various definitions of yield functions and plastic anisotropy in metals, it is referred to Habraken [49] and Siegert [137]. Among the various definitions, in the field of sheet metal forming processes the yield functions proposed in Hill [55], Barlat and Lian [14], are most frequently used. Hill [55] proposes a quadratic yield function with six parameters describing orthotropic plastic material behavior, which cannot account for Bauschinger effects. This is also the case in the yield function proposed in Barlat and Lian [14], where a non quadratic yield function is described. Experimental yield surfaces are found to be better approximated when non-quadratic functions are used, still the latter formulation does not perform well in biaxial loading scenarios, cf. Siegert [137]. Armstrong and Frederick [3] proposed a yield function considering the evolution of back stress and thus enabling an account for the Bauschinger effect. More recently, in Banabic et al. [12] the yield criterion proposed in Barlat and Lian [14] was extended, showing a good ability in predicting the yield surface. However, the coefficients used in the formulation do not bear any physical meaning and have to be identified through experiments. Although these yield functions are used in many applications for the description of anisotropic plastic behavior, they are not able to describe the plastic anisotropy induced by the texture of the underlying microstructure, generally, and the determination of parameters

often requires complex experiments. Darrieulat and Piot [33] have proposed an analytical description of yield surfaces for crystalline materials which can account for shape properties which are also observed experimentally. Kowalczyk and Gambin [75] proposed a texture-dependent yield surface and compared its evolution to the evolution of classical phenomenological yield surfaces in different loading scenarios. The virtual testing of materials with a realistic description of the microstructural morphology and texture is especially inevitable in the field of sheet metals, where only a limited number of stress-strain states can be realized experimentally. Using a full field numerical homogenization approach incorporating crystal plasticity, the yield surface and Lankford coefficients of a mild steel have been analyzed in Baiker et al. [6], showing good agreement with experimental observations. Recently, Zhang et al. [180] have presented a virtual laboratory set up to predict yield surfaces of aluminum alloy. Parameter for analytical yield functions are predicted using an optimization procedure. Good agreement is found for the virtual tests and experimental data as well as the predicted analytical yield surfaces.

The focus of this thesis is the modeling of the material behavior of microheterogeneous materials. In the framework of multiscale modeling, the FE^2-method is used to incorporate the microstructure using an RVE in the simulation. Aiming for efficient computations, the concept of SSRVEs is presented, based on the construction method proposed in Balzani et al. [7; 10], Schröder et al. [132] and Scheunemann et al. [128]. For a real DP steel microstructure, SSRVEs are constructed based on different statistical descriptors and evaluated regarding their ability to describe the mechanical behavior of the DP steel microstructure. Furthermore, the Bauschinger effect is modeled using SSRVEs. The application of SSRVEs in practical engineering problems is demonstrated in a two-scale simulation of a perforated plate. With the goal of incorporating crystallographic texture information of the microstructure into the simulation, different polycrystalline unitcells are used as RVEs in FE^2 simulations. Macroscopic yield surfaces are generated based on SSRVEs and polycrystalline RVEs, demonstrating the possibilities available to a virtual laboratory. Therefore, virtual tests under plane stress conditions are carried out considering different loading ratios. Some results of this work have already been published, see Balzani et al. [9], Balzani et al. [11],Scheunemann et al. [128], Scheunemann et al. [127], Scheunemann et al. [129].

The outline of this work is as follows: Section 2 revisits the main findings in the field of continuum mechanics and material modeling, Section 3 gives an overview on the standard assumptions in the Finite Element method. Aspects on the material properties and computational modeling approaches for DP steel are presented in Section 4, together with the constitutive framework used for its description in this work. Therefore, a J_2-plasticity material model at finite strains is recapitulated based on the formulations given in Simo [138], Weber and Anand [171], Simo and Miehe [142] and the implementations and notes in Simo and Hughes [141]. A small strain rate dependent crystal plasticity model is recapitulated next, which follows the standard assumptions in this field, see e.g. Cuitiño and Ortiz [32], Miehe and Schröder [94]. Different aspects on the multiscale modeling of microheterogeneous materials which become important in this work are presented in Section 5, starting with an overview in hypothesis and concepts in the field of homogenization theory. This is followed by an overview on the FE^2-method,

as proposed in Sect. 5.2. These formulations will be used later on in the simulations of SSRVEs of a DP steel microstructure. Section 6 covers a detailed discussion of the construction of SSRVEs, as proposed in Balzani et al. [7], Schröder et al. [132], Balzani et al. [11], Balzani et al. [10] and Scheunemann et al. [128]. First, an overview on the utilized statistical measures is given, followed by the method of construction for SSRVEs. Different statistical descriptors are then used to construct SSRVEs, whose performance is compared concerning micro- and macroscale properties, as presented in Scheunemann et al. [128]. Section 7 is concerned with the application of SSRVEs in further virtual tests to analyze the yield behavior of a real DP steel microstructure. The Bauschinger effect is analyzed and macroscopic yield curves based on SSRVEs as well as the real microstructure are compared. Section 8 presents the simulation of macroscopic yield curves based on three different polycrystalline RVEs. The thesis is concluded in Section 9 with an outlook on further research.

2 Fundamentals of Continuum Mechanics

In continuum mechanics, physical phenomena in fluids and solids are studied considering the material as a continuous matter with certain field quantities, such as density, temperature and velocity. This approximation does not account for every detail of the structure, yet it is sufficiently accurate in most engineering applications. Within the method of continuum mechanics, a description of the motion and deformation of a body, stress states as a result of the latter and the description of the fundamental balance laws of physics are essential subjects. An overview is given here only, more details can be found in e. g. Truesdell and Noll [167], Ogden [102], Eringen [36] and Šilhavý [169].

2.1 Kinematics

In the continuum mechanics theory, a physical body $\mathcal{B}$ with its surface $\partial\mathcal{B}$ is composed of material points $P \in \mathcal{B}$ in the three-dimensional Euclidean space $\mathbb{R}^3$, where the mass and the volume are assumed to be continuous (or pieceswise continuous) functions over the body.

A *reference configuration* $\mathcal{B}_0 \in \mathbb{R}^3$ at time $t = t_0$ is considered, which is also referred to as *material* or *Lagrangian configuration*, where the location of a material point is denoted by a position vector $\boldsymbol{X}$. In order to account for deformations, the *current configuration* $\mathcal{B}_t \in \mathbb{R}^3$ at a fixed time $t > t_0$, also denoted as *actual* or *Eulerian configuration*, is considered with the position of a material point parameterized by $\boldsymbol{x}$.

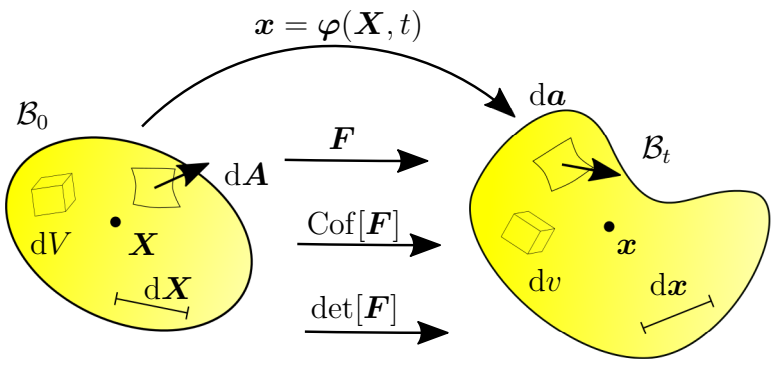

Figure 2.1: Body in the reference configuration $\mathcal{B}_0$ and actual configuration $\mathcal{B}_t$ and transport theorems.

For the definition of the position vectors, a right-handed orthonormal basis system $\{\boldsymbol{E}_A\}$ and $\{\boldsymbol{e}_a\}$, fixed at an origin $\mathbf{0}$ can be used, i. e.

$$\begin{aligned} \boldsymbol{X} &= X^A\, \boldsymbol{E}_A \qquad \text{with } A = 1,2,3 \qquad \text{and} \\ \boldsymbol{x} &= x^a\, \boldsymbol{e}_a \qquad \text{with } a = 1,2,3. \end{aligned} \tag{2.1}$$

The motion of a body can be described by a transformation from the reference configuration to the current configuration at a fixed time t by

$$\boldsymbol{\varphi}(\boldsymbol{X}, t) : \mathcal{B}_0 \to \mathcal{B}_t, \tag{2.2}$$

mapping a material point in the reference configuration to its position in the current configuration. Then the mapping between the configuration is given by

$$\boldsymbol{x} = \boldsymbol{\varphi}(\boldsymbol{X}, t) \qquad \text{and} \qquad \boldsymbol{X} = \boldsymbol{\varphi}^{-1}(\boldsymbol{x}, t). \tag{2.3}$$

The deformation of the body is described by the *deformation gradient* $\boldsymbol{F}$, which is defined by

$$\boldsymbol{F}(\boldsymbol{X}) = \frac{\partial \boldsymbol{\varphi}(\boldsymbol{X}, t)}{\partial \boldsymbol{X}} = \mathrm{Grad}[\boldsymbol{x}(\boldsymbol{X}, t)] = F^a{}_A \, \boldsymbol{e}_a \otimes \boldsymbol{E}^A \qquad \text{with} \qquad F^a{}_A = \frac{\partial x^a}{\partial X^A} \tag{2.4}$$

From Eq. (2.4), it is obvious that the deformation gradient is a two-field tensor, with one basis vector in the current and the other in the reference configuration. An important property of $\boldsymbol{F}$ is its non-singularity, i. e. $\det \boldsymbol{F} > 0$, which implies the deformation gradient being invertible.

The deformation gradient can be understood as a map of line elements from the reference placement to the spatial placement and vice versa by its inverse $\boldsymbol{F}^{-1}$, as

$$\mathrm{d}\boldsymbol{x} = \boldsymbol{F}(\boldsymbol{X}, t)\mathrm{d}\boldsymbol{X} \qquad \text{and} \qquad \mathrm{d}\boldsymbol{X} = \boldsymbol{F}^{-1}(\boldsymbol{X}, t)\mathrm{d}\boldsymbol{x}, \tag{2.5}$$

thus accounting for changes in the length of lines in the body $\mathcal{B}$ during the deformation. Taking a look at the mapping of area elements $\mathrm{d}\boldsymbol{A}$ in the reference configuration to elements $\mathrm{d}\boldsymbol{a}$ in the current configuration, it can be seen that

$$\mathrm{d}\boldsymbol{a} = \det[\boldsymbol{F}]\boldsymbol{F}^{T-1}\mathrm{d}\boldsymbol{A} = \mathrm{Cof}[\boldsymbol{F}]\mathrm{d}\boldsymbol{A}, \tag{2.6}$$

with the area element $\mathrm{d}\boldsymbol{a} = \boldsymbol{n}\,\mathrm{d}a$ and $\mathrm{d}\boldsymbol{A} = \boldsymbol{N}\,\mathrm{d}A$ in the current and reference placement, respectively. The transformation of volume elements $\mathrm{d}V$ from the reference configuration to $\mathrm{d}v$ in the current configuration can be performed by

$$\mathrm{d}v = \det[\boldsymbol{F}]\,\mathrm{d}V = J\,\mathrm{d}V, \tag{2.7}$$

with the volume element as the scalar triple product of vectors $\mathrm{d}\boldsymbol{X}$, e.g., $\mathrm{d}V = (\mathrm{d}\boldsymbol{X}_1 \times \mathrm{d}\boldsymbol{X}_2) \cdot \mathrm{d}\boldsymbol{X}_3$ and the Jacobian $J := \det[\boldsymbol{F}]$. The transport of line, area and volume elements from reference to current configuration is illustrated in Fig. 2.1.

The total deformation of a body consists of a rotation part and a stretch part, which are described jointly by the deformation gradient. $\boldsymbol{F}$ can be multiplicatively decomposed using

$$\boldsymbol{F} \;=\; \boldsymbol{R} \cdot \boldsymbol{U} \;=\; \boldsymbol{V} \cdot \boldsymbol{R} \tag{2.8}$$

with $\boldsymbol{U}$ and $\boldsymbol{V}$ as the right (material) stretch tensor and the left (spatial) stretch tensor, respectively and the proper orthogonal rotation tensor $\boldsymbol{R}$ with $\boldsymbol{R}^T \cdot \boldsymbol{R} = \boldsymbol{I}$. The *Right Cauchy-Green tensor* $\boldsymbol{C}$ and *Left Cauchy-Green (Finger) tensor* $\boldsymbol{B}$ are deformation tensors defined in the reference and current placement. They rest upon the definition of the squared distance between two material points given by $\mathrm{d}\boldsymbol{X}^2$ and $\mathrm{d}\boldsymbol{x}^2$, thus

$$\boldsymbol{C} := \boldsymbol{F}^T \cdot \boldsymbol{F} = (\boldsymbol{R} \cdot \boldsymbol{U})^T \;\cdot\; \boldsymbol{R} \cdot \boldsymbol{U} = \boldsymbol{U}^T \cdot \boldsymbol{R}^T \cdot \boldsymbol{R} \cdot \boldsymbol{U} = \boldsymbol{U}^T \cdot \boldsymbol{U} \tag{2.9}$$

$$\boldsymbol{B} := \boldsymbol{F} \cdot \boldsymbol{F}^T = \boldsymbol{V} \cdot \boldsymbol{R} \;\cdot\; (\boldsymbol{V} \cdot \boldsymbol{R})^T = \boldsymbol{V} \cdot \boldsymbol{R} \cdot \boldsymbol{R}^T \cdot \boldsymbol{V}^T = \boldsymbol{V} \cdot \boldsymbol{V}^T. \tag{2.10}$$

with the tensor coefficients given by

$$C_{AB} := F^a{}_A \, \delta_{ab} \, F^b{}_B \qquad \text{and} \qquad B^{ab} := F^a{}_A \, \delta^{AB} \, F^b{}_B. \tag{2.11}$$

From Eq. (2.9) and Eq. (2.10), it can be seen that $\boldsymbol{C}$ and $\boldsymbol{B}$ only carry information about the stretch of the body $\mathcal{B}$ and no rotational terms, in contrast to the deformation gradient $\boldsymbol{F}$. Strain tensors in the reference and current configuration are defined based on the consideration of the differences of squared distances, i. e. $\mathrm{d}s^2 - \mathrm{d}S^2$ with $\mathrm{d}s = |\mathrm{d}\boldsymbol{x}|$ and $\mathrm{d}S = |\mathrm{d}\boldsymbol{X}|$, and define the *Green-Lagrange strain tensor* $\boldsymbol{E}$ in the reference placement and the *Almansi strain tensor* $\boldsymbol{A}$ in the current placement as

$$\boldsymbol{E} := \frac{1}{2}\left(\boldsymbol{C} - \boldsymbol{I}\right) = \frac{1}{2}\left(\boldsymbol{F}^T \cdot \boldsymbol{F} - \boldsymbol{I}\right), \qquad E_{AB} := \frac{1}{2}(C_{AB} - \delta_{AB}) \tag{2.12}$$

$$\boldsymbol{A} := \frac{1}{2}\left(\boldsymbol{I} - \boldsymbol{B}^{-1}\right) = \frac{1}{2}\left(\boldsymbol{I} - \left(\boldsymbol{F} \cdot \boldsymbol{F}^T\right)^{-1}\right), \qquad A^{ab} := \frac{1}{2}(\delta^{ab} - (B^{ab})^{-1}) \tag{2.13}$$

which are both symmetric tensors. From the indices of the introduced deformation and strain tensors, it becomes clear that $\boldsymbol{C}$ and $\boldsymbol{E}$ are defined in the reference placement and $\boldsymbol{B}$ and $\boldsymbol{A}$ are defined in the actual placement.

The change of tensor fields over time and space are considered in continuum mechanics using their derivation with respect to time or space. A velocity field and an acceleration field can be expressed in the reference setting based on the motion function as

$$\dot{\boldsymbol{x}}(\boldsymbol{X}, t) = \frac{\partial}{\partial t}\boldsymbol{\varphi}(\boldsymbol{X}, t) = \dot{\boldsymbol{\varphi}}(\boldsymbol{X}, t) \tag{2.14}$$

$$\ddot{\boldsymbol{x}}(\boldsymbol{X}, t) = \frac{\partial^2}{\partial t^2}\boldsymbol{\varphi}(\boldsymbol{X}, t) = \ddot{\boldsymbol{\varphi}}(\boldsymbol{X}, t), \tag{2.15}$$

whereas in the actual placement, the respective fields are defined by

$$\boldsymbol{v}(\boldsymbol{x}, t) = \dot{\boldsymbol{x}}(\boldsymbol{\varphi}^{-1}(\boldsymbol{x}, t), t) = \dot{\boldsymbol{x}}(\boldsymbol{X}, t), \tag{2.16}$$

$$\boldsymbol{a}(\boldsymbol{x}, t) = \ddot{\boldsymbol{x}}(\boldsymbol{\varphi}^{-1}(\boldsymbol{x}, t), t) = \ddot{\boldsymbol{x}}(\boldsymbol{X}, t), \tag{2.17}$$

The derivative of the spatial velocity field $\boldsymbol{v}$ with respect to the spatial coordinates $\boldsymbol{x}$ is defined by

$$\boldsymbol{L} := \frac{\partial \boldsymbol{v}(\boldsymbol{x}, t)}{\partial \boldsymbol{x}} = \mathrm{grad}[\boldsymbol{v}(\boldsymbol{x}, t)], \tag{2.18}$$

which is referred to as the *spatial velocity gradient*. The time derivative of the deformation gradient

$$\begin{aligned} \dot{\boldsymbol{F}}(\boldsymbol{X}, t) &= \frac{\partial}{\partial t}\left(\frac{\partial \boldsymbol{\varphi}(\boldsymbol{X}, t)}{\partial \boldsymbol{X}}\right) = \frac{\partial}{\partial \boldsymbol{X}}\left(\frac{\partial \boldsymbol{\varphi}(\boldsymbol{X}, t)}{\partial t}\right) \\ &= \frac{\partial \dot{\boldsymbol{x}}(\boldsymbol{X}, t)}{\partial \boldsymbol{X}} = \mathrm{Grad}[\dot{\boldsymbol{x}}(\boldsymbol{X}, t)], \end{aligned} \tag{2.19}$$

is referred to as the *material velocity gradient*. The spatial velocity gradient $\boldsymbol{L}$ can be rewritten using Eq. (2.19) and Eq. 2.16 as

$$\boldsymbol{L} = \frac{\partial \dot{\boldsymbol{x}}}{\partial \boldsymbol{x}} = \frac{\partial \dot{\boldsymbol{x}}}{\partial \boldsymbol{X}} \, \frac{\partial \boldsymbol{X}}{\partial \boldsymbol{x}} = \dot{\boldsymbol{F}} \cdot \boldsymbol{F}^{-1}, \tag{2.20}$$

and leads to an alternative expression for the material velocity gradient $\dot{\boldsymbol{F}} = \boldsymbol{L} \cdot \boldsymbol{F}$. Further, the spatial velocity gradient can be decomposed additively into a symmetric part $\boldsymbol{D}$ and a skew-symmetric part $\boldsymbol{W}$, which yields

$$\boldsymbol{D} := \frac{1}{2}\left(\boldsymbol{L} + \boldsymbol{L}^T\right), \tag{2.21}$$

$$\boldsymbol{W} := \frac{1}{2}\left(\boldsymbol{L} - \boldsymbol{L}^T\right), \tag{2.22}$$

with the symmetry properties $\boldsymbol{D} = \boldsymbol{D}^T$ and $\boldsymbol{W} = -\boldsymbol{W}^T$. The time change of the Jacobian can be derived as

$$\dot{J} = \frac{\partial \det\left[\boldsymbol{F}\right]}{\partial \boldsymbol{F}} : \frac{\partial \boldsymbol{F}}{\partial t} = \det\left[\boldsymbol{F}\right] \boldsymbol{F}^{\mathrm{T}-1} : \dot{\boldsymbol{F}} = J \operatorname{div}\left[\dot{\boldsymbol{x}}\right]. \tag{2.23}$$

The Concept of Stress

When a mechanical load is applied to a physical body $\mathcal{B}$, inner forces and stresses occur. These can be visualized by imagining a cut through the body with the normal vector acting on the cutting plane. The *traction vector* $\boldsymbol{t} = \boldsymbol{t}(\boldsymbol{x}, t, \boldsymbol{n})$ acts at a point $\boldsymbol{x}$ on an infinitesimal surface element $\mathrm{d}a$ with the outward unit normal vector $\boldsymbol{n}$ on the cutting plane of the current placement at time t. In the reference configuration it is associated to the traction vector $\boldsymbol{t}_0 = \boldsymbol{t}_0(\boldsymbol{X}, t_0, \boldsymbol{N})$ with the associated point of action $\boldsymbol{X}$ and normal vector $\boldsymbol{N}$ acting on a surface element $\mathrm{d}A$ at time $t = t_0$. The resultant force $\mathrm{d}\boldsymbol{f}$ transmitted through a cutting plane can be calculated by

$$\mathrm{d}\boldsymbol{f} \;=\; \boldsymbol{t}\,\mathrm{d}a \;=\; \boldsymbol{t}_0\,\mathrm{d}A. \tag{2.24}$$

as illustrated in Fig. 2.2 for the reference and actual configuration.

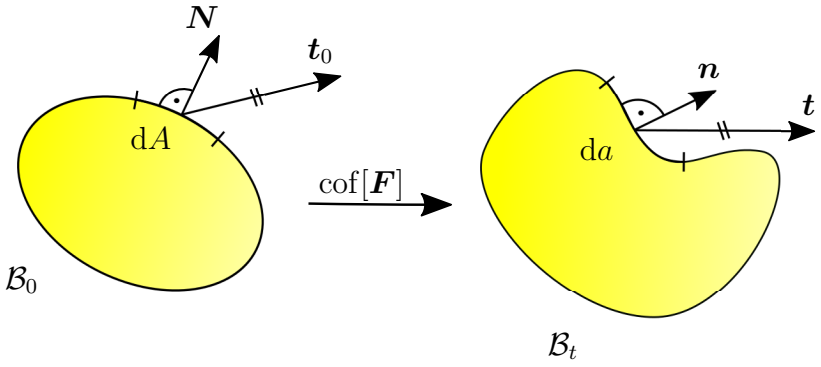

Figure 2.2: Traction vectors in reference and actual configuration.

The traction vectors $\boldsymbol{t}$ and $\boldsymbol{t}_0$ are called *true traction vector* and *nominal traction vector*, measuring force per unit surface in the current configuration and the reference configuration, respectively. Cauchy's stress theorem states that $\boldsymbol{t}$ depends linearly on $\boldsymbol{n}$ and can be mapped by the *Cauchy stress tensor* $\boldsymbol{\sigma}$, i. e.

$$\boldsymbol{t}(\boldsymbol{x}, t, \boldsymbol{n}) = \boldsymbol{\sigma}(\boldsymbol{x}, t) \cdot \boldsymbol{n}, \tag{2.25}$$

where $\boldsymbol{\sigma}$ is a symmetric tensor field defined in the spatial configuration. Similarly, the relation

$$\boldsymbol{t}_0(\boldsymbol{X}, t_0, \boldsymbol{N}) = \boldsymbol{P}(\boldsymbol{X}, t_0) \cdot \boldsymbol{N}, \tag{2.26}$$

holds for a mapping of the nominal traction vector $\boldsymbol{t}_0$ via the *first Piola-Kirchhoff stress tensor* $\boldsymbol{P}$, which is a non-symmetric tensor field. From Eq. (2.24) it can be deduced that

$$\boldsymbol{\sigma}(\boldsymbol{x}, t) \cdot \boldsymbol{n} \, \mathrm{d}a = \boldsymbol{P}(\boldsymbol{X}, t_0) \cdot \boldsymbol{N} \, \mathrm{d}A, \tag{2.27}$$

which provides a relation between the stress tensors using the transport theorem in Eq. (2.6), yielding

$$\boldsymbol{P} = J \, \boldsymbol{\sigma} \cdot \boldsymbol{F}^{-T} \qquad \text{and} \qquad \boldsymbol{\sigma} = J^{-1} \, \boldsymbol{P} \cdot \boldsymbol{F}^{T}. \tag{2.28}$$

Besides the above mentioned stress tensors, further measures for stress can be defined. A frequently used stress tensor is the *Kirchhoff stress tensor* $\boldsymbol{\tau}$, which is obtained from the Cauchy stress tensor by a multiplication with the Jacobian as

$$\boldsymbol{\tau} = J \, \boldsymbol{\sigma}, \tag{2.29}$$

and is a symmetric stress measure. Performing a pullback operation of $\boldsymbol{\tau}$ to the reference configuration yields the symmetric *second Piola-Kirchhoff stress tensor* $\boldsymbol{S}$ defined as

$$\boldsymbol{S} = \boldsymbol{F}^{-1} \cdot \boldsymbol{\tau} \cdot \boldsymbol{F}^{-T}. \tag{2.30}$$

An overview on the relation between different stress tensors can be found in Tab. 2.1. Further definitions of stress measures can be found in the literature, see e.g., Holzapfel [61].

Table 2.1: Relations between stress tensors.

		$\boldsymbol{\sigma}$	$\boldsymbol{\tau}$	$\boldsymbol{P}$	$\boldsymbol{S}$
Cauchy stress	$\boldsymbol{\sigma} =$	$\boldsymbol{\sigma}$	$\frac{1}{J}\boldsymbol{\tau}$	$\frac{1}{J}\boldsymbol{P} \cdot \boldsymbol{F}^{\mathrm{T}}$	$\frac{1}{J}\boldsymbol{F} \cdot \boldsymbol{S} \cdot \boldsymbol{F}^{\mathrm{T}}$
Kirchhoff stress	$\boldsymbol{\tau} =$	$J\boldsymbol{\sigma}$	$\boldsymbol{\tau}$	$\boldsymbol{P} \cdot \boldsymbol{F}^{\mathrm{T}}$	$\boldsymbol{F} \cdot \boldsymbol{S} \cdot \boldsymbol{F}^{\mathrm{T}}$
first P.-K. stress	$\boldsymbol{P} =$	$J\boldsymbol{\sigma} \cdot \boldsymbol{F}^{-\mathrm{T}}$	$\boldsymbol{\tau} \cdot \boldsymbol{F}^{-\mathrm{T}}$	$\boldsymbol{P}$	$\boldsymbol{F} \cdot \boldsymbol{S}$
second P.-K. stress	$\boldsymbol{S} =$	$J\boldsymbol{F}^{-1} \cdot \boldsymbol{\sigma} \cdot \boldsymbol{F}^{-\mathrm{T}}$	$\boldsymbol{F}^{-1} \cdot \boldsymbol{\tau} \cdot \boldsymbol{F}^{-\mathrm{T}}$	$\boldsymbol{F}^{-1} \cdot \boldsymbol{P}$	$\boldsymbol{S}$

2.2 Balance Laws

In the following section, the balance principles and fundamental laws of thermodynamics are discussed. These are the *conservation of mass*, *the balance of momentum*, *balance of moment of momentum* as well as the *balance of energy (1^{st} law of thermodynamics)* and the *entropy inequality (2^{nd} law of thermodynamics)*. These laws have an axiomatic nature, i.e. they are based on observations and experiences in nature and cannot be deduced from other laws. They lay the foundation for classical mechanics and enable postulations for mechanical quantities such as velocity, mass, force, momentum and energy and their influence on a considered system.

Conservation of Mass

The *conservation law of mass* postulates that during motion or deformation of a physical body $\mathcal{B}$, no mass sources producing mass or mass sinks, which destroy mass, exist such that mass can be considered as a conserved quantity. With ρ_0 and ρ as the reference and actual density, the mass of a body in the reference and actual configuration, M and m, remain constant scalar quantities, leading to

$$M = \int_{\mathcal{B}_0} \rho_0(\boldsymbol{X}) \mathrm{d}V = \int_{\mathcal{B}_t} \rho(\boldsymbol{x}, t) \mathrm{d}v = m = \text{const.} \,. \tag{2.31}$$

Considering the transport theorem in Eq. (2.7), the conservation of mass can be rewritten to the form

$$\rho_0 J = \rho. \tag{2.32}$$

The consistency of mass over reference and actual configuration implies that the mass does not change over time, thus

$$\dot{m} = \frac{\mathrm{d}m}{\mathrm{d}t} = \frac{\mathrm{d}}{\mathrm{d}t} \int_{\mathcal{B}_t} \rho \, \mathrm{d}v = 0. \tag{2.33}$$

Since the state of the body in the current configuration $\mathcal{B}_t$ depends on both time and space, a transformation to the reference configuration via Eq. (2.7) is used. Thus, one obtains, together with the time derivative of the jacobian, according to Eq. (2.23)

$$\begin{aligned} \dot{m} = \frac{\mathrm{d}}{\mathrm{d}t} \int_{\mathcal{B}_0} \rho J \, \mathrm{d}V = \int_{\mathcal{B}_0} \dot{\rho} J + \rho \dot{J} \, \mathrm{d}V \\ \int_{\mathcal{B}_0} \left(\dot{\rho} \, J + \rho J \, \mathrm{div}[\dot{\boldsymbol{x}}] \right) \, \mathrm{d}V = \int_{\mathcal{B}_t} \left(\dot{\rho} \, + \, \rho \, \mathrm{div}[\dot{\boldsymbol{x}}] \right) \, \mathrm{d}v = 0 \end{aligned} \tag{2.34}$$

and the local form

$$\dot{\rho} + \rho \, \mathrm{div}[\dot{\boldsymbol{x}}] = 0, \qquad \forall \, \boldsymbol{x} \, \in \, \mathcal{B}_t. \tag{2.35}$$

Balance of Linear Momentum

The *balance of linear momentum* states that the change over time of the linear momentum $\mathbf{I}$ is equal to the resultant force $\boldsymbol{f}$,

$$\dot{\boldsymbol{I}} = \boldsymbol{f} \quad \text{with} \quad \boldsymbol{I} = \int_{\mathcal{B}_t} \rho \, \dot{\boldsymbol{x}} \, \mathrm{d}v \quad \text{and} \quad \boldsymbol{f} = \int_{\partial \mathcal{B}_t} \boldsymbol{t} \, \mathrm{d}a + \int_{\mathcal{B}_t} \rho \, \boldsymbol{b} \, \mathrm{d}v. \tag{2.36}$$

The traction vector $\boldsymbol{t}$ acts on the surface $\partial \mathcal{B}_t$ and $\rho \, \boldsymbol{b}$ defines the body force per unit volume of the body $\mathcal{B}_t$. Evaluating the time derivative of $\boldsymbol{I}$, under consideration of Eq. (2.23) and the local form of conservation of mass, see Eq. (2.35), one obtains

$$\dot{\boldsymbol{I}} = \int_{\mathcal{B}_t} \rho \, \ddot{\boldsymbol{x}} \, \mathrm{d}v \tag{2.37}$$

and by reformulating the expression of resultant forces due to external forces using Cauchy's theorem, Eq. (2.25) and divergence theorem, Eq. (A.9), one obtains

$$\int_{\partial \mathcal{B}_t} \boldsymbol{t} \, \mathrm{d}a = \int_{\partial \mathcal{B}_t} \boldsymbol{\sigma} \cdot \boldsymbol{n} \, \mathrm{d}a = \int_{\mathcal{B}_t} \mathrm{div}[\boldsymbol{\sigma}] \, \mathrm{d}v. \tag{2.38}$$

The balance of linear momentum can be expressed in its global form as

$$\int_{\mathcal{B}_t} \rho\, \ddot{\boldsymbol{x}}\, \mathrm{d}v = \int_{\mathcal{B}_t} (\mathrm{div}[\boldsymbol{\sigma}]\ + \rho\, \boldsymbol{b})\ \mathrm{d}v \quad \Leftrightarrow \quad \int_{\mathcal{B}_t} (\mathrm{div}[\boldsymbol{\sigma}] + \rho\, (\boldsymbol{b}\ -\ \ddot{\boldsymbol{x}}))\ \mathrm{d}v\ =\ \boldsymbol{0}, \tag{2.39}$$

whereas the local form reads

$$\mathrm{div}[\boldsymbol{\sigma}] + \rho\, (\boldsymbol{b}\ -\ \ddot{\boldsymbol{x}}) = \boldsymbol{0} \qquad \forall\ \boldsymbol{x}\ \in \mathcal{B}_t. \tag{2.40}$$

Transferring Eq. 2.39 to the reference placement, one obtains the local statement as

$$\mathrm{Div}[\boldsymbol{P}] + \rho_0(\boldsymbol{b} - \ddot{\boldsymbol{x}}) = \boldsymbol{0} \tag{2.41}$$

with the relation

$$\int_{\mathcal{B}_t} \mathrm{div}[\boldsymbol{\sigma}]\, \mathrm{d}v = \int_{\partial\mathcal{B}_t} \boldsymbol{\sigma} \cdot \boldsymbol{n}\, \mathrm{d}a = \int_{\partial\mathcal{B}_t} \boldsymbol{t}\, \mathrm{d}a = \int_{\partial\mathcal{B}_0} \boldsymbol{P} \cdot \boldsymbol{N} \mathrm{d}A = \int_{\mathcal{B}_0} \mathrm{Div}[\boldsymbol{P}]\, \mathrm{d}V. \tag{2.42}$$

Balance of Angular Momentum

The *balance of angular momentum* states that the temporal change of the angular momentum $\boldsymbol{h}_{(0)}$ with respect to a reference point (0) is equal to the resultant moment $\boldsymbol{m}_{(0)}$ of the forces acting on a body $\mathcal{B}_t$, such that

$$\dot{\boldsymbol{h}}_{(0)} = \boldsymbol{m}_{(0)} \quad \text{with} \tag{2.43}$$

$$\boldsymbol{h}_{(0)} = \int_{\mathcal{B}_t} \boldsymbol{x} \times \rho \boldsymbol{v}\, \mathrm{d}v \quad \text{and} \quad \boldsymbol{m}_{(0)} = \int_{\partial\mathcal{B}_t} \boldsymbol{x} \times \boldsymbol{t}\, \mathrm{d}a + \int_{\mathcal{B}_t} \boldsymbol{x} \times \rho\, \boldsymbol{b}\, \mathrm{d}v. \tag{2.44}$$

with $\boldsymbol{x}$ describing the lever arm with respect to the reference point. The time derivative of angular momentum reads

$$\dot{\boldsymbol{h}}_{(0)} = \frac{\mathrm{d}}{\mathrm{d}}t \int_{\mathcal{B}_t} \boldsymbol{x} \times \rho \boldsymbol{v}\, \mathrm{d}v\ =\ \int_{\mathcal{B}_t} \boldsymbol{x} \times \rho \ddot{\boldsymbol{x}}\, \mathrm{d}v, \tag{2.45}$$

under consideration of the conservation of mass. The resultant moment of forces acting on the body can be reformulated using the divergence theorem, Eq. (A.9), i.e.,

$$\boldsymbol{m}_{(0)} = \int_{\mathcal{B}_t} \boldsymbol{x} \times \rho\, \boldsymbol{b}\, \mathrm{d}v + \int_{\partial\mathcal{B}_t} \boldsymbol{x} \times \boldsymbol{\sigma} \cdot \boldsymbol{n}\, \mathrm{d}a = \int_{\mathcal{B}_t} \left(\boldsymbol{x} \times (\rho\, \boldsymbol{b} + \mathrm{div}\,[\boldsymbol{\sigma}]) + \boldsymbol{\epsilon} : \boldsymbol{\sigma}^{\mathrm{T}}\right) \mathrm{d}v \tag{2.46}$$

with the permutation tensor $\boldsymbol{\epsilon} = \epsilon_{ijk}$, cf. Eq. (A.7). Inserting Eq. (2.45) and Eq. (2.46) into Eq. (2.43) and using the balance of linear momentum, Eq. (2.41), one obtains

$$\int_{\mathcal{B}_t} \boldsymbol{\epsilon} : \boldsymbol{\sigma}^{\mathrm{T}} \mathrm{d}v = 0, \qquad \boldsymbol{\epsilon} : \boldsymbol{\sigma}^{\mathrm{T}} = 0 \qquad \forall\ \boldsymbol{x}\ \in \mathcal{B}_t, \tag{2.47}$$

which due to the definition of $\boldsymbol{\epsilon}$ leads to the important condition

$$\boldsymbol{\sigma} = \boldsymbol{\sigma}^{\mathrm{T}}, \tag{2.48}$$

expressing the symmetry of the Cauchy stress tensor $\boldsymbol{\sigma}$, which is also known as *Cauchy's second equation of motion*. From Eq. (2.29), Eq. (2.30) and Eq. (2.48), the second Piola Kirchhoff stress tensor $\boldsymbol{S}$ and the Kirchhoff stress tensor $\boldsymbol{\tau}$ are obviously symmetric, since

$$\boldsymbol{S}^{\mathrm{T}} = (J\boldsymbol{F}^{-1} \cdot \boldsymbol{\sigma} \cdot \boldsymbol{F}^{-\mathrm{T}})^{\mathrm{T}} = (J(\boldsymbol{F}^{-\mathrm{T}})^{\mathrm{T}} \cdot \boldsymbol{\sigma}^{\mathrm{T}} \cdot \boldsymbol{F}^{-\mathrm{T}}) = J\boldsymbol{F}^{-1} \cdot \boldsymbol{\sigma} \cdot \boldsymbol{F}^{-\mathrm{T}} = \boldsymbol{S} \tag{2.49}$$

and

$$\boldsymbol{\tau}^{\mathrm{T}} = (J\boldsymbol{\sigma})^{\mathrm{T}} = J\boldsymbol{\sigma}^{\mathrm{T}} = J\boldsymbol{\sigma} = \boldsymbol{\tau}. \tag{2.50}$$

The first Piola-Kirchhoff stress tensor is unsymmetric, due to the relation

$$\boldsymbol{P}^{\mathrm{T}} = (\boldsymbol{F} \cdot \boldsymbol{S})^{\mathrm{T}} = \boldsymbol{S}^{\mathrm{T}} \cdot \boldsymbol{F}^{\mathrm{T}} = \boldsymbol{S} \cdot \boldsymbol{F}^{\mathrm{T}} \neq \boldsymbol{P}. \tag{2.51}$$

Balance of Energy

The *first principle of thermodynamics*, also known as the *balance of energy*, postulates that the time derivative of the kinetic energy $\mathcal{K}$ and internal energy $\mathcal{E}$ is equal to the sum of the power of mechanical work and all other energies $\mathcal{U}_\alpha$, e.g. thermal, electromagnetic, chemical or other sources, which enter or leave a body per unit time. The total kinetic energy of the considered body is defined by

$$\mathcal{K} = \frac{1}{2} \int_{\mathcal{B}_\mathrm{t}} \rho \, \dot{\boldsymbol{x}} \cdot \dot{\boldsymbol{x}} \, \mathrm{d}v \tag{2.52}$$

and the total internal energy is defined by

$$\mathcal{E} = \int_{\mathcal{B}_\mathrm{t}} \rho \, e \, \mathrm{d}v \tag{2.53}$$

with the internal energy density given by e. The power of mechanical work is given by

$$\overset{\circ}{\mathcal{W}} = \int_{\partial\mathcal{B}_\mathrm{t}} \boldsymbol{t} \cdot \dot{\boldsymbol{x}} \, \mathrm{d}a + \int_{\mathcal{B}_\mathrm{t}} \rho \boldsymbol{b} \cdot \dot{\boldsymbol{x}} \, \mathrm{d}v. \tag{2.54}$$

The first principle of thermodynamics can be rewritten using these abbreviations to

$$\frac{\mathrm{d}}{\mathrm{d}t}(\mathcal{K} + \mathcal{E}) = \overset{\circ}{\mathcal{W}} + \sum_\alpha \mathcal{U}_\alpha \tag{2.55}$$

Subsequently, the time rate of kinetic and internal energy are derived by

$$\dot{\mathcal{K}} = \int_{\mathcal{B}_\mathrm{t}} \rho \, \dot{\boldsymbol{x}} \cdot \ddot{\boldsymbol{x}} \, \mathrm{d}v \tag{2.56}$$

and

$$\dot{\mathcal{E}} = \int_{\mathcal{B}_\mathrm{t}} \rho \, \dot{e} \, \mathrm{d}v \tag{2.57}$$

with the use of balance equation of mass, Eq. (2.35). The power of mechanical work can be reformulated to

$$\overset{\circ}{\mathcal{W}} = \int_{\mathcal{B}_\mathrm{t}} (\rho \, \dot{\boldsymbol{x}} \cdot \ddot{\boldsymbol{x}} + \boldsymbol{\sigma} : \boldsymbol{D}) \, \mathrm{d}v \tag{2.58}$$

using the divergence theorem Eq. (A.9) and the balance of linear momentum, Eq. (2.41), as well as the symmetry of the stresses arising from the balance of angular momentum,

Eq. (2.48). Here, we restrict ourselves to thermal energy sources only. The rate of thermal energy is given by

$$\mathcal{Q} = \int_{\mathcal{B}_t} \rho\, r \, \mathrm{d}v - \int_{\partial\mathcal{B}_t} \boldsymbol{q} \cdot \mathrm{d}\boldsymbol{a} \;=\; \int_{\mathcal{B}_t} (\rho\, r - \mathrm{div}[\boldsymbol{q}]\,)\, \mathrm{d}v \tag{2.59}$$

with the external heat source per mass unit r and the heat flux $\boldsymbol{q}$. Reformulating the first principle of thermodynamics using Eq. (2.56), Eq. (2.57), Eq. (2.58) and Eq. (2.59), one obtains the form

$$\int_{\mathcal{B}_t} \rho\, \dot{e}\, \mathrm{d}v = \int_{\mathcal{B}_t} (\boldsymbol{\sigma} : \boldsymbol{D} \;+\; \rho\, r \;-\; \mathrm{div}[\boldsymbol{q}])\, \mathrm{d}v. \tag{2.60}$$

which leads to the local form

$$\rho\, \dot{e} = \boldsymbol{\sigma} : \boldsymbol{D} \;+\; \rho\, r \;-\; \mathrm{div}[\boldsymbol{q}]. \tag{2.61}$$

Work Conjugate Pairs

Using Eq. (2.58), the power of mechanical work $\overset{\circ}{\mathcal{W}}$ can be written as the sum of rate of kinetic energy and internal stress power $\overset{\circ}{\mathcal{W}}_{\mathrm{int}}$

$$\overset{\circ}{\mathcal{W}} = \dot{\mathcal{K}} + \overset{\circ}{\mathcal{W}}_{\mathrm{int}}, \tag{2.62}$$

whereas $\overset{\circ}{\mathcal{W}}$ and $\overset{\circ}{\mathcal{W}}_{\mathrm{int}}$ do not represent differentials with respect to time but can be assumed simply as definitions. The integrand of the internal stress power, $\boldsymbol{\sigma} : \boldsymbol{D}$ denotes the physical quantity of mechanical power or work and is thus also named as *work-conjugated pair*. Further work-conjugated pairs can be derived, cf. Stein and Barthold [146], leading to the possible pairs

$$\overset{\circ}{\mathcal{W}}_{\mathrm{int}} = \int_{\mathcal{B}_t} \boldsymbol{\sigma} : \boldsymbol{D} \, \mathrm{d}v \quad = \int_{\mathcal{B}_0} \boldsymbol{\tau} : \boldsymbol{D} \, \mathrm{d}V \quad = \int_{\mathcal{B}_0} \boldsymbol{P} : \dot{\boldsymbol{F}} \, \mathrm{d}V \quad = \int_{\mathcal{B}_0} \boldsymbol{S} : \dot{\boldsymbol{E}} \, \mathrm{d}V. \tag{2.63}$$

Entropy Inequality

The *second law of thermodynamics*, also known as the axiom of *entropy inequality*, states that the time derivative of total entropy is always greater than or equal to the sum of supply of entropy by heat flux r/θ over the surface $\partial\mathcal{B}_t$ of a body and the internal entropy source of a body $\mathcal{B}$, denoted by $(-1/\theta)\ \boldsymbol{q}$, where θ is the absolute temperature. The total entropy and its time derivative are defined by

$$\mathcal{H} = \int_{\mathcal{B}_t} \rho\, \eta \, \mathrm{d}v\,, \tag{2.64}$$

with the entropy density given by η and the time derivative derived with the use of the balance equation of mass, Eq. (2.35) as

$$\dot{\mathcal{H}} = \int_{\mathcal{B}_t} \rho\, \dot{\eta} \, \mathrm{d}v. \tag{2.65}$$

The second law of thermodynamics then yields

$$\int_{\mathcal{B}_t} \rho\, \dot{\eta} \, \mathrm{d}v \geq \int_{\mathcal{B}_t} \frac{r}{\theta}\, \rho \, \mathrm{d}v - \int_{\partial\mathcal{B}_t} \frac{1}{\theta}\, \boldsymbol{q} \cdot \boldsymbol{n} \, \mathrm{d}a \tag{2.66}$$

which can be reformulated using the divergence theorem, Eq. A.9 yielding

$$\int_{\mathcal{B}_t} \rho\, \dot{\eta}\, \mathrm{d}v \geq \int_{\mathcal{B}_t} \frac{r}{\theta}\, \rho\, - \frac{1}{\theta}\, \mathrm{div}[\boldsymbol{q}]\, \mathrm{d}v \tag{2.67}$$

and the local form

$$\rho\, \dot{\eta} \geq \frac{r}{\theta}\, \rho\, -\, \mathrm{div}\left[\frac{1}{\theta}\, \boldsymbol{q}\right], \tag{2.68}$$

which is known as the *Clausius-Duhem inequality*, named after the german physicist Rudolf Clausius (1822-1888) and the french physicist Pierre Duhem (1861-1916). The reformulation of the term

$$\mathrm{div}[\frac{1}{\theta}\, \boldsymbol{q}] = \boldsymbol{q} \cdot \mathrm{grad}\left[\frac{1}{\theta}\right] + \frac{1}{\theta}\, \mathrm{div}\,[\boldsymbol{q}], \tag{2.69}$$

together with

$$\mathrm{grad}\left[\frac{1}{\theta}\right] = \frac{\partial \theta^{-1}}{\partial \boldsymbol{x}} = -\frac{1}{\theta^2}\, \mathrm{grad}\,[\theta], \tag{2.70}$$

yields the Clausius-Duhem inequality in the form

$$\rho\dot{\eta} - \frac{r}{\theta}\, \rho - \frac{1}{\theta^2}\mathrm{grad}\,[\theta] + \frac{1}{\theta}\, \mathrm{div}\,[\boldsymbol{q}] \geq 0. \tag{2.71}$$

The latter equation can be manipulated using the balance equation of energy, Eq. (2.61), i.e. $-\,\rho\, r\, +\, \mathrm{div}[\boldsymbol{q}] = -\rho\, \dot{e} + \boldsymbol{\sigma} : \boldsymbol{D}$, and multiplication with θ yields

$$\rho(\theta\dot{\eta} - \dot{e}) + \boldsymbol{\sigma} : \boldsymbol{D} - \frac{1}{\theta}\, \mathrm{grad}[\theta] \geq 0. \tag{2.72}$$

Introducing the *Helmholtz free energy* $\hat{\psi} = e - \theta\eta$, which can be derived by the Legendre transformation of the internal energy with respect to the entropy, with its time derivative

$$\dot{\hat{\psi}} = \dot{e} - \dot{\theta}\eta - \theta\dot{\eta} \qquad \Leftrightarrow \qquad \theta\dot{\eta} - \dot{e} = -\dot{\hat{\psi}} + \dot{\theta}\eta, \tag{2.73}$$

Eq. (2.72) can be reformulated to

$$-\rho(\dot{\hat{\psi}} + \dot{\theta}\eta) + \boldsymbol{\sigma} : \boldsymbol{D} - \frac{1}{\theta}\, \mathrm{grad}\,[\theta] \geq 0. \tag{2.74}$$

In the case of thermal independent processes ($\theta = \text{const.}, \boldsymbol{q} = \boldsymbol{0}, \rho\, r = 0$), Eq. (2.74) reduces to

$$\boldsymbol{\sigma} : \boldsymbol{D} - \rho\, \dot{\hat{\psi}} \geq 0. \tag{2.75}$$

It is also referred to as dissipation inequality. The respective form in the reference configuration is obtained by multiplying Eq. (2.75) by J and using the conservation of mass, Eq. (2.32), which results in

$$\boldsymbol{P} : \dot{\boldsymbol{F}} - \rho_0\, \dot{\hat{\psi}} \geq 0. \tag{2.76}$$

Alternatively formulating the free energy per reference volume as $\psi\, =\, \rho_0\, \hat{\psi}$, a relationship can be deduced from Eq. 2.76. Considering the free energy $\psi := \psi(\boldsymbol{F})$, we can modify the entropy inequality

$$\boldsymbol{P} : \dot{\boldsymbol{F}} - \frac{\partial \psi}{\partial \boldsymbol{F}} : \dot{\boldsymbol{F}} \geq 0. \tag{2.77}$$

and derive the constitutive relation for the first Piola-Kirchhoff stress tensor given by

$$\boldsymbol{P} = \frac{\partial \psi}{\partial \boldsymbol{F}}\,. \tag{2.78}$$

2.3 Basic Principles of Material Modeling

In Sect 2.2, the fundamental balance laws have been described, which describe the behavior of a solid continuum body. These balance laws constitute 14 differential equations with the scalar notion of mass conservation providing one equation, the balance of linear momentum providing three equations due to the vectorial form, the tensorial balance of angular momentum providing nine equations and the balance of energy providing one equation due to its scalar form, respectively. Assuming the volume acceleration $\boldsymbol{b}$ and the heat source r as given quantities in the problem, the remaining variables, deformation map $\boldsymbol{\varphi}$, stresses $\boldsymbol{\sigma}$, density ρ, entropy η, strain energy ψ, temperature θ and heat flux $\boldsymbol{q}$ give $3 + 9 + 1 + 1 + 1 + 1 + 3 = 19$ unknown quantities. In order to determine all unknowns in the process, an additional number of $19 - 14 = 5$ equations are needed. For this purpose, constitutive equations can be formulated to close the system of equations. In the isothermal case ($\theta = \text{const.}$, $\boldsymbol{q} = \boldsymbol{0}$), where only 14 unknowns ($\boldsymbol{\varphi}$, $\boldsymbol{\sigma}$, ρ and ψ) need to be determined based of 13 equations, not considering the balance of energy, the constitutive equation typically relates the stress response of a material to the free energy. The derivation of mathematical models which describe the behavior of material bodies are part of the material theory. These models have to obey additional principles developed by e.g. Truesdell and Noll [167]. The most important principles therein are the *principle of consistency*, the *principle of determinism*, the *principle of fading memory*, the *principle of local action*, the *principle of material frame indifference* and the *principle of material symmetry* which will be briefly outlined in the following paragraphs. Further literature can be found in e.g. Marsden and Hughes [88].

The *principle of consistency* states that any constitutive description of a material may not violate the balance principles. In the case that a model additionally obeys the 2nd law of thermodynamics, it is said to be thermodynamically consistent. The *principle of determinism* postulates that the physical quantities in a body is determined by the history of motion and temperature of the body, furthermore, the *principle of fading memory* states that the quantities in the large past do not have an effect on the actual quantities. In a region of a material point P, the motion outside a certain neighborhood of P can be disregarded, as stated in the *principle of local action*, and does not influence in P.

The *principle of material frame indifference*, which is also often called *principle of material objectivity* in the literature, postulates that a physical process has to be invariant under a change of observer. A material point in the reference configuration denoted by $\boldsymbol{X}$ is related to two deformed configurations $\boldsymbol{x}(\boldsymbol{X}) \in \mathcal{B}_t$ and $\boldsymbol{x}^+(\boldsymbol{X}) \in \mathcal{B}_t^+$ where the mapping $\boldsymbol{x} \to \boldsymbol{x}^+$ is a time independent rigid transformation with $\boldsymbol{x}^+ = \boldsymbol{Q} \cdot \boldsymbol{x} + \boldsymbol{c}$ with the orthogonal tensor $\boldsymbol{Q} \in SO(3)$. SO(3) is the special orthogonal group of all tensors representing rigid body rotations with $\det[\boldsymbol{Q}] = 1$ and $\boldsymbol{Q}^{-1} = \boldsymbol{Q}^T$. The quantity $\boldsymbol{c}$ represents a translational vector in $\mathbb{R}^3$. In order to obey objectivity, scalar valued quantity β, vector-valued quantity $\boldsymbol{v}$ and tensor-valued quantity $\boldsymbol{T}$ and their counterparts β^+, $\boldsymbol{v}^+$ and $\boldsymbol{T}^+$ with respect to a rigid body rotation have to fulfill

$$\beta^+ = \beta, \qquad \boldsymbol{v}^+ = \boldsymbol{Q} \cdot \boldsymbol{v}, \qquad \boldsymbol{T}^+ = \boldsymbol{Q} \cdot \boldsymbol{T} \cdot \boldsymbol{Q}^{\mathrm{T}}. \tag{2.79}$$

Considering the deformation gradient with respect to a change of observer yields

$$\boldsymbol{F}^{+} = \text{Grad}\,[\boldsymbol{x}^{+}] = \frac{\partial \boldsymbol{x}^{+}}{\partial \boldsymbol{x}} \cdot \frac{\partial \boldsymbol{x}}{\partial \boldsymbol{X}} = \boldsymbol{Q} \cdot \boldsymbol{F} \tag{2.80}$$

which differs from the objectivity requirement in Eq. (2.79). However, it is objective, since it is a two-point tensor referring to the reference and current configuration, where the index referring to the material configuration X_A is always independent of the observer. The right Cauchy-Green deformation tensor shows the objectivity property

$$\boldsymbol{C}^{+} = (\boldsymbol{F}^{+})^{\mathrm{T}} \cdot \boldsymbol{F}^{+} = \boldsymbol{F}^{\mathrm{T}} \cdot \boldsymbol{Q}^{\mathrm{T}} \cdot \boldsymbol{Q} \cdot \boldsymbol{F} = \boldsymbol{C}, \tag{2.81}$$

showing that a rigid body rotation does not have an effect on the tensor due to its description in the reference placement. Free energy functions fulfilling the principle of objectivity must yield

$$\psi(\boldsymbol{F}) = \psi(\boldsymbol{F}^{+}) = \psi(\boldsymbol{Q} \cdot \boldsymbol{F}), \tag{2.82}$$

whereas the objectivity requirement is directly fulfilled for free energy functions with the dependence on $\boldsymbol{C}$ as

$$\psi(\boldsymbol{C}^{+}) = \psi(\boldsymbol{C}). \tag{2.83}$$

The *principle of material symmetry* states an invariance of the constitutive equations with respect to a change of the reference configuration described by $\boldsymbol{Q} \in \mathcal{G}$ with the symmetry group $\mathcal{G} \subset O(3)$, where $O(3)$ defines the full orthogonal group consisting of all proper and improper rotations. Therein, the position vector is transformed via

$$\boldsymbol{X}^{*} = \boldsymbol{Q} \cdot \boldsymbol{X} \quad \forall \quad \boldsymbol{Q} \in \mathcal{G}, \tag{2.84}$$

with the deformation gradient subsequently yielding

$$\boldsymbol{F}^{*} = \frac{\partial \boldsymbol{x}}{\partial \boldsymbol{X}^{*}} = \frac{\partial \boldsymbol{x}}{\partial \boldsymbol{X}} \cdot \frac{\partial \boldsymbol{X}}{\partial \boldsymbol{X}^{*}} = \boldsymbol{F} \cdot \boldsymbol{Q}^{\mathrm{T}} \tag{2.85}$$

and the right Cauchy Green tensor in the transformed reference configuration given by

$$\boldsymbol{C}^{*} = (\boldsymbol{F}^{*})^{\mathrm{T}} \cdot \boldsymbol{F}^{*} = (\boldsymbol{F} \cdot \boldsymbol{Q}^{\mathrm{T}})^{\mathrm{T}} \cdot (\boldsymbol{F} \cdot \boldsymbol{Q}^{\mathrm{T}}) = \boldsymbol{Q} \cdot \boldsymbol{F}^{\mathrm{T}} \cdot \boldsymbol{F} \cdot \boldsymbol{Q}^{\mathrm{T}} = \boldsymbol{Q} \cdot \boldsymbol{C} \cdot \boldsymbol{Q}^{\mathrm{T}}. \tag{2.86}$$

Tensor valued quantities $\hat{\boldsymbol{P}}$ must fulfill

$$\boldsymbol{Q} \cdot \hat{\boldsymbol{P}}(\boldsymbol{C}) \cdot \boldsymbol{Q}^{\mathrm{T}} = \hat{\boldsymbol{P}}(\boldsymbol{C}^{*}) \quad \forall\, \boldsymbol{Q} \in \mathcal{G} \tag{2.87}$$

whereas scalar valued quantities, such as the free energy function must obey

$$\psi(\boldsymbol{C}) = \psi(\boldsymbol{C}^{*}) \quad \forall\, \boldsymbol{Q} \in \mathcal{G} \tag{2.88}$$

If the symmetry group $\mathcal{G} \equiv O(3)$, the material is said to be isotropic.

3 Finite Element Method

The finite element method (FEM) is a feasible tool for the numerical solution of partial differential equations, e.g. the balance laws introduced in Section 2.2. The method has gained much attention in the last decades and has emerged as a standard numerical tool for analysis, design and optimization of structures and materials in various field of engineering practice and science. For a general overview on the method as well as related principles and algorithms, the interested reader is referred to e.g. Wriggers [174], Bathe [17] and Zienkiewicz and Taylor [181].

In the following, the relevant differential equation and its weak forms obtained by variational principles are presented as well as a brief summary of the linearization of the weak form. Aspects of the discretization in a standard single-field formulation are revisited. The formulation of a tetrahedral finite element using quadratic ansatz functions is given, which will be utilized for the calculation of the numerical examples in this work, unless otherwise stated.

3.1 Variational Formulation

The local balance of momentum, cf. Eq. (2.41), is given by

$$\mathrm{Div}[\boldsymbol{P}] + \rho_0 \boldsymbol{b} = \boldsymbol{0} \tag{3.1}$$

in terms of the first Piola-Kirchhoff stress tensor neglecting inertia terms. The density in the reference configuration is given by ρ_0 and $\boldsymbol{b}$ denotes the body forces on the considered body $\mathcal{B}_0$ in the reference configuration with the surface $\partial\mathcal{B}_0$. The displacement and traction boundary conditions are given by

$$\boldsymbol{u} = \hat{\boldsymbol{u}} \quad \text{on} \quad \partial\mathcal{B}_{\boldsymbol{u}} \qquad \text{and} \qquad \boldsymbol{P}\cdot\boldsymbol{N} = \boldsymbol{t}_0 \quad \text{on} \quad \partial\mathcal{B}_{\overline{\boldsymbol{t}}} \tag{3.2}$$

with $\partial\mathcal{B}_0 := \partial\mathcal{B}_{\boldsymbol{u}} \cup \partial\mathcal{B}_{\overline{\boldsymbol{t}}}$ and $\partial\mathcal{B}_{\boldsymbol{u}} \cap \partial\mathcal{B}_{\overline{\boldsymbol{t}}} = \varnothing$. Eq. (3.1) is also often referred to as the *strong form of equilibrium* whereas the *weak form of equilibrium* can be formulated by applying Galerkin's method, i.e. multiplying the strong form with a test function $\delta\boldsymbol{u}$ and integrating over the considered body $\mathcal{B}_0$, leading to

$$G := \int_{\mathcal{B}_0} \left(\mathrm{Div}[\boldsymbol{P}] + \rho_0 \boldsymbol{b}\right) \cdot \delta\boldsymbol{u} \,\mathrm{d}V = 0\,. \tag{3.3}$$

The test function $\delta\boldsymbol{u}$ has to obey the boundary condition $\delta\boldsymbol{u} = \boldsymbol{0}$ on $\partial\mathcal{B}_{\boldsymbol{u}}$. Reformulating the latter equation using the relation $\mathrm{Div}[\boldsymbol{P}]\cdot\delta\boldsymbol{u} = \mathrm{Div}\left[\boldsymbol{P}^T\cdot\delta\boldsymbol{u}\right] - \boldsymbol{P} : \mathrm{Grad}[\delta\boldsymbol{u}]$ together with Eq. A.9, yields

$$G := \underbrace{\int_{\mathcal{B}_0} \boldsymbol{P} : \mathrm{Grad}[\delta\boldsymbol{u}] \,\mathrm{d}V}_{G^{int}} \underbrace{- \int_{\partial\mathcal{B}_{\overline{\boldsymbol{t}}}} \boldsymbol{t}_0 \cdot \delta\boldsymbol{u} \,\mathrm{d}A - \int_{\mathcal{B}_0} \rho_0 \boldsymbol{b}\cdot\delta\boldsymbol{u} \,\mathrm{d}V}_{G^{ext}} = 0, \tag{3.4}$$

which is equivalent to $G := G^{\mathrm{int}} + G^{\mathrm{ext}} = 0$ with the work of internal and external forces G^{int} and G^{ext}, respectively.

A reformulation of G^{int} in terms of the second Piola-Kirchhoff stress tensor $\boldsymbol{S}$ and the Green-Lagrange strain tensor $\boldsymbol{E}$ yields

$$\boldsymbol{P} : \text{Grad}[\delta\boldsymbol{u}] = \boldsymbol{S} : \boldsymbol{F}^T \cdot \text{Grad}[\delta\boldsymbol{u}] = \boldsymbol{S} : \frac{1}{2}(\boldsymbol{F}^T \cdot \delta\boldsymbol{F} \; + \; \delta\boldsymbol{F}^T \cdot \boldsymbol{F}) = \boldsymbol{S} : \delta\boldsymbol{E} \tag{3.5}$$

with the work of internal forces is then given by

$$G^{int} = \int_{\mathcal{B}_0} \boldsymbol{S} : \delta\boldsymbol{E} \, \mathrm{d}V = \int_{\mathcal{B}_0} \frac{1}{2}\boldsymbol{S} : \delta\boldsymbol{C} \, \mathrm{d}V \, . \tag{3.6}$$

The weak form in terms of the second Piola-Kirchhoff stress tensor then reads

$$G := \underbrace{\int_{\mathcal{B}_0} \frac{1}{2}\boldsymbol{S} : \delta\boldsymbol{C} \, \mathrm{d}V}_{G^{int}} \underbrace{- \int_{\partial\mathcal{B}_{\overline{\boldsymbol{t}}}} \boldsymbol{t}_0 \cdot \delta\boldsymbol{u} \, \mathrm{d}A \; - \; \int_{\mathcal{B}_0} \rho_0 \boldsymbol{b} \cdot \delta\boldsymbol{u} \, \mathrm{d}V}_{G^{ext}} = 0 \, . \tag{3.7}$$

In the case of the existence of a total potential energy functional $\Pi^{tot}(\boldsymbol{u}) = \Pi^{\text{int}}(\boldsymbol{u}) \; + \; \Pi^{\text{ext}}(\boldsymbol{u})$ for the description of the physical body, an equivalent representation of the weak form can be obtained from the principle of stationary potential energy, thus the variation $\delta\Pi^{\text{tot}}(\boldsymbol{u})$ must be zero, where the total potential reads

$$\begin{aligned} \Pi^{\text{tot}} &:= \Pi^{\text{int}} \; + \; \Pi^{\text{ext}} \\ &= \int_{\mathcal{B}_0} W(\boldsymbol{F}) \, \mathrm{d}V \; - \; \int_{\mathcal{B}_0} \rho_0 \boldsymbol{b} \cdot \boldsymbol{u} \, \mathrm{d}V \; - \; \int_{\partial\mathcal{B}_0} \boldsymbol{t}_0 \cdot \boldsymbol{u} \, \mathrm{d}A \, . \end{aligned} \tag{3.8}$$

and the internal part of the weak form can be obtained alternatively from the variation of the potential of internal energy

$$G^{\text{int}} = \delta\Pi^{\text{int}} = \int_{\mathcal{B}_0} \frac{\partial W}{\partial \boldsymbol{F}} : \delta\boldsymbol{F} \, \mathrm{d}V = \int_{\mathcal{B}_0} \boldsymbol{P} \; : \; \text{Grad}[\delta\boldsymbol{u}] \, \mathrm{d}V. \tag{3.9}$$

3.2 Linearization

The functional $G = G(\boldsymbol{u}, \delta\boldsymbol{u})$ from Section 3.1 has to be linearized in order to evaluate it using numerical techniques, such as the Newton-Raphson iteration scheme to find the root of the functional. The linearized weak form of equilibrium reads

$$\text{Lin}\, G(\boldsymbol{u}_k, \delta\boldsymbol{u}, \Delta\boldsymbol{u}) := G(\boldsymbol{u}_k, \delta\boldsymbol{u}) \; + \; \Delta G(\boldsymbol{u}_k, \delta\boldsymbol{u}, \Delta\boldsymbol{u}), \tag{3.10}$$

where $\boldsymbol{u} = \boldsymbol{u}_k$ describes the value at which the linearization is performed. The linearization is obtained using the directional derivative $G(\boldsymbol{u}, \delta\boldsymbol{u})$ at $\boldsymbol{u}_k$ in the direction of $\Delta\boldsymbol{u}$ with the linear increment $\Delta G(\boldsymbol{u}_k, \delta\boldsymbol{u}, \Delta\boldsymbol{u})$ given by

$$\Delta G(\boldsymbol{u}_k, \delta\boldsymbol{u}, \Delta\boldsymbol{u}) = \frac{\mathrm{d}}{\mathrm{d}\epsilon} \left[G(\boldsymbol{u}_k + \epsilon\Delta\boldsymbol{u}, \delta\boldsymbol{u}) \right] |_{\epsilon=0} \; = \; \mathrm{D}G(\boldsymbol{u}_k, \delta\boldsymbol{u}) \cdot \Delta\boldsymbol{u} \tag{3.11}$$

where $\Delta\boldsymbol{u}$ are the incremental displacements and ϵ is a small scalar value. Considering conservative loads $\rho_0\boldsymbol{b}$ and $\boldsymbol{t}_0$, the directional derivative of the external parts of work G^{ext} vanish, thus it remains

$$\Delta G(\boldsymbol{u}_k, \delta\boldsymbol{u}, \Delta\boldsymbol{u}) = \mathrm{D}G^{int}(\boldsymbol{u}_k, \delta\boldsymbol{u}) \cdot \Delta\boldsymbol{u} = \int_{\mathcal{B}_0} \frac{1}{2}\Delta\boldsymbol{S} : \delta\boldsymbol{C} \, \mathrm{d}V + \int_{\mathcal{B}_0} \frac{1}{2}\boldsymbol{S} \cdot \Delta\delta\boldsymbol{C} \, \mathrm{d}V \tag{3.12}$$

with the increment of the second Piola-Kirchhoff stress tensor $\boldsymbol{S}$ as well as the increment of the Cauchy Green deformation tensor $\boldsymbol{C}$ given by

$$\begin{aligned} \Delta \boldsymbol{S} &= \mathbb{C} : \frac{1}{2}\Delta \boldsymbol{C} \quad \text{with} \quad \mathbb{C} = 2\frac{\partial \boldsymbol{S}}{\partial \boldsymbol{C}} = 4\frac{\partial^2 \psi}{\partial \boldsymbol{C} \partial \boldsymbol{C}}, \\ \Delta \boldsymbol{C} &= \Delta \boldsymbol{F}^T \boldsymbol{F} \; + \; \boldsymbol{F}^T \Delta \boldsymbol{F}, \\ \Delta \delta \boldsymbol{C} &= \Delta \boldsymbol{F}^T \delta \boldsymbol{F} \; + \; \delta \boldsymbol{F}^T \Delta \boldsymbol{F}. \end{aligned} \tag{3.13}$$

The material tangent is denoted by $\mathbb{C}$ given as a fourth order tensor. The linearization of the weak form then reads

$$\begin{aligned} \operatorname{Lin} G(\boldsymbol{u}_k, \delta \boldsymbol{u}, \Delta \boldsymbol{u}) = &\int_{\mathcal{B}_0} \frac{1}{2}\boldsymbol{S} : \delta \boldsymbol{C} \, \mathrm{d}V - \int_{\mathcal{B}_0} \rho_0 \boldsymbol{b} \cdot \delta \boldsymbol{u} \, \mathrm{d}V \; - \int_{\partial \mathcal{B}_0} \boldsymbol{t}_0 \cdot \delta \boldsymbol{u} \, \mathrm{d}A \\ &+ \int_{\mathcal{B}_0} \frac{1}{2}\delta \boldsymbol{C} \; : \mathbb{C} \; : \; \frac{1}{2}\Delta \boldsymbol{C} \, \mathrm{d}V + \int_{\mathcal{B}_0} \frac{1}{2}\boldsymbol{S} : \Delta \delta \boldsymbol{C} \, \mathrm{d}V \end{aligned} \tag{3.14}$$

considering Eq. (3.12) and Eq. (3.13). With the condition $\operatorname{Lin} G = 0$, Eq. (3.14) is used to compute the discrete incremental displacements $\Delta \boldsymbol{u}$ in each iteration step of the Newton-Raphson scheme. The update of the displacement variable is performed by $\boldsymbol{u}_{k,n+1} = \boldsymbol{u}_{k,n} + \Delta \boldsymbol{u}_{n+1}$. The iteration is continued until the residual $G(\boldsymbol{u}_k, \delta \boldsymbol{u})$ reaches a value below a certain tolerance.

3.3 Discretization

In order to solve the afore mentioned weak form using the finite element method, the considered continuum body $\mathcal{B}_0$ has to be discretized. The body is thereby replaced by an approximation $\mathcal{B}^h$ which consists of a number of n_{ele} finite elements $\mathcal{B}^e$ as illustrated in Fig. 3.1, such that

$$\mathcal{B}_0 \; \approx \; \mathcal{B}^h = \bigcup_{e=1}^{n_{\text{ele}}} \mathcal{B}^e. \tag{3.15}$$

Using the isoparametric concept, the same ansatz functions are used to describe the geometry as well as the field of unknowns, which is here the displacement field $\boldsymbol{u}$. Subsequently,

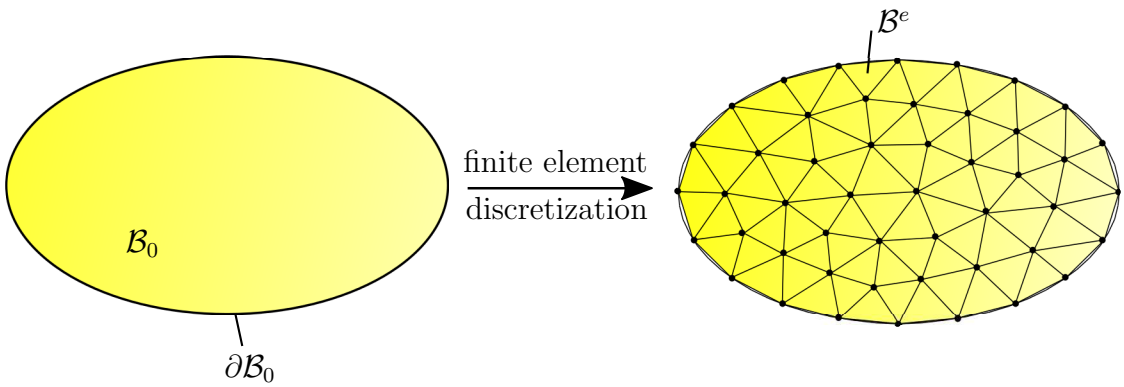

Figure 3.1: Discretization of body $\mathcal{B}_0$ with the boundary $\partial \mathcal{B}_0$ approximated by $\mathcal{B}^h$ resulting from a union of $\mathcal{B}^e$.

the approximation of the geometry given by the position vectors $\boldsymbol{X}$ and $\boldsymbol{x}$ in the reference and actual configuration, respectively, is given by

$$\boldsymbol{X}(\boldsymbol{\xi}) = \sum_{I=1}^{n_{\text{node}}} N_I(\boldsymbol{\xi}) \boldsymbol{X}_I \quad \text{and} \quad \boldsymbol{x}(\boldsymbol{\xi}) = \sum_{I=1}^{n_{\text{node}}} N_I(\boldsymbol{\xi}) \boldsymbol{x}_I \tag{3.16}$$

where $N_I(\boldsymbol{\xi})$ are the ansatz functions dependent on the natural coordinate vector $\boldsymbol{\xi} := [\xi,\, \eta,\, \chi]^T$, n_{node} denotes the total number of nodes per element with I as the local node and $\boldsymbol{X}_I$ and $\boldsymbol{x}_I$ are the nodal coordinates in the reference and actual placement with $\boldsymbol{x}_I = \boldsymbol{X}_I + \boldsymbol{d}_I$, where $\boldsymbol{d}_I$ are the discrete nodal displacements. For the mapping in the isoparametric space to the reference and actual space, the so-called Jacobians in each configuration are introduced with

$$\boldsymbol{J} = \frac{\partial \boldsymbol{X}}{\partial \boldsymbol{\xi}} \quad \text{and} \quad \boldsymbol{j} = \frac{\partial \boldsymbol{x}}{\partial \boldsymbol{\xi}}, \quad \text{with} \quad \boldsymbol{j} = \boldsymbol{F}\boldsymbol{J}. \tag{3.17}$$

The approximation of the physical, incremental and virtual displacements is given by

$$\boldsymbol{u} = \sum_{I=1}^{n_{\text{node}}} N_I(\boldsymbol{\xi}) \boldsymbol{d}_I, \quad \Delta\boldsymbol{u} = \sum_{I=1}^{n_{\text{node}}} N_I(\boldsymbol{\xi}) \Delta\boldsymbol{d}_I, \quad \delta\boldsymbol{u} = \sum_{I=1}^{n_{\text{node}}} N_I(\boldsymbol{\xi}) \delta\boldsymbol{d}_I. \tag{3.18}$$

The virtual and incremental deformation gradient using index notation is given by

$$\delta F^a{}_A = \operatorname{Grad} \delta u^a{}_{,A} = \sum_{I=1}^{n_{\text{node}}} N_{I,A}\, \delta d_I^a \tag{3.19}$$

$$\Delta F^a{}_A = \operatorname{Grad} \Delta u^a{}_{,A} = \sum_{I=1}^{n_{\text{node}}} N_{I,A}\, \Delta d_I^a. \tag{3.20}$$

The derivative of the ansatz function with respect to the reference coordinate X_A can be derived from

$$\frac{\partial N_I}{\partial \boldsymbol{X}} = \frac{\partial N_I}{\partial \boldsymbol{\xi}} \frac{\partial \boldsymbol{\xi}}{\partial \boldsymbol{X}} = \frac{\partial N_I}{\partial \boldsymbol{\xi}} \boldsymbol{J}^{-1}. \tag{3.21}$$

In order to obtain a matrix notation form for the tensorial formulation of the used quantities, the Voigt notation, cf. Appendix A, can be used, where second order tensors are reordered into vector form and fourth order tensors are converted to matrices. Using this notation, the incremental and variation of the right Cauchy-Green tensor Eq. 3.13 reads

$$\frac{1}{2}\Delta\boldsymbol{C} = \sum_{I=1}^{n_{\text{node}}} \boldsymbol{B}_I\, \Delta\boldsymbol{d}_I \quad \text{and} \quad \frac{1}{2}\delta\boldsymbol{C} = \sum_{I=1}^{n_{\text{node}}} \boldsymbol{B}_I\, \delta\boldsymbol{d}_I. \tag{3.22}$$

The so-called *B-matrix* is given by

$$\boldsymbol{B}_I = \begin{bmatrix} F_{11}\, N_{I,1} & F_{21}\, N_{I,1} & F_{31}\, N_{I,1} \\ F_{12}\, N_{I,2} & F_{22}\, N_{I,2} & F_{32}\, N_{I,2} \\ F_{13}\, N_{I,3} & F_{23}\, N_{I,3} & F_{33}\, N_{I,3} \\ F_{11}\, N_{I,2} + F_{12}\, N_{I,1} & F_{21}\, N_{I,2} + F_{22}\, N_{I,1} & F_{31}\, N_{I,2} + F_{32}\, N_{I,1} \\ F_{12}\, N_{I,3} + F_{13}\, N_{I,2} & F_{22}\, N_{I,3} + F_{23}\, N_{I,2} & F_{32}\, N_{I,3} + F_{33}\, N_{I,2} \\ F_{11}\, N_{I,3} + F_{13}\, N_{I,1} & F_{21}\, N_{I,3} + F_{23}\, N_{I,1} & F_{31}\, N_{I,3} + F_{33}\, N_{I,1} \end{bmatrix}, \tag{3.23}$$

which contains the derivative of the ansatz functions $N_{I,A}$ denoting a derivation of N_I with respect to the coordinate X_A.

With Eq. (3.22) and Eq. (3.23) in hand, we insert the discretizations in the weak form, cf. Eq. 3.7 and obtain

$$\begin{aligned} G^e(\boldsymbol{d}, \delta\boldsymbol{d}) &= \sum_{I=1}^{n_{\text{node}}} \delta\boldsymbol{d}_I^T \left(\int_{\mathcal{B}^e} \boldsymbol{B}_I^T \cdot \boldsymbol{S} \, \mathrm{d}V - \int_{\mathcal{B}^e} N_I \, \rho_0 \boldsymbol{b} \, \mathrm{d}V - \int_{\delta\mathcal{B}^e} N_I \, \boldsymbol{t}_0 \, \mathrm{d}A \right) = 0 \\ &=: \sum_{I=1}^{n_{\text{node}}} \delta\boldsymbol{d}_I^T \boldsymbol{r}_I = (\delta\boldsymbol{d}^e)^T \boldsymbol{r}^e. \end{aligned} \tag{3.24}$$

Herein, $\boldsymbol{r}_I$ denotes the nodal residual vector whereas $\boldsymbol{r}^e$ and $\delta\boldsymbol{d}^e$ represent the residual vector and the virtual displacement vector of the element, respectively, given as

$$(\delta\boldsymbol{d}^e) = \left[\delta\boldsymbol{d}_1^T \,|\, \delta\boldsymbol{d}_2^T \,|\, \ldots \,|\, \delta\boldsymbol{d}_{n_{\text{node}}}^T\right]^T \quad \text{and} \quad \boldsymbol{r}^e = \left[\boldsymbol{r}_1^T \,|\, \boldsymbol{r}_2^T \,|\, \ldots \,|\, \boldsymbol{r}_{n_{\text{node}}}^T\right]^T \tag{3.25}$$

The remaining terms in Eq. (3.14) associated with ΔG also have to be discretized. They are often referred to as material part ΔG^{mat} and geometrical part ΔG^{geo}, with

$$\Delta G^{\text{mat}} = \int_{\mathcal{B}_0} \frac{1}{2}\delta\boldsymbol{C} \,:\mathbb{C}:\, \frac{1}{2}\Delta\boldsymbol{C} \, \mathrm{d}V \quad \text{and} \quad \Delta G^{\text{geo}} = \int_{\mathcal{B}_0} \frac{1}{2}\boldsymbol{S} : \Delta\delta\boldsymbol{C} \, \mathrm{d}V \,. \tag{3.26}$$

The approximation of the linearized virtual right Cauchy-Green tensor is obtained using (3.19) and (3.20) and is calculated by

$$\begin{aligned} \frac{1}{2}\Delta\delta C_{AB} &= \frac{1}{2}\left(\delta F^a{}_A \, \delta_{ab} \, \Delta F^b{}_B + \Delta F^a{}_A \, \delta_{ab} \, \delta F^b{}_B\right) \\ &= \frac{1}{2}\left(N_{I,A}\delta d_I^a \, \delta_{ab} \sum_{J=1}^{n_{\text{node}}} \sum_{I=1}^{n_{\text{node}}} N_{J,B}\Delta d_J^b + \sum_{I=1}^{n_{\text{node}}} N_{I,A}\Delta d_I^a \, \delta_{ab} \sum_{J=1}^{n_{\text{node}}} N_{J,B}\delta d_J^b \right) \\ &= \sum_{I=1}^{n_{\text{node}}} \sum_{J=1}^{n_{\text{node}}} N_{I,A}\delta d_I^a \, \delta_{ab} N_{J,B}\Delta d_J^b \,, \end{aligned} \tag{3.27}$$

with δ denoting the Kronecker symbol. Therewith, the discrete formulation of the linearized weak form, cf. Eq. (3.14), for one finite element is given by

$$\mathrm{Lin}\, G^e = \sum_{I=1}^{n_{\text{node}}} \delta\boldsymbol{d}_I^T \boldsymbol{r}_I + \sum_{I=1}^{n_{\text{node}}} \sum_{J=1}^{n_{\text{node}}} \delta\boldsymbol{d}_I^T \underbrace{(\boldsymbol{k}_{IJ}^{e,\text{mat}} + \boldsymbol{k}_{IJ}^{e,\text{geo}})}_{\boldsymbol{k}_{IJ}^e} \Delta\boldsymbol{d}_J = 0 \,. \tag{3.28}$$

The material part of the stiffness matrix is defined by

$$\boldsymbol{k}_{IJ}^{e,\text{mat}} = \int_{\mathcal{B}^e} \boldsymbol{B}_I^T \, \hat{\mathbb{C}} \, \boldsymbol{B}_J \mathrm{d}V \tag{3.29}$$

with $\hat{\mathbb{C}}$ in matrix representation, cf. Eq. (A.17), of the material tangent modulus $\mathbb{C} = 2\partial_{\boldsymbol{C}}\boldsymbol{S}$. The geometric part is defined by

$$\boldsymbol{k}_{IJ}^{e,\text{geo}} = \int_{\mathcal{B}^e} (N_{I,A}N_{J,B}) S^{AB} \mathrm{d}V. \tag{3.30}$$

For the global discrete representation of Eq. (3.14), the use of the assembly operator yields the global stiffness matrix $\boldsymbol{K}$ and residual vector $\boldsymbol{R}$, with

$$\boldsymbol{K} = \mathop{\mathsf{A}}_{e=1}^{n_{\text{ele}}} \boldsymbol{k}^e, \quad \boldsymbol{R} = \mathop{\mathsf{A}}_{e=1}^{n_{\text{ele}}} \boldsymbol{r}^e \quad \Rightarrow \quad \delta \boldsymbol{D}^T (\boldsymbol{K} \Delta \boldsymbol{D} + \boldsymbol{R}) = 0, \tag{3.31}$$

with the global virtual and incremental displacement vectors

$$\begin{aligned} \delta \boldsymbol{D} &= \left[(\delta \boldsymbol{d}^1)^T \,|\, (\delta \boldsymbol{d}^2)^T \,|\, \ldots \,|\, (\delta \boldsymbol{d}^{n_{\text{ele}}})^T \right]^T \\ \Delta \boldsymbol{D} &= \left[(\Delta \boldsymbol{d}^1)^T \,|\, (\Delta \boldsymbol{d}^2)^T \,|\, \ldots \,|\, (\Delta \boldsymbol{d}^{n_{\text{ele}}})^T \right]^T . \end{aligned} \tag{3.32}$$

Eq. (3.31(2)) can be solved using Newton-Raphson scheme where $\Delta \boldsymbol{D} = -\boldsymbol{K}^{-1} \boldsymbol{R}$ is used to update the global nodal displacements by $\boldsymbol{D} \Leftarrow \boldsymbol{D} + \Delta \boldsymbol{D}$ until the global residual vector $\boldsymbol{R}$ is smaller than a given tolerance and convergence is reached.

For the integration of the equations for the element stiffness matrix and element residual vector, analytical solutions are typically not possible. Therefore, numerical integration is used, e.g. Gauss integration procedure. Therein, the integral is evaluated numerically by replacing it with the weighted sum of the integrand's values at predefined points in the considered integration domain. For details on the procedure, the reader is referred to classical textbooks of mathematics and the finite element method, e.g. Zienkiewicz and Taylor [181].

3.4 10-noded Tetrahedral Finite Element

In this work, tetrahedral elements are used for the discretization since they serve well for the discretization of the complex three-dimensional geometries. Finite elements with linear interpolation functions are known to exhibit locking effects. For detailed information on locking effects and formulations which prevent locking, the reader is referred to Bathe [17]. Here, a quadratic formulation is chosen. In the three-dimensional case, 10-noded quadratic tetrahedral finite elements can be formulated in terms of the isoparametric concept with the isoparametric space given by the natural coordinates, i.e. $\xi \in [0,1]$, $\eta \in [0,1]$ and $\zeta \in [0,1]$ with the ansatz functions

$$\begin{aligned} N_1 &= \lambda(2\lambda - 1), & N_6 &= 4\xi\eta, \\ N_2 &= \xi(2\xi - 1), & N_7 &= 4\eta\lambda, \\ N_3 &= \eta(2\eta - 1), & N_8 &= 4\zeta\lambda, \\ N_4 &= \zeta(1\zeta - 1), & N_9 &= 4\xi\zeta, \\ N_5 &= 4\xi\lambda, & N_{10} &= 4\eta\zeta, \end{aligned} \tag{3.33}$$

where $\lambda = 1 - \xi - \eta - \zeta$. These ansatz functions are used to approximate the geometry as well as the displacements using Eq. (3.16) and Eq. (3.18), respectively. Fig. 3.2 illustrates the isoparametric 10-noded tetrahedral finite element in the isoparametric space Ω_e in the undeformed reference state. For Gauss integration, five Gauss points are used with the coordinates

$$\begin{aligned} \xi_1 &= \frac{1}{4}, & \xi_2 &= \frac{1}{6}, & \xi_3 &= \frac{1}{6}, & \xi_4 &= \frac{1}{6} & \xi_5 &= \frac{1}{2}, \\ \eta_1 &= \frac{1}{4}, & \eta_2 &= \frac{1}{6}, & \eta_3 &= \frac{1}{6}, & \eta_4 &= \frac{1}{2} & \xi_5 &= \frac{1}{6}, \\ \zeta_1 &= \frac{1}{4}, & \zeta_2 &= \frac{1}{6}, & \zeta_3 &= \frac{1}{2}, & \zeta_4 &= \frac{1}{6} & \zeta_5 &= \frac{1}{6}, \end{aligned} \tag{3.34}$$

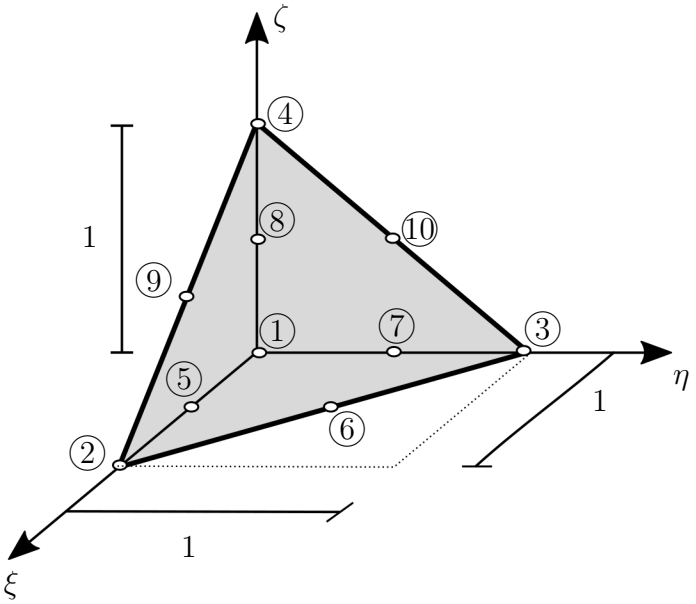

Figure 3.2: Tetrahedral finite element with 10 nodes in isoparametric space.

in the isoparametric space and the associated weighting factors

$$\omega_1 = -\frac{2}{15}\,, \quad \omega_2 = \frac{3}{40}\,, \quad \omega_3 = \frac{3}{40}\,, \quad \omega_4 = \frac{3}{40}\,, \quad \omega_5 = \frac{3}{40}\,. \tag{3.35}$$

4 Modeling of Dual Phase Steel

In this work, an approach to multiscale modeling of the mechanical behavior of dual-phase (DP) steel microstructures is presented. This chapter first gives an overview on the specific material properties of DP steel, its production process and computational approaches found in the literature. Subsequently, the constitutive framework for finite J_2-plasticity which is here used for the material modeling of the individual phases of DP steel, ferrite and martensite, is revisited. This phenomenological material model is used for the numerical examples in Section 6 and Section 7 for the description of the DP steel material behavior. With the aim of including the specific crystallographic texture properties into the modeling approach, an overview on the plastic behavior of a crystalline solid is given. The framework for a small strain crystal plasticity model is discussed, which is used in Section 8 for the simulations incorporating polycrystalline microstructures as an RVE.

4.1 Production, Material Properties and Computational Modeling

In the following, an overview on dual-phase (DP) steel regarding its specific material properties, manufacturing process and computational modeling approaches is given. For further details, it is referred to the extensive overviews given in Rashid [116] and Tasan et al. [157].

DP steel is the most prominent candidate among advanced high-strength steels (AHSS), which were the first alloyed steels finding application in automotive components with the aim for an improvement of crash safety at constant weight. DP steel is typically composed of a ferritic matrix phase with embedded martensitic inclusions. The microstructure morphology can be adapted in the production process and results in a variation of deformation behavior and damage phenomena in the resulting product. The beneficial material properties of DP steel for industrial applications are the high ultimate tensile strength, which is a result of the high strength of the martensite phase, and the low initial yield stress, enabled by the ductility of the ferrite phase. Fig. 4.1 confronts the mechanical properties of DP steel within the class of AHSS comparing the total elongation versus the ultimate tensile strength. More recent generations of AHSS, such as twinning-induced plasticity (TWIP) steels and transformation-induced plasticity (TRIP) steels show a higher ductility compared to DP steels while maintaining or exceeding the strength level. However, they are accompanied by issues in practical application, including welding difficulties, high alloy costs and casting problems, cf. Tasan et al. [157].

The mechanical properties of DP steel strongly depend on the microstructural properties, such as volume fraction of martensite, martensite grain size, martensite carbon content, ferrite grain size and ferrite-martensite morphology. The major driving force for the relevant features of DP steel material properties is the phase contrast between ferrite and martensite, where the complex morphology of the microstructure plays an important role. An increase of martensite carbon content and/or martensite volume fraction results in an increase in strength, but reduces ductility at the same time. The three most critical microstructural parameters were investigated in Pierman et al. [110] in detail, observing that an increase in martensite volume fraction increases both the yield stress and ultimate tensile strength, while a raise of martensite carbon content increases the strain hardening and tensile strength but had no effect on the yield point. Regarding microstructure mor-

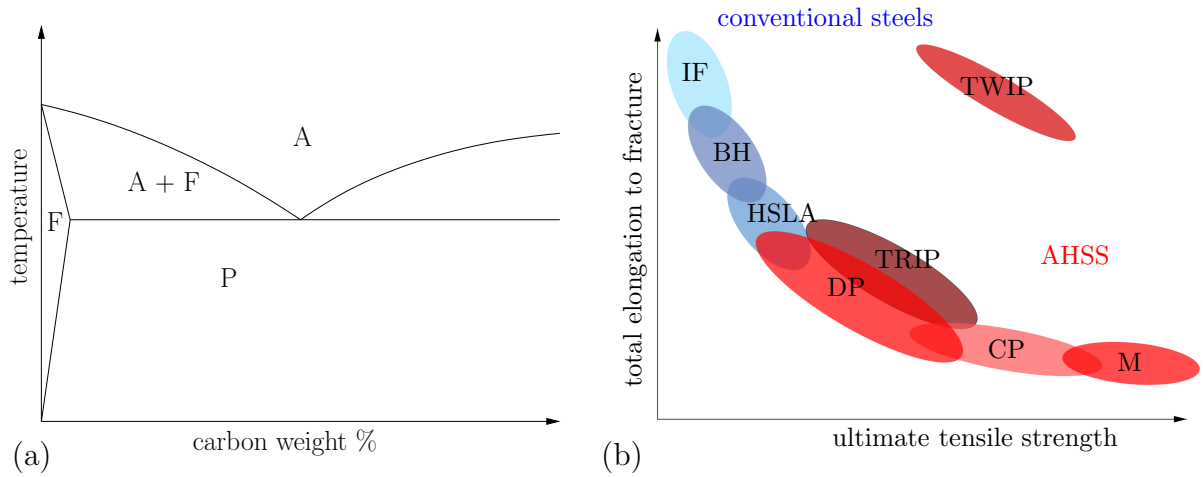

Figure 4.1: (a) Sketch of Fe-C diagram. Abbreviations: ferrite (F), austenite (A), pearlite (P). (b) Comparison of mechanical properties for conventional steels and advanced high strength steels (AHSS). Abbreviations: Interstitial free ferrite- (IF), bake hardening- (BH), high strength low alloy- (HSLA), dual-phase- (DP) transformation induced plasticity- (TRIP), twinning induced plasticity- (TWIP), complex phase- (CP), martensitic (M) steel.

phology, equiaxed microstructures show higher strength and lower ductility in comparison with a microstructure composed of finely dispersed, elongated martensite particles. Various studies have shown that grain refinement of the ferrite phase is capable to improve the DP steel toughness, see ,e.g., Delincé et al. [34] and Mukherjee et al. [101]. Grain refinement can be achieved through, e.g., cold swaging. Following the Hall-Petch relation, grain refinement to the ultrafine grain regime increases tensile as well as yield strength, cf. Calcagnotto et al. [26].

The first attempts in the manufacturing of DP steel go back to the 1970s, industrial manufacturing started to establish in the 1990s. DP steel is produced from ferrite-pearlite steel which is heated to the temperature range of austenite-ferrite regime ($\approx 750°C$), or fully austenitic regime ($\approx 850°C$), followed by a rapid cooling below martensite start temperature ($\approx 220°C$), which causes austenite to transform to martensite, Tasan et al. [157]. A schematic illustration of the Fe-C diagram is shown in Fig. 4.1. It has to be noted that the rapid cooling process in the manufacturing of DP steel leads to the formation of martensite instead of pearlite, contrary to the indication in the classical Fe-C diagram. Therefore, a diagram including the influence of cooling rate is shown in Fig. 4.2. Two cooling rates are indicated, where the first one starts from the ferrite-austenite regime and is cooled to a temperature where martensite forming starts. The second one starts from the pure austenitic regime and passes through a zone where austenite-to-ferrite transformation is present, before reaching the temperature region of martensite formation. During the heating process, recrystallization, phase transformation and carbon diffusion are relevant mechanisms, which influence the resulting material and thus the mechanical properties. Depending on the final temperature during heating as well as heating rate, different combinations of these processes are active. An extensive overview is given in Tasan et al. [157]. DP steel typically has a carbon content of $0.06 - 0.15$ wt.% and further contains small amounts of alloys, among which are manganese (Mn), chrome (Cr) and silicium (Si) leading to a suppression of pearlite and bainite formation as well as promotion of austenite-to-ferrite transformation during cooling. The composition of DP steel may also incorporate austenite, pearlite, bainite and carbides, depending on the

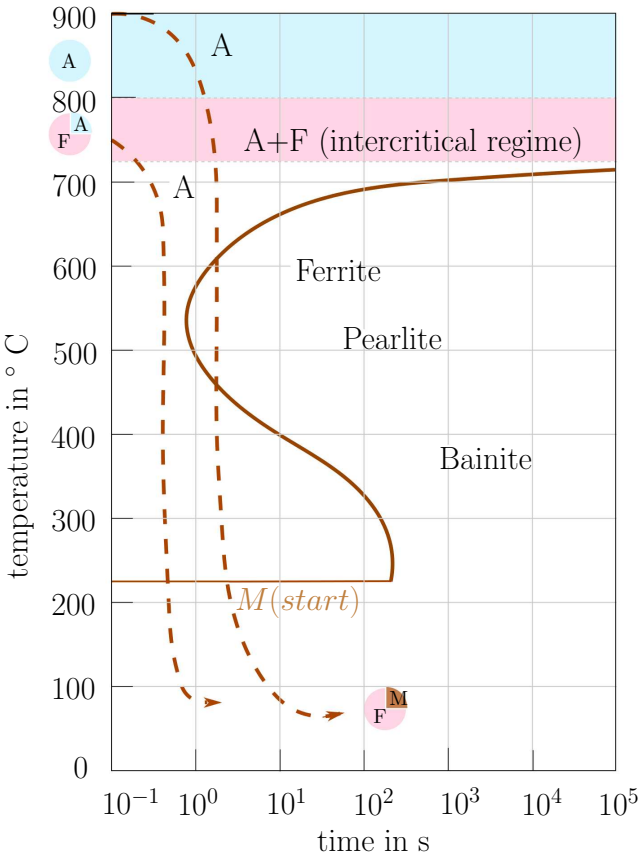

Figure 4.2: Sketch of time-temperature-diagram denoting material composition after different cooling rates. Abbreviations: ferrite (F), austenite (A), martensite (M). Adapted from Tasan et al. [157].

processing route. Retained austenite and bainite can lead to a benefit in formability, cf. Thyssen Krupp Steel Europe AG [163].

Computational modeling of DP steel was performed as early as 1974, Karlsson and Sundström [70], and many effects are still under investigation in current research. The computational approaches target the modeling of different aspects of the material behavior. Approaches modeling the macroscopic behavior often utilize the concept of yield surfaces, however, sophisticated yield surface formulations are necessary to describe the direction-dependent material behavior of DP steel, where e.g. kinematic hardening effects need to be accounted for. The one scale simulation at the component scale, e.g. forming simulations, often disregard microstructural morphology and the crystalline texture of the underlying material in order to achieve a decrease in computational effort. However, accounting for specific phenomena occurring in DP steel due to its microstructural composition, such as the spring-back effect, is necessary for realistic simulations of deformation processes at the component scale. The spring-back effect is an elastic effect resulting in shape discrepancies between the loaded and unloaded state. This effect is especially pronounced in sheet metal forming processes, where major effort of die design for stamping processes is spent upon the investigation and removal of undesired effects due to spring-back, see e.g. Gan and Wagoner [42] and Chen and Koç [28]. The application of anisotropic yield functions combined with isotropic-kinematic hardening laws is utilized in the series Chung et al. [31], Lee et al. [83], Lee et al. [82] to account for the effects due to spring-back.

The aforementioned modeling approaches do not take into account the contribution of microstructural effects directly, contrary to multiscale methods. The latter may utilize representative volume elements (RVEs) of the microstructure, as e.g., the FE^2-method, see Smit et al. [143], Miehe et al. [96], Schröder [130; 131] and the summary in Section 5.2 in this work. Here, a dependence of the macroscopic material behavior on the microstructure is set up. Thereby unmanageable computational costs are avoided which would arise if the microstructure were resolved in the macroscale computation directly. The construction of simplified RVEs, e.g. statistically similar representative volume elements (SSRVEs), possessing statistical similarity compared with an RVE obtained from a real DP steel microstructure can reduce the computational effort, see Section 6. In texture analysis, grain interaction models can be applied for the consideration of microstructural interactions, cf. Tjahjanto et al. [164].

Micromechanical simulations aim for an understanding of the deformation, loading conditions and damage mechanisms on a grain- or even subgrain-scale. Thereby, geometry-oriented models focus on the phase contrast of ferrite and martensite as the main contributor to the specific properties offered by DP steels. In-depth understanding of physical mechanisms involving texture, strain-hardening details, damage models and crystalline deformation models, such as crystal plasticity models, enables scientists to capture extrema in the field quantities, which can be responsible for e.g. damage initiation, using full-field simulations. An issue in micromechanical modeling is the existence of discrepancies between the material properties obtained from bulk material of ferrite and martensite in experiments and the material properties of ferrite and martensite in the DP steel. Varying grain size in ferrite or a variation of carbon content in martensite can lead to different results and, furthermore, the varying material properties due to interactions between the phases are difficult to capture. For instance, the ferritic matrix shows a change in material properties close to martensite grains, which is observed from hardness measurements of ferrite grains at varying distances from martensite inclusions. This local hardening effect in the ferritic matrix originates from the transformation of austenite to martensite. It leads to an accumulation of carbon close to the martensite grains and a volume change of approximately 4% of the martensite phase, cf. Moyer and Ansell [100], Sakaki et al. [124]. The hardness is approximately 1.6 times higher close to the martensitic inclusions, cf. Brands et al. [23]. The local hardening can be represents by models using multiple layers surrounding the inclusion with the yield stress in the layers given as a function of the plastic strain based on experimental results in Kadkhodapour et al. [65]. An approach considering martensitic expansion using volumetric strains is used in Paul [106] and Brands et al. [23], in order to model the increase of yield stress near the martensitic inclusions. A sophisticated approach to model the individual ferrite and martensite behavior in the microstructure based on micropillar measurements is carried out in Chen et al. [29], where computer-generated microstructures are used.

The need for consideration of texture properties in DP steel was recently shown by Pagenkopf et al. [105]. Two modeling approaches for DP steel are compared, one incorporating the morphology of the microstructure and thus accounting for the phase contrast, the second one additionally considering the crystalline texture of the ferrite phase. A comparison of Lankford coefficients shows that the first model fails to describe the material behavior in a realistic way, while the second model achieves a realistic description. This emphasizes the need to consider the complex microstructural

features of materials in order to obtain realistic simulations. Generally, the investigation of the behavior of DP steel at different scales still poses some challenges for future research.

The consideration of a realistic microstructure morphology of DP steel requires three dimensional measurements of the material at a high resolution in the range of micrometers to nanometers. Electron backscatter diffraction (EBSD) combined with a focused ion beam (FIB) can be used to obtain realistic three-dimensional representations of DP steel microstructures, see e.g. Zaafarani et al. [177], Zaefferer et al. [178], Calcagnotto et al. [26], an overview on texture analysis and EBSD is given in Randle and Engler [115]. Fig. 4.3 shows the setup of the EBSD-FIB equipment. EBSD provides a tool for the analysis of the crystallographic structure of a material. The investigated sample is exposed to an electron beam at a specific angle such that the electrons are scattered in different directions as they hit the sample. On a phosphor screen, the backscattered electrons are recorded. Depending on the crystallographic lattice and its global orientation, so-called Kikuchi patterns form on the phosphor screen. Every measured point on the surface of the sample can be associated to a specific texture type by analysis of the Kikuchi pattern, e.g. face centered cubic lattice, and orientation, typically represented in Euler angles. The FIB is used for milling, thus removing a thin layer from the surface of the sample and revealing a new sample surface layer which is measured. The EBSD analysis and FIB milling is performed under different angles of tilt of the sample, see Fig. 4.3, for an automated procedure. The combination of EBSD and FIB thus enables a three dimensional measurement of the microstructure morphology.

In this work, EBSD-FIB measurement of a DP steel are used, which were obtained at Max-Planck Institut für Eisenforschung, Düsseldorf, Germany in the framework of the DFG research group 797 “Microplast”. The measured sample has the size $15.4\,\mu\text{m} \times 16.45\,\mu\text{m} \times 5\,\mu\text{m}$ and has been measured with a spatial resolution of $0.1\,\mu\text{m} \times 0.1\,\mu\text{m} \times 0.1\,\mu\text{m}$ using a hexagonal pattern. The reconstructed DP steel microstructure can be seen in Fig. 4.3, where red and green indicate the ferrite phase and the martensitic inclusions, respectively. Details on the reconstruction of the DP steel microstructure based on the EBSD-FIB data can be found in Brands et al. [23].

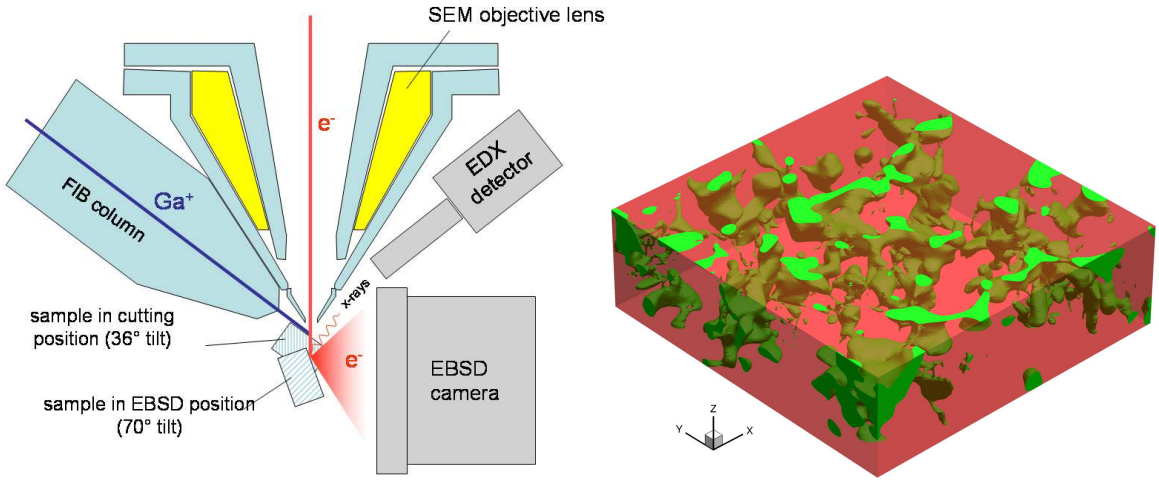

(a) (b)

Figure 4.3: (a) Technical setup for EBSD-FIB analysis, Konrad et al. [74]. (b) Reconstruction of DP steel microstructure based on EBSD-FIB data after postprocessing, Brands et al. [23]. EBSD-FIB measurements were performed at Max-Planck Institut für Eisenforschung, Düsseldorf, Germany.

4.2 Finite J_2-Plasticity

A constitutive framework for the description of elasto-plastic material behavior is presented in the following. It utilizes a von Mises yield criterion, which is suitable for the description of the behavior of ductile materials, such as steel. The presented computational model will be here used to describe the mechanical behavior of the individual phases of DP steel. Computational formulations for elasto-plasticity at finite deformations emerged in the beginning of the 1980s, given by Simo [138; 139], see also Simo and Miehe [142], Peric et al. [109], Miehe and Stein [95] and Miehe [91]. They are based on the multiplicative split of the deformation gradient and utilize a spectral decomposition of the kinematical quantities. The use of a strain measure in terms of the principle logarithmic strain enables the application of return mapping algorithms which have an identical form as in the infinitesimal framework. For more details, it is referred to Simo and Hughes [141], Simo [139; 140] and Klinkel [72] regarding the implementation.

Motivated by the micromechanical description in single crystal metal plasticity, the deformation gradient is locally decomposed multiplicatively into a plastic part and an elastic part, cf. Kröner [78] and Lee [81],

$$\boldsymbol{F} = \boldsymbol{F}^{\mathrm{e}} \cdot \boldsymbol{F}^{\mathrm{p}}, \tag{4.1}$$

introducing a local intermediate configuration which is stress-free and defined by $\boldsymbol{F}^{\mathrm{p}} = \boldsymbol{F}^{\mathrm{e}-1} \cdot \boldsymbol{F}$. The kinematic quantities, i.e. the left and right Cauchy-Green deformation tensor and their corresponding elastic and plastic parts follow as

$$\boldsymbol{C} = \boldsymbol{F}^{\mathrm{T}} \cdot \boldsymbol{F}, \quad \boldsymbol{C}^{\mathrm{e}} = \boldsymbol{F}^{\mathrm{e}\,\mathrm{T}} \cdot \boldsymbol{F}^{\mathrm{e}}, \quad \boldsymbol{C}^{\mathrm{p}} = \boldsymbol{F}^{\mathrm{p}\mathrm{T}} \cdot \boldsymbol{F}^{\mathrm{p}}, \tag{4.2}$$

$$\boldsymbol{B} = \boldsymbol{F} \cdot \boldsymbol{F}^{\mathrm{T}}, \quad \boldsymbol{B}^{\mathrm{e}} = \boldsymbol{F}^{\mathrm{e}} \cdot \boldsymbol{F}^{\mathrm{e}\,\mathrm{T}}, \quad \boldsymbol{B}^{\mathrm{p}} = \boldsymbol{F}^{\mathrm{p}} \cdot \boldsymbol{F}^{\mathrm{p}\,\mathrm{T}}. \tag{4.3}$$

Together with $\boldsymbol{F}^{\mathrm{e}} = \boldsymbol{F} \cdot \boldsymbol{F}^{\mathrm{p}\,-1}$, the relations

$$\boldsymbol{B}^{\mathrm{e}} = \boldsymbol{F} \cdot \boldsymbol{C}^{\mathrm{p}\,-1} \cdot \boldsymbol{F}^{\mathrm{T}} \tag{4.4}$$

$$\boldsymbol{C}^{\mathrm{p}\,-1} = \boldsymbol{F}^{-1} \cdot \boldsymbol{B}^{\mathrm{e}} \cdot \boldsymbol{F}^{\mathrm{T}-1} \tag{4.5}$$

hold, whereas $\boldsymbol{C}^{\mathrm{p}\,-1}$ is defined in the reference configuration, $\boldsymbol{C}^{\mathrm{e}}$ is defined in the intermediate configuration and $\boldsymbol{B}^{\mathrm{e}}$ in the current configuration.

The spectral decomposition of the elastic left Cauchy-Green deformation tensor $\boldsymbol{B}^{\mathrm{e}}$ is given by

$$\boldsymbol{B}^{\mathrm{e}} = \sum_{A=1}^{3} {\lambda_A^{\mathrm{e}}}^2 \, \boldsymbol{n}_A \otimes \boldsymbol{n}_A \tag{4.6}$$

where $\boldsymbol{B}^{\mathrm{e}}$ is reformulated in terms of the principle directions $\boldsymbol{n}_A$ and the principle elastic stretches λ_A^{e}, with ${\lambda_A^{\mathrm{e}}}^2$ as the eigenvalues of $\boldsymbol{B}^{\mathrm{e}}$. Following Simo [139], the elastic stretches λ_1^{e}, λ_2^{e}, λ_3^{e} can be computed by solving the eigenvalue problem $(\boldsymbol{B}^{\mathrm{e}} - {\lambda_A^{\mathrm{e}}}^2 \boldsymbol{I}) \cdot \boldsymbol{n}_A = \boldsymbol{0}$.

The free energy function takes the form

$$\psi = \psi(\boldsymbol{B}^{\mathrm{e}}, \alpha) = \psi^{\mathrm{e}}(\boldsymbol{B}^{\mathrm{e}}) + \psi^{\mathrm{p}}(\alpha), \tag{4.7}$$

where α is a strain-like internal variable. The dissipation inequality for isothermal processes reformulated from Eq. (2.75) reads

$$\mathcal{D} := \boldsymbol{\tau} : \boldsymbol{D} - \dot{\psi} \geq 0. \tag{4.8}$$

with the Kirchhoff stresses $\boldsymbol{\tau}$ and the stretch tensor $\boldsymbol{D}$. The time derivative of Eq. (4.7) is given by

$$\dot{\psi} = \frac{\partial \psi^{\mathrm{e}}}{\partial \boldsymbol{B}^{\mathrm{e}}} : \dot{\boldsymbol{B}}^{\mathrm{e}} \; + \; \frac{\partial \psi^{\mathrm{p}}}{\partial \alpha} \dot{\alpha} \tag{4.9}$$

with the time derivative of $\boldsymbol{B}^{\mathrm{e}}$ defined using the formulation given in (4.4),

$$\dot{\boldsymbol{B}}^{\mathrm{e}} = (\boldsymbol{F} \cdot \boldsymbol{C}^{\mathrm{p}\,-1} \cdot \boldsymbol{F}^{\mathrm{T}})^{\cdot} = \boldsymbol{L} \cdot \boldsymbol{B}^{\mathrm{e}} \; + \; \mathcal{L}(\boldsymbol{B}^{\mathrm{e}}) \; + \; \boldsymbol{B}^{\mathrm{e}} \cdot \boldsymbol{L}^{\mathrm{T}} \tag{4.10}$$

using the Lie-derivative, cf. Eq. A.15 of $\boldsymbol{B}^{\mathrm{e}}$ defined by $\mathcal{L}(\boldsymbol{B}^{\mathrm{e}}) = \boldsymbol{F} \cdot \dot{\boldsymbol{C}}^{\mathrm{p}\,-1} \cdot \boldsymbol{F}^{\mathrm{T}}$. Inserting Eq. (4.9) and Eq. (4.10) into Eq. (4.8), reformulation results in the constitutive equation and the reduced dissipation inequality,

$$\boldsymbol{\tau} = 2 \frac{\partial \psi^{\mathrm{e}}}{\partial \boldsymbol{B}^{\mathrm{e}}} \cdot \boldsymbol{B}^{\mathrm{e}} \quad \text{and} \quad \mathcal{D}_{\mathrm{red}} = -\boldsymbol{\tau} : \left(\frac{1}{2} \mathcal{L}(\boldsymbol{B}^{\mathrm{e}}) \cdot \boldsymbol{B}^{\mathrm{e}\,-1} \right) + \beta\, \dot{\alpha} \geq 0, \tag{4.11}$$

with the stress-like internal variable conjugate to α given by $\beta := -\dfrac{\partial \psi^{\mathrm{p}}}{\partial \alpha}$. The principle of maximum dissipation plays an important role for the existence and uniqueness of the solution. It relates any arbitrary deformation state defined by ($\boldsymbol{B}^{\mathrm{e}}$, α) to a distinct state ($\boldsymbol{\tau}$, β) via the maximum dissipation, see Simo [139]. The principle of maximum dissipation implies the existence of a convex stress region with the yield surface Φ defining the border of this region, i.e.

$$\Phi = \Phi(\boldsymbol{\tau}, \beta) \leq 0. \tag{4.12}$$

With this formulation, an optimization problem can be formulated using a Lagrange functional, leading to

$$\boldsymbol{\tau} : \frac{1}{2} \mathcal{L}(\boldsymbol{B}^{\mathrm{e}}) \boldsymbol{B}^{\mathrm{e}\,-1} - \beta\, \dot{\alpha} + \gamma \Phi \leq 0 \tag{4.13}$$

with the Lagrange multiplier γ. From the partial derivation of Eq. (4.13) with respect to $\boldsymbol{\tau}$ and β, one obtains

$$\frac{1}{2} \mathcal{L}(\boldsymbol{B}^{\mathrm{e}}) \boldsymbol{B}^{\mathrm{e}\,-1} = -\gamma \frac{\partial \Phi}{\partial \boldsymbol{\tau}}, \qquad \dot{\alpha} = \gamma \frac{\partial \Phi}{\partial \beta} \tag{4.14}$$

which are the flow rule and evolution equation of the internal variable α. Eq. (4.13) is fulfilled if the well-known Kuhn-Tucker conditions hold, which are given by

$$\gamma \geq 0, \qquad \Phi \leq 0, \qquad \gamma \Phi = 0. \tag{4.15}$$

The above shown Kuhn-Tucker conditions are also referred to as loading and unloading conditions, describing a stress state on the yield surface, i.e. $\Phi = 0$ as

$$\begin{aligned}
&\dot{\Phi} < 0, \quad \gamma = 0 \quad \rightarrow \text{elastic unloading} \\
&\dot{\Phi} = 0, \quad \gamma > 0 \quad \rightarrow \text{plastic loading} \\
&\dot{\Phi} = 0, \quad \gamma = 0 \quad \rightarrow \text{neutral loading.}
\end{aligned}$$

and achieve the consistency condition

$$\gamma\dot{\Phi} = 0. \tag{4.16}$$

In Simo [139], a logarithmic strain measure is proposed based on principal strains with

$$\boldsymbol{\epsilon}^{\mathrm{e}} = [\epsilon_1^{\mathrm{e}} \;\; \epsilon_2^{\mathrm{e}} \;\; \epsilon_3^{\mathrm{e}}]^{\mathrm{T}} \quad \text{and} \quad \epsilon_A^{\mathrm{e}} = \log(\lambda_A^{\mathrm{e}}) \tag{4.17}$$

is proposed, which has the advantage that the return mapping algorithm used in the infinitesimal theory is identical for the formulation at finite strains. A free energy function in terms of the quadratic principle logarithmic strains is given by

$$\psi^{\mathrm{e}} = \frac{\lambda}{2}[\epsilon_1^{\mathrm{e}} + \epsilon_2^{\mathrm{e}} + \epsilon_3^{\mathrm{e}}]^2 + \mu[(\epsilon_1^{\mathrm{e}})^2 + (\epsilon_2^{\mathrm{e}})^2 + (\epsilon_3^{\mathrm{e}})^2] \tag{4.18}$$

with the Lamé constant λ and the shear modulus μ. The plastic behavior is considered using a von Mises yield criterion which is given by

$$\Phi = ||\mathrm{dev}\boldsymbol{\tau}|| - \sqrt{\frac{2}{3}}\beta \leq 0 \tag{4.19}$$

and the conjugated internal variable describing exponential isotropic hardening as

$$\beta = y_\infty + (y_0 - y_\infty)\exp(-\eta\alpha) + h\alpha \tag{4.20}$$

where y_0 is the initial yield strength, y_∞ and η are material parameters for the description of exponential hardening behavior and h is the slope of the linear hardening term. An implicit exponential update algorithm, preserving plastic incompressibility, cf. Weber and Anand [171], Simo [139], Miehe and Stein [95], is used for the integration of the flow rule. The numerical implementation is based on the algorithmic formulation in a material setting, as proposed in Klinkel [72].

4.3 Crystal Plasticity

The mechanism of plastic deformation in crystalline solids were investigated as early as 1934, Taylor [159; 160], however only decades later, the first finite element simulations were carried out, see Rice [119], Asaro and Rice [4], Peirce et al. [107]. An extensive overview on crystal plasticity finite element models is given in Roters et al. [121].

The crystallographic structure of a crystalline solid is characterized by the arrangement of atoms in the crystallographic lattice. Different types can be described by the concept of unitcells describing the repetitive three-dimensional arrangement of atoms and resulting in the bulk material of a crystal if they are extended in three-dimensional space. Among the different types of unitcells: face-centered cubic (fcc) unitcells, body-centered cubic (bcc) unitcells and hexagonal closed packing (hcp) unitcells are arrangements frequently observed in materials. An illustration of these three types of unitcells is given in Fig. 4.4. Aluminum (Al), copper (Cu), nickel (Ni), silver (Ag) and gold (Au) possess a crystallographic structure of face-centered cubic type, α-iron (α-Fe) and wolfram (W) have a body-centered cubic crystallographic structure, while magnesium (Mg) is the most prominent representative of hcp unitcells.

Elastic and plastic deformation in a crystalline solid are governed by different changes of the atomic lattice. In the case of elastic deformation, the deformation acts on the lattice structure without changing the relative positions of atoms in the lattice, see Fig. 4.5(a). Plastic deformation occurs when atoms slip along a slip plane, as indicated in Fig. 4.5(b), and a permanent rearrangement of the atoms happens.

The well known *Schmid's law* relates the overall stress on the crystal to the resolved shear stress on a slip plane in a slip direction and thereby concludes that stresses perpendicular to the slip system have no effect on its slip. Once a critical shear stress on the slip system

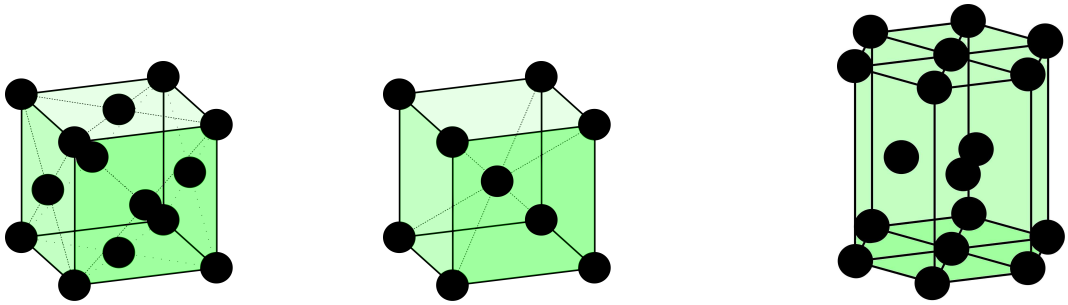

Figure 4.4: (a) Face-centered cubic, (b) body-centered cubic and (c) hexagonal close packed unitcells.

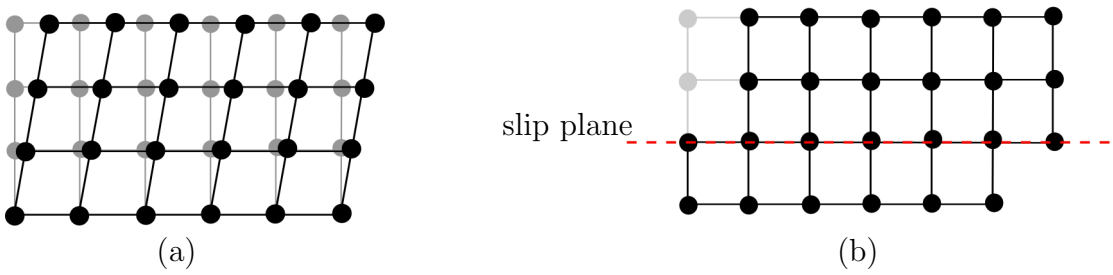

Figure 4.5: (a) Elastic deformation of crystal lattice and (b) plastic slip along slip plane. The undeformed crystal lattice is shown in grey.

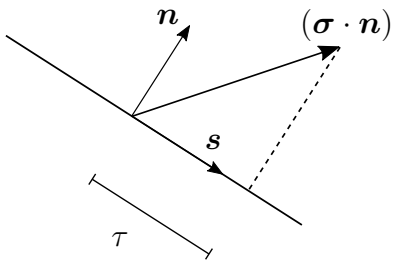

Schmid's law:
$\tau = (\boldsymbol{\sigma} \cdot \boldsymbol{n}) \cdot \boldsymbol{s}$

Figure 4.6: Schematic illustration of Schmid's law

is exceeded, slip will occur. Fig. 4.6(b) illustrates Schmid's law, where $\boldsymbol{\sigma}$ is the stress tensor acting in the crystal and τ represents the resolved shear stress on a slip system, which is defined by the normal vector $\boldsymbol{n}$ and direction vector $\boldsymbol{s}$.

The number and position of slip planes and slip directions depends on the arrangement of atoms in the crystalline solid. Generally, slip occurs in the plane of high atom packing density in direction of the highest linear atom packing density. In a crystal, there typically exist symmetrically equivalent planes, which can be described using Miller indices, proposed in 1839 by W. H. Miller. For cubic unitcells, a family of symmetrically equivalent planes is denoted using the index $\{hkl\}$ and equivalent directions are denoted by $\langle uvw \rangle$. Distinct planes are denoted by (hkl) and distinct directions by $[uvw]$. The indices h, k and l describe the orientation of a normal vector to a plane in euclidean space and u, v and w describe the orientation of the directional vector in euclidean space. Using this description, the slip planes in an fcc unitcell are defined by the family $\{1\,1\,1\}$, which summarizes the equivalent planes

$$\begin{aligned} \{1\,1\,1\} \rightarrow \quad & (1\,1\,1), \quad (\text{-}1\;1\;1), \quad (1\;\text{-}1\;1), \quad (1\;1\;\text{-}1), \\ & (\text{-}1\;\text{-}1\;1), \quad (1\;\text{-}1\;\text{-}1), \quad (\text{-}1\;1\;\text{-}1), \quad (\text{-}1\;\text{-}1\;\text{-}1), \end{aligned}$$

forming an octahedral arrangement of slip planes. The three slip directions on each plane are denoted by the family $\langle 1\,1\,0 \rangle$, summarizing the equivalent directional vectors

$$\langle 1\,1\,0 \rangle \rightarrow \quad [1\;1\;0], \quad [\text{-}1\;1\;0], \quad [1\;\text{-}1\;0],$$

which corresponds to the face diagonals of the fcc unitcell. The arrangement of slip planes in fcc crystals is illustrated in Fig. 4.7 and the respective slip directions are shown exemplarily for one slip plane. Based thereon, a slip system is defined by the consideration of slip plane and slip direction together. Subsequently in an fcc crystal, 24 possible slip systems can be identified, which can be reduced to 12 slip directions considering the permutations of directions and slip plane normals.

Slip phenomena in bcc unitcells are more complex than in fcc unitcells. Slip occurs in the closest packed $\langle 1\,1\,1 \rangle$ direction, however the identification of slip planes is not as clear, cf. Weinberger et al. [172], Watanabe [170]. The planes of largest interplanar spacing are $\{1\,1\,0\}$ and $\{1\,1\,2\}$ followed by $\{1\,2\,3\}$. Since the slip mechanisms in bcc crystals are strongly temperature and orientation dependent, not all of these planes seem to be active at all times. Different experimental observations lead to the conclusion that only the $\{1\,1\,0\}$ planes are active at room temperature. Furthermore, in contrast to fcc

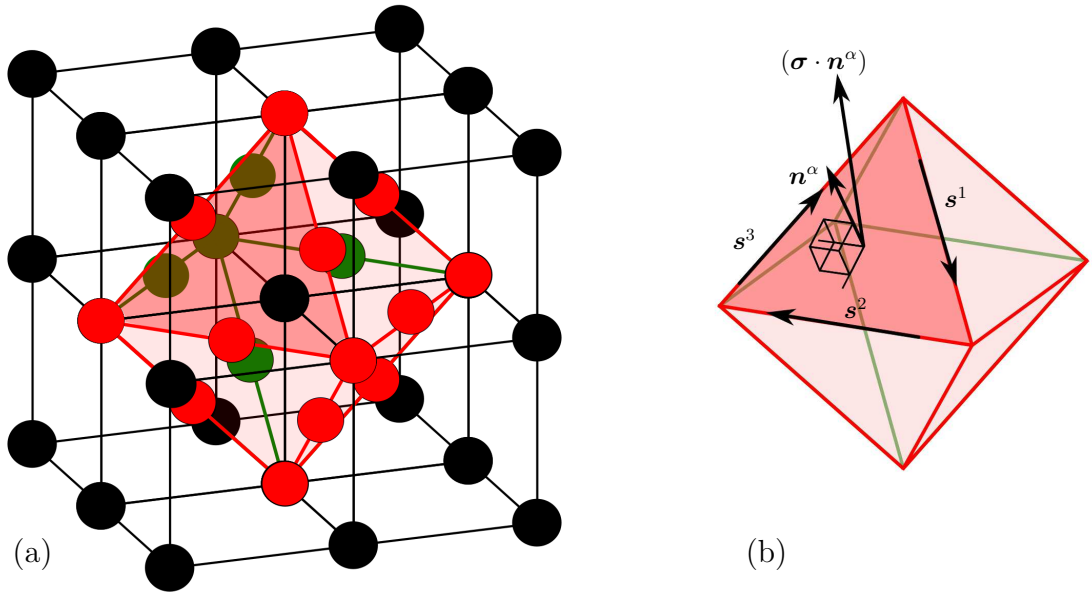

Figure 4.7: (a) Illustration of octahedral arrangement of slip planes in an fcc crystal lattice. (b) Sketch of slip systems defined by slip plane with $\boldsymbol{n}^\alpha$ and one out of the three slip directions $\boldsymbol{s}^1$, $\boldsymbol{s}^2$ and $\boldsymbol{s}^3$.

crystals, the Schmid law is violated and other stress components have an effect on the slip. Also, the slip resistance is not independent of the slip system, as it is the case for fcc crystals, but can be different in a slip direction and its opposite, which is indicated as twinning/anti-twinning asymmetry, cf. Yalcinkaya et al. [175].

Naturally, crystalline materials do not occur with a perfectly arranged crystallographic lattice, as lattice defects play an important role in the behavior of the crystal. The lattice defects, i.e. irregularities in the crystallographic lattice, are also referred to as dislocations. Two primary types are screw dislocations and edge dislocations, whereby mixed forms of the latter two exist. The important role of dislocations in the framework of plastic slip becomes clear in the following examples. Dislocations can move through the material when a force is applied on the material. This movement results in plastic deformation, however moving a dislocation, i.e. detaching and reattaching one atom at a time, requires much less energy than moving an entire slip plane, i.e. detaching all atoms in the slip direction from each other. Thus, plastic slip along a slip plane happens through the movement of dislocation. This is often comprehensively explained using the example of moving a carpet: Pulling on one end of the carpet to move it a certain distance requires much more force than forming a 'dent' at one end and moving this dent through the carpet. Dislocations can however not move across grain boundaries, where two crystals of different orientations are adjacent. Here, the mismatch in the crystal lattice causes the dislocation movement to stop and dislocation to accumulate in this region. The important effects of strain hardening (or work hardening), which is the effect that a material increases in yield strength as it is plastically deformed, arises from the increase of dislocation density in the material due to the plastic deformation. As a result of the higher dislocation density, the ability of the dislocations to move is restricted, leading to a higher yield strength. The Hall-Petch effect, i.e. increased strength coinciding with a reduction of grain size, is also a result of more obstacles for dislocation movement due to more grain boundaries with smaller distances.

For the consideration of polycrystalline structures based on the behavior of the underlying single grains, an isostress approach was first proposed by Sachs [123], assuming the resolved shear stress on all slip systems in the polycrystal to be equal to the highest resolved shear stress in the compound. The isostrain assumption, Taylor [158], Bishop and Hill [20], also called Taylor or Taylor-Bishop-Hill (TBH) model, in which all grains undergo the same state of deformation, shows good results in the prediction of deformation textures, however violates the equilibrium condition between individual grains. While no grain interaction is considered in the latter approaches, grain cluster models, see e.g. Van Houtte et al. [168], or grain interaction models, see e.g. Raabe [113], include some grain interaction and relax the rigid isostrain assumption set up in the TBH models. Self-consistent models, first developed by Kröner [77] and later extended by Budiansky and Wu [25], Hill [57], consider each grain as an inclusion embedded in a homogeneous effective medium. Thereby grain interaction is considered as well, however most models treat the grain itself using simplified geometries. Full-field models, which enable a consideration of morphological information of the polycrystal as well as local grain interaction and intra-grain inhomogeneities of the micromechanical fields, can be described using FEM models, also called crystal plasticity (CP) FEM models in this case, see e.g. Roters et al. [120]. As mentioned earlier, these methods require a sufficiently high resolution of the considered polycrystalline RVE and due to their multiscale nature result in large computational costs. A crystal plasticity implementation within a finite-strain continuum mechanical framework which utilizes a spectral solver has been developed at Max-Planck Institut für Eisenforschung, Düsseldorf, see, e.g., Roters et al. [122].

In this work, the framework of single crystal plasticity is restricted to the case of fcc unitcells. A rate dependent crystal plasticity model at small strains is presented below, closely following the formulations proposed in Cuitiño and Ortiz [32], see also Miehe and Schröder [94].

4.4 Rate Dependent Small Strain Crystal Plasticity

Let $\mathcal{B}_0$ be the body of interest and $\boldsymbol{u} : \mathcal{B}_0 \to \mathbb{R}^3$ a given displacement field. Based on the displacement gradient, the linear strain tensor is given as its symmetric part by $\boldsymbol{\varepsilon} = \mathrm{sym}[\nabla \boldsymbol{u}]$. The linear strain tensor can be additively decomposed

$$\boldsymbol{\varepsilon} = \boldsymbol{\varepsilon}^{\mathrm{e}} + \boldsymbol{\varepsilon}^{\mathrm{p}} \tag{4.21}$$

into a plastic part $\boldsymbol{\varepsilon}^{\mathrm{p}}$ and an elastic part $\boldsymbol{\varepsilon}^{\mathrm{e}}$. The overall stresses in the crystalline solid are given by

$$\boldsymbol{\sigma} = \mathbb{C}^{\mathrm{e}} : \boldsymbol{\varepsilon}^{\mathrm{e}} \tag{4.22}$$

where the material tangent $\mathbb{C}^{\mathrm{e}}$ is related to a free energy function $\hat{\psi}$ by $\hat{\psi} = \frac{1}{2}\,\boldsymbol{\varepsilon}^{\mathrm{e}} : \mathbb{C}^{\mathrm{e}} : \boldsymbol{\varepsilon}^{\mathrm{e}}$. The so called scalar-valued *Schmid resolved shear stress* on a slip system α is defined by

$$\tau^{\alpha} := \boldsymbol{\sigma} : \boldsymbol{P}^{\alpha} \quad \text{with} \quad \boldsymbol{P}^{\alpha} := \mathrm{sym}(\boldsymbol{s}^{\alpha} \otimes \boldsymbol{n}^{\alpha}) \tag{4.23}$$

which is essentially the shear stress resolved on a specific slip plane in the specific slip direction, defined by the orthonormal vectors ($\boldsymbol{s}^{\alpha} \perp \boldsymbol{n}^{\alpha}$), forming a slip system. Here, $\boldsymbol{n}^{\alpha}$

defines the normal vector on a slip plane and $\boldsymbol{s}^\alpha$ defines the direction of slip on this slip plane. An illustration is shown in Fig. 4.6 in the previous section. The evolution of plastic strain is given in the form

$$\dot{\boldsymbol{\varepsilon}}^{\mathrm{p}} = \sum_\alpha \dot{\gamma}^\alpha \; \boldsymbol{P}^\alpha \tag{4.24}$$

with the plastic slip rate $\dot{\gamma}^\alpha$. In the rate-dependent formulation, the slip rate $\dot{\gamma}^\alpha$ is given in the form of a kinetic law, as e.g. proposed by Hutchinson [64] as

$$\dot{\gamma}^\alpha = \dot{\gamma}_0 \left| \frac{\tau^\alpha}{g^\alpha} \right|^{p-1} \left(\frac{\tau^\alpha}{g^\alpha} \right), \tag{4.25}$$

where the reference slip rate is denoted by $\dot{\gamma}_0$, the slip resistance is defined by g^α and the exponent p characterizes the material rate sensitivity. Allowing positive and negative values of slip rates, the two slip systems $(\boldsymbol{s}^\alpha, \boldsymbol{n}^\alpha)$ and $(-\boldsymbol{s}^\alpha, \boldsymbol{n}^\alpha)$ can be considered jointly. The definition of slip systems used in this thesis is given in Tab. C.1. Strain hardening of a slip system can be described by an evolution of g^α as

$$\dot{g}^\alpha = \sum_\beta h^{\alpha\beta} \left| \dot{\gamma}^\beta \right| \qquad \text{with} \quad g^\alpha(t=0) = \tau_0 \tag{4.26}$$

where $h^{\alpha\beta}$ is the hardening modulus. This rate dependent formulation of single crystal plasticity does not have a explicit point where yielding initiates, as it is defined for elastic-plastic formulation by the yield strength. The slip on each slip system is always defined by Eq. (4.25) and is nonzero for any nonzero value of τ^α. If the exponent p is large, e.g. $p > 50$ as stated in Asaro [5], the evolution of slip is exceedingly small for ratios $\tau^\alpha / g^\alpha < 1$. Relevant magnitudes of slip occur only if τ^α / g^α approaches one.

The hardening modulus $h^{\alpha\beta}$ essentially defines the self hardening ratio for $\alpha = \beta$ and latent hardening ratio for $\alpha \neq \beta$. Different types of hardening laws are defined in the literature, see e.g. Asaro [5], Peirce et al. [107], Hutchinson [64] for more details. Most hardening laws propose a symmetric form, where $h^{\alpha\beta} = h^{\beta\alpha}$. The hardening modulus can be formulated in the classical assumption proposed in Hutchinson [64], Peirce et al. [107] as

$$h^{\alpha\beta} = \hat{h}(A) \left[q + (1-q)\delta^{\alpha\beta} \right], \tag{4.27}$$

where A is a strain-like internal variable defined by the evolution equation $\dot{A} = \sum_\alpha |\dot{\gamma}^\alpha|$, which is the sum of accumulated plastic slip on all slip systems. The material parameter q defines the ratio of latent hardening to self hardening and has been specified for fcc crystals in Kocks [73] through experiments in a range $[1, 1.4]$. If $q = 1$ holds, Eq. (4.27) results in the constant hardening modulus $h^{\alpha\beta} = \hat{h}(A)$, producing an equal rate of flow stress on all slip systems. This case is commonly referred to as *Taylor hardening* or *isotropic hardening*. For $\hat{h}(A)$, a scalar-valued function which reads

$$\hat{h}(A) = h_0 \, \mathrm{sech}^2 \left[\frac{h_0 \, A}{\tau_\infty \; - \; \tau_0} \right], \tag{4.28}$$

is proposed by Peirce et al. [107] based on the single slip law

$$\tau(A) = \tau_0 + (\tau_\infty - \tau_0) \tanh \left(\frac{h_0 \, A}{\tau_\infty - \tau_0} \right). \tag{4.29}$$

Table 4.1: Constitutive framework for the presented single crystal plasticity formulation.

strain tensor	$\boldsymbol{\varepsilon} = \mathrm{sym}[\nabla \boldsymbol{u}]$ with $\boldsymbol{\varepsilon} = \boldsymbol{\varepsilon}^{\mathrm{e}} + \boldsymbol{\varepsilon}^{\mathrm{p}}$
macro stress	$\boldsymbol{\sigma} = \mathbb{C}^{\mathrm{e}} : \boldsymbol{\varepsilon}^{\mathrm{e}}$
Schmid stress	$\tau^{\alpha} = \boldsymbol{\sigma} : \mathrm{sym}[\boldsymbol{s}^{\alpha} \otimes \boldsymbol{n}^{\alpha}]$
kinetic law	$\dot{\gamma}^{\alpha} = \dot{\gamma}_0 \left\lvert \frac{\tau^{\alpha}}{g^{\alpha}} \right\rvert^{p-1} \left(\frac{\tau^{\alpha}}{g^{\alpha}} \right)$
flow rule	$\dot{\boldsymbol{\varepsilon}}^{\mathrm{p}} = \sum_{\alpha} \dot{\gamma}^{\alpha}\, \mathrm{sym}[\boldsymbol{s}^{\alpha} \otimes \boldsymbol{n}^{\alpha}]$
evolution	$\dot{A} = \sum_{\alpha} \lvert \dot{\gamma}^{\alpha} \rvert$
hardening	$\dot{g}^{\alpha} = \sum_{\beta} \hat{h}(A) \left[q + (1-q)\delta^{\alpha\beta} \right] \lvert \dot{\gamma}^{\beta} \rvert$

Here, the initial hardening is described by h_0, the saturation stress is given by τ_∞ and the initial slip resistance is represented by τ_0. $\tau(A)$ defines the current value of flow stress in single slip. The hyperbolic secant function is defined by sech. This description is found to describe the overshoot, i.e. the larger amount of shear stress on conjugate slip systems than on the primary slip system, adequately compared with experimental results from Chang and Asaro [27] for a tensile test on aluminum-copper single crystals. An alternative form is proposed therein, where the hardening module is defined by

$$\hat{h}(A) = h_0 + (h_\infty - h_0) \left[1 - \mathrm{sech} \left(\frac{(h_0 - h_\infty)\, A}{\xi} \right) \right], \tag{4.30}$$

based on the single slip law

$$\tau(A) = \tau_\infty + \xi \tanh \left(\frac{(h_0 - h_\infty)\, A}{\xi} \right), \tag{4.31}$$

where ξ is a saturation parameter, h_∞ is the saturated hardening and h_0 and τ_∞ are the initial hardening and saturation stress as above. Furthermore, Miehe et al. [96] proposed an exponential type form scalar hardening function which reads

$$\hat{h}(A) = h_0 + (h_\infty - h_0) \left[1 - \exp\left(-\xi\, A \right) \right], \tag{4.32}$$

based on the single slip law

$$\tau(A) = \tau_\infty + (h_\infty - h_0)(-\xi^{-1}) \exp\left(-\xi\, A \right). \tag{4.33}$$

The hardening module of the form given in Eq. (4.27) is widely used in the literature, other approaches for the definition of $h_{\alpha\beta}$ have been proposed, e.g. in Bassani and Wu [16]. A summary of the constitutive framework for the formulation of rate dependent single crystal plasticity for small strains is given in Table 4.1.

Stress update algorithm

The algorithmic implementation for the foregoing small strain rate dependent single crystal plasticity constitutive model is discussed in the following. For a viscoplastic solid, Hughes and Taylor [62] formulated an implicit algorithm which exactly satisfies equilibrium and a suitable state-update rule in every load step. The algorithmic treatment follows the concept described in Cuitiño and Ortiz [32] and Miehe et al. [96], which

constructs a fully implicit stress-update algorithm. A time step $[t_n, t_{n+1}]$ is considered where all variables at time t_n are known. Applying a backward Euler scheme on the evolution equations given in Table 4.1 yields

$$\begin{aligned} \boldsymbol{\varepsilon}^{\mathrm{p}}_{n+1} &= \boldsymbol{\varepsilon}^{\mathrm{p}}_{n} + \sum_{\alpha} \gamma^{\alpha}\, \boldsymbol{P}^{\alpha} \\ A_{n+1} &= A_n + \sum_{\alpha} |\gamma^{\alpha}| \\ g^{\alpha}_{n+1} &= g^{\alpha}_{n} + \sum_{\beta} \hat{h}(A)\left[q + (1-q)\delta^{\alpha\beta}\right]\, |\gamma^{\beta}| \end{aligned} \tag{4.34}$$

with the incremental plastic parameter $\gamma^{\alpha} = \dot{\gamma}^{\alpha}\,(t_{n+1} - t_n) = \dot{\gamma}^{\alpha}\Delta t$. The beginning of the process is defined by the initial conditions $\boldsymbol{\varepsilon}^{p} = \mathbf{0}$, $A = 0$ and $g^{\alpha} = \tau^{\alpha}_0$. In the following, all variables without a subscript index are evaluated at t_{n+1}. For the derivation of the incremental plastic slip in the current time step, it holds

$$\gamma^{\alpha} = \gamma_0 \left|\frac{\tau^{\alpha}}{g^{\alpha}}\right|^{p-1} \left(\frac{\tau^{\alpha}}{g^{\alpha}}\right) \tag{4.35}$$

with $\gamma_0 = \dot{\gamma_0}\Delta t$. Using Newton-Raphson scheme, the residual function

$$r^{\alpha} = \frac{\gamma^{\alpha}}{\gamma_0} \;-\; \left|\frac{\tau^{\alpha}}{g^{\alpha}}\right|^{p-1} \left(\frac{\tau^{\alpha}}{g^{\alpha}}\right) = 0 \tag{4.36}$$

can be solved. The linearization is given by

$$r^{\alpha} + \frac{\partial r^{\alpha}}{\partial \gamma^{\beta}} \Delta\gamma^{\beta} = 0 \tag{4.37}$$

with the jacobian

$$D^{\alpha\beta *} = -\frac{\partial r^{\alpha}}{\partial \gamma^{\beta}} = \frac{1}{\gamma_0}\delta^{\alpha\beta} \;-\; \frac{p}{g^{\alpha}} \left|\frac{\tau^{\alpha}}{g^{\alpha}}\right|^{p-1} \left(\boldsymbol{P}^{\alpha} : \mathbb{C}^{e} : \boldsymbol{P}^{\beta} \;+\; h^{*\alpha\beta}\frac{\tau^{\alpha}}{g^{\alpha}}\right), \tag{4.38}$$

where

$$h^{*\alpha\beta} = \frac{\partial g^{\alpha}}{\partial \gamma^{\beta}} = \sum_{\delta} [q + (1-q)\delta^{\alpha\delta}][\hat{h}(A)\delta^{\delta\beta} + \hat{h}'(A)\gamma^{\delta}]\,, \tag{4.39}$$

with $\hat{h}' = \mathrm{d}\hat{h}/\mathrm{d}A$. The slip increment is then calculated by iteratively solving Eq. (4.37) in a Newton-Raphson scheme where the update of slip is performed via

$$\gamma^{\alpha} \leftarrow \gamma^{\alpha} + \Delta\gamma^{\alpha} \quad \text{with} \quad \Delta\gamma^{\alpha} = (D^{\alpha\beta *})^{-1} r^{\beta}. \tag{4.40}$$

As reported in Ling et al. [84], the formulation of the residual function can be done in different ways, where numerical obstacles arise in all proposed functions therein. Here, in the case of large exponents p, the term $(\tau^{\alpha}/g^{\alpha})^{p-1}$ becomes large if the term τ^{α}/g^{α} is even only slightly larger than 1. This leads to numerical issues in the evaluation of the residual r^{α} and the jacobian $D^{\alpha\beta *}$, cf. Eq.(4.37) and Eq. (4.38). Different solutions can be found to solve this problem. For example, Steinmann and Stein [147] reformulate the residual and in case τ^{α}/g^{α} becomes larger than 1, an alternative residual is evaluated. However, the system becomes ill-conditioned again once the increment γ^{α} approaches zero. A

stable but time consuming alternative is the stepwise increase of the rate sensitivity parameter p, in case τ^α/g^α exceeds a critical value, cf. Steinmann and Stein [147].

Consistent Material Tangent Moduli

The derivation of the material tangent moduli $\mathbb{C}^{\mathrm{ep}}$ is obtained through differentiation of the incremental constitutive equation $\Delta\boldsymbol{\sigma} = \Delta\boldsymbol{\sigma}(\Delta\boldsymbol{\varepsilon})$ with respect to the total strains. For a timestep t_{n+1}, it follows for the material tangent operator

$$\mathbb{C}^{\mathrm{ep}} = \frac{\partial \boldsymbol{\sigma}_{n+1}}{\partial \boldsymbol{\varepsilon}_{n+1}} \tag{4.41}$$

Reformulating Eq. (4.21) in the current time step and inserting into Eq. (4.41) yields

$$\begin{aligned} \Delta\boldsymbol{\sigma}_{n+1} &= \mathbb{C}^{\mathrm{e}} : \Delta\boldsymbol{\varepsilon}_{n+1} = \mathbb{C}^{\mathrm{e}} : \left[\Delta\boldsymbol{\varepsilon}_{n+1} - \Delta\boldsymbol{\varepsilon}^{p}_{n+1}\right] \\ &= \mathbb{C}^{\mathrm{e}} : \Delta\boldsymbol{\varepsilon}_{n+1} - \mathbb{C}^{\mathrm{e}} : \sum_{\beta} \gamma^{\beta}_{n+1} \boldsymbol{P}^{\beta}, \end{aligned} \tag{4.42}$$

subsequently, the elastic-plastic tangent moduli $\mathbb{C}^{\mathrm{ep}}$ can be written as

$$\mathbb{C}^{\mathrm{ep}} = \mathbb{C}^{\mathrm{e}} - \sum_{\beta} \mathbb{C}^{\mathrm{e}} : \boldsymbol{P}^{\beta} \otimes \frac{\partial \gamma^{\beta}_{n+1}}{\partial \boldsymbol{\varepsilon}_{n+1}}, \tag{4.43}$$

where the plastic slip in the current time step results from the solution of the local Newton iteration with Eq. (4.40), hence $\gamma^{\beta}_{n+1} = \gamma^{\beta}_{n} + \Delta\gamma^{\beta}_{n+1} = \gamma^{\beta}_{n} + \sum_{\alpha}(D^{\alpha\beta})^{-1} r^{\alpha}$. The partial derivation of the plastic slip in the current time step with respect to the total strains in the current time step is derived by

$$\frac{\partial \gamma^{\beta}_{n+1}}{\partial \boldsymbol{\varepsilon}_{n+1}} = \frac{\partial \gamma^{\beta}_{n+1}}{\partial r^{\alpha}} \frac{\partial r^{\alpha}}{\partial \boldsymbol{\varepsilon}_{n+1}} = \sum_{\alpha} (D^{\alpha\beta *})^{-1} \frac{\partial r^{\alpha}}{\partial \tau^{\delta}} \frac{\partial \tau^{\delta}}{\partial \boldsymbol{\varepsilon}_{n+1}}, \tag{4.44}$$

where the partial derivation of the residual with respect to the Schmid stress is given by

$$\begin{aligned} \frac{\partial r^{\alpha}}{\partial \tau^{\delta}} &= -\left((p-1) \left|\frac{\tau^{\alpha}}{g^{\alpha}}\right|^{p-2} \left(\frac{\tau^{\alpha}}{g^{\alpha}}\right) \left|\frac{\tau^{\alpha}}{g^{\alpha}}\right|^{-1} \frac{1}{g^{\alpha}} \delta^{\alpha\delta} \frac{\tau^{\alpha}}{g^{\alpha}} + \left|\frac{\tau^{\alpha}}{g^{\alpha}}\right|^{p-1} \frac{1}{g^{\alpha}} \delta^{\alpha\delta} \right) \\ &= -\left((p-1) \frac{1}{g^{\alpha}} \left|\frac{\tau^{\alpha}}{g^{\alpha}}\right|^{p-1} + \frac{1}{g^{\alpha}} \left|\frac{\tau^{\alpha}}{g^{\alpha}}\right|^{p-1} \right) \delta^{\alpha\delta} \\ &= -\left|\frac{\tau^{\alpha}}{g^{\alpha}}\right|^{p-1} \frac{1}{g^{\alpha}} (p-1+1)\, \delta^{\alpha\delta} \\ &= -\frac{p}{g^{\alpha}} \left|\frac{\tau^{\alpha}}{g^{\alpha}}\right|^{p-1} \delta^{\alpha\delta} \\ &= f^{\alpha}\, \delta^{\alpha\delta} \quad \text{with} \quad f^{\alpha} = -\frac{p}{g^{\alpha}} \left|\frac{\tau^{\alpha}}{g^{\alpha}}\right|^{p-1}. \end{aligned} \tag{4.45}$$

The partial derivative of the Schmid stress with respect to the total strains is computed

by

$$\begin{aligned}\frac{\partial \tau^{\delta}}{\partial \boldsymbol{\varepsilon}_{n+1}} &= \partial_{\boldsymbol{\varepsilon}_{n+1}} \left(\boldsymbol{\sigma}_{n+1} : \boldsymbol{P}^{\delta}\right) \\ &= \partial_{\boldsymbol{\varepsilon}_{n+1}} \left(\mathbb{C}^{\mathrm{e}} : \boldsymbol{\varepsilon}^{\mathrm{e}}_{n+1}\right) : \boldsymbol{P}^{\delta} \\ &= \partial_{\boldsymbol{\varepsilon}_{n+1}} \boldsymbol{P}^{\delta} : \mathbb{C}^{\mathrm{e}} : \left(\boldsymbol{\varepsilon}_{n+1} - \boldsymbol{\varepsilon}^{\mathrm{p}}_{n+1}\right) \\ &= \boldsymbol{P}^{\delta} : \mathbb{C}^{\mathrm{e}}\end{aligned} \tag{4.46}$$

Finally, inserting Eq. (4.44), (4.45) and (4.46) into Eq. (4.43), the elastic-plastic tangent moduli yields

$$\mathbb{C}^{\mathrm{ep}} = \mathbb{C}^{\mathrm{e}} - \sum_{\beta} \sum_{\alpha} (D^{\alpha\beta *})^{-1} \, f^{\alpha} \, \mathbb{C}^{\mathrm{e}} : \boldsymbol{P}^{\beta} \otimes \boldsymbol{P}^{\alpha} : \mathbb{C}^{\mathrm{e}}. \tag{4.47}$$

5 Multiscale Modeling of Microheterogeneous Materials

Multiscale modeling of microheterogeneous materials is related to many disciplines, e.g. physics, material science, engineering and mathematics. In the following, multiscale methods are discussed from a computational point of view presenting an approach to bridge between two different length scales. Specifically, a description of the material response in a point on the macroscale is obtained by homogenization of the material response on the microscale. This procedure is referred to as direct micro-macro transition approach, which is also often termed FE^2-method, see e.g Smit et al. [143], Moulinec and Suquet [99], Miehe et al. [96], Miehe and Schröder [93], Feyel [40], Schröder [130], Terada et al. [162], Feyel and Chaboche [41], Geers et al. [43], Schröder [131]. First, the concepts and hypotheses in the framework of homogenization theory are summarized with special attention to examples of dual-phase (DP) steels and the definition of suitable representative volume elements (RVEs). The direct micro-macro transition approach is outlined following the steps presented in Schröder [131]. Therefore, the macro- and microscopic boundary value problems (BVP) are set up and the definition of macroscopic quantities based on volume averages of the microscopic counterparts is given. The Hill-Mandel condition is revisited which is used for a definition of suitable boundary conditions on the microscopic BVP. Aspects on the numerical implementation as well as the consistent macroscopic tangent moduli are given.

5.1 Basic Concepts and Hypotheses of Homogenization

In the field of microheterogeneous materials, the description of the material behavior at different length scales becomes important when effects arising on small scale shall be considered at a larger scale. Typically, these materials have a distinct appearance at these different scales, which is assumed to be homogeneous at the macroscale but is dominated by heterogeneities on the microscale. The concept of scale separation distinguishes different length scales into e.g. macroscale, mesoscale, microscale and nanoscale, whereas not all of them have to be considered at once. Their definition varies with respect to the scope of the modeling and can be adjusted depending on the specific problem under observation. In structural mechanics, the macroscale typically describes a material at an engineering scale, where typically, geometrical characteristics are in the size of meters. The term mesoscale is frequently used for a description of an inherent microstructure at a magnitude of micrometers, whereas this scale is also referred to as microscale in other works. Microscale interactions could also refer to interactions of grains at boundaries. The nanoscale often refers to interactions and phenomena on an atomistic level. In this work, it is distinguished between the macroscale, which captures characteristics in the size of meters and the microscale, describing a material's microstructure in the range of 100 nanometers to a few micrometers. In order to use the concept of homogenization, the *separation of scales* between the scale levels has to be considered, i.e. $L >> l$. Therby, L and l are the typical length scales of the larger and the smaller scale, respectively, in order for the assumption to hold. In the consideration of DP steel, the different scales can be e.g. an engineering part in a production process at the macroscale, the microstructure composed of a ferritic matrix with martensitic inclusions can then be described by the microscale. The term *homogenization* refers to the derivation of macroscopic quantities based on suitable

averaging techniques over their microstructural counterparts. In this field, semi-analytical approximation schemes based on the findings proposed in Eshelby [37], Eshelby [38] have been developed, such as the *dilute distribution approach*, Christensen [30], the differential scheme, Gross and Seelig [48], and the *self-consistent approach*, Hill [57], are some examples. In contrast to this, computational homogenization schemes have been proposed in the last decades, one examples is the direct micro-macro homogenization approach, Smit et al. [143], Moulinec and Suquet [99], Miehe et al. [96], Miehe and Schröder [93], Feyel [40], Schröder [130], Terada et al. [162], Feyel and Chaboche [41], Geers et al. [43], Schröder [131], which will be summarized in Section 5.2 and applied in the multiscale simulations in this work. The fundamental assumptions for the computation of the overall macroscopic response based on microscopic counterparts will be briefly summarized in the following.

Concept of Ensemble: Considering a collection of samples α of a random microstructure $\mathcal{S}$, the ensemble average $\overline{\mathcal{F}}$ of the material response $\mathcal{F}$ is given by

$$\overline{\mathcal{F}(\boldsymbol{x})} = \int_{\mathcal{S}} \mathcal{F}(\boldsymbol{x}, \alpha) p(\alpha) \, \mathrm{d}\alpha \tag{5.1}$$

with $p(\alpha)$ as the probability density of an individual sample and $\mathcal{F}$ as a placeholder for some geometrical or mechanical material property at a position $\boldsymbol{x}$ under consideration. When enough samples are considered, then the averaged response can be considered as a good approximation of the overall (effective) material response.

Ergodicity Hypothesis: The ergodicity hypothesis states that the ensemble average over a collection of samples can be replaced by the volume average over one sample $\mathcal{B}(\alpha)$ if this sample is large enough, thus

$$\begin{aligned} \overline{\mathcal{F}(\boldsymbol{x})} &= \langle \mathcal{F}(\boldsymbol{x}, \alpha) \rangle \quad \text{with} \\ \langle \mathcal{F}(\boldsymbol{x}, \alpha) \rangle &= \frac{1}{V} \int_{\mathcal{B}(\alpha)} \mathcal{F}(\boldsymbol{x} + \boldsymbol{y}, \alpha) \, \mathrm{d}\boldsymbol{y} \quad \text{if} \quad V \to \infty \end{aligned} \tag{5.2}$$

with V being the volume of the sample $\mathcal{B}(\alpha)$ and $\boldsymbol{y}$. In other words, this hypothesis means that all states of the microstructure available to the ensemble are also available to one sample if this sample is chosen large enough. If a periodic microstructure is considered, this hypothesis is apriori satisfied for a periodic unitcell $\mathcal{B}_Y$, i.e.

$$\lim_{V \to \infty} \frac{1}{V} \int_{\mathcal{B}(\alpha)} \mathcal{F}(\boldsymbol{x} + \boldsymbol{y}, \alpha) \, d\boldsymbol{y} = \frac{1}{Y} \int_{\mathcal{B}_Y} \mathcal{F}(\boldsymbol{x} + \boldsymbol{y}, \alpha) \, d\boldsymbol{y}, \tag{5.3}$$

with Y being the volume of the periodic unitcell.

Concept of a representative volume element: This concept is closely related to the latter two hypotheses and offers their use in practical applications. For a given microstructure, a representative volume element (RVE) is a subsection of the microstructure which is able to resemble the properties and behavior of the complete microstructure to a certain degree of accurateness. If the RVE satisfies to represent the overall microstructure, then the volume average

$$\langle \mathcal{F}(\boldsymbol{x}) \rangle = \frac{1}{V_{\mathrm{RVE}}} \int_{\mathcal{B}_{\mathrm{RVE}}} \mathcal{F}(\boldsymbol{x} + \boldsymbol{y}, \alpha) \, d\boldsymbol{y} \tag{5.4}$$

can be interpreted as a good approximation of the macroscopic response of the microstructure. The definition of an RVE is not unique, there exist several definitions in the literature, see also Zeman [179], which are revisited in the following.

- **Hill (1963)** An RVE has to be a typical representation of an entire structure and shall consist of a sufficient number of characteristic heterogeneities, to ensure that the overall moduli are independent of the surface value of traction and displacement, as long as these values are " macroscopically uniform".
- **Hashin (1983)** The RVE is used to determine the effective properties of a homogenized macroscopic model. The RVE has to be large enough to contain sufficient information about the microstructure but also much smaller than the macroscopic body.
- **Drugan and Willis (1996)** An RVE is the smallest volume element of a heterogeneous structure for which the overall effective modulus is able to provide a sufficiently accurate representation of the mean constitutive response.
- **Ostoja-Starzewski (2001)** The RVE is i) a unit cell of a periodic microstructure or ii) a volume containing a large set of microscale elements, having statistically homogeneous and ergodic properties.
- **Stroeven, Askes and Sluis (2002)** The determination of an RVE is not straight forward. It depends not only on the material under consideration but also on the structure sensitivity of the physical quantity that is measured.

As mentioned above, the definition of an RVE is not unique and there has been much research on the definition of an RVE for different cases. In Trias et al. [166], the authors compare the influence of different mechanical and morphological properties in a carbon reinforced polymer and find the appropriate size of an RVE to depend on the properties under consideration. Kanit et al. [66] present a method for the estimation of the necessary RVE size of a random two-phase microstructure for a predefined permissible error in the measured property based on the concept of integral ranges, which contain information of the domain for which a considered parameter shows good statistical representativity. The method is modified in Pelissou et al. [108] and increased in efficiency. Integral ranges were used as well in Madi et al. [86] for the definition of RVE size in viscoplastic composites. Specific sizes of an RVE for dual-phase steel were determined for equiaxed and banded microstructures in Ramazani et al. [114] considering a convergence of the mechanical behavior under different boundary conditions to an effective value. Saylor et al. [125] proposed a construction method based on a simulated annealing procedure for statistically representative three-dimensional microstructures describing geometric and crystallographic properties using orientation maps on observations on two orthogonal planes in the material. In the sequel Swaminathan et al. [155], Swaminathan and Ghosh [154], the authors construct statistically equivalent representative volume elements based in convergence of the stiffness tensor and marked correlation functions for fiber composites with and without damage, noting that the RVE size must increase with an evolution of damage. The existence of RVEs under different material behavior is analyzed in Gitman et al. [44], where it was stated that due to localization in material undergoing softening, an RVE does not exist since the material

looses its representativeness. Furthermore, the size of an RVE describing a linear elastic material behavior is found to be much smaller than for material undergoing hardening.

Frequently, a section of a real microstructure is considered as an RVE in order to account for microstructural effects realistically. However, the measurable portion of a microstructure using microscopy techniques is limited due to technical aspects. Considering the largest measurable section of a material as an RVE, the involved microstructural morphology of a real material is typically very complex and aggravates a computationally efficient application of such RVEs in an FE analysis due to complex discretizations. In order to reduce the necessary computational effort, a reduction of RVE size could be considered as long as the overall material response does not change outside a certain tolerance. However, this size reduction does not solve the issue of modeling of complex morphologies completely and still requires discretizations with high numbers of degrees of freedom. An approach to circumvent this issue is presented in this work within the construction of statistically similar RVEs (SSRVEs), see Section 6.

5.2 Direct Micro-Macro Homogenization

In the direct micro-macro homogenization approach, which is also known as FE^2-method, a separation of the larger scale and the smaller scale distinguishes the macroscopic boundary value problem and the microscopic boundary value problem. Therein, the boundary value problem on the macroscale describes e.g. construction part such as a specimen in a deep-drawing process, while the microscale describes the level of heterogeneities, e.g., grains or defects in the underlying microstructure of the material. In any case, the separation of length scales has to be obeyed, such that $L >> l$, with L and l being the characteristic dimensions on the macroscale and microscale, respectively. The general idea of the FE^2-method is illustrated in Fig. 5.1.

The microscale is represented by a suitable representative volume element (RVE), some definitions are discussed in the previous section. In order to bridge between the two scales, the *macrohomogeneity-condition*, also know as *Hill-Mandel condition*, is used, see Hill [56]. It asserts the equality of virtual work on both scales and enables to defined boundary conditions on the microscopic boundary value problem based on macroscopic quantities. In the following, the definition of the macroscopic and microscopic boundary value problem are discussed followed by a review of the scale transition procedure. Throughout the Section, an overline, i.e. $\overline{\bullet}$, denotes quantities defined on the macroscale while their microscopic counterparts $\bullet$ are unmarked.

5.2.1 Macroscopic and Microscopic Boundary Value Problem

The reference configuration of the body of interest on the macroscale $\overline{\mathcal{B}}_0 \in R^3$ is parameterized using $\overline{\boldsymbol{X}}$ defining the position of a material point. The deformation map $\overline{\varphi}_t(\overline{\boldsymbol{X}})$ then maps a material point from the reference configuration to the actual configuration $\overline{\mathcal{B}}_t$, where its position is given by $\overline{\boldsymbol{x}}$. The macroscopic deformation gradient is then defined by

$$\overline{\boldsymbol{F}}(\overline{\boldsymbol{X}}) := \mathrm{Grad}_{\overline{\boldsymbol{X}}}\left[\overline{\boldsymbol{\varphi}}_t\right]. \tag{5.5}$$

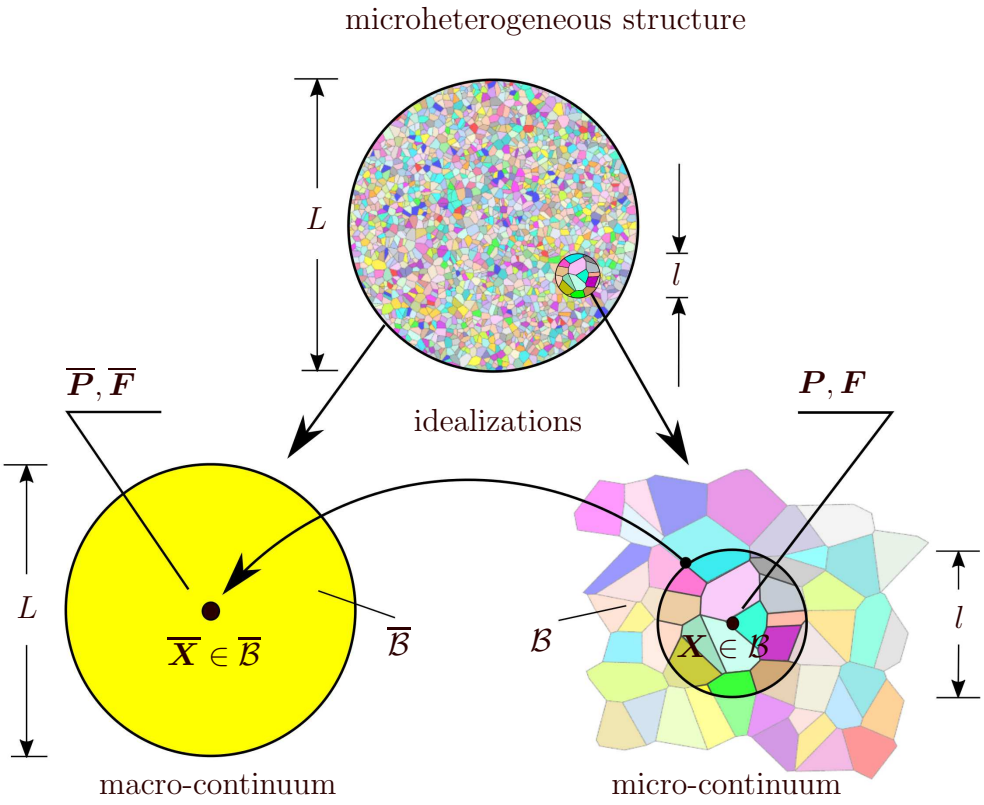

Figure 5.1: Schematic illustration of scale separation. Adapted from SCHRÖDER [131].

The balance of linear momentum at the macroscale demands for

$$\mathrm{Div}_{\overline{\boldsymbol{X}}}[\overline{\boldsymbol{P}}] + \rho_0 \, \overline{\boldsymbol{b}} = \boldsymbol{0}, \tag{5.6}$$

with the body forces $\overline{\boldsymbol{b}}$ and where acceleration terms are neglected. Furthermore, the macroscopic balance of angular momentum requires

$$\overline{\boldsymbol{P}} \cdot \overline{\boldsymbol{F}}^T = \overline{\boldsymbol{F}} \cdot \overline{\boldsymbol{P}}^T. \tag{5.7}$$

On the microscale, the body of interest in the reference configuration $\mathcal{B}_0 \in R^3$ is parameterized by the position vector $\boldsymbol{X}$ for a material point. The deformation map $\varphi_t(\boldsymbol{X})$ maps a material point from the reference configuration to the actual configuration $\mathcal{B}_t$, where the position vector is given by $\boldsymbol{x}$. The deformation gradient on the microscale is given by

$$\boldsymbol{F}(\boldsymbol{X}) := \mathrm{Grad}_{\boldsymbol{X}} \left[\boldsymbol{\varphi}_t\right]. \tag{5.8}$$

The balance of linear momentum on the microscale neglecting acceleration terms and body forces is given by

$$\mathrm{Div}_{\boldsymbol{X}}[\boldsymbol{P}] = \boldsymbol{0}. \tag{5.9}$$

5.2.2 Macroscopic Quantities based on Microscopic Counterparts

In the following, the definition of the macroscopic variables based on their microscopic counterparts is derived. An RVE in the reference placement is considered with a hole $\mathcal{L}_0$

and its boundary $\partial\mathcal{L}_0$. In all cases, the macroscopic measures are described based on boundary data of the microscopic variables on the RVE. The concept of volume averaging is used, thus for an arbitrary tensorial, vectorial or scalar measure $(\bullet)$ one obtains

$$\langle(\bullet)\rangle = \frac{1}{V}\int_{\mathcal{B}_0}(\bullet)\ \mathrm{d}V\,, \tag{5.10}$$

with the volume of the RVE given by V. The volume average of the microscopic deformation gradient is given by

$$\langle\boldsymbol{F}\rangle = \frac{1}{V}\int_{\mathcal{B}_0}\boldsymbol{F}\,\mathrm{d}V = \frac{1}{V}\int_{\partial\mathcal{B}_0}\boldsymbol{x}\otimes\boldsymbol{N}\,\mathrm{d}A + \frac{1}{V}\int_{\partial\mathcal{L}_0}\boldsymbol{x}\otimes\boldsymbol{N}\,\mathrm{d}A, \tag{5.11}$$

using the divergence theorem, Eq. (A.9). Furthermore the volume average of the first Piola-Kirchhoff stress tensor can be expressed as

$$\langle\boldsymbol{P}\rangle = \frac{1}{V}\int_{\mathcal{B}_0}\boldsymbol{P}\,\mathrm{d}V = \frac{1}{V}\int_{\partial\mathcal{B}_0}\boldsymbol{t}_0\otimes\boldsymbol{X}\,\mathrm{d}A + \frac{1}{V}\int_{\partial\mathcal{L}_0}\boldsymbol{t}_0\otimes\boldsymbol{X}\,\mathrm{d}A\,, \tag{5.12}$$

with $\boldsymbol{t}_0 = \boldsymbol{P}\cdot\boldsymbol{N}$ and the outward unit normal $\boldsymbol{N}$. In the following, a body $\mathcal{B}_0$ without holes is considered. Here, the divergence theorem, Eq. (A.9), is applied together with the reformulation in index notation

$$\begin{aligned}\langle\boldsymbol{P}\rangle &= \frac{1}{V}\int_{\mathcal{B}_0}P_{ij}\,\mathrm{d}V = \frac{1}{V}\int_{\mathcal{B}_0}P_{ik}\,X_{j,k}\,\mathrm{d}V = \frac{1}{V}\int_{\mathcal{B}_0}[P_{ik}\,X_j]_{,k}\ -\ P_{ik,k}\,X_j\,\mathrm{d}V\\ &= \frac{1}{V}\int_{\partial\mathcal{B}_0}P_{ik}\,N_k\,X_j\,\mathrm{d}A = \frac{1}{V}\int_{\partial\mathcal{B}_0}[\boldsymbol{P}\cdot\boldsymbol{N}]\otimes\boldsymbol{X}\,\mathrm{d}A\end{aligned} \tag{5.13}$$

where the microscale balance of linear momentum $\mathrm{Div}_X[\boldsymbol{P}] = \boldsymbol{0}$ is considered. The macroscopic quantities are defined based of surface integrals on the RVE, leading to

$$\overline{\boldsymbol{F}} = \frac{1}{V}\int_{\partial\mathcal{B}_0}\boldsymbol{x}\otimes\boldsymbol{N}\,\mathrm{d}A \qquad \text{and} \qquad \overline{\boldsymbol{P}} = \frac{1}{V}\int_{\partial\mathcal{B}_0}\boldsymbol{t}_0\otimes\boldsymbol{X}\,\mathrm{d}A. \tag{5.14}$$

Subsequently, one obtains an equality of the definition of macroscopic variables, $\overline{\boldsymbol{F}}$ and $\overline{\boldsymbol{P}}$, and the volume average for stress and deformation gradient, $\langle\boldsymbol{F}\rangle$ and $\langle\boldsymbol{P}\rangle$. Introducing an additive decomposition of the microscopic deformation gradient in a constant and a fluctuation part,

$$\boldsymbol{F} = \overline{\boldsymbol{F}} + \tilde{\boldsymbol{F}}, \tag{5.15}$$

integration over the RVE yields

$$\overline{\boldsymbol{F}} = \frac{1}{V}\int_{\mathcal{B}_0}\boldsymbol{F}\,\mathrm{d}V = \frac{1}{V}\int_{\mathcal{B}_0}\left(\overline{\boldsymbol{F}} + \tilde{\boldsymbol{F}}\right)\mathrm{d}V = \overline{\boldsymbol{F}} + \frac{1}{V}\int_{\mathcal{B}_0}\tilde{\boldsymbol{F}}\,\mathrm{d}V. \tag{5.16}$$

The latter equation implies that the volume average of the fluctuation part of the deformation gradient vanishes, thus

$$\frac{1}{V}\int_{\mathcal{B}_0}\tilde{\boldsymbol{F}}\,\mathrm{d}V = \boldsymbol{0}. \tag{5.17}$$

With the assumption that the fluctuation part can be computed by $\tilde{\boldsymbol{F}} = \mathrm{Grad}_{\boldsymbol{X}}[\tilde{\boldsymbol{w}}]$ with $\tilde{\boldsymbol{w}}$ being the fluctuation part of the deformation field, Eq. (5.17) can be reformulated to

$$\frac{1}{V}\int_{\partial\mathcal{B}_0}\tilde{\boldsymbol{w}}\otimes\boldsymbol{N}\,\mathrm{d}A = \boldsymbol{0}\,, \tag{5.18}$$

where a fluctuation field $\tilde{\boldsymbol{w}}$ is defined as

$$\tilde{\boldsymbol{w}} := \boldsymbol{x} - \overline{\boldsymbol{F}} \cdot \boldsymbol{X}\,, \tag{5.19}$$

with $\overline{\boldsymbol{F}}$ being a known quantity from the macroscale. In analogy to the decomposition of the deformation gradient, an additive decomposition of the first Piola-Kirchhoff stress tensor is assumed by

$$\boldsymbol{P} = \overline{\boldsymbol{P}} + \tilde{\boldsymbol{P}}, \tag{5.20}$$

leading to the vanishing of the volume average of the stress fluctuations with

$$\overline{\boldsymbol{P}} = \frac{1}{V}\int_{\mathcal{B}_0} \boldsymbol{P}\,\mathrm{d}V = \frac{1}{V}\int_{\mathcal{B}_0} \left(\overline{\boldsymbol{P}} + \tilde{\boldsymbol{P}}\right)\,\mathrm{d}V = \overline{\boldsymbol{P}} + \frac{1}{V}\int_{\mathcal{B}_0} \tilde{\boldsymbol{P}}\,\mathrm{d}V. \tag{5.21}$$

With the definition of the traction vector $\boldsymbol{t}_0 = \boldsymbol{P}\cdot\boldsymbol{N} = (\overline{\boldsymbol{P}} + \tilde{\boldsymbol{P}})\cdot\boldsymbol{N} = \overline{\boldsymbol{t}}_0 + \tilde{\boldsymbol{t}}_0$, the abbreviations $\overline{\boldsymbol{t}}_0 = \overline{\boldsymbol{P}}\cdot\boldsymbol{N}$ and $\tilde{\boldsymbol{t}}_0 = \tilde{\boldsymbol{P}}\cdot\boldsymbol{N}$ are made. From Eq. (5.21), it can be concluded that

$$\frac{1}{V}\int_{\partial\mathcal{B}_0} \tilde{\boldsymbol{t}}_0 \otimes \boldsymbol{X}\,\mathrm{d}A = \boldsymbol{0}. \tag{5.22}$$

5.2.3 Macro-Homogeneity Condition

The *macro-homogeneity condition*, also known as *Hill condition* or *Hill-Mandel condition*, Hill [57], Mandel [87], proposes an energetically consistent localization approach which postulates the equality of the stress power on the macro level and the volume average of the stress power on the micro level, i.e.,

$$\overline{\boldsymbol{P}} : \dot{\overline{\boldsymbol{F}}} = \frac{1}{V}\int_{\mathcal{B}_0} \boldsymbol{P} : \dot{\boldsymbol{F}}\,\mathrm{d}V\,. \tag{5.23}$$

In the following, microscopic boundary conditions will be derived which fulfill the Hill-Mandel condition. Reformulating Eq. (5.23), one obtains

$$\frac{1}{V}\int_{\mathcal{B}_0} \boldsymbol{P} : \dot{\boldsymbol{F}}\,\mathrm{d}V \;-\; \overline{\boldsymbol{P}} : \dot{\overline{\boldsymbol{F}}} = \frac{1}{V}\int_{\mathcal{B}_0} \left((\boldsymbol{P} - \overline{\boldsymbol{P}}) : (\dot{\boldsymbol{F}} - \dot{\overline{\boldsymbol{F}}})\right)\,\mathrm{d}V \;=\; 0. \tag{5.24}$$

The latter equation is directly fulfilled for the cases

$$\boldsymbol{P} = \overline{\boldsymbol{P}} \quad \forall\, \boldsymbol{X} \in \mathcal{B}_0 \qquad \text{and} \qquad \boldsymbol{F} = \overline{\boldsymbol{F}} \quad \forall\, \boldsymbol{X} \in \mathcal{B}_0, \tag{5.25}$$

representing the Reuss estimation (constant stresses over the RVE) and the Voigt estimation (constant deformation over the RVE). Reformulating the right side term of Eq. (5.24), one obtains

$$\frac{1}{V}\int_{\mathcal{B}_0} \left((\boldsymbol{P} - \overline{\boldsymbol{P}}) : (\mathrm{Grad}_{\boldsymbol{X}}[\dot{\boldsymbol{x}}] - \dot{\overline{\boldsymbol{F}}}\cdot\mathrm{Grad}_{\boldsymbol{X}}[\boldsymbol{X}])\right)\,\mathrm{d}V = 0\,. \tag{5.26}$$

This can be manipulated using index notation, leading to

$$\begin{aligned}
&\frac{1}{V}\int_{\mathcal{B}_0} \left((P_{ij} - \overline{P}_{ij}) : (\dot{x}_{i,j} - \dot{\overline{F}}_{ik}X_{k,j})\right)\,\mathrm{d}V \\
&= \frac{1}{V}\int_{\mathcal{B}_0} \left(\left((P_{ij} - \overline{P}_{ij}) : (\dot{x}_i - \dot{\overline{F}}_{ik}X_k)\right)_{,j} \;-\; (P_{ij} - \overline{P}_{ij})_{,j} : (\dot{x}_i - \dot{\overline{F}}_{ik}X_k)\right)\,\mathrm{d}V \\
&= \frac{1}{V}\int_{\partial\mathcal{B}_0} \left((P_{ij} - \overline{P}_{ij}) : (\dot{x}_i - \dot{\overline{F}}_{ik}X_k)\right) N_j\,\mathrm{d}A\,.
\end{aligned} \tag{5.27}$$

Finally, one obtains

$$\frac{1}{V}\int_{\mathcal{B}_0} \boldsymbol{P} : \dot{\boldsymbol{F}}\, \mathrm{d}V \;-\; \overline{\boldsymbol{P}} : \dot{\overline{\boldsymbol{F}}} = \frac{1}{V}\int_{\partial\mathcal{B}_0} (\mathbf{t}_0 - \overline{\boldsymbol{P}}\cdot\boldsymbol{N})\cdot(\dot{\boldsymbol{x}} - \dot{\overline{\boldsymbol{F}}}\cdot\boldsymbol{X})\, \mathrm{d}A\,, \tag{5.28}$$

which must be fulfilled by suitable microscopic boundary conditions. *Dirichlet boundary conditions* are defined by $\boldsymbol{x} = \overline{\boldsymbol{F}}\cdot\boldsymbol{X}\ \forall\ \boldsymbol{X} \in \partial\mathcal{B}_0$, analogously, setting $\mathbf{t}_0 = \overline{\boldsymbol{P}}\cdot\boldsymbol{N}\ \forall\ \boldsymbol{X} \in \partial\mathcal{B}_0$ leads to *Neumann boundary conditions*. For *periodic boundary conditions*, the boundary of the RVE is divided into a two associated parts, "-" and "+", which hold

$$\partial\mathcal{B}_0 = \partial\mathcal{B}_0^- \cup \partial\mathcal{B}_0^+, \tag{5.29}$$

with the outward unit normals $\boldsymbol{N}^-$ and $\boldsymbol{N}^+$, respectively and a point $\boldsymbol{X}^+ \in \partial\mathcal{B}_0^+$ is assumed to have an associated point $\boldsymbol{X}^- \in \partial\mathcal{B}_0^-$. These assumptions are illustrated in Fig. 5.2.

With this definition, the reformulated Hill-Mandel condition, Eq. (5.27) holds if the following conditions are valid

$$\tilde{\boldsymbol{w}}^+ = \tilde{\boldsymbol{w}}^-, \qquad \boldsymbol{t}_0^+ = -\boldsymbol{t}_0^- \quad \text{and} \quad \boldsymbol{N}^- = -\boldsymbol{N}^+, \tag{5.30}$$

i.e. equal fluctuation of deformation, opposing traction vectors and opposing normal vectors on the associated faces $\partial\mathcal{B}_0^+$ and $\partial\mathcal{B}_0^-$.

In the case of a periodic microstructure, periodic boundary conditions lead to the best result when different possible choices of RVEs are compared. Fig. 5.3 shows an artificial microstructure with (cubic) periodically arranged inclusions. All possible choices of an RVE as a periodic unitcell, indicated by the white, blue and black dashed squares, are able to construct the complete microstructure by being placed next to each other in horizontal and vertical direction. In Schröder [131], the boundary conditions on such different choices of RVEs are compared, showing that only periodic boundary conditions are able to produce a periodic stress distribution, independent of the choice of the RVE. This demonstrates that periodic boundary conditions are the best choice in the case of periodic microstructures. There exist additional definitions for suitable boundary conditions, see, e.g., Glüge [45].

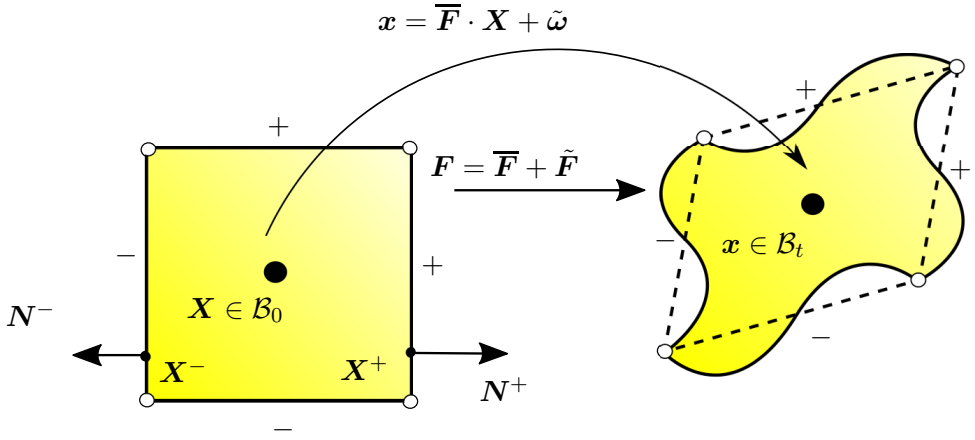

Figure 5.2: Deformation of the RVE considering periodic boundary conditions. Adapted from Schröder [131].

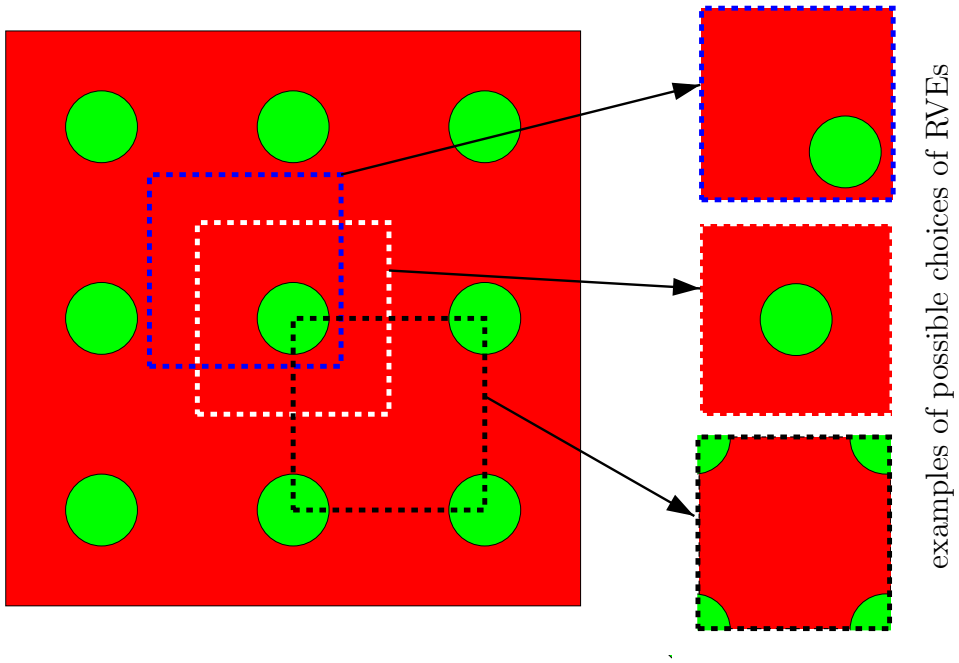

Figure 5.3: Artificial microstructure with cubically, periodically arranged inclusions.

In real microstructures, periodicity can only very rarely be detected and is most often an assumption. However, Gitman et al. [44] justify the assumption of periodicity conditions for the definition of RVEs by comparing different RVEs as choices to represent a larger sample of a microstructure. If so-called wall effects occur, inclusions are not able to cross through the boundary of the RVE from one side to another. Thus, a construction of RVEs not showing these wall effects is favored. They especially analyzed the effect this wall effect has on the needed RVE size to obtain realistic behavior in tension and shear tests. While in a tension tests the effect does not show a major influence, wall effects in a comparison of shear tests lead to much larger RVE sizes than in the case of periodic RVEs.

In the case of random microstructures, statistical volume elements (SVEs) are analyzed instead of RVEs, frequently. These SVEs are smaller than RVEs and pose a weaker requirement on the length scale separation by introducing the parameter $\delta = l/d$ where l is the size of the SVE and d is the characteristic length scale of the microstructure. For $\delta \to \infty$ the SVE approaches the corresponding RVE. Often, the determination of an RVE in a real microstructure is not even possible due to limitations in measuring techniques, which is why the usage of SVEs is needed. Due to this, the definition of an RVE in many cases can be seen as an assumption, since its representativeness can only be shown to a limited extent. In the following, the term RVE will be used, even if this representativeness is an assumption.

Fig. 5.4 shows a two-dimensional representation of a real microstructure obtained from a DP steel sample which does not possess periodic properties. With a look at the morphological complexity of the real microstructure, it is unquestionable that using the complete microstructure as an RVE leads to large number of degrees of freedom, which is disadvantageous. A possible reduction of degrees of freedom is the choice of

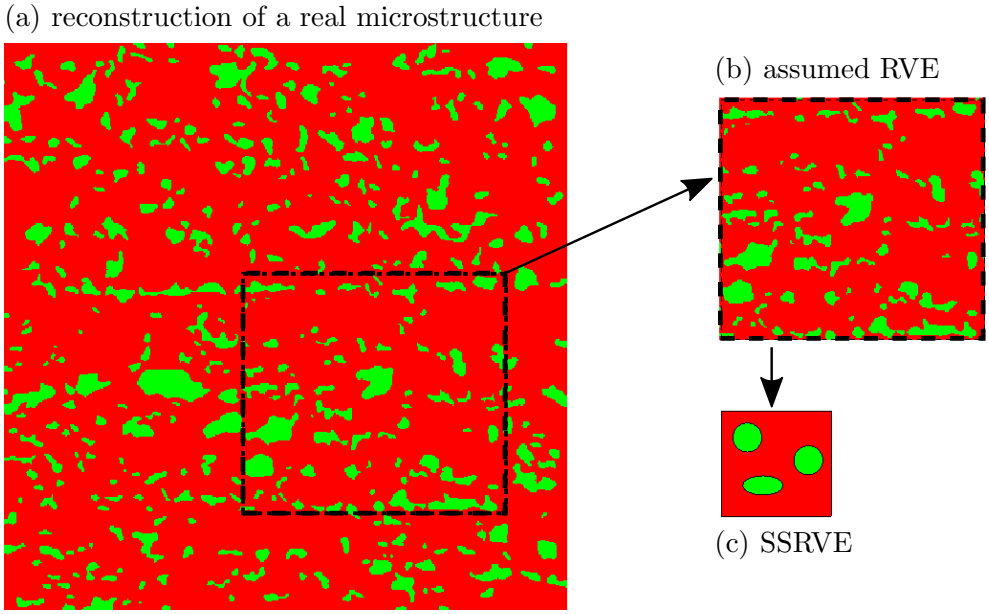

Figure 5.4: (a) Real DP steel microstructure reconstruction, Balzani et al. [10]. (b) Assumption of RVEs and (c) schematic sketch of SSRVE of lower complexity.

a smaller region of the microstructure as RVE instead under the assumption that the statistical properties are still maintained to a certain level of accurateness. However, the inherent complexity of the microstructure is still apparent, as can be seen in the top right illustration in Fig. 5.4. The construction of statistically similar RVEs (SSRVEs) instead can lead to a significant reduction of complexity. These artificial microstructures possess similar statistical properties as the underlying real microstructure but possess a much less complex morphology, represented by a distinct number of inclusions of simple shape. The method of construction of SSRVEs has been proposed in Schröder et al. [132] for two-dimensional and Balzani et al. [11] in 3D and will be summarized in Section 6 in this work. The here presented method produces three-dimensional SSRVEs with periodic properties to allow a periodic extension in three-dimensional space.

In the case of polycrystalline materials, the consideration of the underlying microstructure also requires much effort regarding the discretization. An example of a polycrystalline microstructure constructed using polycrystalline unitcells can be seen in Fig. 5.5. Here, the periodic unitcells do not possess a cubic shape, but a polyhedral concave shape. An example of a periodic unitcell of a polycrystal, being a polycrystal itself with 50 grains, can be seen in Fig. 5.5. For the use of these polycrystalline unitcells in the framework of the FE^2-method, the periodicity properties of two associated surfaces is indicated by normal vectors pointing in opposite direction. These polycrystalline structures were constructed using the open-source software *Neper*, see Quey et al. [112] for details.

5.2.4 Numerical Implementation and Macroscopic Tangent Moduli

The numerical implementation of the macroscopic and microscopic boundary value problem in the framework of the Finite Element Method, see Section 3, is discussed in the following, where the main attention is put on the variational formulation and the deriva-

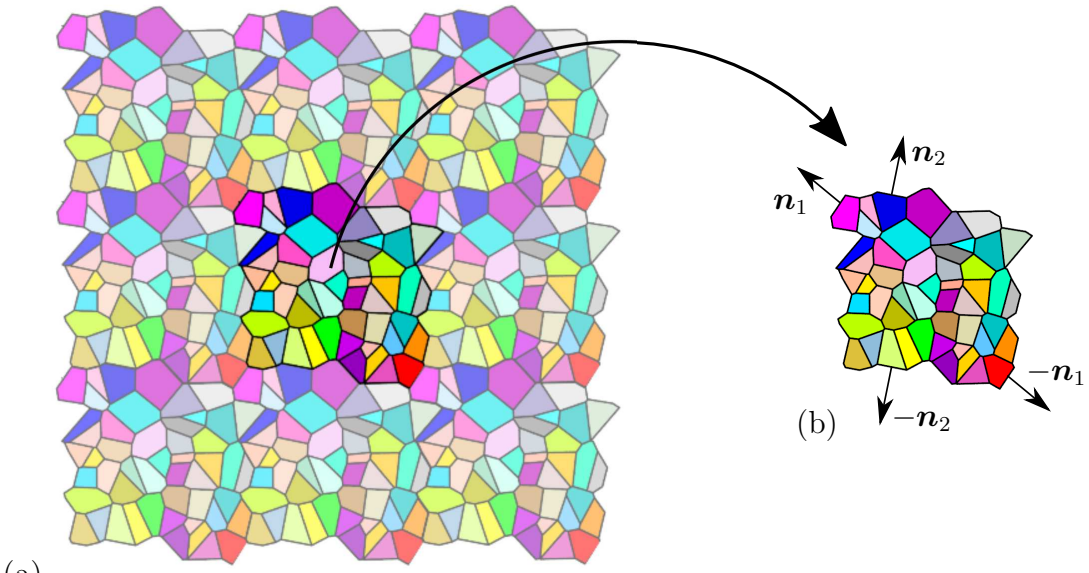

Figure 5.5: (a) RVE of an artificial polycrystalline microstructure. (b) Periodic polycrystalline unitcell with indication of opposite normal vectors.

tion of the algorithmic consistent macroscopic tangent moduli. Therein, the approach proposed in SCHRÖDER [131] is followed. The weak form of linear momentum balance, Eq. 2.41, at the macroscale can be written as

$$\overline{G} = \underbrace{\int_{\overline{\mathcal{B}}_0} \delta\overline{\boldsymbol{F}} : \overline{\boldsymbol{P}} \, \mathrm{d}V}_{\overline{G}^{\mathrm{int}}} - \underbrace{\left(\int_{\overline{\mathcal{B}}_0} \delta\overline{\boldsymbol{x}} \cdot \overline{\boldsymbol{f}} \, \mathrm{d}V + \int_{\partial\overline{\mathcal{B}}_0} \delta\overline{\boldsymbol{x}} \cdot \overline{\boldsymbol{t}}_0 \, \mathrm{d}A \right)}_{\overline{G}^{\mathrm{ext}}} = 0 \tag{5.31}$$

where $\delta\overline{\boldsymbol{F}} = \mathrm{Grad}_{\overline{\boldsymbol{X}}}[\delta\overline{\boldsymbol{x}}]$. In order to solve the nonlinear weak form using a Newton-Raphson scheme, the linearization is computed as

$$\Delta\overline{G}^{\mathrm{int}} = \int_{\overline{\mathcal{B}}_0} \delta\overline{\boldsymbol{F}}^T : \overline{\mathbb{A}} : \Delta\overline{\boldsymbol{F}} \, \mathrm{d}V \,, \tag{5.32}$$

where the algorithmic consistent macroscopic moduli $\overline{\mathbb{A}}$ is defined by

$$\overline{\mathbb{A}} = \frac{\partial\overline{\boldsymbol{P}}}{\partial\overline{\boldsymbol{F}}} \,. \tag{5.33}$$

The moduli cannot be computed directly, since there is no explicit expression $\overline{\boldsymbol{P}}(\overline{\boldsymbol{F}})$. An efficient algorithm for the computation is presented in MIEHE ET AL. [96]. The system of equations resulting from the linearization

$$\overline{G} + \Delta\overline{G} = \delta\overline{\boldsymbol{D}}^T(\overline{\boldsymbol{K}}\Delta\overline{\boldsymbol{D}} + \overline{\boldsymbol{R}}) = 0 \quad \rightarrow \quad \overline{\boldsymbol{K}}\Delta\overline{\boldsymbol{D}} + \overline{\boldsymbol{R}} = \boldsymbol{0} \tag{5.34}$$

has to be solved iteratively with respect to the global incremental displacement vector $\Delta\overline{\boldsymbol{D}}$. For the treatment of the microscopic boundary value problem, the weak form of linear momentum balance reads

$$G = \int_{\mathcal{B}_0} \delta\tilde{\boldsymbol{F}} : \boldsymbol{P} \, \mathrm{d}V \; = 0 \,, \tag{5.35}$$

neglecting volume acceleration and inertia terms. Here, the fluctuations of the displacement field on the microscale $\tilde{\boldsymbol{w}}$ are discretized and the displacements can be obtained from $\boldsymbol{x} = \overline{\boldsymbol{F}}\boldsymbol{X} + \tilde{\boldsymbol{w}}$. Then, $\delta\tilde{\boldsymbol{F}} = \mathrm{Grad}[\delta\tilde{\boldsymbol{w}}]$ and $\Delta\tilde{\boldsymbol{F}} = \mathrm{Grad}[\Delta\tilde{\boldsymbol{w}}]$. The linearization of the microscale yields

$$\Delta G = \int_{\mathcal{B}_0} \delta\tilde{\boldsymbol{F}}^T : \mathbb{A} : \Delta\boldsymbol{F}\, \mathrm{d}V = \int_{\mathcal{B}_0} \delta\tilde{\boldsymbol{F}}^T : \mathbb{A} : (\Delta\overline{\boldsymbol{F}} + \Delta\tilde{\boldsymbol{F}})\, \mathrm{d}V, \tag{5.36}$$

which together with the approximation $\tilde{\boldsymbol{F}} = \boldsymbol{B} \cdot \tilde{\boldsymbol{d}}$ leads to the system of equations

$$G + \Delta G = \delta\tilde{\boldsymbol{D}}^T(\boldsymbol{K}\Delta\tilde{\boldsymbol{D}} + \boldsymbol{L}\Delta\overline{\boldsymbol{F}} + \boldsymbol{R}) = 0 \quad \rightarrow \quad \boldsymbol{K}\Delta\tilde{\boldsymbol{D}} + \boldsymbol{L}\Delta\overline{\boldsymbol{F}} + \boldsymbol{R} = \boldsymbol{0}\,, \tag{5.37}$$

with the assembled matrices

$$\boldsymbol{K} = \mathop{\mathsf{A}}_{\mathrm{e}=1}^{n_{\mathrm{ele}}} \int_{\mathcal{B}_0^e} \boldsymbol{B}^T\mathbb{A}\boldsymbol{B}\, \mathrm{d}V\,, \quad \boldsymbol{L} = \mathop{\mathsf{A}}_{\mathrm{e}=1}^{n_{\mathrm{ele}}} \int_{\mathcal{B}_0^e} \boldsymbol{B}^T\mathbb{A}\, \mathrm{d}V\,, \quad \boldsymbol{R} = \mathop{\mathsf{A}}_{\mathrm{e}=1}^{n_{\mathrm{ele}}} \int_{\mathcal{B}_0^e} \boldsymbol{B}^T\boldsymbol{P}\, \mathrm{d}V\,. \tag{5.38}$$

Note that during the solution of the microscopic boundary value problem, the macroscopic deformation gradient is constant, thus $\Delta\overline{\boldsymbol{F}} = \boldsymbol{0}$. Then Eq. (5.37(2)) reduces to $\boldsymbol{K}\Delta\tilde{\boldsymbol{D}} + \boldsymbol{R} = \boldsymbol{0}$. After the microscopic boundary value problem has been iteratively solved and convergence is obtained such that $\boldsymbol{R} = \boldsymbol{0}$, the computation of the algorithmic consistent macroscopic moduli $\overline{\mathbb{A}}$ follows. Starting from the incremental relation of Eq. (5.21) at the macroscale and the incremental constitutive relation $\Delta\boldsymbol{P} = \mathbb{A} : \Delta\boldsymbol{F}$, one obtains

$$\Delta\overline{\boldsymbol{P}} = \frac{1}{V}\int_{\mathcal{B}_0} \Delta\boldsymbol{P}\, \mathrm{d}V = \frac{1}{V}\int_{\mathcal{B}_0} \mathbb{A} : \Delta\boldsymbol{F}\, \mathrm{d}V = \frac{1}{V}\int_{\mathcal{B}_0} \mathbb{A} : (\Delta\overline{\boldsymbol{F}} + \Delta\tilde{\boldsymbol{F}})\, \mathrm{d}V, \tag{5.39}$$

with the additive incremental decomposition $\Delta\boldsymbol{F} = \Delta\overline{\boldsymbol{F}} + \Delta\tilde{\boldsymbol{F}}$. The increment of the gradient of the fluctuations is obtained from Eq. (5.37(2)) by

$$\Delta\tilde{\boldsymbol{F}} = \boldsymbol{B}\Delta\tilde{\boldsymbol{D}} = -\boldsymbol{B}\boldsymbol{K}^{-1}\boldsymbol{L}\Delta\overline{\boldsymbol{F}}\,, \tag{5.40}$$

with $\Delta\overline{\boldsymbol{F}}$ being the current increment of the macroscopic deformation gradient, which in the macroscopic iteration not zero, and the equilibrium state in the microscopic boundary value problem, i.e. $\boldsymbol{R} = \boldsymbol{0}$. Together with this relation, Eq. (5.39) becomes

$$\begin{aligned} \Delta\overline{\boldsymbol{P}} &= \frac{1}{V}\int_{\mathcal{B}_0} \mathbb{A} : (\Delta\overline{\boldsymbol{F}} - \boldsymbol{B}\boldsymbol{K}^{-1}\boldsymbol{L}\Delta\overline{\boldsymbol{F}})\, \mathrm{d}V \\ &= \left(\frac{1}{V}\int_{\mathcal{B}_0} \mathbb{A}\, \mathrm{d}V - \frac{1}{V}\boldsymbol{L}^T\boldsymbol{K}^{-1}\boldsymbol{L}\right) : \Delta\overline{\boldsymbol{F}}\,, \end{aligned} \tag{5.41}$$

with the consistent algorithmic macroscopic moduli given by

$$\overline{\mathbb{A}} = \frac{1}{V}\int_{\mathcal{B}_0} \mathbb{A}\, \mathrm{d}V - \frac{1}{V}\boldsymbol{L}^T\boldsymbol{K}^{-1}\boldsymbol{L}\,. \tag{5.42}$$

The microscopic module is known from the solution of the microscopic boundary value problem, whereas strategies for an efficient computation of the second term of the macroscopic module are described in, Miehe et al. [96], Miehe and Koch [92] and Schröder [131].

6 Statistically Similar Representative Volume Elements

With the aim to model microstructural properties of a material in the framework of the FE^2-method, RVEs based on realistic microstructures often lead to enormous computational expenses. The use of simplified RVEs, which are reduced in size as well as complexity of the inherent morphology, can lead to a reduction in computational costs. They can be constructed such that selected morphological properties in the simplified RVE and the real microstructure are similar. These structures are then referred to as statistically similar RVEs (SSRVEs).

In this chapter, the concept of SSRVEs will be outlined. The method has been presented for two-dimensional microstructures in Balzani et al. [7; 8; 10] and Schröder et al. [132], It has been extended to 3D microstructures in Balzani et al. [11] and Scheunemann et al. [128], analyzing alternative statistical measures. An SSRVE is governed by similarities with respect to statistical properties of the real microstructure morphology, while the SSRVE exhibits a smaller size and lower level of complexity in terms of microstructure morphology. The statistical similarity is enforced by matching considered statistical measures, which is based on the ideas proposed in Povirk [111] for microstructures with circular inclusions. A least-square functional is minimized in an optimization process, which considers the difference of the statistical properties computed from the real microstructure and the SSRVE. If the mechanical response of the microheterogeneous materials is mainly governed by the phase contrast, the replication of morphological properties in the SSRVE then results in a similarity of the mechanical response compared to the real microstructure.

In the motivation of this work, a literature overview is given for reconstruction approaches of real microstructures based on the minimization of least-square functionals as well as examples for the application of SSRVEs, see e.g. Rauch et al. [117], Ambrozinski et al. [2], Rauch et al. [118]. With regard to the ability of the SSRVE to represent the real microstructure in terms of morphology and mechanical behavior, the statistical measures used in the construction process play a crucial role. A comparison of measures for the construction of SSRVEs is presented in Balzani et al. [8]. Further measures are presented in Scheunemann et al. [128] and compared regarding their applicability in the construction of SSRVEs.

The need for considering microstructural information in the material modeling is often necessary to describe effects observed at a large scale in order to circumvent complex macroscopic constitutive laws. In order to reconstruct an SSRVE based on properties of a real microstructure, its morphology needs to be known. The measurement of real microstructures using microscopy techniques is a costly task and limited in terms of the size which can be captured. Consequently, different approaches to reconstruct microstructures in order to, e.g., obtain a certain number of samples with similar properties as the real microstructure have been proposed. In the literature, different approaches for the construction of artificial microstructures based on a fitting of statistical measures can be found. Yeong and Torquato [176] proposed a technique for the reconstruction of random media based on a least-square fit of two-point probability function and lineal-path function. Similarly, in Kumar et al. [79] 2D microstructures of a DP steel are reconstructed by minimizing a least-square functional taking into account the two-point probability function and lineal-path function as statistical measures in a simulated

annealing process. The reconstructed artificial microstructures show similar distribution of stress as well as peak stresses as the related real microstructure. A Monte-Carlo approach is utilized in Baniassadi et al. [13] to reconstruct 3D microstructures based on a comparison of two-point cluster function and two-point correlation function. Feng et al. [39] present a method for rapid construction of artificial microstructures considering first and second order statistical moments using fast fourier transformation.

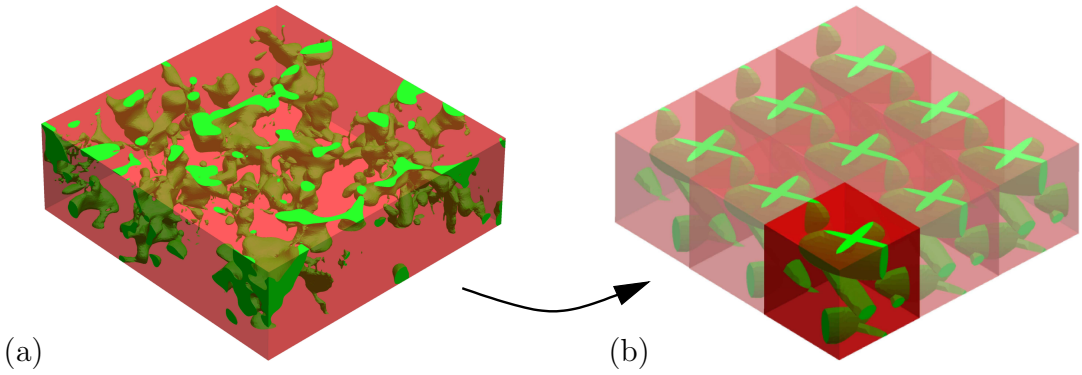

Figure 6.1: Random target microstructure of an inclusion-matrix microstructure and associated periodic microstructure with SSRVE as periodic unitcell. Taken from Balzani et al. [10].

In order to apply the method of SSRVEs, several premises have to be obeyed. The reduction of size of the SSRVE compared with the real microstructure is possible due to the periodic morphology of the SSRVE. As can be seen in Fig. 6.1, the periodicity of the SSRVE enables a construction of an infinitely large microstructure using the SSRVE as a periodic unitcell. Thus, it is assumed that the considered random microstructure may be represented by such a periodic microstructure. Furthermore, the macroscopic material behavior shall depend only on the microstructure morphology and the local constitutive laws, describing the microscopic behavior of each phase, which needs to be known.

In the following sections, an overview on selected statistical measures for the description of microstructures is presented. The construction method of SSRVEs is described in detail and candidates of SSRVEs are constructed for a dual-phase (DP) steel microstructure obtained from EBSD-FIB measurements, see Section 4. The constructed SSRVE candidates are compared to one another and their performance is analyzed in a comparison of mechanical response. Therein, virtual monotonic tests are applied (tension and shear tests). An analysis of microscale stresses in each phase is shown and the possibilities of substructures of a real microstructure as SSRVEs is discussed. Furthermore, other virtual mechanical tests are simulated compare the ability of the SSRVE to describe effects related to the yield behavior of the material.

6.1 Statistical Measures for Spatial Structures

In contrast to the frequent assumption of homogeneous materials, heterogeneity is commonly observed in nature, with the material often being composed of multiple phases at

a small scale, referred to as microheterogeneity. The macroscopic material behavior and properties are a result of not only the properties of the individual constituents, but also the geometrical composition of the compound material. The morphological quantification is of large interests in many disciplines and can be realized using the models and methods developed in the field of stochastic geometry. With the help of these methods, three-dimensional microstructures can be characterized quantitatively in terms of their morphology and conclusions can be drawn upon the relation of morphological properties and the material behavior. These methods are given by e.g. measures characterizing particle systems, planar objects and three dimensional structures. In the following, a selection of statistical measures which are able to characterize a two-phase material with inclusions embedded in a matrix, are discussed. The consideration of two-phase materials enables a description of the morphology of one phase with the help of statistical measures and obtain a description of the second phase using the negative image. In the case of the two-phase microstructure of DP steel, the described phase is the martensitic inclusion phase. An overview on statistical descriptors can be found in, e.g., Ohser and Mücklich [103] and Torquato [165].

6.1.1 Scalar Measures

A basic characterization can be made based upon different scalar descriptors. The *phase fraction* $\mathcal{P}_\mathrm{V}$ relates the volume of a single phase to the volume of the entire material

$$\mathcal{P}_\mathrm{V} = V^P/V\,, \tag{6.1}$$

with V^P denoting the volume of phase P and V as the complete volume. This basic measure gives rise to general information about the amount of the phases, yet it does not carry information about the shape of the individual phases. The *internal surface area* of the inclusion phase I can be quantified by

$$\mathcal{S}_\mathrm{I} = \sum_i \mathcal{S}^i \qquad \text{with} \qquad \mathcal{S}^i = \int_{\partial\mathcal{B}^i} \mathrm{d}a\,, \tag{6.2}$$

with the infinitesimal surface element $\mathrm{d}a$ and the internal surface of an inclusion $\partial\mathcal{B}^i$. A characterization on the shape of an internal phase surface can be given by the *integral of mean curvature* for the inclusion phase

$$\mathcal{M}_\mathrm{I} = \sum_i \mathcal{M}^i \qquad \text{with} \qquad \mathcal{M}^i = \int_{\partial\mathcal{B}^i} \frac{1}{2}\left(\frac{1}{r_1} + \frac{1}{r_2}\right) \mathrm{d}a \tag{6.3}$$

and the *integral of total curvature* for the inclusion phase

$$\mathcal{K}_\mathrm{I} = \sum_i \mathcal{K}^i \qquad \text{with} \qquad \mathcal{K}^i = \int_{\partial\mathcal{B}^i} \frac{1}{r_1\, r_2} \mathrm{d}a, \tag{6.4}$$

with $\mathcal{M}^i$ and $\mathcal{K}^i$ denoting the respective measure for an individual inclusion i. The maximal and minimal radii of the surface element are defined by r_1 and r_2, where $1/r_1$ and $1/r_2$ then denote the maximal and minimal curvature of the surface element. The *internal surface density*, *density of integral of mean curvature* and *integral of total curvature* are then defined as

$$\mathcal{P}_S = \mathcal{S}_I/V, \quad \mathcal{M}_S = \mathcal{M}_I/V, \quad \mathcal{P}_K = \mathcal{K}_I/V. \tag{6.5}$$

6.1.2 n-Point Probability Functions

The characterization for microstructures based on n-point probability functions is an important concept for microstructural characterization, details can be found in e.g. TORQUATO [165]. An indicator function is introduced in order to distinguish the phases in a composite. Thus, in a two-phase composite the indicator function describing the domain $D^{(P)}$ occupied by phase P is defined by

$$\chi^{(P)}(\boldsymbol{x}) := \begin{cases} 1 \text{ if } \boldsymbol{x} \in D^{(P)} \\ 0 \text{ otherwise}\,, \end{cases} \tag{6.6}$$

where $\boldsymbol{x}$ is a position vector of material points and the indicator function takes the value 1 for every material point located in the phase P and zero for all other points. Based on this indicator function, the n-point probability function is defined by the ensemble average over individual realizations α as

$$\mathcal{S}_n^{(P)}(\boldsymbol{x}_1, \boldsymbol{x}_2, ..., \boldsymbol{x}_n) := \overline{\chi^{(P)}(\boldsymbol{x}_1, \alpha)\chi^{(P)}(\boldsymbol{x}_2, \alpha)...\chi^{(P)}(\boldsymbol{x}_n, \alpha)}, \tag{6.7}$$

where the overline denotes the ensemble average of a considered quantity. In the literature, the function is also referred to as n-point correlation function and describes the probability of n material points with the position vectors $\boldsymbol{x}_1, \ldots, \boldsymbol{x}_n$ being located in phase P. Together with the ergodicity hypothesis, see Section 5.1, the ensemble average can be reformulated to

$$\mathcal{S}_n^{(P)}(\boldsymbol{x}_1, \boldsymbol{x}_2, ..., \boldsymbol{x}_n) = \lim_{V\to\infty} \frac{1}{V} \int_{\mathcal{B}} \chi^{(P)}(\boldsymbol{y} + \boldsymbol{x}_1)\chi^{(P)}(\boldsymbol{y} + \boldsymbol{x}_2)...\chi^{(P)}(\boldsymbol{y} + \boldsymbol{x}_n)\, \mathrm{d}\boldsymbol{y}\,, \tag{6.8}$$

with the volume average over an infinitely large sample $\mathcal{B}$ with the volume $V(\mathcal{B}) = V$. Note that due to practical reasons, a sufficiently large volume can be considered here instead of an infinitely one. With the difference vector between points $\boldsymbol{x}_{12} = \boldsymbol{x}_2 - \boldsymbol{x}_1$, Eq. (6.8) can be rewritten to

$$\mathcal{S}_n^{(P)}(\boldsymbol{x}_{12}, ..., \boldsymbol{x}_{1n}) = \lim_{V\to\infty} \frac{1}{V} \int_{\mathcal{B}} \chi^{(P)}(\boldsymbol{y})\ \chi^{(P)}(\boldsymbol{y} + \boldsymbol{x}_{12})...\chi^{(P)}(\boldsymbol{y} + \boldsymbol{x}_{1n})\, \mathrm{d}\boldsymbol{y}. \tag{6.9}$$

In most applications, the use of *one-* and *two-point probability functions*, $\mathcal{S}_1^{(P)}$ and $\mathcal{S}_2^{(P)}$, is feasible due to a still manageable computational effort. They are defined by

$$\mathcal{S}_1^{(P)}(\boldsymbol{x}) = \lim_{V\to\infty} \frac{1}{V} \int_{\mathcal{B}} \chi^{(P)}(\boldsymbol{y} + \boldsymbol{x})\, \mathrm{d}\boldsymbol{y} \tag{6.10}$$

and

$$\mathcal{S}_2^{(P)}(\boldsymbol{x}_1, \boldsymbol{x}_2) = \lim_{V\to\infty} \frac{1}{V} \int_{\mathcal{B}} \chi^{(P)}(\boldsymbol{y} + \boldsymbol{x}_1)\ \chi^{(P)}(\boldsymbol{y} + \boldsymbol{x}_2)\, \mathrm{d}\boldsymbol{y}. \tag{6.11}$$

While the one-point probability function is equal to the phase fraction $\mathcal{P}_V^{(P)}$ and describes the probability of a point being located in phase P, the two-point probability function, also known as two-point correlation or autocorrelation function, describes the probability of two material points located in the same phase. Probability functions for $n > 2$ require high computational effort. MIKDAM ET AL. [97] have proposed an approximation approach for *three-point probability functions* based on two-point probability

functions. Two-point probability functions can be efficiently computed, since they can be related to the power spectral density via the Wiener-Khinchin theorem, cf. WIENER [173], KHINTCHINE [71]. The Wiener-Khinchin theorem describes the relation between the autocorrelation function and the power spectral density, here further named spectral density, where the spectral density is equal to the Fourier transform of the autocorrelation function and, vice versa, the autocorrelation function is the inverse Fourier transform of the spectral density, cf. STENGEL [148].

6.1.3 Spectral Density

The spectral density of a discrete three-dimensional data set can be calculated based in the discrete Fourier transformation, which maps the discrete spatial data set to a frequency domain via

$$\mathcal{F}^{(P)}(k_x, k_y, k_z) := \sum_{n_x=1}^{N_x} \sum_{n_y=1}^{N_y} \sum_{n_z=1}^{N_z} \exp\left(-2\pi\mathrm{i}\left(\frac{n_x\, k_x}{N_x} + \frac{n_y\, k_y}{N_y} + \frac{n_z\, k_z}{N_z}\right)\right) \chi^{(P)}(n_x, n_y, n_z), \tag{6.12}$$

where the discrete data set is given by the indicator function $\chi^{(P)}$, cf. Eq. (6.6), and the position vector $\boldsymbol{x} = [n_x\ n_y\ n_z]^{\mathrm{T}}$ with $n_x = 1 \ldots N_x$, $n_y = 1 \ldots N_y$ and $n_z = 1 \ldots N_z$ and the total size of the data set given by N_x, N_y and N_z. The coordinates in the frequency domain are k_x, k_y and k_z. The discrete inverse Fourier transformation is then given by

$$\begin{aligned} \chi^{(P)}(n_x, n_y, n_z) :=& \frac{1}{N_x\, N_y\, N_z} \sum_{k_x=1}^{N_x} \sum_{k_y=1}^{N_y} \sum_{k_z=1}^{N_z} \\ & \exp\left(2\pi\mathrm{i}\left(\frac{n_x\, k_x}{N_x} + \frac{n_y\, k_y}{N_y} + \frac{n_z\, k_z}{N_z}\right)\right) \mathcal{F}^{(P)}(k_x, k_y, k_z), \end{aligned} \tag{6.13}$$

mapping the data from the frequency domain to the spatial domain. In the discrete Fourier transformation, the data set is considered as periodically extendable. The spectral density is then calculated by

$$\mathcal{P}_{\mathrm{SD}}^{(P)} := \frac{(\mathcal{F}^{(P)})^* \mathcal{F}^{(P)}}{N_x N_y N_z}, \tag{6.14}$$

where $(\mathcal{F}^{(P)})^*$ denotes the conjugate complex of the Fourier transform $\mathcal{F}^{(P)}$. As mentioned above, the spectral density and auto-correlation function are related, thus an alternative method in order to obtain the spectral density involves computing the Fourier transformation of the autocorrelation function. However, Eq. (6.14) allows for rapid computations of the spectral density, since fast algorithms are available for the computation of Fourier transformations, e.g. the "FFTW", ("Fastest Fourier Transform in the West"), developed at the Massachusetts Institute of Technology by M. Frigo and S.G. Johnson (www.fftw.org). In contrast to this, computing the autocorrelation function would require more computational effort.

Example of Spectral Density Calculation for Discrete 1D Pulse

As an example, the computation of the spectral density based on the two above mentioned methods is presented for a discrete signal, which is assumed to be repeated periodically. The signal sequence x has the period $N = 6$ and the spatial coordinates n, such that

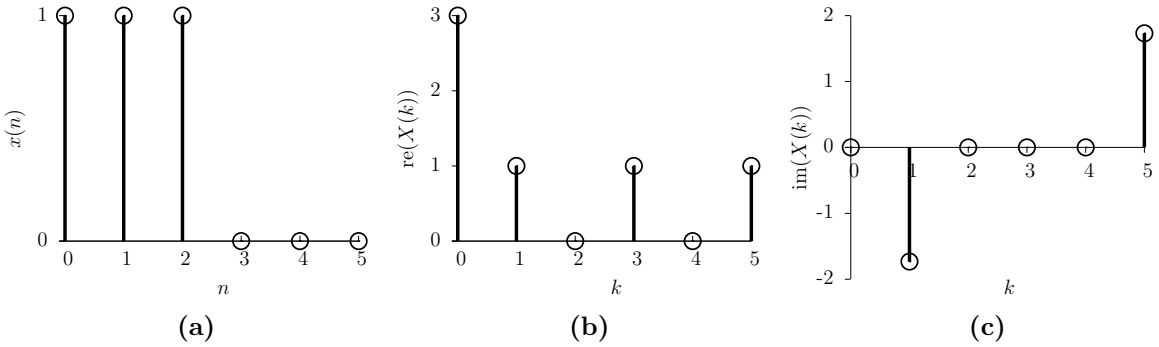

Figure 6.2: (a) Sample pulse, (b) real and (c) imaginary part of discrete Fourier transform of sample pulse.

$x(n+N) = x(n)$ is given by

$$x(n) = \begin{cases} 1 \text{ for } n = 0, 1, 2\,, \\ 0 \text{ for } n = 3, 4, 5\,, \end{cases} \tag{6.15}$$

it depicted in Fig. 6.2a. The discrete Fourier transform for a 1D discrete signal sequence is given by

$$X(k) = \sum_{n=0}^{N-1} x(n)\, \exp(-\mathrm{i}\, 2\pi k\, n/N), \tag{6.16}$$

which maps the periodic signal into a periodic, discrete frequency spectrum, described by the coordinate k. The discrete Fourier transform $X(k)$ is calculated via Eq. (6.16) and is shown in Fig. 6.2.

The value $X(k = 0)$ is simply $X(k = 0) = \sum_{n=0}^{N-1} \exp(0)\, x(n)$, thus the sum over all entries, and referred to as the zero component. Reversibly, the inverse discrete Fourier transform is defined by

$$x(n) = \frac{1}{N} \sum_{k=0}^{N-1} X(k)\, \exp(\mathrm{i}\, 2\pi k\, n/N)\,, \tag{6.17}$$

which maps the discrete Fourier transform, $X(k)$, given in the frequency domain back to $x(n)$ in the spatial domain. Furthermore, the autocorrelation function $\varphi(s)$ describes the correlation of the function with itself with respect to a time shift s. The autocorrelation function of $x(n)$ is defined by

$$\varphi(s) := \frac{1}{N} \sum_{n=0}^{N-1} x(n)\, x(n+s), \tag{6.18}$$

which is depicted in Fig. 6.3a and where $\varphi(s + N) = \varphi(s)$, thus the autocorrelation function itself is periodic with period N. The computation of the spectral density can be now carried out based on $X(k)$ given by

$$\mathcal{SD}(k) := \frac{X(k)\, X^*(k)}{N} \tag{6.19}$$

where $X^*(k)$ is the conjugate complex of $X(k)$. Alternatively, the spectral density can be defined based on the discrete Fourier transform of the autocorrelation function, hence

$$\mathcal{SD}(k) := \sum_{s=0}^{N-1} \varphi(s) \exp(-\mathrm{i}\, 2\pi k\, s/N). \tag{6.20}$$

The spectral density is depicted in Fig. 6.3b, where the entry zero entry $\mathcal{SD}(0)$ is apriori known as $(X(0))^2/N$.

In the discrete spectral density, the frequency coordinates k_x, k_y and k_z and the coordinates in the spatial domain n_x, n_y and n_z are related by $k_i = 2\,\pi\, n_i/N_i$ where $i = x, y, z$. Subsequently, the number of spatial data points $N_{x,y,z}$ and the number of data points in the frequency domain is the same. The entry in the zero component is deleted from the spectral density and a normalization with respect to the largest entry in the spectral density is computed afterwards. In order to compare the spectral density of structures with different sizes, i.e. different number of data points $N_{x,y,z}$, a rebinning procedure to adjust the resolution must be applied. Thereby, the data set of fine resolution is transferred to a data set of coarse resolution computing mean values of sections of the original set. This is straight forward if the data set size of fine resolution is an integer multiple of the set size of coarse resolution. Then, the mean value of all entries of the set of fine resolution being associated to an entry in the coarsely resolved set is computed. The rebinning procedure in this case is illustrated in Fig. 6.4a. If the size of the finely resolved set is not an integer multiple of the coarsely resolved set's size, the rebinning must consider the affiliation of one entry in the one grid to two cells in the other grid. Then, the computation of the mean value of the associated entries in the finely resolved set considers a weighting factor which describes the amount of the entry in the currently considered coarse entry. This rebinning case is illustrated in Fig. 6.4b. Rebinning procedures, also called binning procedures, are often found in digital photography. The spectral density is then reordered as indicated in Fig. 6.5. The reordering enables to choose a reduced center section of the reordered spectral density later on to be compared in the optimization process. This section then contains the relevant entries of the spectral density as the values typically abate with increasing distance from the zero component.

The ability of the spectral density to describe periodicity properties is shown with an example of an artificial, periodic microstructure in 2D, see Fig. 6.6. It shows the microstructure, which is composed of periodically arranged unitcells, one of them is also shown in the

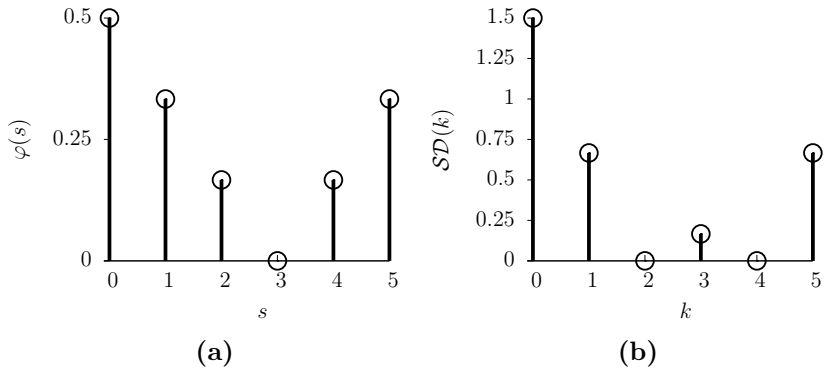

Figure 6.3: (a) Autocorrelation function and (b) spectral density of sample pulse.

same figure. When the spectral densities of the two structures are compared, considering the rebinning and reordering operations described above, the similarity of the spectral densities is obvious. This example emphasizes the ability of the spectral density to detect similarities in the microstructural morphology especially in periodic structures.

6.1.4 Lineal-Path Function

The lineal-path function considers information on the connectedness of a phase and was first proposed as a statistical measure by Lu and Torquato [85]. This function captures the probability of a line segment $\overrightarrow{\boldsymbol{x}_1\boldsymbol{x}_2}$, with the start and end points given by the vectors $\boldsymbol{x}_1$ and $\boldsymbol{x}_2$, be tion is defined

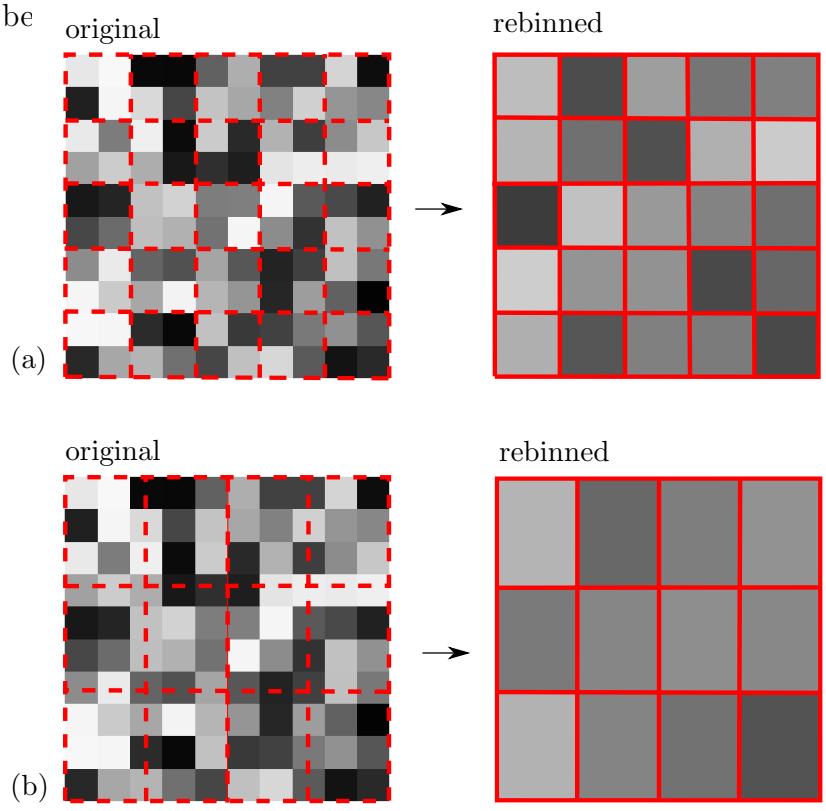

Figure 6.4: Schematic illustration of the rebinning procedure used on a 2D spectral density.

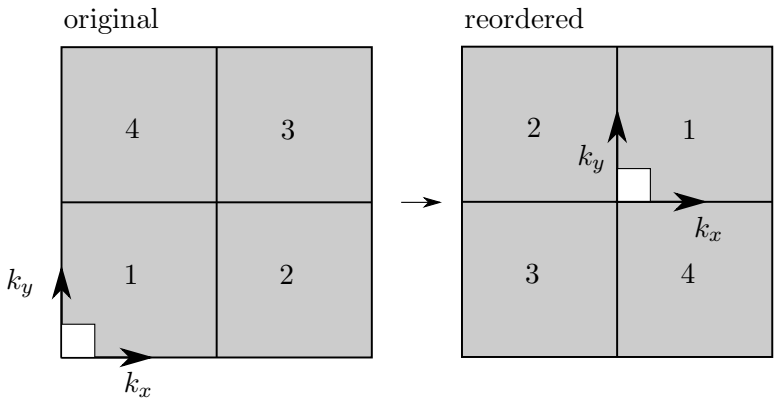

Figure 6.5: Schematic illustration of reordering scheme used on a 2D spectral density. The zero component is marked with a white square.

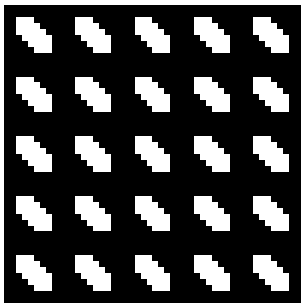

(a) periodic microstructure

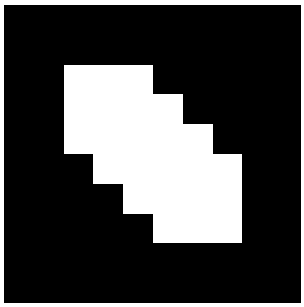

(b) unitcell

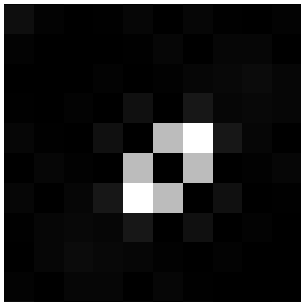

(c) rebinned and reordered spectral density of periodic microstructure

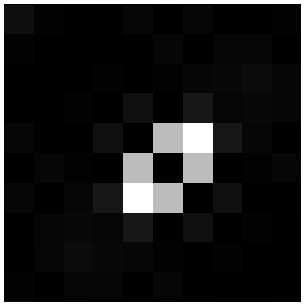

(d) reordered spectral density of unitcell

Figure 6.6: (a) Periodic microstructure and (c) its spectral density. (b) Periodic unitcell and (d) its spectral density.

by

$$\chi_{\mathrm{LP}}^{(P)}(\overrightarrow{\boldsymbol{x}_1\,\boldsymbol{x}_2}) := \begin{cases} 1 \text{ if } \overrightarrow{\boldsymbol{x}_1\boldsymbol{x}_2} \in D^{(P)}\,, \\ 0 \text{ otherwise.} \end{cases} \tag{6.21}$$

The lineal-path function is defined by the ensemble average over a series of samples α

$$\mathcal{P}_{\mathrm{LP}}^{(P)}(\overrightarrow{\boldsymbol{x}_1\,\boldsymbol{x}_2}) := \overline{\chi_{\mathrm{LP}}^{(P)}(\overrightarrow{\boldsymbol{x}_1\,\boldsymbol{x}_2}, \alpha)}, \tag{6.22}$$

whereas for ergodic microstructures the volume average over an infinite domain $\mathcal{B}$ can be considered instead of the ensemble average, hence

$$\mathcal{P}_{\mathrm{LP}}^{(P)}(\overrightarrow{\boldsymbol{x}_1\,\boldsymbol{x}_2}) := \lim_{V(\mathcal{B})\to\infty} \int_{\mathcal{B}} \chi_{\mathrm{LP}}^{(P)}(\boldsymbol{y} + \overrightarrow{\boldsymbol{x}_1\,\boldsymbol{x}_2})\,\mathrm{d}\boldsymbol{y}, \tag{6.23}$$

where $\boldsymbol{y} + \overrightarrow{\boldsymbol{x}_1\,\boldsymbol{x}_2}$ denotes a shift of the line $\overrightarrow{\boldsymbol{x}_1\,\boldsymbol{x}_2}$ by the position vector $\boldsymbol{y}$. Note again that the volume integral over an infinite volume is replaced by the integral over a sufficiently large volume for practical reasons. The lineal-path function has been used as a statistical descriptor in, e.g., Yeong and Torquato [176], where three-dimensional microstructures are reconstructed based on two-dimensional cuts using different combinations of statistical measures. Havelka et al. [53] propose an accelerated method for the computation of lineal path functions in the reconstruction of random microstructures using a parallelization of its computation.

The computation of a complete lineal-path function would require an analysis of all possible line segments with varying length and orientation which is a tremendous computational effort even for reasonably sized microstructures and increases with higher dimensions. Therefore, sampling techniques have been developed which lower the computational expenses. In SEATON AND GLANDT [136], a sampling technique based on Monte-Carlo method was proposed for the computation of spatial correlation functions. In application to the lineal-path function, this can be understood as an evaluation of a large number of line segments which are randomly thrown into a medium. Another approach presented in SMITH AND TORQUATO [144] uses a sampling template for the evaluation of two-point correlation functions. In ZEMAN [179], the sampling template is constructed for lineal-path functions, comprising a fixed number of line segments. The template is a discrete field where entries marked with the value 1 represent the end point of a line starting from the center. All other entries are zero. In order to construct such templates, the digitalization of line elements can be carried out using suitable algorithms, as given in BRESENHAM [24]. The size of the template is defined by $T_x = 2\ N_x - 1$, $T_y = 2\ N_y - 1$ and $T_z = 2\ N_z - 1$ for a three-dimensional discrete medium of the size N_x, N_y and N_z. Thereby, it comprises all possible line length which can be placed in the medium. Since the lineal-path function is invariant with respect to reflections of line segments, it is admissible to neglect the reflection of line segments in one direction, such that the template size reduces to $T_x = 2\ N_x - 1$, $T_y = 2\ N_y - 1$ and $T_z = N_z$. An example of such a template for the three dimensional case is shown in Fig. 6.7. All line segments start start from the center point. For the discrete case, the computation of the lineal-path function can then be carried out evaluating

$$\mathcal{P}_{\mathrm{LP}}^{(P)}(m,k) := \frac{1}{\tilde{N}} \sum_{p=p_m}^{p_M} \sum_{q=q_k}^{q_K} \chi^{(P)}(\overrightarrow{\boldsymbol{x}_1\, \boldsymbol{x}_2}) \tag{6.24}$$

for the two-dimensional case and

$$\mathcal{P}_{\mathrm{LP}}^{(P)}(m,k,l) := \frac{1}{\tilde{N}} \sum_{p=p_m}^{p_M} \sum_{q=q_k}^{q_K} \sum_{r=r_l}^{r_L} \chi^{(P)}(\overrightarrow{\boldsymbol{x}_1\, \boldsymbol{x}_2}) \tag{6.25}$$

for the three-dimensional case. The line segment is defined by the start and end points $\boldsymbol{x}_1 = [p,q]^{\mathrm{T}}$ and $\boldsymbol{x}_2 = [m,k]^{\mathrm{T}}$ in 2D and $\boldsymbol{x}_1 = [p,q,r]^{\mathrm{T}}$ and $\boldsymbol{x}_2 = [m,k,l]^{\mathrm{T}}$ in 3D, respectively. $\tilde{N}$ is the number of admissible discrete points in the range of the summation limits. The summation limits are given by

$$\begin{aligned} p_m &= \max[0,\, -m], & p_M &= \min[N_x,\, (N_x - m)]\,, \\ q_k &= \max[0,\, -k], & q_K &= \min[N_y,\, (N_y - k)]\,, \\ r_l &= \max[0,\, -l], & r_L &= \min[N_z,\, (N_z - l)]\,, \end{aligned} \tag{6.26}$$

thus $\tilde{N} = (p_M - 1 - p_m)(q_K - 1 - q_k)(r_L - 1 - r_l)$ in the three-dimensional case. The computation of the lineal-path function is carried out by placing the template with the center point in a selected point in the admissible range $p \in [p_m, p_M]$ and $q \in [q_k, q_K]$, which has to belong to the considered phase P. All points of the line segment are then checked for their phase affiliation. By summing over all admissible points, i.e. points inside the limit given in Eq. (6.26), and normalizing by $\tilde{N}$, the lineal-path function can be computed. Alternatively, the template can be placed at random points using Monte-Carlo method, where normalization is performed over the number of random placements.

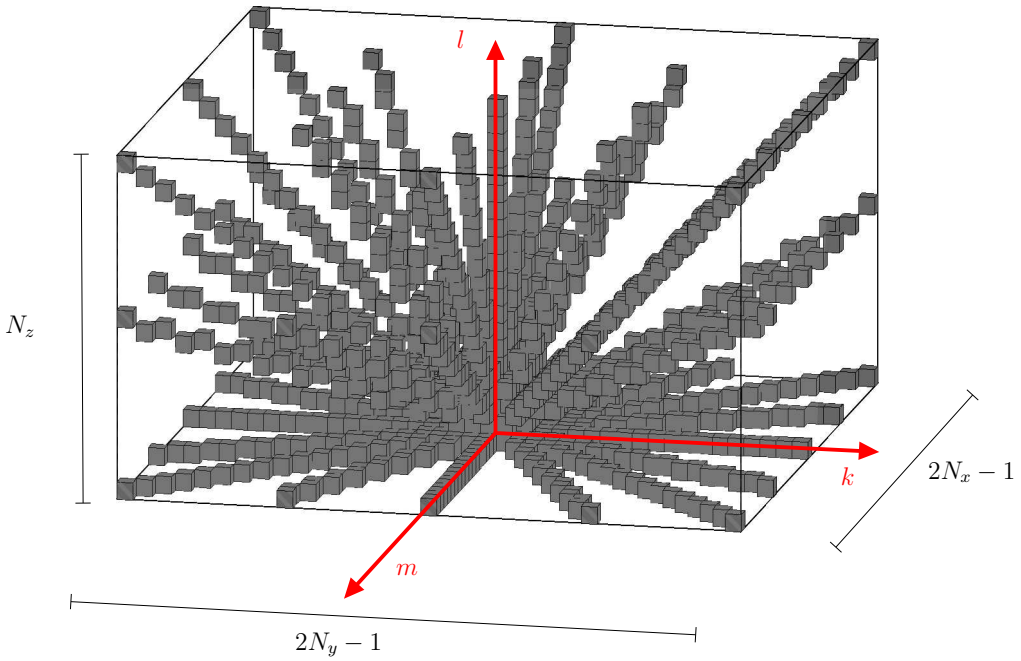

Figure 6.7: Reduced template for the computation of the 3D lineal-path function.

For periodic media, where only a periodic unitcell has to be analyzed, Eq. (6.24) and Eq. (6.25) can be reformulated to

$$\mathcal{P}_{\mathrm{LP}}^{(P)}(m,k) := \frac{1}{\tilde{N}} \sum_{0}^{N_x} \sum_{0}^{N_y} \chi^{(P)}(\overrightarrow{\boldsymbol{x}_1\, \boldsymbol{x}_2}) \tag{6.27}$$

and

$$\mathcal{P}_{\mathrm{LP}}^{(P)}(m,k,l) := \frac{1}{\tilde{N}} \sum_{0}^{N_x} \sum_{0}^{N_y} \sum_{0}^{N_z} \chi^{(P)}(\overrightarrow{\boldsymbol{x}_1\, \boldsymbol{x}_2}), \tag{6.28}$$

respectively, where lines continuing outside of the limits of the data set "reenter" the set of the respective other side due to periodicity. For a reduction of computational effort, the number of analyzed lines in the template can be altered as well. Therein, this reduction implies a reduction of the amount of information which is captured, which should to be done in a reasonable sense of the application.

Fig. 6.8 shows the lineal-path function for the DP steel microstructure analyzed in this work, where only a relevant section with a distinct probability threshold is shown. The lineal-path function enables the identification of an average inclusion size with a definition of relevant threshold p^{thres} of the probability of a line segment being located in the analyzed phase, this will be further discussed in Section 6.2.7.

6.1.5 Minkowski Functionals

In order to quantify and measure the morphology of a material, Minkowski functionals, also known as intrinsic volume, quermassintegrals or curvature integrals) provide a robust morphometric methodology. This class of functionals provides scalar-valued, vectorial and tensorial shape indices applicable for a morphological characterization to many types of structure. Possible ones are porous materials, patterns on nanometer scale in

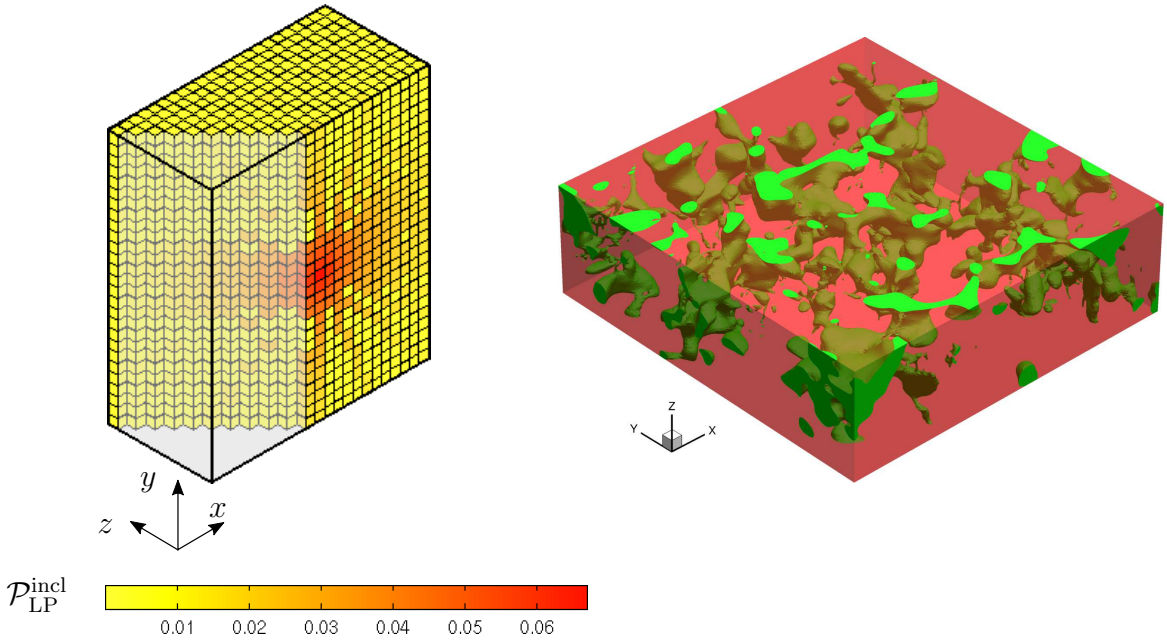

Figure 6.8: Illustration of the relevant section of the lineal-path function of DP steel microstructure, shown in Fig. 4.3.

co-polymers, dewetting dynamics of thin films, Turing patterns and many more, see e.g. Kapfer et al. [68], Schröder-Turk et al. [133; 134; 135]. Scalar Minkowski functionals are well-known measures for the description of a body. They can be understood as essential shape measures based on the theorem due to Hadwiger and Meier [51], which states that any motion-invariant conditionally continuous additive functional of a body can be entirely described by a linear combination of Minkowski functionals. Tensorial Minkowski functionals are capable of describing orientational and geometrical anisotropy properties of the underlying body and are related to well-known engineering measures, such as the moment of inertia.

Minkowski functionals can be defined in two ways: a fundamental definition is given by the approach of integral geometry, see e.g. Hadwiger [50], Hadwiger and Meier [51]. Alternatively, an equivalent description can be derived based on curvature weighted integrals of position and surface normal vectors of a considered body, see, e.g., Schröder-Turk et al. [133] for an overview. A body is here defined as a compact domain Ω with the regular bounding surface $\partial\Omega$. Minkowski functionals in their scalar, vectorial or tensorial nature can describe different aspects of the morphology of a body. The scalar valued Minkowski functionals are given by

$$\mathcal{W}_\nu(\Omega) := \frac{1}{\nu \cdot \binom{d}{\nu}} \int_{\partial\Omega} \mathcal{S}_{\nu-1}(\kappa_1, \ldots, \kappa_{d-1}) \, \mathrm{d}S^{d-1}, \qquad \text{with} \quad \nu = 1, \ldots, d \tag{6.29}$$

and

$$\mathcal{W}_0(\Omega) := \int_\Omega \mathrm{d}S^d \tag{6.30}$$

with the dimension d and the elementary symmetric function $\mathcal{S}_\nu$

$$\begin{aligned}\mathcal{S}_0(\kappa_1, ..., \kappa_{d-1}) &:= 1 \\ \mathcal{S}_1(\kappa_1, ..., \kappa_{d-1}) &:= \sum_{1\le j\le d-1} \kappa_j \\ \mathcal{S}_2(\kappa_1, ..., \kappa_{d-1}) &:= \sum_{1\le j<k\le d-1} \kappa_j\, \kappa_k\end{aligned} \tag{6.31}$$

and the principle curvatures $\kappa_1 \dots \kappa_{d-1}$ as well as the d- and $(d-1)$-dimensional element $\mathrm{d}S^d$ and $\mathrm{d}S^{d-1}$, respectively. Here, $\binom{d}{\nu}$ represents the binomial coefficient. In the two-dimensional space, i.e. $d = 2$ and Ω is given as a planar body, three scalar Minkowski functionals are defined as

$$\mathcal{W}_0(\Omega) = \int_\Omega \mathrm{d}A\,, \qquad \mathcal{W}_1(\Omega) = \frac{1}{2}\int_{\partial\Omega} \mathrm{d}r\,, \qquad \mathcal{W}_2(\Omega) = \frac{1}{2}\int_{\partial\Omega} \kappa\, \mathrm{d}r\,, \tag{6.32}$$

with $\mathrm{d}r$ as a one-dimensional line element on the boundary curve of Ω. These three values are related to the area, boundary length and Euler characteristic of the two-dimensional body Ω. In three-dimensional space, i.e. d=3 and Ω being a three-dimensional body, four scalar Minkowski functionals are defined by

$$\begin{aligned}\mathcal{W}_0(\Omega) &= \int_\Omega \mathrm{d}V\,, & \mathcal{W}_1(\Omega) &= \frac{1}{3}\int_{\partial\Omega} \mathrm{d}A\,, \\ \mathcal{W}_2(\Omega) &= \frac{1}{3}\int_{\partial\Omega} \mathcal{G}_2\, \mathrm{d}A\,, & \mathcal{W}_3(\Omega) &= \frac{1}{3}\int_{\partial\Omega} \mathcal{G}_3\, \mathrm{d}A\,,\end{aligned} \tag{6.33}$$

with $\mathrm{d}A$ being a two-dimensional surface element on the boundary $\partial\Omega$, $\mathcal{G}_2 = \frac{1}{2}(\kappa_1 + \kappa_2)$ is the mean curvature and $\mathcal{G}_3 = \kappa_1\, \kappa_2$ is the Gaussian curvature. These four functionals are connected to the geometric quantities of the volume, surface area, mean curvature and Euler characteristic of Ω.

An important property of the Minkowski functionals is additivity. The Minkowski functional of a union $A \cup B$ of two domains A and B is the sum of the functional of the individual domains subtracted by the intersection $A \cap B$, i.e.

$$\mathcal{W}_\nu(A \cup B) = \mathcal{W}_\nu(A) + \mathcal{W}_\nu(B) - \mathcal{W}_\nu(A \cap B). \tag{6.34}$$

From Eq. (6.32) and Eq. (6.33), it becomes clear that the information captured by the scalar valued Minkowski functionals is limited. Since only curvature-based measures are considered, the measures cannot account for motion invariance, i.e., distinguish between individual bodies with different positions and the same shape. Furthermore, for a cluster of multiple bodies with the same shape but different positions, a clear distinction cannot be made due to the additivity property of Minkowski functionals. In Fig. 6.9 schematic examples of clusters are depicted. In the cluster in Fig. 6.9a and Fig. 6.9b, three domains of different shape are shown with varying position. Due to the additivity and motion invariance of the scalar Minkowski functionals, these two cluster cannot be discriminated. Similarly, in the clusters in Fig. 6.9c and Fig. 6.9d the rotation of one of the domains cannot be detected by scalar Minkowski functionals. However, it is inevitable to distinguish these clusters for a thorough analysis of their morphology.

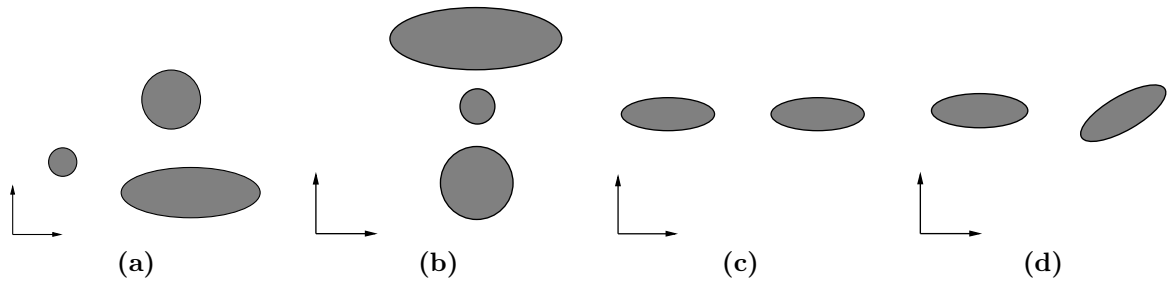

Figure 6.9: Schematic clusters of multiple domains. Scalar Minkowski functionals can neither distinguish between clusters (a) and (b) nor between clusters (c) and (d).

Vectorial and tensorial Minkowski functionals can be understood as a generalization of their scalar valued counterparts and are defined by

$$\boldsymbol{\mathcal{W}}_{\nu}^{a,b} = \frac{1}{\nu \cdot \binom{d}{\nu}} \int_{\partial\Omega} \mathcal{S}_{\nu-1} \mathbf{r}^a \,\overline{\otimes}\, \mathbf{n}^b \,\mathrm{d}S^{d-1} \qquad \text{with } \nu = 1, \ldots, d \tag{6.35}$$

and

$$\boldsymbol{\mathcal{W}}_{0}^{a,0} = \int_{\Omega} \mathbf{r}^a \,\mathrm{d}S \tag{6.36}$$

with the tensor products of the position vector $\mathbf{r}$ and normal vectors $\mathbf{n}$ on the boundary $\partial\Omega$ defined by

$$\mathbf{r}^a \,\overline{\otimes}\, \mathbf{n}^b := \underbrace{\mathbf{r} \,\overline{\otimes}\, \ldots \,\overline{\otimes}\, \mathbf{r}}_{a \text{ times}} \,\overline{\otimes}\, \underbrace{\mathbf{n} \,\overline{\otimes}\, \ldots \,\overline{\otimes}\, \mathbf{n}}_{b \text{ times}}, \tag{6.37}$$

with the symmetric tensor product $(a \;\overline{\otimes}\; b)_{ij} = (a_i b_j + a_j b_i)/2$. Vectorial Minkowski functionals are defined by Eq. (6.35) and Eq. (6.36) with $a = 1$ and $b = 0$ with $\boldsymbol{\mathcal{W}}_0^{1,0} = \int_\Omega \boldsymbol{r} \,\mathrm{d}S^d$ and $\boldsymbol{\mathcal{W}}_\nu^{1,0} = \frac{1}{3} \int_{\partial\Omega} \mathcal{S}_{\nu-1} \boldsymbol{r} \,\mathrm{d}S^{d-1}$ for $\nu \leq d$. Any case of $a = 0$ and $b = 1$ would be proportional to $\int_{\partial\Omega} \boldsymbol{n} \,\mathrm{d}S^{d-1}$, which vanishes for bodies with a closed bounding surface. Subsequently in the two-dimensional case, one obtains three vectorial Minkowski functionals

$$\boldsymbol{\mathcal{W}}_0^{1,0}(\Omega) = \int_\Omega \boldsymbol{r} \,\mathrm{d}A, \qquad \boldsymbol{\mathcal{W}}_1^{1,0}(\Omega) = \frac{1}{2} \int_{\partial\Omega} \boldsymbol{r} \,\mathrm{d}r, \qquad \boldsymbol{\mathcal{W}}_2^{1,0}(\Omega) = \frac{1}{2} \int_{\partial\Omega} \kappa \boldsymbol{r} \,\mathrm{d}r \tag{6.38}$$

and four Minkowski functionals for 3D, i.e.,

$$\begin{aligned} \boldsymbol{\mathcal{W}}_0^{1,0}(\Omega) &= \int_\Omega \boldsymbol{r} \,\mathrm{d}V, & \boldsymbol{\mathcal{W}}_1^{1,0}(\Omega) &= \frac{1}{3} \int_{\partial\Omega} \boldsymbol{r} \,\mathrm{d}A, \\ \boldsymbol{\mathcal{W}}_2^{1,0}(\Omega) &= \frac{1}{3} \int_{\partial\Omega} \mathcal{G}_2 \,\boldsymbol{r} \,\mathrm{d}A, & \mathcal{W}_3^{1,0}(\Omega) &= \frac{1}{3} \int_{\partial\Omega} \mathcal{G}_3 \,\boldsymbol{r} \,\mathrm{d}A\,. \end{aligned} \tag{6.39}$$

For the tensorial Minkowski functionals of second order, i.e. with $a + b = 2$, one obtains the tensors $\boldsymbol{r} \,\overline{\otimes}\, \boldsymbol{r}$, $\boldsymbol{r} \,\overline{\otimes}\, \boldsymbol{n}$ and $\boldsymbol{n} \,\overline{\otimes}\, \boldsymbol{n}$ as the basis for the Minkowski functionals. According to Schröder-Turk et al. [133], the number of relevant Minkowski functionals can be reduced due to linear dependencies. One obtains four tensors in 2D and six tensors in 3D and additional Minkowski tensors are given by the multiplication of scalar Minkowski functionals with the unit tensor $\boldsymbol{I}$ in the respective dimension. In 2D the linear independent tensors are given by

$$\begin{aligned} \boldsymbol{\mathcal{W}}_0^{2,0}(\Omega) &= \int_\Omega \boldsymbol{r} \,\overline{\otimes}\, \boldsymbol{r} \,\mathrm{d}A, & \boldsymbol{\mathcal{W}}_1^{2,0}(\Omega) &= \frac{1}{2} \int_{\partial\Omega} \boldsymbol{r} \,\overline{\otimes}\, \boldsymbol{r} \,\mathrm{d}r, \\ \boldsymbol{\mathcal{W}}_1^{0,2}(\Omega) &= \frac{1}{2} \int_{\partial\Omega} \boldsymbol{n} \,\overline{\otimes}\, \boldsymbol{n} \,\mathrm{d}r, & \boldsymbol{\mathcal{W}}_2^{2,0}(\Omega) &= \frac{1}{2} \int_{\Omega} \kappa \,\boldsymbol{r} \,\overline{\otimes}\, \boldsymbol{r} \,\mathrm{d}r, \end{aligned} \tag{6.40}$$

whereas in the 3D case the linear independent Minkowski tensors are defined by

$$\begin{aligned}
\boldsymbol{\mathcal{W}}_0^{2,0}(\Omega) &= \int_\Omega \boldsymbol{r} \,\overline{\otimes}\, \boldsymbol{r}\,\mathrm{d}V, & \boldsymbol{\mathcal{W}}_1^{2,0}(\Omega) &= \frac{1}{3}\int_{\partial\Omega} \boldsymbol{r} \,\overline{\otimes}\, \boldsymbol{r}\,\mathrm{d}A,\\
\boldsymbol{\mathcal{W}}_1^{0,2}(\Omega) &= \frac{1}{3}\int_{\partial\Omega} \boldsymbol{n} \,\overline{\otimes}\, \boldsymbol{n}\,\mathrm{d}A, & \boldsymbol{\mathcal{W}}_2^{2,0}(\Omega) &= \frac{1}{3}\int_{\Omega} \mathcal{G}_2\,\boldsymbol{r} \,\overline{\otimes}\, \boldsymbol{r}\,\mathrm{d}A,\\
\boldsymbol{\mathcal{W}}_2^{0,2}(\Omega) &= \frac{1}{3}\int_{\partial\Omega} \mathcal{G}_2\,\boldsymbol{n} \,\overline{\otimes}\, \boldsymbol{n}\,\mathrm{d}A, & \boldsymbol{\mathcal{W}}_3^{2,0}(\Omega) &= \frac{1}{3}\int_{\Omega} \mathcal{G}_3\,\boldsymbol{r} \,\overline{\otimes}\, \boldsymbol{r}\,\mathrm{d}A.
\end{aligned} \tag{6.41}$$

Higher-order Minkowski tensors are well defined, see e.g., Sporer et al. [145], but are not considered further in this context.

A geometrical interpretation of the non-scalar Minkowski functionals is described in e.g. Kapfer [67], see also Schröder-Turk et al. [133; 135]. The center of mass of an underlying body Ω is related to the vectorial Minkowski functional $\boldsymbol{\mathcal{W}}_0^{1,0}$, whereas the tensorial Minkowski functionals $\boldsymbol{\mathcal{W}}_\nu^{2,0}$ can be interpreted as tensors of inertia, with $\boldsymbol{\mathcal{W}}_0^{2,0}$ characterizing the tensor of inertia $\boldsymbol{\mathcal{I}}$ of the solid body Ω itself as $\boldsymbol{\mathcal{I}}(\Omega) = -\boldsymbol{\mathcal{W}}_0^{2,0} + \mathrm{tr}(\boldsymbol{\mathcal{W}}_0^{2,0})\boldsymbol{I}$. The moment tensor of inertia of a hollow body described by the surface $\partial\Omega$ with homogeneous mass distribution on this surface is similarly defined by $\boldsymbol{\mathcal{W}}_1^{2,0}$ and the moment tensor of inertia of a body with the mass concentrated only at the vertices is described by $\boldsymbol{\mathcal{W}}_2^{2,0}$.

The Minkowski tensors of second order can be distinguished into tensors which are sensitive or insensitive to a change of origin of the position vector $\boldsymbol{r}$. Naturally, Minkowski tensors considering the tensor product of normal vectors, i.e. $\boldsymbol{n}\otimes\boldsymbol{n}$, do not change when a different origin is considered, on the other hand when considering the position vector $\boldsymbol{r}$, a dependence on its origin and thus a change with varying origin can be seen. This is a well-known property of the tensor of inertia. This property is also referred to as motion covariance. While the origin can be defined, e.g. based on the center of mass, this specification can complicate the analysis for non-convex structures with multiple bodies and elaborate connectivities, cf. Kapfer [67]. Even when choosing the origin as a fixed arbitrary point in space, a dependence on the size and aspect ratio of the observed cutout can be seen. Considering Minkowski tensors which do not depend on an origin can circumvent many obstacles in the analysis of a complex morphology. In Schröder-Turk et al. [133], the application of such motion invariant Minkowski tensors, which are $\boldsymbol{\mathcal{W}}_1^{0,2}$ (for 2D and 3D) and $\boldsymbol{\mathcal{W}}_2^{0,2}$ (for 3D), is proposed for an analysis of Turing patterns, microscopy data of co-polymer thin films, granular matters and liquid foams. These shape indices contain information on the orientational distribution of surface patches and curvatures. Based on this proposition, these Minkowski tensors will also be considered in the following.

The additivity property of Minkowski tensors is based on the expression for their scalar counterparts, see Eq. (6.34), leading to

$$\boldsymbol{\mathcal{W}}_\nu^{a,b}(A \cup B) = \boldsymbol{\mathcal{W}}_\nu^{a,b}(A) + \boldsymbol{\mathcal{W}}_\nu^{a,b}(B) - \boldsymbol{\mathcal{W}}_\nu^{a,b}(A \cap B). \tag{6.42}$$

The generalization of Hadwiger's theorem to second-order Minkowski tensors by Alesker, Alesker [1], states that any conditionally continuous, additive, motion covariant functional of a body Ω can be expressed by a linear combination of Minkowski functionals, which enforces the significance of Minkowski functionals also in the higher

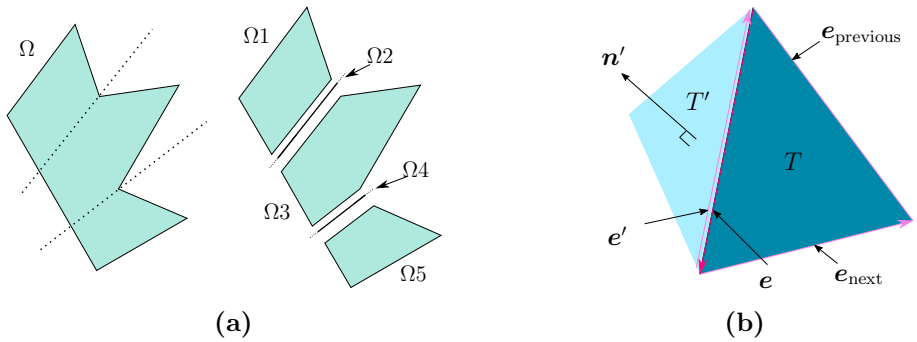

Figure 6.10: (a) Subdivision of a non-convex body into convex sub-bodies. $\Omega = \Omega_1 \cup \Omega_2 \cup \Omega_3 \cup \Omega_4 \cup \Omega_5$. (b) Definition of geometric properties of a triangulated surface $\partial\Omega$. Adapted from Schröder-Turk et al. [135].

dimensional case. The definition of Minkowski functionals is restricted to convex bodies Ω, however nonconvex bodies can be considered due to the additivity theorem, see also Schröder-Turk et al. [133], since every nonconvex body can be subdivided into then convex parts, as illustrated in Fig. 6.10a.

Computation of Tensorial Minkowski Functionals

For the evaluation of Minkowski functionals explicitly for planar or spatial structures given in the form of pixel or voxel data, expressions are given in e.g. Kapfer [67] and Schröder-Turk et al. [133]. The algorithms evaluate Minkowski functionals based on a polygonized representation of the body Ω, which is given as a closed polygonal boundary for planar geometries and a triangulated bounding surface for spatial geometries, respectively. In the following, the details of the procedure are described for 3D, thus triangulated surfaces are the foundation for the computation of Minkowski functionals. To handle localizations in curvature, i.e. at sharp corners occurring at vertices in the boundary, a parallel body construction is used, see Schröder-Turk et al. [133] for details.

Every voxel in the binary data set is assigned a value of 1 or 0, depending on whether the voxel belongs to the body Ω or not. In order to obtain a triangulated surface from the binary voxel data set, simple algorithms such as the marching cube algorithm or more complex meshing tools can be used. Here, a Marching cube algorithms implemented in Matlab, cf. Helm [54], is utilized. This algorithms runs over the data set and considers a region of $2 \times 2 \times 2$ voxel. Each voxel is considered as a vertex in the center of the voxel, resulting in a cube with eight corner vertices. Each vertex is assigned the specific value of the according voxel, 1 or 0. Depending on the arrangement of vertices with different values 0 and 1, a specific case of boundary inside the considered region is recorded. There exist $2^8 = 256$ different possibilities of composition of values in the corner nodes, due to symmetry only 15 cases have to be considered. Finally, a list of vertices and triangles results as an outcome from the Marching cube algorithm. This triangulation is used for the computation of the Minkowski functionals. A detailed description of the construction of parallel bodies and the expressions for Minkowski functionals based on triangulations obtained by e.g. marching cube algorithms can be found in Schröder-Turk et al. [135].

For the here considered tensorial Minkowski tensor $\boldsymbol{\mathcal{W}}_1^{0,2}$ the expression yield s

$$\boldsymbol{\mathcal{W}}_1^{0,2} = \frac{1}{3} \sum_{T \in F_2} |T| (\boldsymbol{n}_{\mathrm{T}}^2)_{ij} \tag{6.43}$$

with the nomenclature of the triangulation as described in Fig. 6.10b. Therein, the facets of the triangulation F is F_2, T is the specific triangle from the set. $\boldsymbol{n}_{\mathrm{T}}$ is the normal vector on T pointing out of the body Ω and $(\boldsymbol{n}_{\mathrm{T}}^2)_{ij} = \boldsymbol{n}_{\mathrm{T}i} \otimes \boldsymbol{n}_{\mathrm{T}j}$ the dyadic product of the normal vector.

Anisotropy Measure Based on Minkowski Functional $\boldsymbol{\mathcal{W}}_1^{0,2}$

In view of an application as microstructural descriptors, the aim is to deduce the relevant information from the Minkowski tensors. Therefore, it can be conveniently reduced to scalar indices resembling the degree of anisotropy of a body Ω using the ratio of minimal and maximal eigenvalue of the Minkowski tensor, following Kapfer et al. [68], as

$$\beta_\nu^{a,b} := \frac{|\mu_{min}|}{|\mu_{max}|} \in [0,1]\,, \tag{6.44}$$

for a considered Minkowski tensor $\boldsymbol{\mathcal{W}}_\nu^{a,b}$. Depending on the Minkowski tensor analyzed, the anisotropy regarding its geometrical resemblance can be described. In Schröder-Turk et al. [133], examples of anisotropy analysis of planar and spatial structures are given. Two different methods are proposed, considering a global Minkowski functional for a data set by the use of the additivity theorem and a local analysis, where a moving window of a certain size analyzes a subregion of the data set. Using the first method, 2D boolean models of overlapping ellipses, which have different preferred orientations (ranging from the isotropic case with no preferred orientation to aligned ellipsoids with one overall preferred orientation), are analyzed regarding the orientation distribution using the anisotropy measure $\beta_1^{0,2}$. Constant values are found for increasing numbers of particles with the isotropic case (no orientation preference) resulting in $\beta_1^{0,2} = 1$ and the perfectly aligned ellipsoids giving approximately $\beta_1^{0,2} = 0.44$, which is the expected value for the analysis of a pixelized ellipse using a marching square algorithm. An example of a local Minkowski analysis is given in Schröder-Turk et al. [133; 134], where a 2D Turing pattern, which naturally lacks of long-range order, is investigated. Here, the regions of interest are regions with non-lamellar concentration of a chemical. Focus is laid on the Minkowski tensor $\mathcal{W}_1^{0,2}$, which clearly distinguishes the local non-lamellar region in the pattern,corresponding to an isotropic value, i.e., $\beta_1^{0,2} = 1$. In this local Minkowski analysis, the window method is used instead of applying the additivity theorem in order to capture region-specific properties. Therefore, a window of observation with a smaller size than the data set is moved across the complete region pixel by pixel, allowing an overlap of the individual window regions. The Minkowski tensor, or respective measures deduced therefrom, are assigned to the specific region and capture the local phenomena. Details on this method can be found in Schröder-Turk et al. [133].

In this work, another method of analysis is proposed, which can be applied for structures with distinct inclusions. Therefore, each inclusion is analyzed separately and a Minkowski tensor is computed. In the case of a structure with multiple inclusions, the binary voxel data set has to be processed with a labeling technique, which indicates the individual inclusions as separate bodies. Then, the triangulation using a marching cube

algorithm and the computation of the Minkowski tensors is carried out for each inclusion individually. The computation of the measures based on the individual inclusions is explained in the following.

Orientation Measure Based on Minkowski Functional $\mathcal{W}_1^{0,2}$

Based on the eigenvalue analysis of a Minkowski tensor, the eigenvectors possess further relevant information. In the case of $\mathcal{W}_1^{0,2}$, the global orientation of the analyzed body Ω can be deduced from the direction of eigenvectors, which correspond to the direction of main axes in the case of ellipsoidal bodies. Ellipsoids can be defined as a special case of generalized ellipsoids by

$$\sum_{i=1}^{d} \left(\frac{|\boldsymbol{v}_i \cdot (\boldsymbol{x} - \boldsymbol{x}_c)|}{r_i} \right)^{p_i} = 1 \tag{6.45}$$

with the d denoting the dimension, $\boldsymbol{x}_c$ is a vector defining the center point of the ellipsoid, the vector $\boldsymbol{v}_i$ described the principal axis of the ellipsoid and r_i is the radius on axis i. The exponent determines the shape of the generalized ellipsoid, for $p_i = 2$, classical convex ellipsoids are obtained. Every point in d-dimensional space defined by $\boldsymbol{x}$ which satisfies Eq. (6.45) describes a point on the surface of the ellipsoid.

For a detailed view on the properties of eigenvectors for specific types of ellipsoidal bodies, a separation and individual consideration of three cases is reasonable, where the three cases of ellipsoids are: ellipsoids without axial rotational symmetry, i.e., three different radii, treated under case **(a)**, ellipsoids possessing rotational symmetry on one axis, thus two radii are equal, cf. case **(b)** and spheres, which are a special case of ellipsoids with three equal radii, handled in case **(c)**. For each case, the resulting eigenvectors exhibit specific properties:

(a) In the case of an ellipsoidal body with no rotational symmetry axis, the eigenvalue analysis of the Minkowski tensor $\mathcal{W}_1^{0,2}$ yield three distinct eigenvalues $\mu_1 \neq \mu_2 \neq \mu_3$, where μ_1, μ_2 and μ_3 are given in descending order, and one eigenvector is associated to each distinct eigenvalue. These eigenvectors $\boldsymbol{v}_1$, $\boldsymbol{v}_2$ and $\boldsymbol{v}_3$, with $\boldsymbol{v}_i$ associated to μ_i for $i = 1, 2, 3$, correspond to the three axis of the ellipsoid, which define the main directions of orientation. The case is pictured in Fig. 6.11a.

(b) Ellipsoids with rotational symmetry on one axis result in a Minkowski tensor $\mathcal{W}_1^{0,2}$ with one double and one single eigenvalue, i.e. $\mu_1 = \mu_2 \neq \mu_3$ or $\mu_1 \neq \mu_2 = \mu_3$, and associated eigenvectors. Here, the eigenvector associated to single eigenvalue coincides with the direction of symmetry axis of the ellipsoid. Therefore, this eigenvector possesses information on the preferred orientation of the ellipsoidal body. The eigenvectors associated to the double eigenvalue span a plane which is perpendicular to the axis of symmetry and span the plane of all possible eigenvectors associated to the double eigenvalue, since these cannot be uniquely defined. Fig. 6.11b illustrates this case.

(c) For spheres as a special case of ellipsoids, an isotropic distribution of surfaces orientation is present (here $\beta_1^{0,2} = 1$) with all three eigenvalue being equal, i.e. $\mu_1 = \mu_2 = \mu_3$,

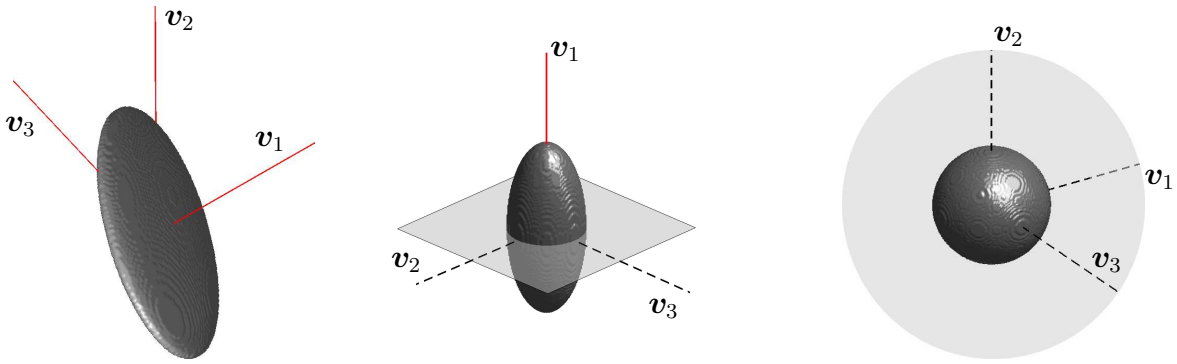

(a) Ellipsoid without rotational symmetry: three distinct eigenvalues $\mu_1 \neq \mu_2 \neq \mu_3$ with associated eigenvectors $\boldsymbol{v}_1$, $\boldsymbol{v}_2$ and $\boldsymbol{v}_3$.

(b) Ellipsoid with rotational symmetry: one distinct eigenvalue and a double eigenvalue $\mu_1 \neq \mu_2 = \mu_3$ with a distinct eigenvector $\boldsymbol{v}_1$ and a plane of possible eigenvectors $\boldsymbol{v}_2$ and $\boldsymbol{v}_3$.

(c) Sphere: triple eigenvalue $\mu_1 = \mu_2 = \mu_3$ and three ambiguous vectors $\boldsymbol{v}_1$, $\boldsymbol{v}_2$ and $\boldsymbol{v}_3$ spanning the associated eigenspace.

Figure 6.11: Illustration of possible cases for an ellipsoid and associated eigenvectors of $\mathcal{W}_1^{0,2}$. Dashed lines denote directions of eigenvectors associated to multiple eigenvalues, which span the possible space of all eigenvectors associated to these eigenvalues (gray plane or space). Red solid lines denote directions of eigenvectors associated to distinct eigenvalues, describing distinct orientation directions of the ellipsoidal bodies. Taken from Scheunemann et al. [128].

thus a triple eigenvalue exists. This leads to three ambiguous eigenvectors. This observation is in agreement with the arbitrariness of rotational symmetry axis of a sphere, for which an infinite number of symmetry axis exist due to spherical symmetry. For a sphere, no distinct axis of symmetry can be discovered and subsequently no distinct orientation of the spherical body is found. The space of possible eigenvectors is generated by the three detected eigenvectors, meaning any vector starting from the center of the sphere is a permissible eigenvector. This case is illustrated in Fig. 6.11c.

From the above described cases, one can observe a correspondence between the direction of eigenvectors of Minkowski tensor $\boldsymbol{\mathcal{W}}_1^{0,2}$ of an ellipsoid and the orientation of its principal axes. Therefore, eigenvectors of Minkowski tensors carry important orientational information related to the morphology of the underlying body. With a description of the eigenvectors in spherical coordinates, the angles θ and φ can be used to capture the direction of orientation of a body. The definition of θ and φ is illustrated in Fig. 6.12. A direction and its inversion are considered together, thus the range of both angles is then given by $\theta, \varphi \in [-\pi/2, \pi/2]$.

Microstructural Descriptors Based on Probability Density Functions

In view of using Minkowski functionals as descriptors of real microstructures, different approaches can be followed, as described in the previous paragraphs. For the present case of a two-phase material consisting of an inclusion phase embedded in a matrix phase, the afore-mentioned measures based on Minkowski tensor $\boldsymbol{\mathcal{W}}_1^{0,2}$ will be used. With the definition of the Minkowski tensor for single bodies, the above described measures for anisotropy and orientation are computed for each inclusion in a microstructure separately.

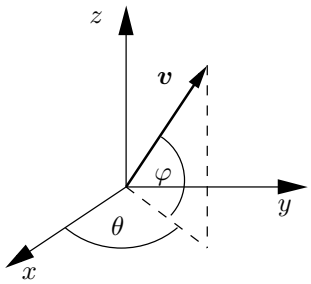

Figure 6.12: Definition of orientation of eigenvectors using spherical coordinates (θ, φ).

Therefore, a microstructure consisting of multiple inclusions given by a voxel data set has to be modified in order to distinguish the individual inclusions. This is done using a labeling technique, which assigns a label to every inclusion Ω_m with $m = 1...n_{\text{incl}}$, n_{incl} being the total number of inclusions, and thus allows a distinct analysis. Starting the analysis, the anisotropy measure $\beta_1^{0,2}$ and the orientation defined by θ and φ are determined based on the computation of the Minkowski tensor $\boldsymbol{\mathcal{W}}_1^{0,2}$ for every inclusion. Additional information regarding the analyzed inclusion, i.e. the volume ratio relating the volume of the individual inclusion to the total volume of all inclusions, is recorded and will be used lateron for weighting purposes, see Section 6.2.2. Next, a probability density function is computed to take into account the distribution of the respective measure in the complete microstructure. This probability density function $\mathcal{P}_{\text{MA}}$ for the scalar anisotropy measure $\beta_m = \beta_1^{0,2}$ for an inclusion Ω_m is defined by

$$\mathcal{P}_{\text{MA}}(i_\beta) := \frac{1}{d_\beta \, n_{\text{incl}}} \sum_{m=1}^{n_{\text{incl}}} \xi(i_\beta) \quad \text{with} \quad \xi := \begin{cases} 1 \text{ if } \beta_m \in c_{i_\beta} \\ 0 \text{ else,} \end{cases} \tag{6.46}$$

with a number of n_β categories c_{i_β}, $i_\beta = 1...n_\beta$ with equal category size $d_\beta = 1/n_\beta$, since the possible range is given by $\beta \in [0, 1]$. The probability density function is computed based on a histogram of the distribution of β over the microstructure which is normalized to fulfill $\int_0^1 (\mathcal{P}_{\text{MA}}) = 1$ over the admissible range of β.

Similarly, a probability density function is computed for the orientation measure introduced previously. Here, the variable is two-dimensional (angles θ and φ), thus a number of $n_\theta n_\varphi$ categories c_{i_θ, i_φ} with $i_\theta = 1...n_\theta$ and $i_\varphi = 1...n_\varphi$ is used together with an equal category size $d_\theta = \pi/n_\theta$ and $d_\varphi = \pi/n_\varphi$, which results from the admissible range of the angles, i.e. $\theta, \varphi \in [-\pi/2, \pi/2]$. The probability density function for the orientation measure based on $\boldsymbol{\mathcal{W}}_1^{0,2}$ then reads

$$\mathcal{P}_{\text{MO},k}(i_\theta, i_\varphi) := \frac{1}{d_\theta \, d_\varphi \, n_{\text{incl}}} \sum_{m=1}^{n_{\text{incl}}} \xi(i_\theta, i_\varphi) \quad \text{with} \quad \xi := \begin{cases} 1 \text{ if } \Omega_m \in \mathcal{B}_k \cup \left\{ \theta_m \in c_{i_\theta}, \varphi_m \in c_{i_\varphi} \right\} \\ 0 \text{ else.} \end{cases} \tag{6.47}$$

Here, equivalently to the distinguishable cases **(a)**, **(b)** and **(c)** described in the previous paragraph, Minkowski tensors matching the different cases are captured separately in probability density functions. Each individual inclusion Ω_m is assigned to a set $\mathcal{B}_k$, whereas

these sets are described by

$$\begin{aligned} \mathcal{B}_{k=1,2,3} &:= \{\Omega_m \,|\, \mu_1 > \mu_2 > \mu_3\} \quad \rightarrow \text{ case}(\mathbf{a}), \\ \mathcal{B}_{k=4} &:= \{\Omega_m \,|\, \mu_1 = \mu_2 > \mu_3\} \quad \rightarrow \text{ case}(\mathbf{b}), \\ \mathcal{B}_{k=5} &:= \{\Omega_m \,|\, \mu_1 > \mu_2 = \mu_3\} \quad \rightarrow \text{ case}(\mathbf{b}), \\ \mathcal{B}_{k=6} &:= \{\Omega_m \,|\, \mu_1 = \mu_2 = \mu_3\} \quad \rightarrow \text{ case}(\mathbf{c}). \end{aligned} \tag{6.48}$$

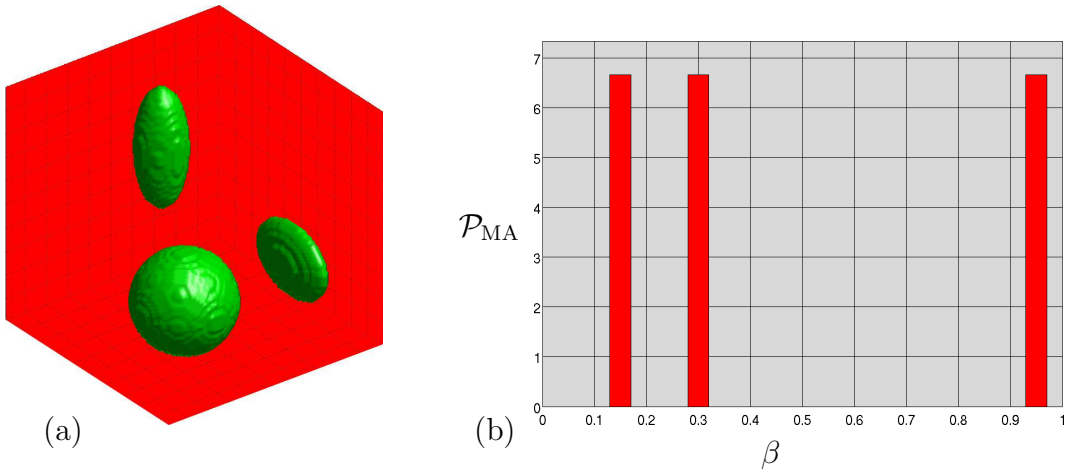

Figure 6.13: (a) Simple microstructure with three ellipsoidal inclusions and (b) probability density function $\mathcal{P}_{MA}$.

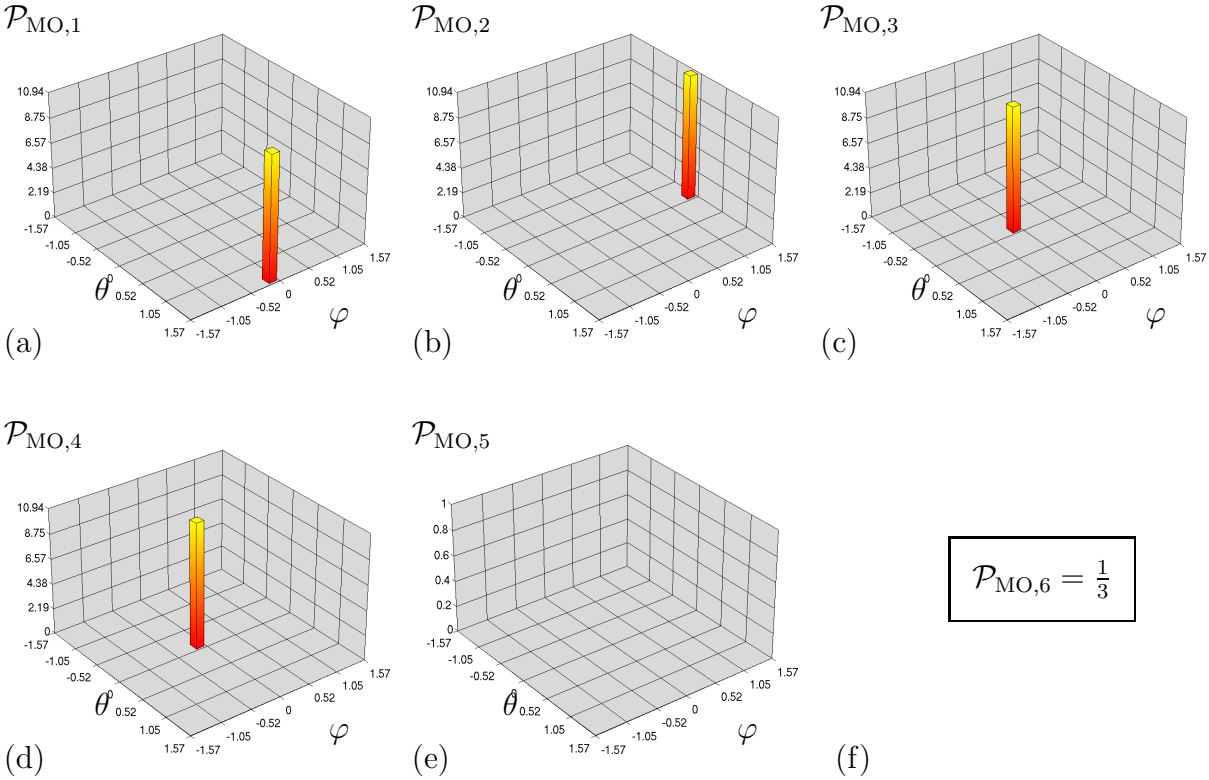

Figure 6.14: Probability density functions for orientation measure computed for microstructure with three inclusion. (a) $\mathcal{P}_{\mathrm{MO},1}$, (b) $\mathcal{P}_{\mathrm{MO},2}$ (c) $\mathcal{P}_{\mathrm{MO},3}$, (d) $\mathcal{P}_{\mathrm{MO},4}$, (e) $\mathcal{P}_{\mathrm{MO},4}$ and (f) $\mathcal{P}_{\mathrm{MO},6}$

The cases here represent the different combinations of eigenvalues. For case **(a)**, the three distinct eigenvectors related to three distinct eigenvalues are captured in three individual probability density functions with $k = i$ related to the eigenvalue and eigenvector μ_i and $\boldsymbol{v}_i$ for $i = 1, 2, 3$. The orientation of this type of inclusion is thus captured in three probability density functions $\mathcal{P}_{\mathrm{MO},1}$, $\mathcal{P}_{\mathrm{MO},2}$ and $\mathcal{P}_{\mathrm{MO},3}$, each related to one distinct direction (or orientation). For $k = 4$ and $k = 5$, the case of inclusions with only one distinct direction of orientation is covered, cf. case **(b)**. Here, the direction of the eigenvector related to the distinct eigenvalue is captured, i.e. μ_3 for $k = 4$ and μ_1 for $k = 5$ resulting in the two probability density functions $\mathcal{P}_{\mathrm{MO},4}$ and $\mathcal{P}_{\mathrm{MO},5}$. For inclusions with an isotropic distribution of surface orientations, with $\beta_1^{0,2} = 1$ thus no distinct orientational direction, the probability density function $\mathcal{P}_{\mathrm{MO},6}$ is formulated with only one category c_{i_θ, i_φ} with $n_\theta = n_\varphi = 1$ and $d_\theta = d_\varphi = \pi$. With this formulation, the mere existence of an inclusion of this type is captured rather than an orientation. Note that in the implementation of the algorithm, the equality of two eigenvalues is checked, allowing for a small deviation. Then two eigenvalues, which only slightly differ are still considered as equal. Here, a 3% deviation is used.

An example is given to illustrate the described definitions of probability density functions. Fig 6.13a shows an artificial microstructure with three inclusions, with one ellipsoid belonging to each of the three afore mentioned cases. According to the described procedure, probability density functions for the anisotropy and orientation measure are generated. The probability density function for the anisotropy measure β can be seen in Fig. 6.13b. Each entry in the function corresponds to one ellipsoid, the entry $\beta = 1$ clearly being associated to the spherical inclusion. For the probability density functions of the orientation, six different functions are obtained, where $\mathcal{P}_{\mathrm{MO},5}$ is empty since there are no such configurations found. These are depicted in Fig. 6.14. In Fig. 6.15 and Fig. 6.16, the analysis of the presented microstructural descriptors is shown for the DP steel microstructure treated in this work. Note that only the probability density functions of orientation distribution for the cases $k = 1, 2, 3$ are shown, since the remaining cases are of lesser relevance.

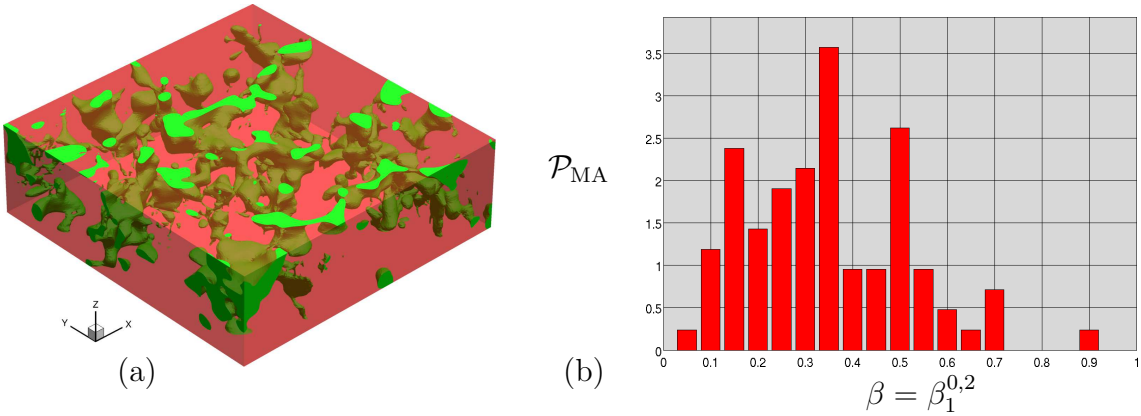

Figure 6.15: (a) Realistic DP-steel microstructure (green indicating the martensitic inclusion phase and red indicating the ferritic inclusion phase), cf. Fig. 4.3b and (b) probability density function $\mathcal{P}_{MA}$ versus $\beta = \beta_1^{0,2}$. Taken from Scheunemann et al. [128].

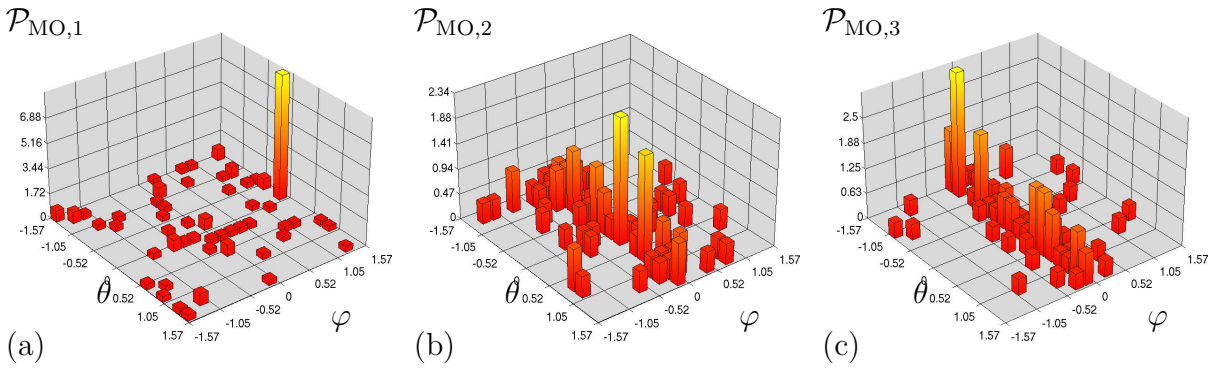

Figure 6.16: Probability density distributions for the orientation measure computed for real DP steel microstructure: (a) $\mathcal{P}_{\mathrm{MO},1}$, (b) $\mathcal{P}_{\mathrm{MO},2}$ (c) $\mathcal{P}_{\mathrm{MO},3}$. Taken from Scheunemann et al. [128].

6.2 Construction of Statistically Similar RVEs

The construction of SSRVEs is based on the minimization of a least-square functional which considers the differences of statistical measures computed for the real microstructure and the SSRVE. It is based on the method proposed in Povirk [111]. Under consideration of a two-phase material, a description of either phase is sufficient, since the properties of the second phase can be constructed therefrom. Here, the inclusion phase of the SSRVE is parametrized by a vector $\boldsymbol{\gamma}$. It is aimed for an analysis of different types of inclusion parameterization i, which can be, e.g., varying numbers or shapes of inclusions, which are then considered by $\boldsymbol{\gamma}_i$. For a comparison, sets of different statistical descriptors are given by G, and the set ω contains the individual weighting factors ω_L, which level the individual measures in the objective function. The least-square functional reads

$$\mathcal{E}_{G,\omega}(\boldsymbol{\gamma}_i) := \sum_{L \in G} \omega_L \mathcal{L}_L(\boldsymbol{\gamma}_i) \quad \text{with} \quad \mathcal{L}_L(\boldsymbol{\gamma}_i) := \left(\mathcal{P}_L^{\text{real}} - \mathcal{P}_L^{\text{SSRVE}}(\boldsymbol{\gamma}_i)\right)^2, \tag{6.49}$$

with the respective least-square functional for an individual statistical measure $\mathcal{P}_L$ given by $\mathcal{L}_L(\boldsymbol{\gamma}_i)$. Herein, the statistical measure is evaluated for the real microstructure by $\mathcal{P}_L^{\text{real}}$ and for the SSRVE by $\mathcal{P}_L^{\text{SSRVE}}(\boldsymbol{\gamma}_i)$. The individual least-square functionals $\mathcal{L}_L$ are here combined in a weighted sum approach, forming one functional out of multiple least-square functionals. An essential question in the solution of the minimization problem in Eq. (6.49) is the definition of an inclusion parameterization for the SSRVE. While a parameterization allowing arbitrary inclusion morphologies would lead to a closer fitting of the statistical properties of the real microstructure and the SSRVE, this approach would result in a large number of parameters to describe the morphology and thus the optimization problem could not be solved in a reasonable amount of time. Furthermore, the resulting arbitrary morphology could lead to complex discretizations, lowering the attempted benefits of the SSRVE regarding computational effort in FE^2 calculations. Thus, an analysis of a suitable parameterization is needed. In view of the statistical measures considered, a large number of descriptors capturing different properties of the microstructure would be beneficial for a complete description of the microstructure. However, large numbers of statistical measures, which have to be evaluated in each optimization step, would also lead to higher solution times for the optimization problem. Therefore, the choice of a set of statistical measures is an essential one and has to consider the information captured by the specific measure as well as the computation time. Since the weighting factors influence the impact of each statistical measure in the optimization process, their choice should be made reasonably. To this end, the choice of the above mentioned variables influence the resulting SSRVE and their definition is cumbersome and interconnected. In Balzani et al. [11], a staggered optimization scheme is proposed for the minimization of Eq. (6.49). Therein, the optimal morphology $\tilde{\boldsymbol{\gamma}}$ of an SSRVE is determined by solving an inner and an outer optimization problem sequentially. In the inner optimization problem, an optimal inclusion morphology $\tilde{\boldsymbol{\gamma}}_i$ is determined for a fixed type of parameterization, a fixed set of statistical measures and a fixed set of weighting factors. In order to evaluate whether the chosen parameterization, statistical measures and weighting factors are reasonable, the outer optimization problem considers a suitable mechanical objective function $\tilde{r}_{\varnothing}$, comparing the mechanical response of the real microstructure and the SSRVE candidate given by $\tilde{\boldsymbol{\gamma}}_i$

in a least-square manner. The staggered optimization scheme then reads

$$\tilde{\boldsymbol{\gamma}} = \arg \underbrace{\left\{ \min_{i,G,\omega} \left[\tilde{r}_{\varnothing} \left(\tilde{\boldsymbol{\gamma}}_i = \arg \underbrace{\left[\min_{\boldsymbol{\gamma}_i} \left[\mathcal{E}_{G,\omega}(\boldsymbol{\gamma}_i) \right] \right]}_{\text{inner problem}} \right) \right] \right\}}_{\text{outer problem}} . \tag{6.50}$$

Resulting from this optimization problem, an optimal SSRVE defined by $\tilde{\boldsymbol{\gamma}}$, can be determined based on an optimal set of statistical measures together with suitable weighting factors and a suitable parameterization type. This staggered scheme is beneficial as long as the evaluation of $\mathcal{E}_{G,\omega}(\boldsymbol{\gamma}_i)$ can be computed more efficiently than the evaluation of $\tilde{r}_{\varnothing}$, since the number of evaluations of the latter is lower. Thus, the efficiency of the inner optimization problem, especially with regard to the choice of statistical measures, is important. In the following sections, the different influences and aspects for the construction of SSRVEs are discussed.

6.2.1 Parameterization of Inclusion Morphology

In order to describe the inclusion morphology of the SSRVE, a parameterization using generalized ellipsoids is used, where the outer surface of an ellipsoid is defined by Eq. (6.45). The global orientation of the semiaxis $\boldsymbol{v}_i$, which are restricted to be cartesian base systems, can be given via Euler angles which define the rotation of a given triad of base vectors. Here, the transformation of a shifted local cartesian coordinate system $\overline{\boldsymbol{e}}_i$ is carried out by three subsequent rotations, where the angles φ, θ and ϑ represent the three angles of rotation. The rotation of a vector $\boldsymbol{u}$ is given by

$$\boldsymbol{w} = \boldsymbol{R} \cdot \boldsymbol{u} \tag{6.51}$$

where $\boldsymbol{R}$ defines a rotation matrix and $\boldsymbol{w}$ is the rotated version of $\boldsymbol{u}$. For a rotation with respect to the x-, y- or z-axis, the respective rotation matrices are defined by

$$\begin{aligned} \boldsymbol{R}_x = \begin{pmatrix} 1 & 0 & 0 \\ 0 & \cos\alpha & -\sin\alpha \\ 0 & \sin\alpha & \cos\alpha \end{pmatrix}, \quad \boldsymbol{R}_y = \begin{pmatrix} \cos\alpha & 0 & \sin\alpha \\ 0 & 1 & 0 \\ -\sin\alpha & 0 & \cos\alpha \end{pmatrix}, \\ \boldsymbol{R}_z = \begin{pmatrix} \cos\alpha & -\sin\alpha & 0 \\ \sin\alpha & \cos\alpha & 0 \\ 0 & 0 & 1 \end{pmatrix}. \end{aligned} \tag{6.52}$$

These rotations are named *geometric rotations*, whereas a rotation of the coordinate system is called *passive rotation* and the respective transposed matrix $\boldsymbol{R}^{\mathrm{T}}$ applies. In order to describe the orientation of an object in space, three rotations with respect to different axes are necessary. Different conventions exist with different rotation axes and a different order of rotation, cf. Goldstein [46]. Here, the z, y', z''-convention is used. Therefore, we consider a global coordinate system (XYZ) and a local coordinate system (xyz), which is related to the vector to be rotated. Before the rotation, these coordinate systems coincide. The global coordinate system will remain fixed throughout the rotation process and the local coordinate system will be rotated together with the vector. In detail, the

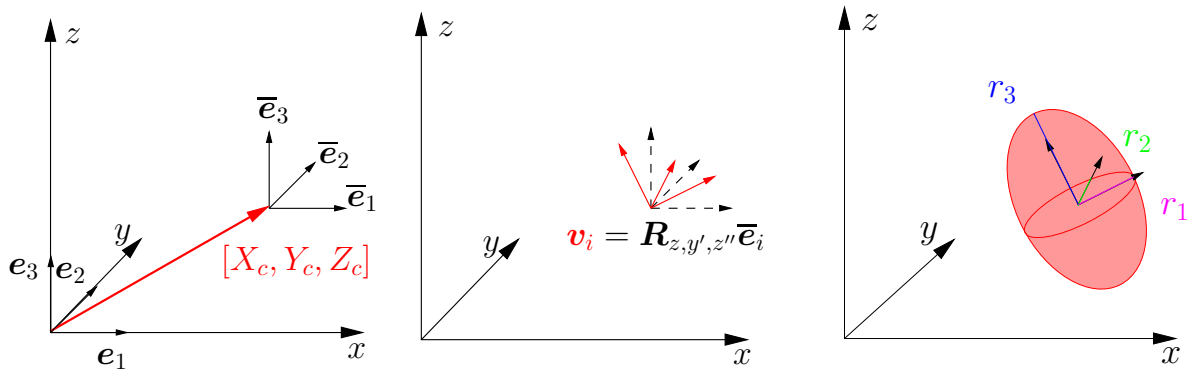

Figure 6.17: Illustration of parameterization vector $\boldsymbol{\gamma}^{(j)}$ for an ellipsoid.

local coordinate system is firstly rotated around the z-axis by an angle of φ, resulting in a new coordinate system $(x'y'z')$. The next rotation by the angle θ is performed about the y'-axis, thus the y-axis of the new local coordinate system, leading to the local coordinate system $(x''y''z'')$. The third rotation by the angle ϑ is performed around the z''-axis and results in the entirely rotated local coordinate system $(x'''y'''z''')$. All rotations are carried out with regard to "Ampère's right hand screw rule", where positive rotations act counterclockwise. The matrix representing the described rotation of a vector is given by

$$\boldsymbol{R}_{z,y',z''} = \boldsymbol{R}_{z''}(\vartheta) \cdot \boldsymbol{R}_{y'}(\theta) \cdot \boldsymbol{R}_{z}(\varphi) \tag{6.53}$$

with $\boldsymbol{R}_{z,y',z''}$ specifically given by

$$\boldsymbol{R}_{z,y',z''} = \begin{pmatrix} \cos\vartheta\cos\theta\cos\varphi - \sin\vartheta\sin\varphi & -\cos\theta\cos\varphi\sin\vartheta - \sin\varphi\cos\vartheta & \cos\varphi\sin\theta \\ \sin\varphi\cos\theta\cos\vartheta + \cos\varphi\sin\vartheta & -\sin\varphi\cos\theta\sin\vartheta - \cos\varphi\cos\vartheta & \sin\varphi\sin\theta \\ \sin\theta\cos\vartheta & \sin\theta\sin\vartheta & \cos\theta \end{pmatrix}. \tag{6.54}$$

The definition of the triad of base vectors is thus given by

$$\boldsymbol{v}_i = \boldsymbol{R}_{z,y',z''} \cdot \overline{\boldsymbol{e}_i} \tag{6.55}$$

from a rotation of the global coordinate system $\overline{\boldsymbol{e}_i}$. This rotation procedure is used to define the global orientation of an ellipsoid in space. Fig. 6.17 illustrates the parameterization. The center coordinates X_c, Y_c and Z_c represent the shift vector of the center of the ellipsoid to the global origin. The shifted triad of base vectors is then rotated by the angles φ, θ and ϑ. Within this base system $\boldsymbol{v}_i$, the ellipsoid is created with the given radii r_i.

With the description of the ellipsoid by Eq. (6.45), nine parameters are needed to describe this ellipsoid uniquely, thus

$$\boldsymbol{\gamma}^{(j)} := \left[X_c^{(j)}\ Y_c^{(j)}\ Z_c^{(j)}\ \varphi^{(j)}\ \theta^{(j)}\ \vartheta^{(j)}\ r_1^{(j)}\ r_2^{(j)}\ r_3^{(j)} \right]^{\mathrm{T}}. \tag{6.56}$$

Different parameterizations based on ellipsoids are obtained by using different numbers of ellipsoidal inclusions, thus the vector of parameterization type i is given by

$$\boldsymbol{\gamma}_i := \left[(\boldsymbol{\gamma}^{(1)})^{\mathrm{T}}\ (\boldsymbol{\gamma}^{(2)})^{\mathrm{T}}\ (\boldsymbol{\gamma}^{(3)})^{\mathrm{T}}\ \ldots\ (\boldsymbol{\gamma}^{(i)})^{\mathrm{T}} \right]^{\mathrm{T}}, \tag{6.57}$$

where i denotes the number of ellipsoids used in the parameterization type. Since the SSRVEs are constructed as periodic cells, a redundancy shall be avoided for a translational shifts, therefore the center coordinates of the first ellipsoid, i.e., $X_c^{(1)}$, $Y_c^{(1)}$ and $Z_c^{(1)}$ in each parameterization type are held fixed.

6.2.2 Objective Functions

Since the different statistical measures presented in Section 6.1 capture different properties of the microstructure, an analysis of different combinations is of interest. Instead of using only one statistical measure, the combination of multiple measures capturing different properties of the microstructure has been found to be beneficial in Yeong and Torquato [176]. Three objective functions, which follow the form given in Eq. (6.49)(1), combining different statistical measures will be presented in the following.

The first objective function takes into account the volume fraction and spectral density, thus one obtains

$$\mathcal{E}_I := \omega_\mathrm{V}\mathcal{L}_\mathrm{V} + \omega_\mathrm{SD}\mathcal{L}_\mathrm{SD}\,, \tag{6.58}$$

where ω_V and ω_SD represent the weighting factors for the volume fraction and spectral density, respectively. The least-square functional

$$\mathcal{L}_\mathrm{V}(\boldsymbol{\gamma}_i) := \left(1 - \frac{\mathcal{P}_\mathrm{V}^\mathrm{SSRVE}(\boldsymbol{\gamma}_i)}{\mathcal{P}_\mathrm{V}^\mathrm{target}}\right)^2 \tag{6.59}$$

describes the normalized difference of the volume fraction of the inclusion phase in the real microstructure, which is denoted by $\mathcal{P}_\mathrm{V}^\mathrm{target}$, and the SSRVE, which is denoted by $\mathcal{P}_\mathrm{V}^\mathrm{SSRVE}(\boldsymbol{\gamma}_i)$. The least-square functional accounting for the deviation of the spectral density of the SSRVE and the real microstructure is defined by

$$\mathcal{L}_\mathrm{SD}(\boldsymbol{\gamma}_i) := \frac{1}{\tilde{N}_\mathrm{SD}} \sum_{m=1}^{\tilde{N}_\mathrm{SD}} \left[\mathcal{P}_\mathrm{SD}^\mathrm{target}(\boldsymbol{y}_m) - \mathcal{P}_\mathrm{SD}^\mathrm{SSRVE}(\boldsymbol{y}_m, \boldsymbol{\gamma}_i)\right]^2\,, \tag{6.60}$$

where $\mathcal{P}_\mathrm{SD}^\mathrm{target}$ denotes the spectral density of the real microstructure and $\mathcal{P}_\mathrm{SD}^\mathrm{SSRVE}$ denotes the spectral density of the SSRVE, cf. Eq. (6.14). The vector $\boldsymbol{y}_m$ describes the position of the considered entries in the spectral density, which has the same dimensionality as the analyzed structure, as shown in Section 6.1.3. In the comparison of the spectral density of the target microstructure and the SSRVE, the difference in size has to be handled via the rebinning procedure described in Section 6.1.3. Before the optimization is started, the complete spectral density of the target microstructure is determined and rebinned to a suitable size as a reference. The number of evaluation point for the spectral density after rebinning and possibly reducing the relevant region, cf. Section 6.1.3, is denoted by $\tilde{N}_\mathrm{SD}$. Then, the evaluation of $\mathcal{L}_\mathrm{SD}$ in Eq. (6.60) is carried out by a comparison of the individual entries $\boldsymbol{y}_m$ with $m = 1 \dots \tilde{N}_\mathrm{SD}$ in the relevant area of the spectral density in the target microstructure and the SSRVE.

By additionally considering the lineal-path function, Eq. (6.58) can be extended to form another objective function

$$\mathcal{E}_{II} := \omega_\mathrm{V}\mathcal{L}_\mathrm{V} + \omega_\mathrm{SD}\mathcal{L}_\mathrm{SD} + \omega_\mathrm{LP}\mathcal{L}_\mathrm{LP}\,, \tag{6.61}$$

with the least square functional for the lineal-path function computed by

$$\mathcal{L}_\mathrm{LP}(\boldsymbol{\gamma}_i) := \frac{1}{\tilde{N}_\mathrm{LP}} \sum_{m=1}^{\tilde{N}_\mathrm{LP}} \left[\mathcal{P}_\mathrm{LP}^\mathrm{target}(\boldsymbol{y}_m) - \mathcal{P}_\mathrm{LP}^\mathrm{SSRVE}(\boldsymbol{y}_m, \boldsymbol{\gamma}_i)\right]^2, \tag{6.62}$$

where $\mathcal{P}_{\mathrm{LP}}^{\mathrm{target}}$ denotes the lineal-path function computed for the target microstructure and $\mathcal{P}_{\mathrm{LP}}^{\mathrm{SSRVE}}$ denotes its counterpart based on the SSRVE. Similarly as for the spectral density, $\boldsymbol{y}_m$ denotes to position vector to an individual entry in the lineal-path function, which is also computed in the same dimensionality as the analyzed structure. The total number of entries is given by $\tilde{N}_{\mathrm{LP}}$. In a similar sense as for the spectral density, a relevant section of the lineal-path function is defined based on a threshold value, neglecting values in the lineal-path function of the real microstructure which do not reach this threshold. Therefore, the lineal-path function of the target microstructure is computed and the relevant section is identified. Subsequently, the template used for the computation of the lineal-path function can be reduced to the size of the relevant section. This leads to a reduced effort in the optimization since a reduced number of line segments has to be analyzed only, cf. Section 6.1.4.

Since the computation of the lineal-path function is rather expensive, the statistical measures based on Minkowski functionals, cf. Section 6.1.5 are investigated as an alternative descriptor. The related objective function based on Minkowski tensor $\boldsymbol{\mathcal{W}}_1^{0,2}$ then reads

$$\mathcal{E}_{III} := \omega_{\mathrm{V}}\mathcal{L}_{\mathrm{V}} + \omega_{\mathrm{SD}}\mathcal{L}_{\mathrm{SD}} + \omega_{\mathrm{MA}}\mathcal{L}_{\mathrm{MA}} + \omega_{\mathrm{MO}}\mathcal{L}_{\mathrm{MO}}\,, \tag{6.63}$$

with the least-square functionals

$$\mathcal{L}_{\mathrm{MA}} = \frac{1}{N_{\mathrm{MA}}} \sum_{m=1}^{N_{\mathrm{MA}}} \left(\frac{V_{\mathrm{MA}}^{\mathrm{target}}(m)}{V^{\mathrm{target}}} \mathcal{P}_{\mathrm{MA}}^{\mathrm{target}}(m) - \frac{V_{\mathrm{MA}}^{\mathrm{SSRVE}}(m)}{V^{\mathrm{SSRVE}}} \mathcal{P}_{\mathrm{MA}}^{\mathrm{SSRVE}}(m, \boldsymbol{\gamma}_i) \right)^2 , \tag{6.64}$$

$$\mathcal{L}_{\mathrm{MO}} = \frac{1}{\sum_{k=1}^{6} N_{\mathrm{MO},k}} \sum_{k=1}^{6} \sum_{m=1}^{N_{\mathrm{MO}}} \left(\frac{V_{\mathrm{MO},k}^{\mathrm{target}}(m)}{V_k^{\mathrm{target}}} \mathcal{P}_{\mathrm{MO},k}^{\mathrm{target}}(m) - \frac{V_{\mathrm{MO},k}^{\mathrm{SSRVE}}(m)}{V_k^{\mathrm{SSRVE}}} \mathcal{P}_{\mathrm{MO},k}^{\mathrm{SSRVE}}(m, \boldsymbol{\gamma}_i) \right)^2 . \tag{6.65}$$

The probability density functions characterizing the anisotropy measure are denoted by $\mathcal{P}_{\mathrm{MA}}^{\mathrm{target}}$ and $\mathcal{P}_{\mathrm{MA}}^{\mathrm{SSRVE}}$ for the target structure and the SSRVE, respectively. Each of these probability density functions is weighted individually with the factor $V_{\mathrm{MA}}^{\mathrm{target}}(m)/V^{\mathrm{target}}$ and $V_{\mathrm{MA}}^{\mathrm{SSRVE}}(m)/V^{\mathrm{SSRVE}}$, respectively, where $V_{\mathrm{MA}}^{\mathrm{target|SSRVE}}(m)$ is the total volume of all inclusion of the target structure and SSRVE, respectively, belonging to category m and $V^{\mathrm{target|SSRVE}}$ is the total volume of inclusions in the target microstructure or SSRVE, respectively. Using this weighting, larger inclusions are weighted with a higher value than small inclusions and their response is enforced. The total number of entries of the probability density functions is given by N_{MA}. Similarly, the probability density functions for the orientation measure are given by $\mathcal{P}_{\mathrm{MO},k}^{\mathrm{target}}$ and $\mathcal{P}_{\mathrm{MO},k}^{\mathrm{SSRVE}}$ for the target structure and the SSRVE, respectively, where k denotes the different classifications as described in Section 6.1.5.

6.2.3 Proof of Concept: Retrieve a Given Microstructure

For a proof of concept, the ability of the objective functions to reconstruct a known microstructure is discussed in the following. This exploration analyzes an objective function in view of its ability to describe a known microstructure appropriately and capture the relevant information which is needed to reconstruct it in the optimization procedure. Depending on the statistical measures used in the objective function, certain geometrical properties of the analyzed microstructure can (or cannot) be described in the optimization process. For example, if an objective function solely depending on the volume fraction is considered, no morphological feature concerning inclusion shape would be taken into account in the optimization. For a given microstructure, for example consisting of one ellipsoidal inclusion, the optimization would detect redundancies since microstructures with inclusions with arbitrary shape but a correct volume fraction would be considered optimal. Some improvement can be made considering further statistical measures, however, due to limited computational resources the number of considered statistical measures cannot be increased endlessly. Two different types of artificial microstructures are considered for a reconstruction here, which are shown in Fig. 6.18a and Fig. 6.18b. In the first case, the microstructure consist of eight identical unitcells with a spherical inclusion which are arranged to form a cube, see Fig. 6.18a. In the optimization, the goal is to detect the unitcell only, thus a unitcell with one spherical inclusion. The second case considers a unitcell with two ellipsoidal inclusions with specific orientation in space, see Fig. 6.18b. Here, the unitcell shall be constructed in the optimization. Both microstructures consist of inclusion shapes which can be perfectly resembled with the chosen parameterization here, i.e. ellipsoidal inclusions. Among the objective functions presented in Section 6.2.2, $\mathcal{E}_I$, (Eq. (6.58)), $\mathcal{E}_{II}$, (Eq. (6.61)) and $\mathcal{E}_{III}$, (Eq. (6.63)) are used to construct the above described microstructures.

Retrieve Microstructure A

In the first case, the unitcell with a single spherical inclusion shall be reconstructed based on the analysis of a microstructure consisting of a $2 \times 2 \times 2$ spatial arrangement of this unitcell. The optimization succeeds in finding the unitcell for all objective functions. The

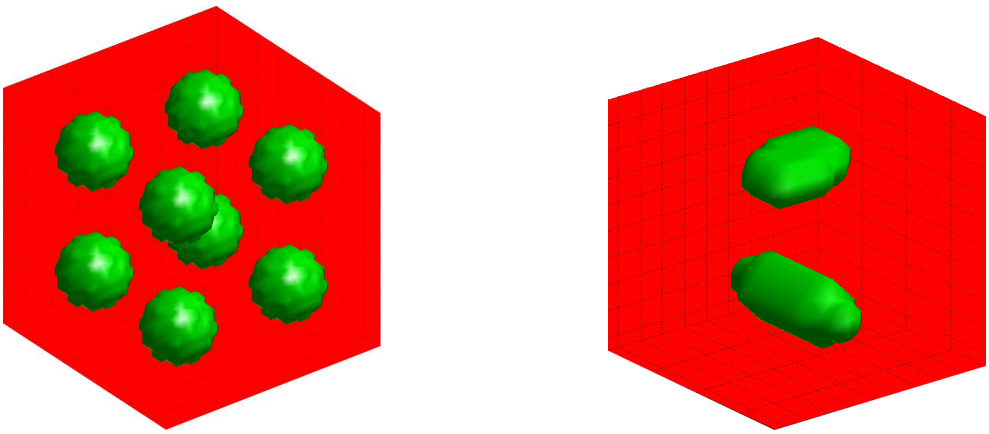

(a) (b)

Figure 6.18: (a) Microstructure A composed of a $2 \times 2 \times 2$ arrangement of a unitcell with a single spherical inclusion. (b) Unitcell to be obtained in the optimization process.

Table 6.1: Optimization results of the objective functions and individual errors from the considered statistical measures for reconstruction of microstructure A.

	$\mathcal{E}_i$	$\mathcal{L}_{\mathrm{V}}$	$\mathcal{L}_{\mathrm{SD}}$	$\mathcal{L}_{\mathrm{LP}}$	$\mathcal{L}_{\mathrm{MA}}$	$\mathcal{L}_{\mathrm{MO}}$
i=I	$2.88 \cdot 10^{-33}$	0.0	$2.88 \cdot 10^{-33}$	-	-	-
i=II	$2.88 \cdot 10^{-33}$	0.0	$2.88 \cdot 10^{-33}$	0.0	-	-
i=III	33.34	$1.31 \cdot 10^{-5}$	$2.21 \cdot 10^{-5}$	-	0.51	32.83

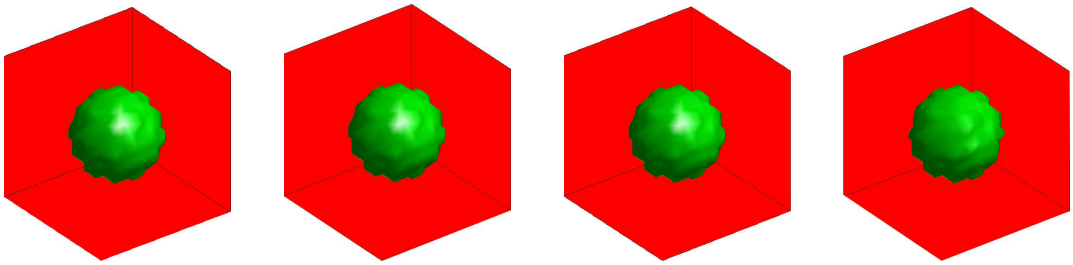

(a) **(b)** **(c)** **(d)**

Figure 6.19: (a) Original unitcell, which is used to construct artificial microstructure A, see Fig. 6.18, (b) unitcell reconstruction using $\mathcal{E}_{II}$ and (c) unitcell reconstruction using $\mathcal{E}_{III}$.

results of the optimization are summarized in Tab. 6.1, illustrations of the reconstructed unitcells are shown in Fig. 6.19b-d, together with the original unitcell, see Fig. 6.19a.

For $\mathcal{E}_I$ and $\mathcal{E}_{II}$, the reconstruction leads to the same values in the objective functions, with $\mathcal{L}_{\mathrm{V}} = 0$ and the error solely arising from the spectral density, which is however negligible. In $\mathcal{E}_{II}$, the lineal-path function is perfectly matched. A higher error value arises in $\mathcal{E}_{III}$, where it is mainly resulting from the anisotropy measure. In this specific case, the large error in the anisotropy measures based on the Minkowski functional result from the handling in the optimization procedure: A perfectly spherical inclusion, with all eigenvalues of the Minkowski tensor being equal, results in an entry in $\mathcal{P}_{MO,6}$. This rather strict condition of $\mu_1 = \mu_2 = \mu_3$ is relaxed introducing a tolerance, as described in Section 6.1.5. However, in this case the tolerance seems to be slightly exceeded, leading to a high statistical error. With regard to the construction of SSRVEs based on real microstructures, this special case is expected to be of minor interest, since the evaluation of inclusions rarely results in the case of three identical eigenvalues, thus spherical inclusions.

A comparison of the parameterization vectors in Tab. 6.1 also illustrates the success of all three optimizations. While the differences in φ, θ and ϑ do not have an effect on the spherical inclusion and could be chosen arbitrarily, the radii show slight differences compared with the original. Here, it has to be considered that the resolution of the given microstructure and the unitcell, here given by 1 voxel/µm in all three spatial directions, cannot reflect small differences in physical lengths. In order to detect whether a voxel belongs to the inclusion or not, its center coordinate is considered. The given resolution then influences the precision in modeling the geometry and here a deviation of up to 1 µm cannot be distinguished. With this in mind, the optimizations can be considered to have successfully reconstructed the unitcell.

Table 6.2: Comparison of parameterization vectors for the reconstruction of known microstructure A using the objective functions $\mathcal{E}_I$, $\mathcal{E}_{II}$ and $\mathcal{E}_{III}$.

	φ	θ	ϑ	r_1	r_2	r_3
original	10.0	30.0	0.0	5.0	5.0	5.0
i=I	42.78	14.42	70.03	4.99	4.99	5.03
i=II	19.65	5.28	4.70	5.03	5.17	5.00
i=III	47.16	29.24	10.66	5.18	4.96	5.13

Retrieve Microstructure B

The reconstruction of microstructure B leads to good overall results, although not all objective functions are able to reconstruct the microstructure as well as in the previous case. The values of objective functions and the individual errors for each statistical measure are shown in Tab. 6.3. The original unitcell is shown in Fig. 6.20a, the reconstructions based on $\mathcal{E}_{\mathrm{I}}$, $\mathcal{E}_{\mathrm{II}}$ and $\mathcal{E}_{\mathrm{III}}$ are depicted in Fig. 6.20b-d, respectively. A comparison of the unitcell first shows that all reconstructions achieve to resemble two ellipsoids with an appropriate distance to each other. Fig. 6.20c, showing the reconstruction based on phase fraction, spectral density and lineal-path function, looks most similar to the original unitcell. This can also be seen from a comparison of the parameterization vectors, see Tab. 6.4. Note that the data of the parameterization vector has been rearranged in order to avoid confusion in the direct comparison of the parameterization vectors. There can exist different parameterization vectors defining the same unitcell when, e.g., the first and second ellipsoid switch their position, which due to the assumption of periodicity still describes the same unitcell. This becomes clear if one considers a periodically extended microstructure built up by the unitcells and considers a different section, also being a periodic unitcell, from the large structure. Furthermore, a redundancy can occur for the description of rotationally symmetric ellipsoids. The position of the first ellipsoid is held fixed, in the original unitcell this was chosen as $X_c^{(1)} = 10.0$, $Y_c^{(1)} = 10.0$, $Z_c^{(1)} = 5.0$, whereas in the optimization $X_c^{(1)} = 10.0$, $Y_c^{(1)} = 10.0$, $Z_c^{(1)} = 10.0$ was used. However, due to the periodicity, only the relative position of the ellipsoids to each other is important. Its reconstruction is achieved by all three objective functions. For the reconstruction based on $\mathcal{E}_{\mathrm{I}}$, a mismatch in the orientation can be seen for one ellipsoid. For $\mathcal{E}_{\mathrm{III}}$, it can be seen from Fig. 6.20d that the volume fraction of each ellipsoid was not matched and also the match of orientations and radii is not as good as in the other two cases. The reason for this could be the choice of categories for the probability density functions for anisotropy and orientation value, which might be not sensitive enough for slight changes here. However, an adequate representation of the unitcell is found. Overall, $\mathcal{E}_{\mathrm{II}}$ performed best in the reconstruction of microstructure B.

Table 6.3: Optimization results of the objective functions and individual errors from the considered statistical measures for reconstruction of microstructure B.

	$\mathcal{E}_i$	$\mathcal{L}_{\mathrm{V}}$	$\mathcal{L}_{\mathrm{SD}}$	$\mathcal{L}_{\mathrm{LP}}$	$\mathcal{L}_{\mathrm{MA}}$	$\mathcal{L}_{\mathrm{MO}}$
i=I	$3.81 \cdot 10^{-4}$	0.0	$3.81 \cdot 10^{-4}$	-	-	-
i=II	$9.27 \cdot 10^{-6}$	0.0	$9.27 \cdot 10^{-6}$	0.0	-	-
i=III	$8.57 \cdot 10^{-4}$	0.0	$8.57 \cdot 10^{-4}$	-	0.0	0.0

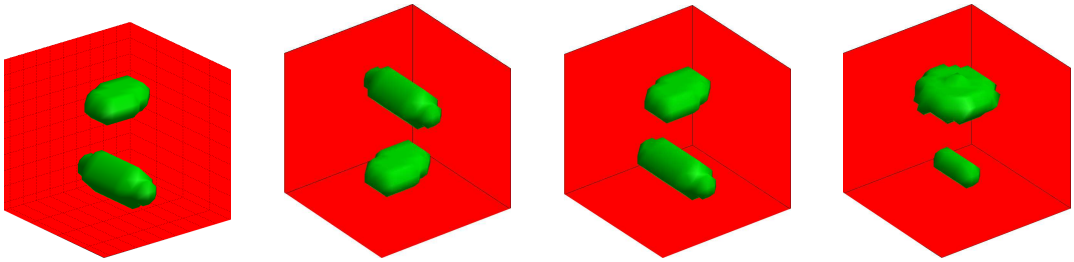

(a) **(b)** **(c)** **(d)**

Figure 6.20: (a) Original unitcell, which is used to construct artificial microstructure B and (b) unitcell reconstruction using $\mathcal{E}_{II}$ and (c) unitcell reconstruction using $\mathcal{E}_{III}$.

Table 6.4: Comparison of (reordered) parameterization vectors for the reconstruction of known microstructure B using the objective functions $\mathcal{E}_I$, $\mathcal{E}_{II}$ and $\mathcal{E}_{III}$.

	$\varphi^{(1)}$	$\theta^{(1)}$	$\vartheta^{(1)}$	$r_1^{(1)}$	$r_2^{(1)}$	$r_3^{(1)}$	$X_c^{(2)}$	$Y_c^{(2)}$	$Z_c^{(2)}$	$\varphi^{(2)}$	$\theta^{(2)}$	$\vartheta^{(2)}$	$r_1^{(2)}$	$r_2^{(2)}$	$r_3^{(2)}$
original	90.0	0.0	0.0	6.0	2.0	2.0	10.0	10.0	15.0	0.0	0.0	30.0	5.0	3.0	1.5
i=I	80.25	87.03	72.11	2.56	1.88	6.01	10.17	8.46	0.33	69.79	8.07	29.88	3.71	4.74	0.88
i=II	1.94	89.29	0.37	2.00	6.39	2.02	9.94	10.18	0.01	4.59	0.25	27.39	5.01	3.13	1.27
i=III	0.16	22.89	88.42	3.79	1.24	1.20	10.17	10.39	19.75	40.41	0.04	89.56	4.63	4.85	1.79

6.2.4 Comparison of Mechanical Response

For the comparison of the mechanical response of the target microstructure and the SSRVE, virtual mechanical tests are carried out, i.e. tension test in x- and z-direction, (lateron indicated by subscript x and z, respectively) as well as two simple shear tests, where a displacement in introduced on the xy-plane in x- and y-direction, respectively (indicated by subscript xy and yx). The virtual tests are illustrated in Fig. 6.21. With these tests carried out for the target microstructre and an SSRVE, a deviation is calculated for the macroscopic stress-strain response, defined by

$$r_{e,j} = \frac{\bar{\sigma}_{e,j}^{\text{target}}(\bar{\varepsilon}_{e,j}) \; - \; \bar{\sigma}_{e,j}^{\text{SSRVE}}(\bar{\varepsilon}_{e,j})}{\bar{\sigma}_{e,j}^{\text{target}}(\bar{\varepsilon}_{e,j})}\,, \tag{6.66}$$

where $\bar{\sigma}$ denotes the macroscopic Cauchy stress, $\bar{\varepsilon}$ denotes the macroscopic engineering strain and e denotes the respective experiment. Here, j defines the evaluation point with $j = 1...n_{\text{ep}}$ with a total number of evaluation point n_{ep}. Only values with nonzero denominator are considered in Eq. (6.66). For every experiment, an average error is computed using

$$\tilde{r}_e = \sqrt{\frac{1}{n_{\text{ep}}} \sum_{j=1}^{n_{\text{ep}}} \left[r_{e,j}(\bar{\varepsilon}_{e,j})\right]^2} \qquad \text{with} \qquad \bar{\varepsilon}_{e,j} = \frac{j}{n_{\text{ep}}} \bar{\varepsilon}_e^{\max},\; j = 1...n_{\text{ep}}\,, \tag{6.67}$$

with the maximum strain in each experiment denoted by $\bar{\varepsilon}_e^{\max}$. In order to obtain one comparative measure combining the error computed in the individual mechanical tests, an overall average error is defined by

$$\tilde{r}_{\varnothing} = \sqrt{\frac{1}{n_{\text{exp}}} \sum_{e=1}^{n_{\text{exp}}} \tilde{r}_e^2}\,, \tag{6.68}$$

for a total number of experiments n_{exp} considered. In order to analyze the difference in the error in the two phases, martensite and ferrite, more closely, the error measure defined in Eq. (6.67) is computed for each phase separately, denoted by r_e^{fer} and r_e^{mar}, for ferrite and martensite, respectively with $e = x, z, xy, yx$ denoting the four virtual experiments.

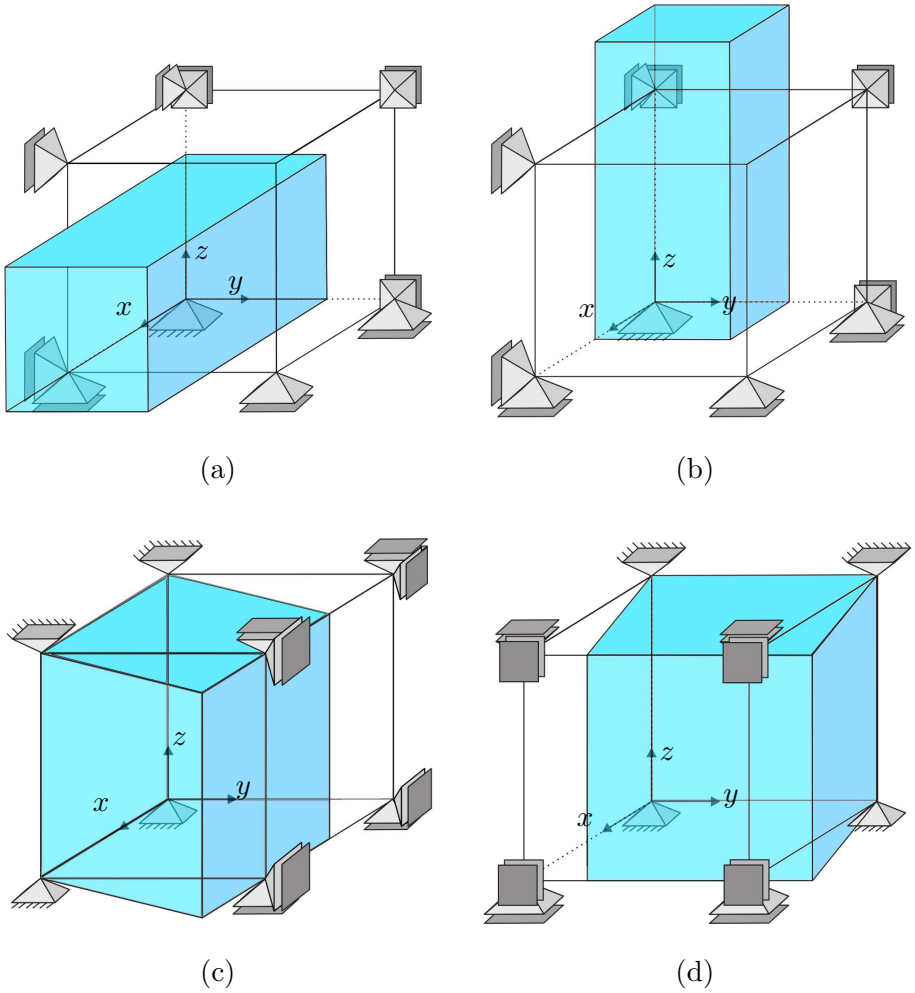

Figure 6.21: Four virtual mechanical tests: (a) tension in x-direction, (b) tension in z-direction, (c) shear of xy-plane in x-direction and (d) shear of xy-plane in y-direction.

Finite element meshes of the SSRVE candidate geometry defined by $\tilde{\boldsymbol{\gamma}}_i$ in the inner optimization are generated using 10-noded tetrahedral elements, for a convergency analysis of the finite element meshes, see Appendix B. Macroscopic deformation states are prescribed resembling the virtual experiments and the microscopic mechanical response is homogenized to obtain the macroscopic counterpart. The DP steel microstructure, cf. Section 4 is discretized using a finite element mesh with $2,013,525$ 10-noded tetrahedral finite elements. The computations are performed using FEAP, Taylor [161]. Periodic boundary conditions are used on the microscale in the case of the SSRVEs whereas linear displacement boundary conditions are used for the real microstructure, where *ParFEAP* was used. The computation for the real microstructure was computed on the supercomputer *Cray XT6m* at University Duisburg-Essen using *ParFEAP* on 96 cores. Details on the material model can be found in Section 4.2.

For both material phases, an isotropic finite J_2-plasticity material model including ex-

	matrix	inclusion
λ in MPa	118,846.2	
μ in MPa	79,230.77	
y_0 in MPa	260.0	1000.0
y_∞ in MPa	580.0	2750.0
ξ	9.0	35.0
h in MPa	70.0	10.0

(a)

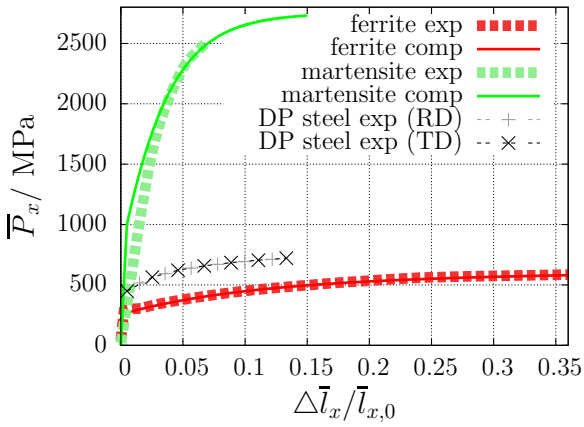

(b)

Figure 6.22: (a) Material parameters adjusted to experimental curves and (b) nominal stresses $\overline{\boldsymbol{P}}_{11}$ in MPa versus strains $\Delta\overline{l}/\overline{l}_0$ in uniaxial tension (loading direction: rolling direction) for the experimental data (courtesy of ThyssenKrupp Steel Europe) and the resulting modeling response: pure ferrite which is reproduced in the laboratory adjusting for a similar alloying composition as in the ferrite of the DP steel, pure martensite (produced in the laboratory) adjusting for a similar carbon content as in the martensite in the DP steel, and experimental response in rolling and transverse direction of the considered DP steel. Taken from Brands et al. [23].

ponential hardening with superimposed linear hardening is used to describe the material behavior. The material parameters, namely Lamé constants λ and μ, initial yield strength y_0, plastic yield strength at initialization of linear hardening y_∞, degree of exponential hardening η and slope of superimposed hardening h, can be found in Fig. 6.22a. The plastic strain energy function reads

$$\psi^{\mathrm{P}} = y_\infty\,\alpha \;-\; \frac{1}{\eta}\,(y_0 \;-\; y_\infty)\,\exp\left(-\eta\,\alpha\right) \;+\; \frac{1}{2}\,h\,\alpha^2\,. \tag{6.69}$$

More sophisticated material models could be used, which consider kinematic hardening of DP steel or the intricate material behavior resulting from the granular behavior of e.g. the ferrite phase.

6.2.5 Optimization Method

The minimization of the optimization problem defined in Eq. (6.50) is based on a semi-automated approach, where the solution of the inner and outer problem is achieved sequentially. For a predefined set of statistical measures $\mathcal{G}$, weighting factors ω and a specific type of morphology parameterization $\boldsymbol{\gamma}_i$, the optimal morphology, $\tilde{\boldsymbol{\gamma}}_i$, is determined by minimizing the objective functions given in Section 6.2.2 using a differential evolution algorithm based on the algorithm of Storn and Price [150]. It has been found to be highly efficient for global optimization of non-differentiable, nonlinear functions using a direct search approach with simultaneously solving different solution vectors in a parallel algorithm to avoid the solution of being "trapped" in a local minimum. This differential evolution strategy is implemented in the optimization environment *Mystic*, cf. McKerns et al. [89; 90], which is an open source tool providing a broad collection of optimization algorithms. The differential evolution algorithm is steered by a number of parameters, which are chosen according to the suggestions made in Storn [149].

The analysis of the influence of different optimization parameters is not in the scope of this work. Alternative optimization techniques could be used, Strohmann [152] uses a multi-objective optimization framework for the construction of SSRVEs. In contrast to the weighted sum objective function multi-objective optimization treats every statistical measure as a separate objective. When the inner optimization problem is solved, the evaluation of the outer optimization problem involves the computation of virtual mechanical experiments. Several SSRVE candidates are compared with regard to their ability to resemble the mechanical behavior of the real DP steel microstructure in the virtual mechanical experiments, see Section 6.2.4. The minimization of the error measure described in Eq. (6.68) identifies the "best" SSRVE out of the candidates, giving rise to the most suitable inclusion morphology and set of statistical parameters.

Note that the objective functions used here are non-smooth due to the underlying discrete evaluation of statistical measures. This was shown in Balzani et al. [7] for an objective functions considering volume fraction and spectral density where the optimization problem was reduced for visualization. There also the non-convexity of the optimization problem becomes visible. These properties preclude the use of standard gradient based optimization procedures and also require to cope with many local minima. The differential evolution algorithm is well suited for this, however, the optimization result can only be considered as a local minimum.

6.2.6 Weighting Factors

The optimization problem given in Eq. (6.50) is defined by a weighted sum of multiple objectives, i.e., the individual least-square functionals of the statistical measures, into one scalar objective function, which is then minimized. This involves a set of weighting factors which determine the influence of the individual objectives. Different weighting factors result in a different influence of the individual objective in the overall objective function and therefore different combinations of weighting factors yield different overall objective functions. In order to fully analyze the influence of the weighting factors on the optimization problem, the response of the outer optimization, i.e., minimization of the mechanical error between SSRVE and real microstructure, would have to be analyzed for a large number of sets of weighting factors, which is unfeasible due to the high computational effort. In Scheunemann et al. [128], a limited analysis of the weighting factors for the presented approach is carried out. The weighting factors in the optimization problem presented in Eq. (6.50) are then used to trigger the optimization problem such that a first estimation for a good fitting of the statistical measures in the SSRVE and the target structure is obtained. In detail, several optimizations based on the weighted least-square functionals are carried out and the performance of an equally weighted objective function is evaluated. The results are shown in Fig. 6.23 using a logarithmic scale on the abscissa. The objective functions with equal weighting, i.e., $\omega_L = 1$ for $L = V, SD, LP, MA, MO$ for all statistical measures, are defined by

$$\begin{aligned} \mathcal{E}_I^{\text{even}}(\boldsymbol{\gamma}_i) &:= \mathcal{L}_{\text{V}} + \mathcal{L}_{\text{SD}} \\ \mathcal{E}_{II}^{\text{even}}(\boldsymbol{\gamma}_i) &:= \mathcal{L}_{\text{V}} + \mathcal{L}_{\text{SD}} + \mathcal{L}_{\text{LP}} \\ \mathcal{E}_{III}^{\text{even}}(\boldsymbol{\gamma}_i) &:= \mathcal{L}_{\text{V}} + \mathcal{L}_{\text{SD}} + \mathcal{L}_{\text{MA}} + \mathcal{L}_{\text{MO}}. \end{aligned} \tag{6.70}$$

For an analysis of the influence of weighting factors in $\mathcal{E}_I$, the ratio between the weighting factors is varied, holding $\omega_{\text{V}} = 1$ fixed. The objective function is evaluated for ω_{SD} ranging

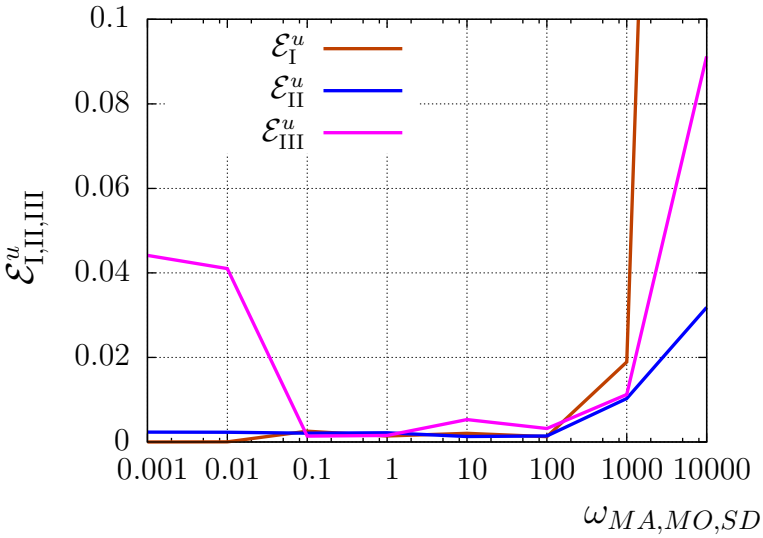

Figure 6.23: Section with lineal-path function values higher than the threshold of 0.02 representing an estimation for the average inclusion size computed for the DP steel microstructure.

from $1 \cdot 10^{-2}$ to $1 \cdot 10^{4}$. The change of the unweighted objective functions, Eq. 6.70(1) is analyzed with respect to change of ω_{SD}. It is observed that changing weighting factor does not influence the value of $\mathcal{L}_{\mathrm{SD}}$ largely, which is in a range of $1 \cdot 10^{-2}$ to $1 \cdot 10^{-4}$. However, when for $\omega_{\mathrm{SD}} \geq$ is larger than 10, the error in the volume fraction rises, with $\mathcal{L}_{\mathrm{V}} < 1 \cdot 10^{-6}$ for $\omega_{\mathrm{SD}} \leq 1$ but $\mathcal{L}_{\mathrm{V}}$ increasing steadily when $\omega_{\mathrm{SD}} > 1$. On the other hand, when ω_{SD} is chosen too small, the important information captured in the spectral density might be underestimated. Therefore, $\omega_{\mathrm{SD}} = \omega_{\mathrm{V}} = 1$ is chosen. For $\mathcal{E}_{II}$, it is observed that $\mathcal{L}_{\mathrm{LP}}$ is typically much smaller than $\mathcal{L}_{\mathrm{V}}$. Therefore, a fixed ratio of $\omega_{\mathrm{V}}/\,\omega_{\mathrm{LP}} = 1/\,1000$ to achieve a good relation between the volume fraction and the lineal-path function is chosen and ω_{SD} is varied in the range $1 \cdot 10^{-2}$ to $1 \cdot 10^{-4}$. It is observed that for values of $\omega_{\mathrm{SD}} > 1000$ the unweighted error measure $\mathcal{E}^{\mathrm{even}}_{II}$ increases drastically in value. A variation below this value does not change the value of the unweighted objective function. Therefore, the weighting of ω_{SD} is assumed to be suitable in the case as well.

For the objective function $\mathcal{E}_{\mathrm{III}}$, considering spectral density, volume fraction and anisotropy and orientation measures based on Minkowski tensor $\mathcal{W}_1^{0,2}$, the weighting factors ω_{MA} and ω_{MO} are treated with the same value, i.e., $\omega_{\mathrm{MA}} = \omega_{\mathrm{MO}}$, since they rest upon the same statistical measure. The ratio of the remaining weighting factors is kept from the previous objective functions with $\omega_{\mathrm{V}} = \omega_{\mathrm{SD}} = 1$. Now, $\omega_{\mathrm{MA|MO}}$ is varied in a range of $1 \cdot 10^{-3}$ to $1 \cdot 10^{4}$ and the change of $\mathcal{E}^{\mathrm{even}}_{\mathrm{III}}$ is analyzed. Here, the lowest value of the unweighted objective function is found in a range of $1 \cdot 10^{-1} < \omega_{\mathrm{MA|MO}} < 1 \cdot 10^{2}$. We choose a weighting factor of $\omega_{\mathrm{MA|MO}} = 1$ for the subsequent analysis.

Since the weighting factors are used to emphasize the influence of each individual objective on the overall objective function, Different sets of weighting factors are evaluated using $\mathcal{E}_I$, $\mathcal{E}_{II}$ and $\mathcal{E}_{III}$ and the resulting parameterization $\tilde{\gamma}_i$ is used to evaluate the objective functions in Eq. 6.70.

6.2.7 Estimation of SSRVE Size

The size of a suitable RVE is discussed in the literature and depends on various aspects. A brief summary on the topic is given in Section 1. Generally, since the SSRVE size not apriori given, different sizes could be analyzed, which would however raise large computational effort. Therefore, an estimation of the SSRVE's size is made here. For the construction of SSRVEs, the size of the SSRVE is dependent on the statistical measures used in the objective function, since the statistical measures are not necessarily dimensionless. The lineal-path function carries information about the characteristic size of an inclusion in a microstructure. If it is used together with the phase fraction, the measures are found to interfere if the size of the SSRVE is chosen too small or too large. Furthermore, a large size of the SSRVE contributes to large computation times in the construction process. Therefore, the size of the SSRVE is estimated apriori, while this estimation circumvents the contradiction between volume fraction and lineal-path function. This estimation depends on the number of inclusions used in the parameterization and is used for all SSRVEs of this type, even if the lineal-path function is not considered in the objective function. The steps used for the estimation are outlined in the following.

1. The lineal-path function is used for the estimation of an average inclusion volume in the target microstructure. Defining a threshold p^{thres}, all entries/voxel in the lineal-path function with a value smaller than p^{thres} are neglected leaving a number of $n_{\text{LP}}^{\text{thres}}$ relevant entries/voxel. These entries correspond to line segments with a relevant probability and define an average inclusion. The volume of the average inclusion can be calculated by $\bar{V}_{\text{inc}}^{\text{target}} = \sum_{i=1}^{n_{\text{LP}}^{\text{thres}}} V_i$, with V_i as the volume of a single voxel in the lineal-path function, which is here $0.1\mu\text{m} \times 0.1\mu\text{m} \times 0.1\mu\text{m}$. Here, the threshold chosen is $p^{\text{thres}} = 0.02$ and an illustration of the average inclusion of the target microstructure is shown in Fig. 6.24.

2. The average inclusion size aimed for in the SSRVE and the target microstructure are equal, hence $\overline{V}_{\text{inc}}^{\text{target}} = V_{\text{inc}}^{\text{SSRVE}}$. With the inclusion number in the SSRVE given by i, the phase fraction of the SSRVE is estimated by

$$\mathcal{P}_{\text{V}}^{\text{SSRVE}} = \frac{i\, V_{\text{inc}}^{\text{SSRVE}}}{V^{\text{SSRVE}}} = \frac{i\, \bar{V}_{\text{inc}}^{\text{target}}}{V^{\text{SSRVE}}}\,, \tag{6.71}$$

   with the total volume of the SSRVE denoted by V^{SSRVE}. With the aim of having the same volume fraction in the target microstructure and the SSRVE, i.e. $\mathcal{P}_{\text{V}}^{\text{SSRVE}} \equiv \mathcal{P}_{\text{V}}^{\text{target}}$, one can rearrange Eq. (6.71) with respect to V^{SSRVE}, hence the volume of the SSRVE is estimated by

$$V^{\text{SSRVE}} = \frac{i\, \bar{V}_{\text{inc}}^{\text{target}}}{\mathcal{P}_{\text{V}}^{\text{target}}}\,. \tag{6.72}$$

3. Assuming a cubic SSRVE with equal edge lengths in x-, y- and z-direction, the estimation yields this edge length as

$$L^{\text{SSRVE}} = L_x^{\text{SSRVE}} = L_y^{\text{SSRVE}} = L_z^{\text{SSRVE}} = \sqrt[3]{\frac{i\, \bar{V}_{\text{inc}}^{\text{target}}}{\mathcal{P}_{\text{V}}^{\text{target}}}}. \tag{6.73}$$

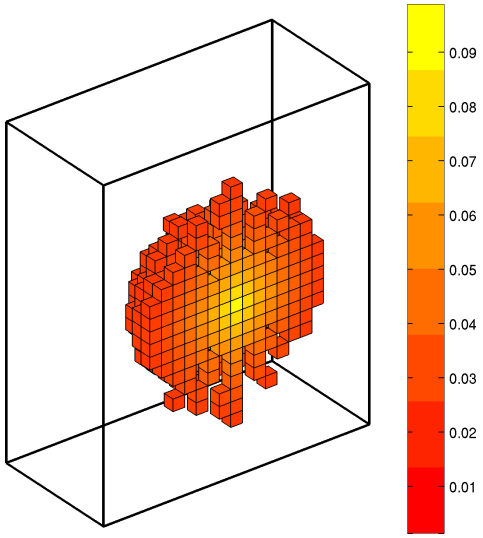

Figure 6.24: Section with lineal-path function values higher than the threshold of 0.02 representing an estimation for the average inclusion size computed for the DP steel microstructure. Taken from Balzani et al. [11]

With the above described estimation method, the prescribed SSRVE's sizes given by the edge length L^{SSRVE} for different inclusion numbers $i = 1, 2, 3, 4$ is obtained as $L^{\text{SSRVE}}_{i=1} = 3.0\,\mu\text{m}$ for one inclusion, $L^{\text{SSRVE}}_{i=2} = 3.8\,\mu\text{m}$ for two inclusions, $L^{\text{SSRVE}}_{i=3} = 4.3\,\mu\text{m}$ for three inclusions and $L^{\text{SSRVE}}_{i=4} = 4.8\,\mu\text{m}$ for four inclusions. The other statistical measures applied here do not show a comparable dependence, hence they do not contribute to the size estimation of the SSRVE. The SSRVE size is considered as given above for all SSRVEs constructed here for better comparability.

6.3 SSRVEs Based on Different Sets of Statistical Descriptors[1.)]

This section is based on results published in Balzani et al. [11] and Scheunemann et al. [128]. In the following the construction method for SSRVEs proposed in the previous sections is used for the construction of SSRVEs utilizing different combinations of statistical measures based on a minimization of the objective functions proposed in Section 6.2.2. Specifically, phase fraction and spectral density are used for the construction of all SSRVEs. The details of this first set are summarized in Section 6.3.1. Additionally, the lineal-path function are used for a second set of SSRVEs, which is detailed in Section 6.3.2. In a third set, see Section 6.3.3, phase fraction, lineal-path function and statistical measures for the description of anisotropy and orientational properties of the inclusion morphology based on Minkowski functionals, as proposed in Section 6.1.5 are be presented. For all sets, SSRVEs with one, two, three and four inclusions are constructed by a minimization of the according objective function, cf. Section 6.2.2. The mechanical comparison with regard to the real target microstructure is carried out based on the virtual experiments described in Section 6.2.4 and error measures presented therein are used to range the performance of the SSRVE.

[1.)] The results have been published in Scheunemann et al. [128]

6.3.1 SSRVEs Based on Objective Function $\mathcal{E}_{\mathrm{I}}$

SSRVEs solely based on scalar statistical measures, such as phase fraction, internal surface density and integral of mean curvature, see Section 6.1.1, show a larger deviation of the mechanical behavior with respect to a real microstructure compared to SSRVEs which are additionally based on higher order measures. This was shown in the two-dimensional case in Balzani et al. [8] and it is assumed that this behavior is also valid in 3D. Therefore, the first set of SSRVEs constructed is based on a fitting of the volume fraction and the spectral density. Therefore, $\mathcal{E}_I$, cf. Eq. (6.58), is minimized. The SSRVE candidates are depicted in Fig. 6.25 and the statistical measures and errors of the mechanical comparison are summarized in Tab. 6.5. It can be seen that an increased complexity of the inclusion morphology, realized by a higher number of inclusions, results in a lower value of the objective function which describes a closer resemblance of the statistical properties of the SSRVE with regard to the real target microstructure. Furthermore, the overall error $r_{\varnothing}$ in the mechanical comparison also decreases with an increase of the number of inclusions. Out of this set of SSRVEs, the one based on four inclusions provides the lowest overall mechanical error, namely 2.65%.

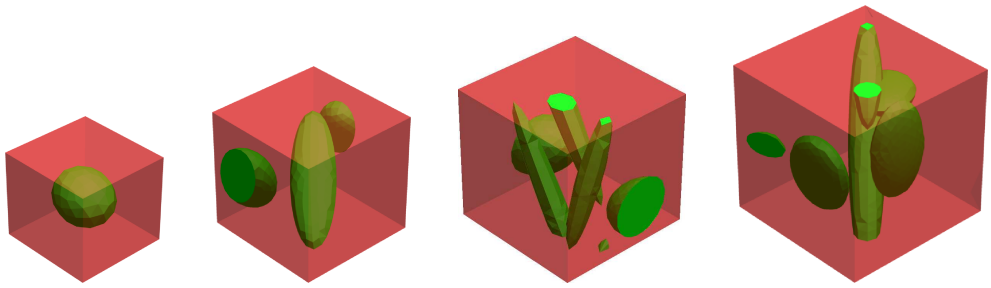

Figure 6.25: SSRVEs based on a minimization of $\mathcal{E}_{\mathrm{I}}$ considering volume fraction and spectral density with different numbers of inclusions $n_{\mathrm{inc}} = 1, 2, 3, 4$ from left to right. Taken from Scheunemann et al. [128].

Table 6.5: Results of SSRVEs based on volume fraction and spectral density - values of objective function $\mathcal{E}_{\mathrm{I}}$, and individual least square functionals, number of tetrahedral elements n_{ele} and mechanical errors $\tilde{r}$ in % for the individual SSRVEs. Taken from Scheunemann et al. [128].

n_{inc}	$\mathcal{E}_{\mathrm{I}}/\ 10^{-3}$	$\mathcal{L}_{\mathrm{V}}/\ 10^{-7}$	$\mathcal{L}_{\mathrm{SD}}/\ 10^{-3}$	n_{ele}	$\tilde{r}_x$	$\tilde{r}_z$	$\tilde{r}_{xy}$	$\tilde{r}_{yx}$	$\tilde{r}_{\varnothing}$
1	4.17	8.83	4.17	1638	3.3	3.7	5.0	5.0	4.32
2	2.03	1.35	2.03	8455	4.2	3.9	2.0	2.0	3.20
3	1.16	0.97	1.16	10759	2.6	1.2	3.9	3.9	3.11
4	0.74	3.38	0.74	17118	2.7	0.5	3.2	3.2	2.65

6.3.2 SSRVEs Based on Objective Function $\mathcal{E}_{\mathrm{II}}$

Based on the minimization of $\mathcal{E}_{II}$, cf. Eq. (6.61), SSRVEs are constructed which are based on a similarity of volume fraction, spectral density and lineal-path function with respect to the real target microstructure. The resulting SSRVEs are shown in Fig. 6.26 and the comparison of the statistical measures and mechanical response is given in Tab. 6.6. As seen in Section 6.3.1, the deviation of the statistical measures of the SSRVE from the counterparts measured in the real target microstructure decreases with an increased

complexity of inclusion morphology. Additionally, the deviation of the mechanical response, summarized in the overall error measure $r_{\varnothing}$, decreases with a higher number of inclusions. The behavior converges for three and four ellipsoidal inclusions, where the overall mechanical error $r_{\varnothing} = 1.45\%$ and $r_{\varnothing} = 1.47\%$ are found, respectively, which is considered to be an adequate level of similarity with respect to the real microstructure. The SSRVE with three ellipsoidal inclusions here is the most beneficial SSRVE with a low overall mechanical error and an appropriate number of $15,714$ finite elements, used for the discretization in view of efficient computation. This SSRVE is denoted by $\text{SSRVE}^{\text{LP}}_{\text{best}}$ and is used in a detailed comparison of SSRVEs in Section 6.3.4.

Comparing the results of the SSRVEs constructed in this section with the ones constructed in chapter 6.3.1, i.e., based on volume fraction and spectral density, it is observed that SSRVEs with three and four inclusions lead to better results using SSRVEs additionally based on the lineal-path function. For SSRVEs with lower numbers of inclusions, slightly better results are obtained from SSRVEs based on spectral density and volume fraction only. A reason for this can be possibly found in the optimization process. As described in Section 6.2.5, the detection of a global minimum of the optimization problem is not possible and maybe it even does not exist. Due to the higher computational effort needed for the evaluation of the lineal-path function, the optimization might lead to a "less optimal" SSRVE when comparable computational effort is assumed. With a focus on the individual errors in the statistical measures, it is observed that in the case of SSRVEs with one inclusion, the one based on volume fraction and spectral density shows a much better fitting of the volume fraction than the SSRVE based on volume fraction, spectral density and lineal-path function. For the latter, a value $\mathcal{L}_{\text{V}} = 0.048529$ is computed whereas the former leads to a value of $\mathcal{L}_{\text{V}} = 0.00000883$.

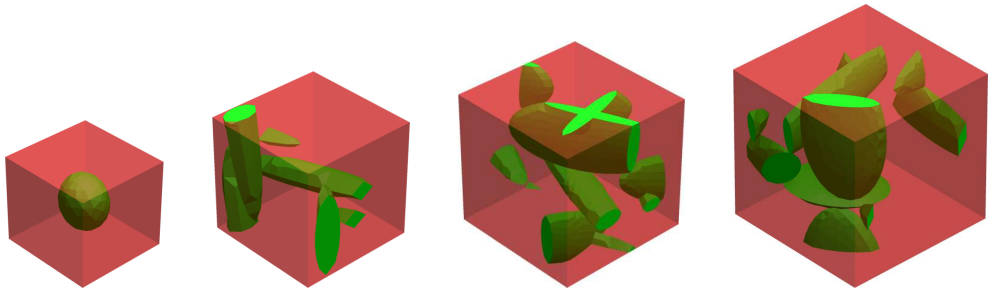

Figure 6.26: SSRVEs based on a minimization of $\mathcal{E}_{\text{II}}$ considering volume fraction, spectral density and lineal-path function with different numbers of inclusions $n_{\text{inc}} = 1, 2, 3, 4$ from left to right. Taken from Scheunemann et al. [128].

6.3.3 SSRVEs Based on Objective Function $\mathcal{E}_{III}$

In the third set, SSRVEs are constructed based on a minimization of $\mathcal{E}_{III}$, cf. Eq.(6.63). The resulting SSRVEs are shown in Fig. 6.27, the results of the statistical and mechanical comparison with the real microstructure are summarized in Tab. 6.7. Similarly as in the SSRVE sets presented in Section 6.3.1 and Section 6.3.2, an increased number of inclusions leads to a lower value of the objective function $\mathcal{E}_{III}$, which is related to a better fitting of the SSRVE to the real microstructure regarding the considered statistical measures. Similarly, the overall mechanical error $r_{\varnothing}$ decreases with an increased inclusion complexity.

Table 6.6: Results of SSRVEs based on volume fraction, spectral density and lineal-path function - values of objective function $\mathcal{E}_{\mathrm{II}}$, and individual least square functionals, number of tetrahedral elements n_{ele} and mechanical errors $\tilde{r}$ in % for the individual SSRVEs. Taken from Scheunemann et al. [128].

n_{inc}	$\mathcal{E}_{\mathrm{II}}/\ 10^{-2}$	$\mathcal{L}_{\mathrm{V}}/\ 10^{-4}$	$\mathcal{L}_{\mathrm{SD}}/\ 10^{-3}$	$\mathcal{L}_{\mathrm{LP}}/\ 10^{-4}$	n_{ele}	$\tilde{r}_x$	$\tilde{r}_z$	$\tilde{r}_{xy}$	$\tilde{r}_{yx}$	$\tilde{r}_{\varnothing}$
1	8.432	485.29	4.5	0.31	2851	5.3	4.6	5.5	5.5	5.24
2	0.98	32.07	3.5	0.031	5015	0.5	3.6	4.4	4.4	3.60
3	0.53	3.37	3.3	0.017	15714	0.2	2.4	1.2	1.1	1.45
4	0.38	3.11	2.33	0.014	19196	1.2	2.5	0.7	0.7	1.47

Here, the SSRVE with four inclusions results in an overall mechanical error of $r_{\varnothing} = 1.92\%$ with a number of $12,133$ elements used for the discretization. The mechanical error here is slightly higher than in the $\mathrm{SSRVE}^{\mathrm{LP}}_{\mathrm{best}}$, however, the lower number of finite elements is beneficial. The SSRVE with four ellipsoidal inclusions is denoted by $\mathrm{SSRVE}^{\mathrm{MA|MO}}_{\mathrm{best}}$ in a detailed comparison in Section 6.3.4.

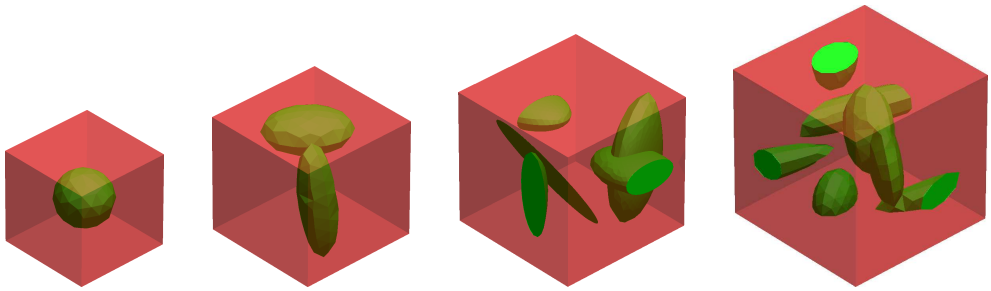

Figure 6.27: SSRVEs based on a minimization of $\mathcal{E}_{\mathrm{III}}$considering volume fraction, spectral density and Minkowski measures with different numbers of inclusions $n_{\mathrm{inc}} = 1, 2, 3, 4$ from left to right. Taken from Scheunemann et al. [128].

Table 6.7: Results of SSRVEs based on volume fraction, spectral density and Minkowski measures - values of objective function $\mathcal{E}_{\mathrm{III}}$, and individual least square functionals, number of tetrahedral elements n_{ele} and mechanical errors $\tilde{r}$ in % for the individual SSRVEs. Taken from Scheunemann et al. [128].

n_{inc}	$\mathcal{E}_{\mathrm{III}}/\ 10^{-2}$	$\mathcal{L}_{\mathrm{V}}/\ 10^{-4}$	$\mathcal{L}_{\mathrm{SD}}/\ 10^{-3}$	$\mathcal{L}_{\mathrm{MA}}/\ 10^{-2}$	$\mathcal{L}_{\mathrm{MO}}/\ 10^{-2}$	n_{ele}	$\tilde{r}_x$	$\tilde{r}_z$	$\tilde{r}_{xy}$	$\tilde{r}_{yx}$	$\tilde{r}_{\varnothing}$
1	6.47	0.001	4.56	5.88	1.27	2519	4.0	3.7	5.4	5.4	4.69
2	4.20	0.006	2.48	1.55	2.39	5358	3.4	1.9	3.4	3.5	3.12
3	1.95	1.65	3.3	0.39	1.2	10087	2.5	0.7	3.5	3.5	2.79
4	1.41	0.19	2.01	0.38	0.82	12133	3.3	1.1	1.1	1.2	1.92

6.3.4 Comparison of Microscale Stress and Optimization Effort

The average stresses computed over both phases of the real microstructures and SSRVEs in the previous sections give a first impression of the stress magnitudes. However, in many cases an insight into the specific stress distribution on the micro level is of interest. For this purpose, the stress in the individual phases is analyzed and compared for the "best" SSRVEs constructed, i.e. $\mathrm{SSRVE}^{\mathrm{best}}_{\mathrm{LP}}$ and $\mathrm{SSRVE}^{\mathrm{best}}_{\mathrm{MA|MO}}$. Therefore, volume averages of the stress for the ferrite phase and the martensite phase, individually, are

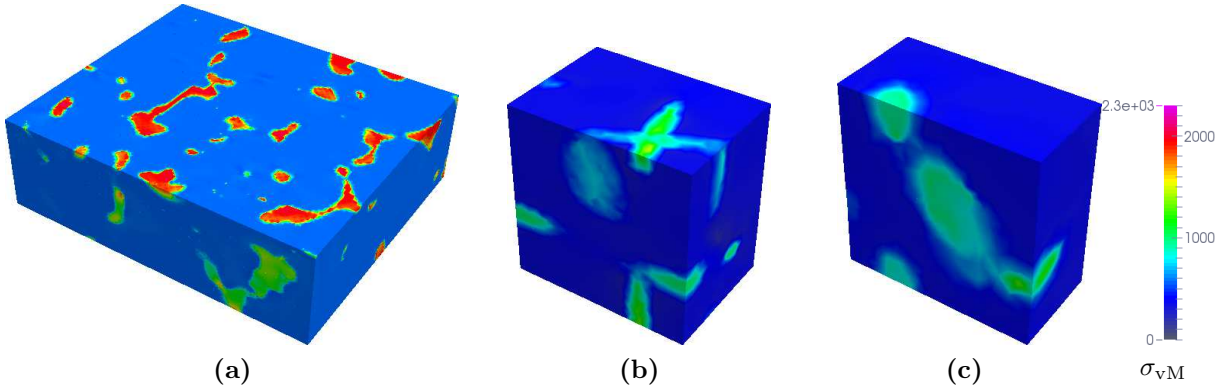

Figure 6.28: Von Mises stress σ_{vM} in MPa for tension test in x-direction showing the cross-section obtained from cutting through (a) the target structure (15.9 µm × 16.45 µm × 5.0 µm), (b) $\mathrm{SSRVE}^{\mathrm{best}}_{\mathrm{LP}}$ (4.3 µm × 4.3 µm × 4.3 µm) and (c) $\mathrm{SSRVE}^{\mathrm{best}}_{\mathrm{MA|MO}}$ (4.3 µm × 4.3 µm × 4.3 µm) and respective volume average values $\langle\sigma_{\mathrm{vM}}\rangle$. Taken from Scheunemann et al. [128].

computed. The individual error measures r_e^{fer} and r_e^{mar} are computed, describing the average stress deviation in the ferrite phase and the martensite phase, respectively. Here, $e = x, z, xy, yx$ denotes the respective virtual experiment. The results of this comparison is shown in Fig. 6.29-6.32. Furthermore averaged error measures $\tilde{r}_{\varnothing}^{\mathrm{fer}}$ and $\tilde{r}_{\varnothing}^{\mathrm{mar}}$ are defined for the ferrite phase and the martensite phase, which are summarized in Tab. 6.8. All error measures are computed in analogy to Section 6.2.4.

Good agreement is observed for the average stress in the ferrite phase, where the overall errors $\tilde{r}_{\varnothing}^{\mathrm{fer}}$ for both "best" SSRVEs are lower than 1%. Only a minor advantage is observed for $\mathrm{SSRVE}^{\mathrm{best}}_{\mathrm{MA|MO}}$ with 0.62% compared with 0.85% for $\mathrm{SSRVE}^{\mathrm{best}}_{\mathrm{LP}}$. In the martensite phase, larger deviations are observed, where the averaged errors $\tilde{r}_{\varnothing}^{\mathrm{mar}}$ are 13.38% for $\mathrm{SSRVE}^{\mathrm{best}}_{\mathrm{LP}}$ and 17.69% for $\mathrm{SSRVE}^{\mathrm{best}}_{\mathrm{MA|MO}}$, respectively, showing an advantage for the former. This discrepancies are not observable in the averaged errors considering both phases, $\tilde{r}_{\varnothing}$, since the volume fraction of the martensite is much lower than the one of ferrite and thus the significance of the martensite microscopic response is reduced. The discrepancies in the conformability of the average stress in the martensite phase are associated with the different treatment of boundary conditions for the SSRVEs and the real microstructure. While periodic boundary conditions are applied in the case of the SSRVEs, linear displacement boundary conditions are used in the case of the real microstructure due to the non-periodicity of the data. These boundary conditions lead to a stiffening effect occurring predominantly in the stiffer martensite phase. Fig. 6.28 illustrates this circumstance, where the von Mises stress σ_{vm} is shown for the tension test in x-direction for the real microstructure, $\mathrm{SSRVE}^{\mathrm{best}}_{\mathrm{LP}}$ and $\mathrm{SSRVE}^{\mathrm{best}}_{\mathrm{MA|MO}}$. A cut through each structure shows the concentration of high stresses in the real microstructure close to the boundary, which cannot be seen in the SSRVEs. Based on this comparison, $\mathrm{SSRVE}^{\mathrm{best}}_{\mathrm{LP}}$ will be used in the applications presented in Section 7.

Considering the computational effort necessary for the construction of SSRVEs based on the different statistical measures, large differences can be seen. The objective functions $\mathcal{E}_{II}$ and $\mathcal{E}_{III}$ lead to appropriate SSRVEs in terms of their ability to resemble the

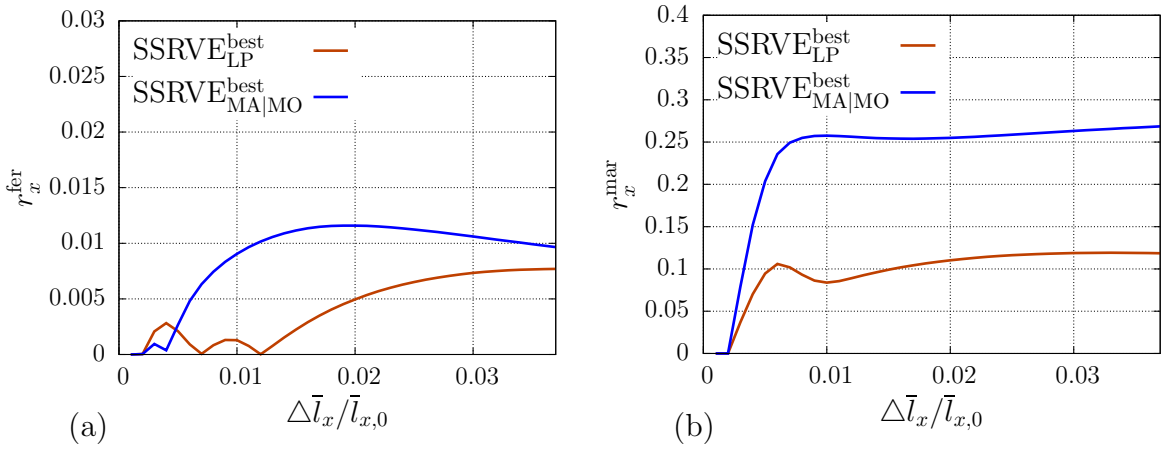

Figure 6.29: Deviation r_x of averaged stress in x-direction of SSRVE$^{\text{best}}_{\text{LP}}$ and SSRVE$^{\text{best}}_{\text{MA|MO}}$ with (a) r_x^{fer} for ferrite and (b) r_x^{mar} for martensite. Taken from Scheunemann et al. [128].

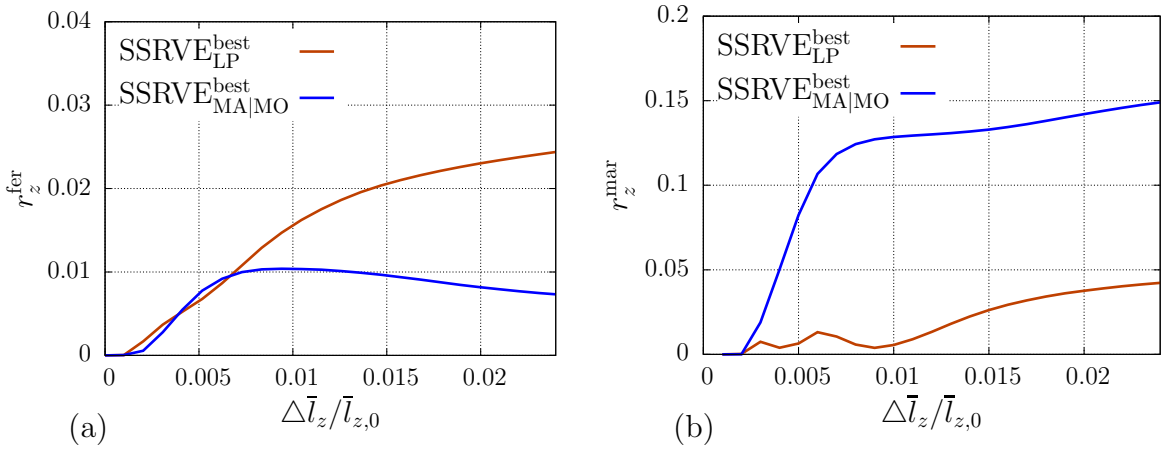

Figure 6.30: Deviation of averaged stress in z-direction of SSRVE$^{\text{best}}_{\text{LP}}$ and SSRVE$^{\text{best}}_{\text{MA|MO}}$ with (a) r_z^{fer} for ferrite and (b) r_z^{mar} for martensite. Taken from Scheunemann et al. [128].

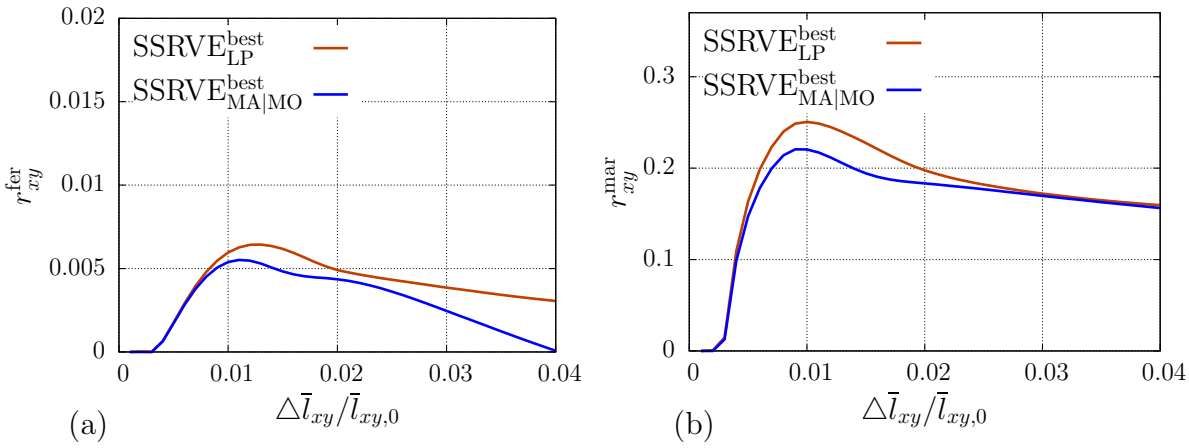

Figure 6.31: Deviation of averaged stress in shear test xy of SSRVE$^{\text{best}}_{\text{LP}}$ and SSRVE$^{\text{best}}_{\text{MA|MO}}$ with (a) r_{xy}^{fer} for ferrite and (b) r_{xy}^{mar} for martensite. Taken from Scheunemann et al. [128].

mechanical behavior of the real microstructure and thus will be compared further.

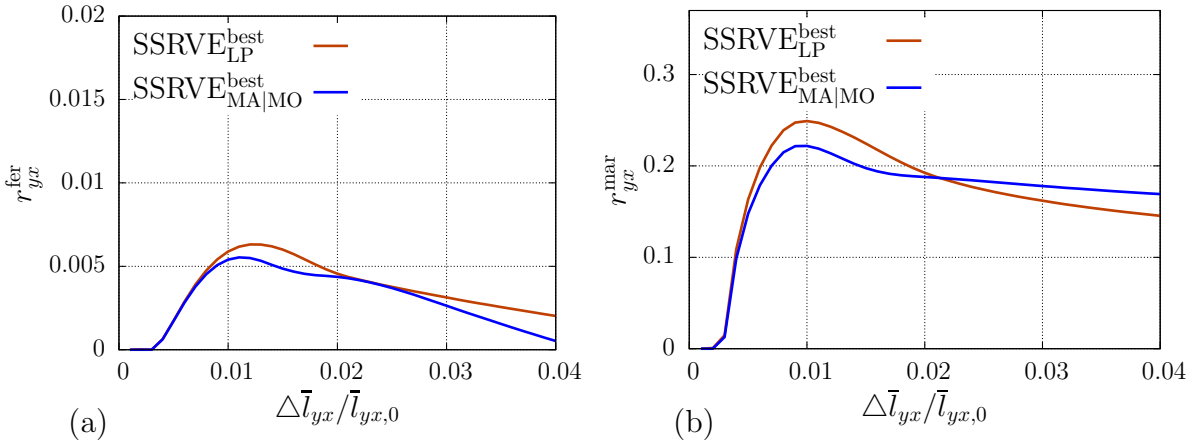

Figure 6.32: Deviation of averaged stress in shear test yx of SSRVE$^{\text{best}}_{\text{LP}}$ and SSRVE$^{\text{best}}_{\text{MA|MO}}$ with (a) r^{fer}_{yx} for ferrite and (b) r^{mar}_{yx} for martensite. Taken from Scheunemann et al. [128].

Table 6.8: Comparison of stresses on microscale for individual phases in SSRVE$^{\text{best}}_{\text{LP}}$ and SSRVE$^{\text{best}}_{\text{MA|MO}}$ evaluated for all four virtual experiments. Taken from Scheunemann et al. [128].

Ferrite	$\tilde{r}^{\text{fer}}_{x}$ in %	$\tilde{r}^{\text{fer}}_{z}$ in %	$\tilde{r}^{\text{fer}}_{xy}$ in %	$\tilde{r}^{\text{fer}}_{yx}$ in %	$\tilde{r}^{\text{fer}}_{\varnothing}$ in %
SSRVE$^{\text{best}}_{\text{LP}}$	0.43	1.55	0.40	0.36	0.85
SSRVE$^{\text{best}}_{\text{MA|MO}}$	0.90	0.75	0.29	0.30	0.62
Martensite	$\tilde{r}^{\text{mar}}_{x}$ in %	$\tilde{r}^{\text{mar}}_{z}$ in %	$\tilde{r}^{\text{mar}}_{xy}$ in %	$\tilde{r}^{\text{mar}}_{yx}$ in %	$\tilde{r}^{\text{mar}}_{\varnothing}$ in %
SSRVE$^{\text{best}}_{\text{LP}}$	9.94	2.08	17.82	17.19	13.38
SSRVE$^{\text{best}}_{\text{MA|MO}}$	23.59	11.36	16.56	16.10	17.69

Table 6.9: Comparison of estimated optimization time for individual phases in SSRVE$^{\text{best}}_{\text{LP}}$ and SSRVE$^{\text{best}}_{\text{MA|MO}}$ evaluated for all four virtual experiments. Taken from Scheunemann et al. [128].

t_{LP}/s	$t_{\text{MA|MO}}$	$t_{\text{LP}}\,/\,t_{\text{MA|MO}}$
5.98	0.0031	1,929.03

The time needed for one evaluation of the objective functions strongly depends on the statistical measures which are evaluated and the inclusion morphology. Especially for the lineal-path function, the evaluation times can greatly differ, increasing with the size of inclusions. For the Minkowski measures, the number of inclusions is more relevant than the individual size. For a decent comparison of the evaluation time of the objective functions, the evaluation time for the best SSRVE candidate of every generation is summed up and divided by the number of generations to identify the SSRVE. These average evaluation times t_{LP} and $t_{\text{MA|MO}}$ are listed in Tab. 6.9 together with their ration $t_{\text{LP}}\,/\,t_{\text{MA|MO}}$. With an estimated factor of computation time of 2000, the objective function based on Minkowski functionals offers a large speed-up compared with the one based on the lineal-path function.

6.4 SSRVEs as Substructures of the Real Microstructure[2.)]

A natural choice of an SSRVE would be choosing a substructure of the RVE which is still able to resemble the macroscopic response of the complete RVE adequately. Therefore, SSRVEs are obtained as substructures from the real microstructure by comparing the volume fraction $\mathcal{P}_V$, internal surface density $\mathcal{P}_S$, integral of mean curvature $\mathcal{P}_M$, spectral density $\mathcal{P}_{SD}$ and lineal-path function $\mathcal{P}_{LP}$. The objective function then reads

$$\mathcal{E}_{\text{sub}} := \omega_{\text{V}}\,\mathcal{L}_{\text{V}} + \omega_{\text{S}}\,\mathcal{L}_{\text{S}} + \omega_{\text{M}}\,\mathcal{L}_{\text{M}} + \omega_{\text{SD}}\,\mathcal{L}_{\text{SD}} + \omega_{\text{LP}}\,\mathcal{L}_{\text{LP}}\,. \tag{6.74}$$

Note that an analysis of different weighting factors was not performed here. Now, the substructure with the lowest summed error is sought, which is then the SSRVE based on substructures. Therefore, different sizes were considered, namely cubic structures with an edge length of $a = 1.25\,\mu\text{m}, 2.5\,\mu\text{m}$ and $5\,\mu\text{m}$. The obtained substructures are shown in Fig. 6.33. Tab. 6.10 shows the results from the comparison of statistical errors.

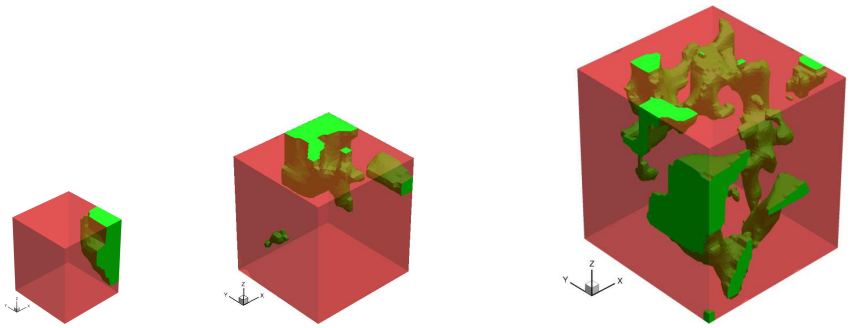

Figure 6.33: Construction of SSRVE based on substructuring: (a) SSRVE substructure with $a = 1.25\mu\text{m}$, (b) SSRVE substructure with $a = 2.5\mu\text{m}$ (scaled view) and (c) SSRVE substructure with $a = 5.0\mu\text{m}$ (scaled view). Taken from Balzani et al. [9]

Table 6.10: Error of statistical measures for SSRVEs based on substructuring. Adapted from Balzani et al. [9]

SSRVE	$\mathcal{E}_{\text{sub}}$ $[10^{-2}]$	$\mathcal{L}_{\text{V}}$ $[10^{-4}]$	$\mathcal{L}_{\text{S}}$ $[10^{-3}]$	$\mathcal{L}_{\text{M}}$ $[10^{-3}]$	$\mathcal{L}_{\text{SD}}$ $[10^{-3}]$	$\mathcal{L}_{\text{LP}}$ $[10^{-4}]$	n_{ele}
ω	-	1	1	1	1	1000	-
$a = 1.25\mu\text{m}$	12.83	77.0	1.9	6.0	12.0	1.0	5 695
$a = 2.5\mu\text{m}$	2.33	3.0	0.36	0.1	4.6	0.2	42 279
$a = 5.0\mu\text{m}$	0.78	1.3	1.2	2.4	1.7	0.024	707 676

It is not surprising to find that the substructure with the smallest dimensions leads to the largest error in the statistical measures while the one with the largest dimensions achieves the lowest error, since it allows the largest portion of the microstructure to be resembled. However, the latter requires a large number of elements for the discretization, which disqualifies it as a suitable SSRVE candidate due to the arising computational effort. For the mechanical comparison, only one tension and shear test are evaluated.

[2.)] These results were first published in Balzani et al. [9].

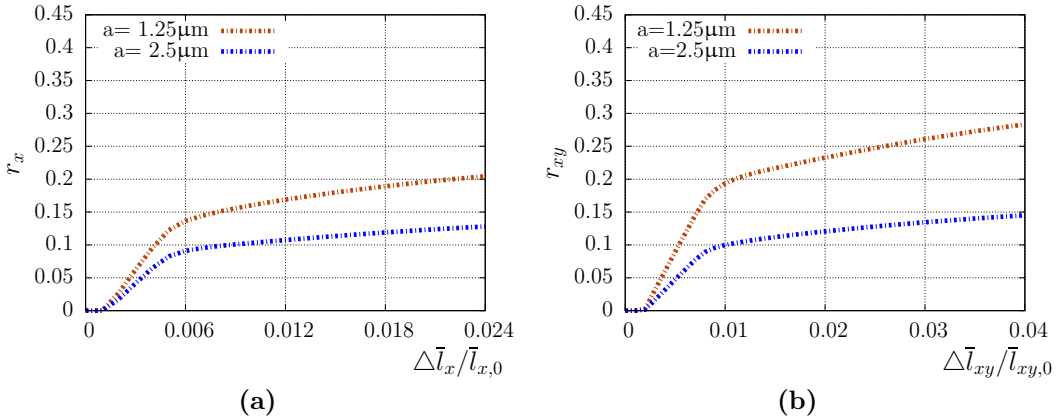

Figure 6.34: Error of mechanical response of SSRVEs based on substructuring in virtual experiments: (a) tension test $[x]$ and (b) shear test $[xy]$.

Table 6.11: Error in % of mechanical response of SSRVEs based on substructuring.

SSRVE	$\tilde{r}_x$	$\tilde{r}_{xy}$	$\tilde{r}$
$a = 1.25\,\mu\text{m}$	14.6	20.5	17.80
$a = 2.5\,\mu\text{m}$	9.4	10.6	10.02

Comparing the mechanical response of the two smaller substructures, the substructure with $a = 2.5\mu\text{m}$ reaches a smaller overall mechanical error, although it is still large compared to the errors of the SSRVEs with artificial inclusion morphology. It can be seen from Fig. 6.33, that both SSRVEs constructed as substructures are governed by a large inclusion which does not fullfill periodicity conditions on the boundary. Linear displacement boundary conditions are applied in the computation in this case. These are known to be too stiff if an inclusion with higher stiffness than the matrix is located at the boundary, which is the case here. This influence is considerably large here due to the small size of the structures, where boundary effects have a higher influence. Due to the large error in the mechanical comparison and the relatively large number of elements needed for a discretization, the SSRVEs obtained as substructures cannot compete with the ones generated using an artificial inclusion morphology.

7 Applications of SSRVEs

In the following, the ability of SSRVEs to describe the complex material behavior of DP steel is investigated. Therefore, the Bauschinger effect as well as macroscopic yield surfaces are compared for an SSRVE and the real DP steel microstructure. Finally, a macroscopically inhomogeneous FE^2 simulation of a perforated plate using an SSRVE on the microscale is carried out and compared with a purely macroscopic representation of DP steel.

7.1 Comparison of Bauschinger Effect[3.)]

The yield behavior of steel shows specific characteristics, which cannot be revealed in monotonic, homogeneous deformation processes. One example is the Bauschinger effect, cf. Bauschinger [18], which is characterized by an earlier re-yielding during reversed loading in, e.g., tension-compression tests. This effect is related to kinematic hardening in the material and can be connected to an interaction of the constituents in the micro-heterogeneous material: due to the heterogeneous structure, stresses introduced during a first loading cannot be fully reversed during unloading. This is the case due to, e.g., the phase contrast, when some regions have been plastically deformed and restrict the unloading of regions which are still in the elastic regime. In a macroscopically unloaded state, the material still contains some stressed regions. This prestressed state results in the shift of macroscopic yield strength during reversed loading. Fig. 7.1 illustrates the Bauschinger effect schematically using a stress-strain curve of a tension-compression test.

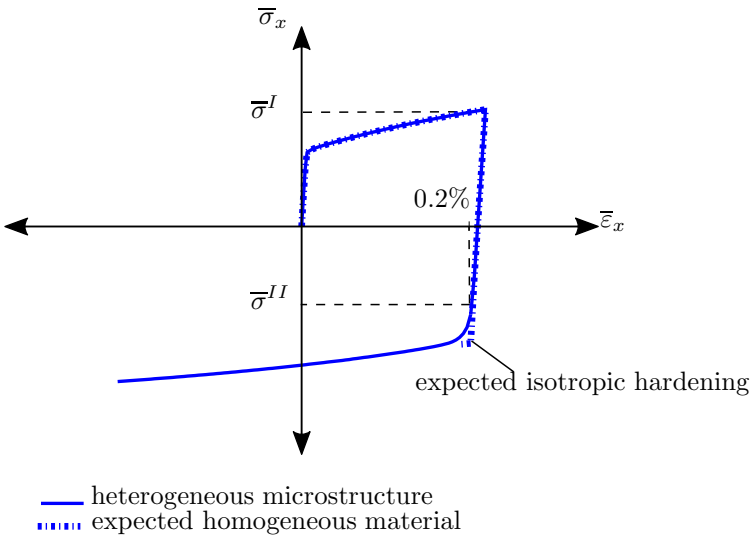

Figure 7.1: Schematic illustration of Bauschinger effect visible in the reversed loading in a tension-compression test in x-direction.

An approach describing the Bauschinger effect in ferritic steel is presented in Kraska et al. [76] where the above described effect is solely introduced by the microstructural interaction of the granular material. No explicit kinematic hardening is

[3.)] The results in this section were first published in Scheunemann et al. [129].

implemented in the applied material model. The Bauschinger effect influences other phenomena, such as spring-back, where large geometrical changes in a construction part are observed after the release of forces in the forming tool. This effect is especially pronounced in sheet metal forming, such as stamping or deep drawing, where DP steel is applied frequently.

In the following, the ability of SSRVEs to resemble the Bauschinger effect in DP steel is shown. Similar to the observations in Kraska et al. [76], the effect solely due to the interaction of the phases is considered. The individual phases are described using the material model with an exponential isotropic hardening law with superimposed linear hardening, cf. Section 6.2.4, whereby no kinematic hardening is introduced by this material model. A virtual tension-compression test in x-direction is carried out for the real microstructure and the SSRVE, here the $\text{SSRVE}_{\text{LP}}^{\text{best}}$ constructed in Section 6.3.2 is used. A comparison with an RVE, denoted by $\text{RVE}_{\text{sphere}}$, with a spherical inclusion of matching phase fraction compared to the real microstructure, is made to range the performance of the SSRVE. Note that a coarser discretization of the real microstructure is used here, containing 182180 10-noded tetrahedral finite elements. For the SSRVE a discretization with 12,811 elements was utilized. The load path is illustrated in Fig. 7.2 with a tensile and compressive deformation $\overline{F}_{11} = 0.05$ and $\overline{F}_{11} = -0.05$.

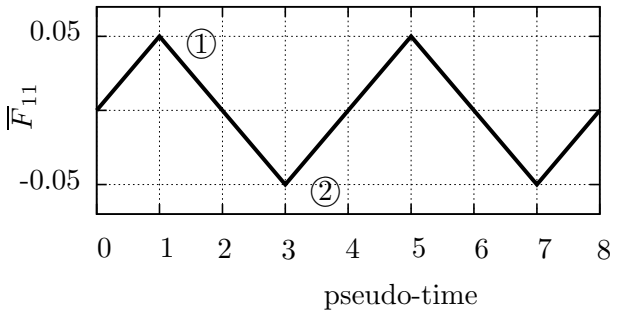

Figure 7.2: Deformation path for cyclic tension-compression test.

The stress-strain curves are shown in Fig. 7.3 for all three structures. Note that only one cycle of tension and compression is computed for the real microstructure. Even though a coarser discretization is used, the computation is limited by technical resources, such as available computation times. This emphasizes the benefit in the use of SSRVEs, which increase computational efficiency drastically. Two full cycles including unloading are computed for the SSRVE and the $\text{RVE}_{\text{sphere}}$. For the first cycles, a good approximation by the SSRVE can be seen, whereas $\text{RVE}_{\text{sphere}}$ does not reach the maximal stress during first loading of the real microstructure.

For a quantification of the Bauschinger effect, different definitions of a so-called *Bauschinger factor* exist. Here, the Bauschinger factor is defined by

$$f_{\text{B}} = \frac{\overline{\sigma}^{\text{I}} - \left|\overline{\sigma}^{\text{II}}\right|}{\overline{\sigma}^{\text{I}}}, \tag{7.1}$$

for a tension-compression test. Therein, $\overline{\sigma}^{\text{I}}$ defines the macroscopic stress in loading direction at full tensile load and $\overline{\sigma}^{\text{II}}$ defines the stress level in loading direction at re-yielding. The latter value is obtained considering a 0.2% offset in macroscopic strain after macroscopic unloading at $\overline{\sigma}_x = 0$. Both values are indicated in Fig. 7.1. If no Bauschinger

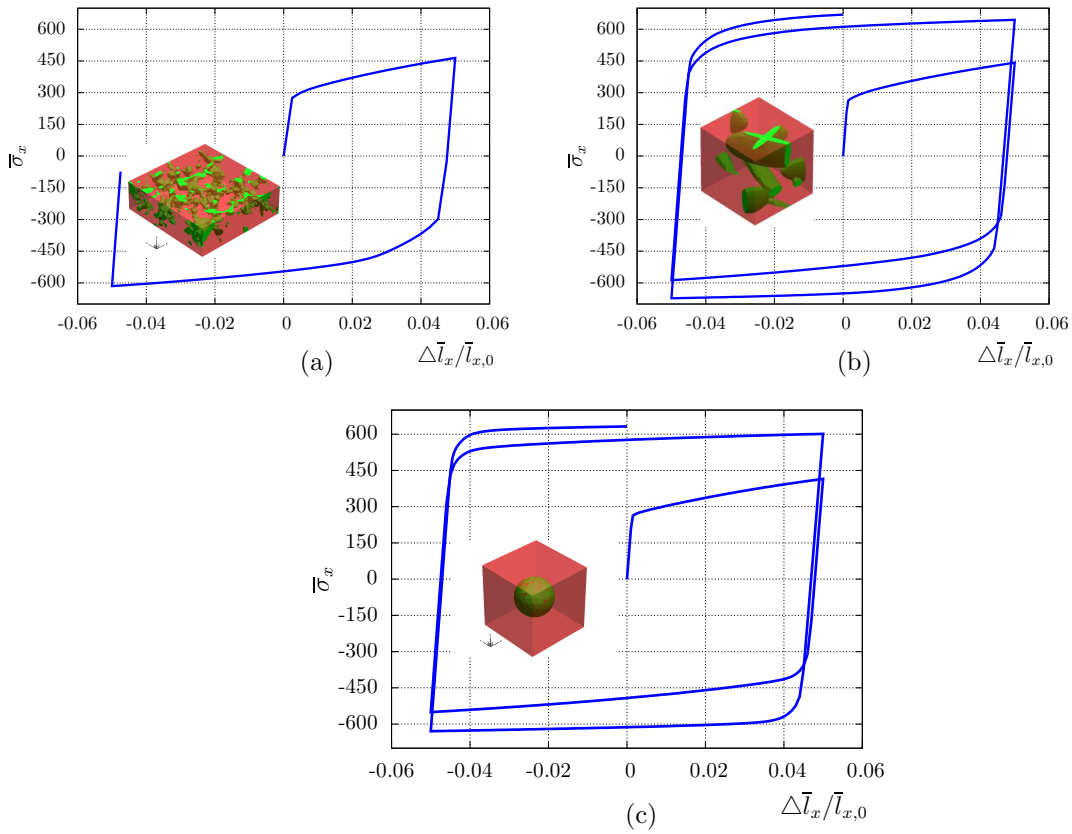

Figure 7.3: Stress-strain curve for virtual cyclic tension-compression test in x-direction for (a) real microstructure, (b) $\text{SSRVE}_{\text{LP}}^{\text{best}}$ and (c) $\text{RVE}_{\text{sphere}}$.

effect is observed, one obtains $\overline{\sigma}^{\text{II}} = -\overline{\sigma}^{\text{I}}$, thus the yield strength is the same during reversed loading. The virtual mechanical tests are computed using the same steps as in Section 6.2.4, where a macroscopic deformation state is applied on the RVE which resembles the desired loading case. The Bauschinger factor computed during the first cycle of reloading for the real microstructure, SSRVE and $\text{RVE}_{\text{sphere}}$ are given in Tab. 7.1. A more pronounced Bauschinger effect can be observed in the real microstructure, the SSRVE reaches a level of 66% of the Bauschinger effect measured in the real microstructure. The SSRVE shows superior performance compared with the Bauschinger factor calculated for $\text{RVE}_{\text{sphere}}$, which shows a Bauschinger factor smaller than 50% of the one found in the real microstructure.

Table 7.1: Analysis of Bauschinger factor f_{B}.

	$\overline{\sigma}^{\text{I}}$ in MPa	$\overline{\sigma}^{\text{II}}$ in MPa	f_{B}
real microstructure	464.32	-229.64	0.5054
SSRVE	441.88	-294.25	0.334
$\text{RVE}_{\text{sphere}}$	415.25	-318.34	0.233

More insight into the yield behavior is obtained with a comparison of the equivalent plastic strains $\varepsilon_{\text{pl,v}}$ on the microscale in Fig. 7.4. The equivalent plastic strains are defined by

$$\varepsilon_{\text{pl,v}} = \sqrt{2/3\,\boldsymbol{\varepsilon}_{\text{D}}^{\text{p}} : \boldsymbol{\varepsilon}_{\text{D}}^{\text{p}}}\,, \tag{7.2}$$

where $\boldsymbol{\varepsilon}_{\mathrm{D}}^{\mathrm{p}}$ represents the deviatoric part of the plastic strain tensor. The distribution of $\varepsilon_{\mathrm{pl,v}}$ in the real microstructure and the SSRVE is shown at two different states of loading, $\overline{F}_{11} = 0.05$ (indicated by point ①) and $\overline{F}_{11} = -0.05$ (indicated by point ②) during the first cycle, respectively. These points correspond to full tensile loading and full compressive loading, the respective states are marked in the load path in Fig. 7.2. A similar distribution at both states in the microstructure and the SSRVE can be seen. The volumetric average of equivalent plastic strain is shown in Tab. 7.2 for the two indicated points on the load curve. It can be seen that the SSRVE only shows a small deviation with respect to the volumetric average at these points. One can conclude that the SSRVE can approximate the equivalent plastic strains in the real microstructure well.

Table 7.2: Comparison of $\langle \varepsilon_{\mathrm{pl,v}} \rangle$ for real microstructure and $\mathrm{SSRVE}_{\mathrm{LP}}^{\mathrm{best}}$.

	$\langle \varepsilon_{\mathrm{pl,v}} \rangle$	
$\overline{F}_{11}$	real microstructure	$\mathrm{SSRVE}_{\mathrm{LP}}^{\mathrm{best}}$
0.05	0.0480	0.0487
-0.05	0.146	0.148

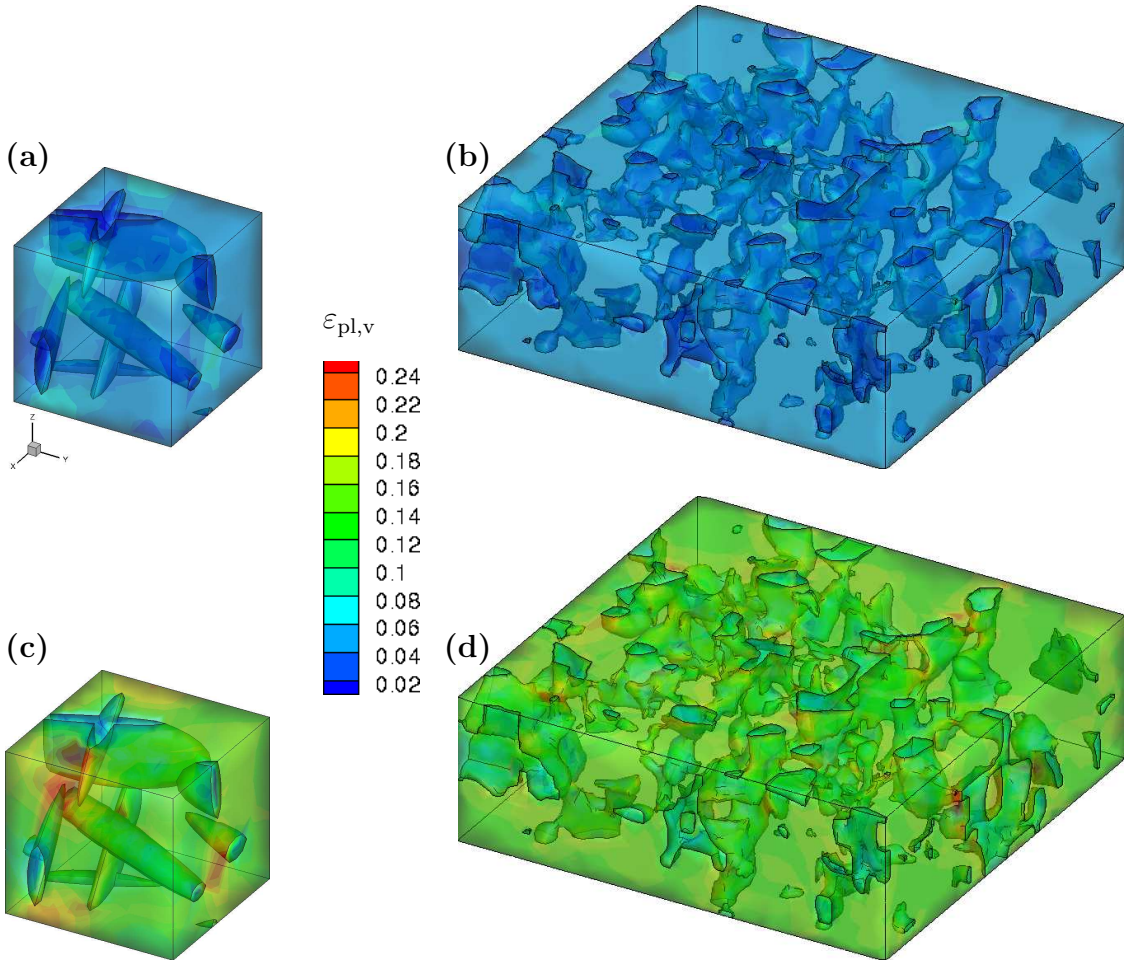

Figure 7.4: Distribution of equivalent plastic strain in the microstructure in deformation state $F_{11} = 0.05$ at ① for (a) SSRVE and (b) real microstructure and in deformation state $\overline{F}_{11} = -0.05$ at ② for (c) SSRVE and (d) real microstructure.

7.2 Comparison of Macroscopic Yield Surfaces[4.)]

The SSRVEs and the real microstructure are compared regarding their macroscopic yield behavior described by yield surfaces in the following. Therefore, yield surfaces in the $\overline{\sigma}_1$-$\overline{\sigma}_3$ plane are computed using virtual uniaxial tension- and compression tests in x- and z-direction as well as virtual biaxial tension and compression tests with $\overline{\sigma}_\mathrm{x} = \overline{\sigma}_\mathrm{z}$ and $\overline{\sigma}_\mathrm{x} = -\overline{\sigma}_\mathrm{z}$. A total number of 8 virtual tests is computed. The tests are carried out as described previously, prescribing a macroscopic deformation state which represents the desired virtual test on the respective RVE (or real microstructure). Then, suitable volume averages of the microscopic quantities are computed to obtain the macroscopic response. As in the previous section, $\mathrm{RVE}_\mathrm{sphere}$ is considered to range the results of the SSRVE in the comparison with the real microstructure. Again, periodic boundary conditions are used for the SSRVE and $\mathrm{RVE}_\mathrm{sphere}$ and linear displacement boundary conditions for the real microstructure due to its lack of periodicity. The same discretizations for the real microstructure and the SSRVE are used as in the previous section.

The 2D yield surface is described by an isoline of states of equivalent plastic strain in the 2D stress space, therein characterizing stress states of equal plasticization. In the literature, there exist different analytical yield functions, which aim at describing the direction dependent yield behavior of materials. An overview can be found in, e.g., Habraken [49]. The volumetric average of equivalent plastic strains is defined by

$$\langle \varepsilon_\mathrm{pl,v} \rangle = \frac{1}{V} \int_V \varepsilon_\mathrm{pl,v} \, \mathrm{d}V \,, \tag{7.3}$$

which is used as a comparative measure for the computation of macroscopic yield surfaces here. Note that the volume average of equivalent plastic strains is not equal to the effective macroscopic equivalent plastic strains. Fig. 7.5a shows the yield surfaces obtained at a value of $\langle \varepsilon_\mathrm{pl,v} \rangle = 0.01$ and Fig. 7.5b compares the yield surfaces with $\langle \varepsilon_\mathrm{pl,v} \rangle = 0.05$.

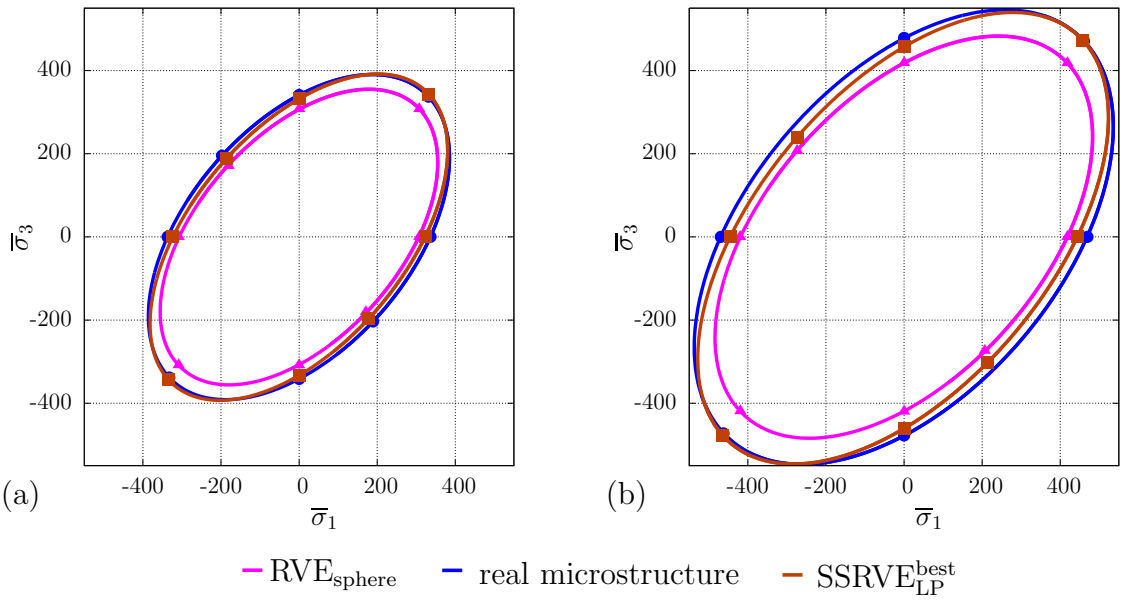

Figure 7.5: Comparison of yield surfaces computed for the real microstructure, $\mathrm{RVE}_\mathrm{sphere}$ and $\mathrm{SSRVE}_\mathrm{LP}^\mathrm{best}$ for (a) $\langle \varepsilon_\mathrm{pl,v} \rangle = 0.01$ and (b) $\langle \varepsilon_\mathrm{pl,v} \rangle = 0.05$.

[4.)] The results were first published in Scheunemann et al. [129].

Linear interpolation is used to obtain the stress state at equal values of equivalent plastic strains. An ellipse is fitted to the data of the obtained stress states from the biaxial virtual tests using a least-square fit. A comparison of the yield surfaces for the different states of plastic strain shows that the SSRVE is able to approximate the yield surfaces of the real microstructure, while the yield surface of $\mathrm{RVE}_{\mathrm{sphere}}$ differs significantly. This is especially the case in biaxial tension ($\sigma_1 = \sigma_3$) and the respective compression loading. It emphasizes the importance of the influence of the microstructure in the description of the macroscopic yield behavior of the underlying real microstructure.

7.3 Perforated Plate under Tensile Load

In the following, the mechanical response of a perforated plate under tensile load is analyzed using the presented modeling approach for a DP steel based on SSRVEs. A purely macroscopic FE calculation considering the DP steel as a homogeneous material is compared with an FE^2-simulation considering the DP steel microstructure using $SSRVE_{LP}^{best}$ as an RVE on the microscale. It has been shown in the previous sections that the SSRVE is able to describe the mechanical behavior of the DP steel microstructure well. With its application instead of the real microstructure, the efficiency of the simulation can be increase drastically. In Balzani et al. [10], it is shown that the application of an SSRVE reduces the computation time drastically, where a factor of 200 is reported for the simulation of 2D real microstructure and SSRVE. Furthermore, data storage can be reduced by 95%, cf. Brands [22]. Due to symmetry, only a quarter of the plate is considered in the simulation. Fig. 7.6 shows the dimensions of a quarter of the perforated plate as well as the supporting conditions. On the planar face at $x = 5$, indicated in green, a displacement $u_x = 0.5$ is applied in x-direction, which corresponds to 10% strain in the plate. The supporting conditions for the quarter of the plate are chosen such that the displacement in y-direction is prohibited for all points with $y = 0$, and displacement in x-direction is prohibited for all points with $x = 0$ (both indicated as blue planes). Additionally, displacement in z-direction is prohibited at the coordinates $(5, 0, 0.5)$.

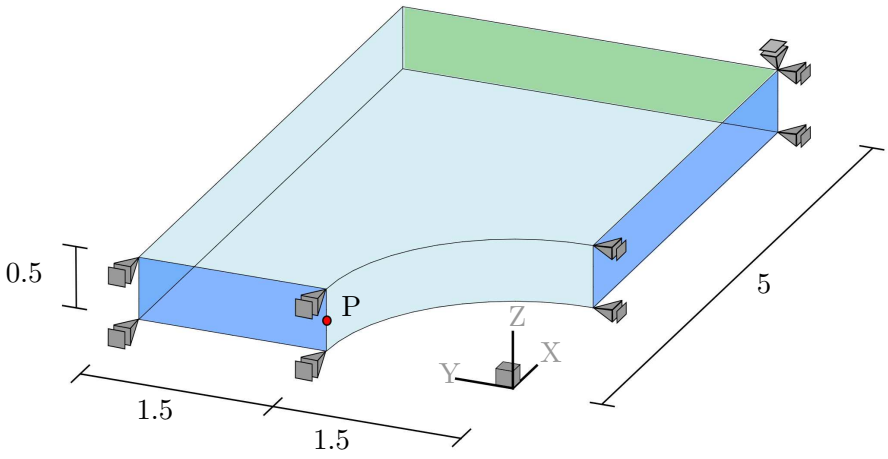

Figure 7.6: Sketch of perforated plate and supporting conditions. Point P is used for mesh convergency study.

7.3.1 Convergence Study

First, an analysis is carried out regarding the convergence of von Mises stress σ_{vM} in the region of stress concentration comparing different mesh densities. Therefore, a nonlinear elastic material model is applied, based on the free energy function in Eq. (4.18). The point P with the coordinates $(0, 3, 0.25)$ (marked in Fig. 7.6) is located in the center of the region of stress concentration, thus it is considered in the analysis of convergency. The result of the convergency study is shown in Fig. 7.7a, where four different meshes with 279, 1169, 6308 and 13800 10-noded tetrahedral elements are compared. Convergency is observed for a mesh using 6308 elements, which is then used in the subsequent simulations.

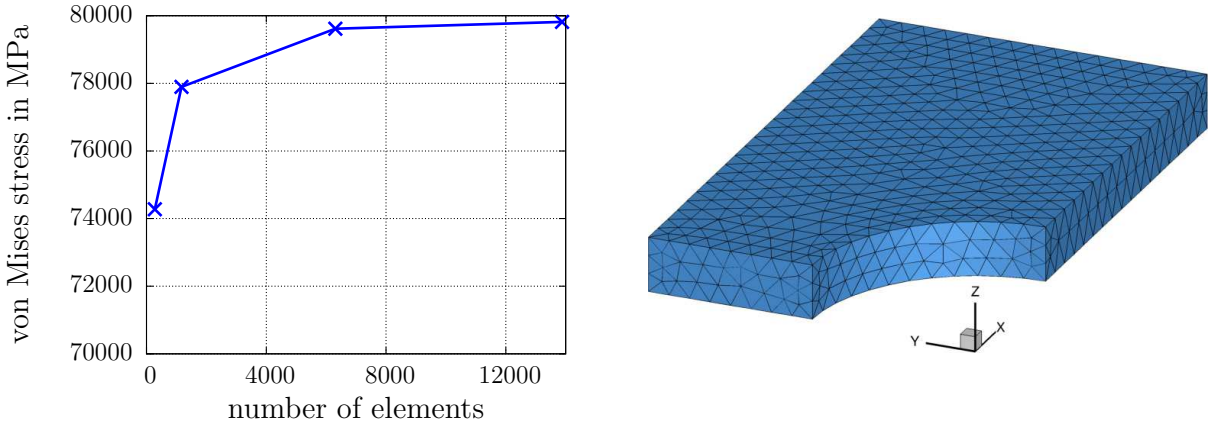

(a) **(b)**

Figure 7.7: (a) Convergency of von Mises stress at point P, see Fig. 7.6. (b) Finite element mesh of perforated plate with 6308 elements.

7.3.2 Purely Macroscopic FE-Simulation

For the purely macroscopic FE calculation of the perforated plate, DP steel is considered as a homogeneous material. The material model for finite J_2 plasticity presented in Section 4.2 is applied, using the plastic strain energy function given in Eq. (6.69). The material parameters given in Balzani et al. [10] are used, which are summarized in Tab. 7.3. These were obtained from fitting the results of three virtual experiments using a purely macroscopic material model to FE^2-simulations based on a real microstructure as an RVE. The fitting was carried out using virtual tension and shear tests.

Table 7.3: Material parameters for DP steel in purely macroscopic FE calculation, cf. Balzani et al. [10].

Lame constant	λ	115,384.6 MPa
shear modulus	μ	76,923.1 MPa
initial yield strength	y_0	230.0 MPa
saturation yield strength	y_∞	436.0 MPa
exponential hardening parameter	η	16.7
slope of linear hardening	h	7.0 MPa

7.3.3 FE^2-Simulation

For the FE^2-simulation of the perforated plate, the macroscopic mesh from the purely macroscopic computation is used. In order to lower the computational effort, a consideration of the microscale via the attachment of an RVE is only made in the region of relevant plastic activity. Therefore, the elements in the according region are detected from the purely macroscopic computation by checking whether $\varepsilon_{\mathrm{pl,v}}$ exceeds a certain

threshold. The region which will be treated using a multiscale simulation is described by 604 elements. The two regions are shown in Fig. 7.8. Red indicates the macroscopic elements in which plastic strains exceeds the threshold, thus, in which an RVE is attached to represent the microscale. The remaining region (blue) is treated using a finite J_2 plasticity model with the material parameters given in Tab. 7.3 in a single scale computation. The simulation is performed on the supercomputer *magnitUDE*, using 3021 cores, where one core is used per gausspoint, i.e., the microscopic boundary value problem, in the relevant region on the macroscale (604 finite elements with 5 gauss points each) and one core is used for the macroscopic problem. The simulations are carried out using FEAP, cf. Taylor [161] with an embedded self-written FE^2 environment, where the solution of the microscopic boundary value problem is achieved using the multiprocessing parallel direct sparse solver *Pardiso*, cf. Schenk et al. [126], which is provided by the Intel Math Kernel library in Version 2017.1.132. The results shown here correspond to the state of 7% of the applied load, thus $u_x = 0.0035$. For a comparison, the respective loading state is also considered for the purely macroscopic simulation. The state at the microscale is captured throughout the computation at specific points in the macroscopic boundary value problem. The locations are shown in Fig. 7.9.

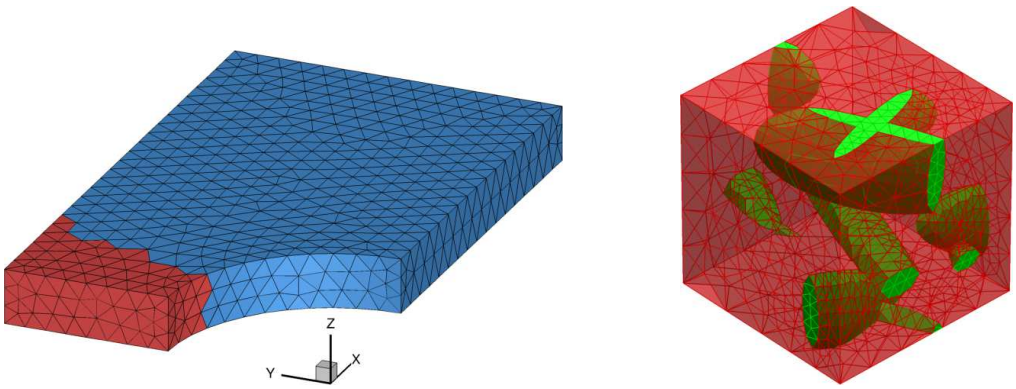

Figure 7.8: (a) Macroscopic FE mesh with two separate regions: red elements indicate region where an RVE is attached in the FE^2-scheme, blue marks elements which are treated by a single scale macroscopic simulation. (b) Finite element mesh of $\text{SSRVE}_{\text{LP}}^{\text{best}}$ which is used as an RVE in the microscale simulation.

7.3.4 Comparison of Purely Macroscopic and FE^2-Simulation

The results of the purely macroscopic simulation are compared with the results of the FE^2-simulation of the perforated plate. Fig. 7.10 shows the distribution of macroscopic von Mises stress $\overline{\sigma}_{\text{vM}}$ for both simulations.

While the overall distribution of $\overline{\sigma}_{\text{vM}}$ is comparable, deviations can be seen at the corner of the perforation, where the region of high stress is found. The purely macroscopic simulation shows a smaller region related to high stresses in the range of $\sigma_{\text{vM}} \geq 350$ MPa than the multiscale simulation. The maximal values arise to $\overline{\sigma}_{\text{vM}} = 362.52$ MPa in the purely macroscopic simulation and $\overline{\sigma}_{\text{vM}} = 403.59$MPa in the multiscale simulation, thus a wider range of stress values is found in the multiscale simulation.

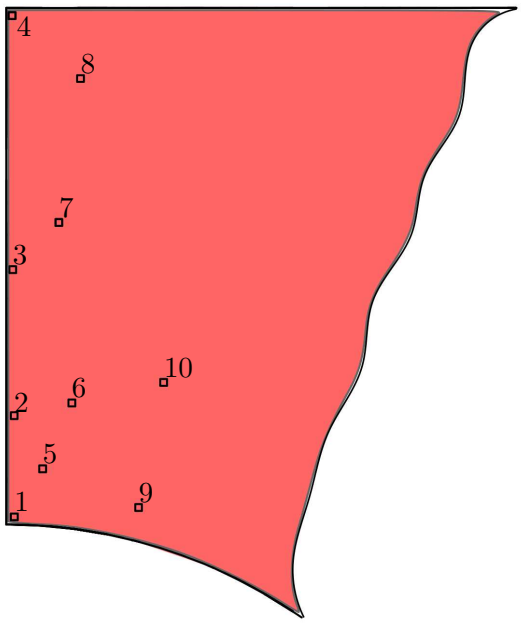

Figure 7.9: Location of the respective points in a projection to the xy-plane which are chosen for microscale output.

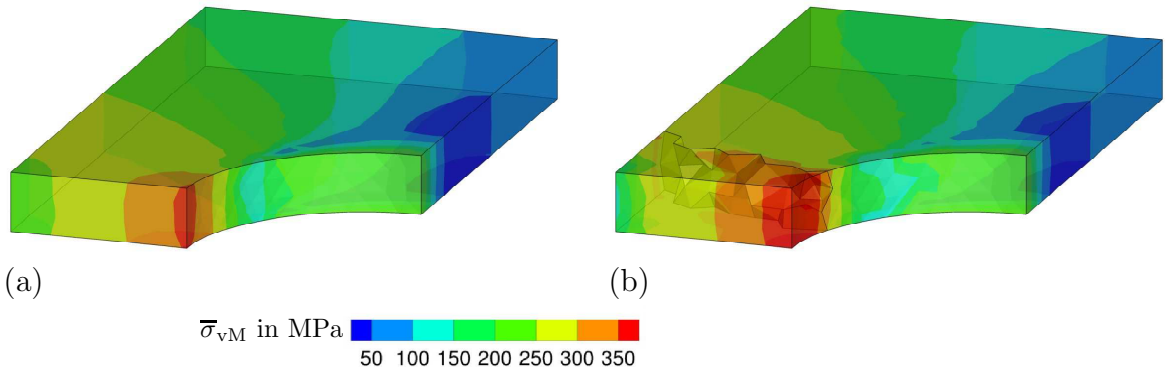

Figure 7.10: Distribution of $\overline{\sigma}_{\mathrm{vM}}$ on the macroscale of (a) the purely macroscopic simulation and (b) the FE^2-simulation of the perforated plate.

Fig. 7.11 shows the distribution of von Mises stress on the microscale at selected points which were found to differ significantly from zero. These are the six points located near the boundary of the hole, namely point 1, 5, 2, 6, 9 and 10. Additionally, point 8 is evaluated, where no plastic deformation takes place and the von Mises stress does not vary largely. The stress distribution of the region in the macroscopic boundary value problem which is computed using an FE^2-scheme is shown in the center of the figure. The region treated as purely macroscopic material is shown in faded color, since it is not of interest here. The stress distribution is shown on the surface of the SSRVE as well as on slices placed in regions of high stresses for better visibility.

Depending on the location of the point position on the macroscale, the magnitude of stress differs. Point 1 shows the highest values of σ_{vM}, where a maximal value $\sigma_{\mathrm{vM}} = 1764.52$ MPa is found. The distribution clearly shows a concentration of stress in the martensitic inclusions. In the ferritic matrix material, lower values are found, where

σ_{vM} is in the range of 350 MPa for points 1, 2 and 10 and in the range of 300 MPa for points 5, 6 and 9. For point 8, σ_{vM} is found to be in a range of 205 MPa to 324 MPa overall (matrix material and inclusions), where a nearly homogeneous stress distribution is found without any regions of significantly high stress. Note that the morphology of the SSRVE, i.e. inclusions, is not visible here due to the choice of plotted stress range.

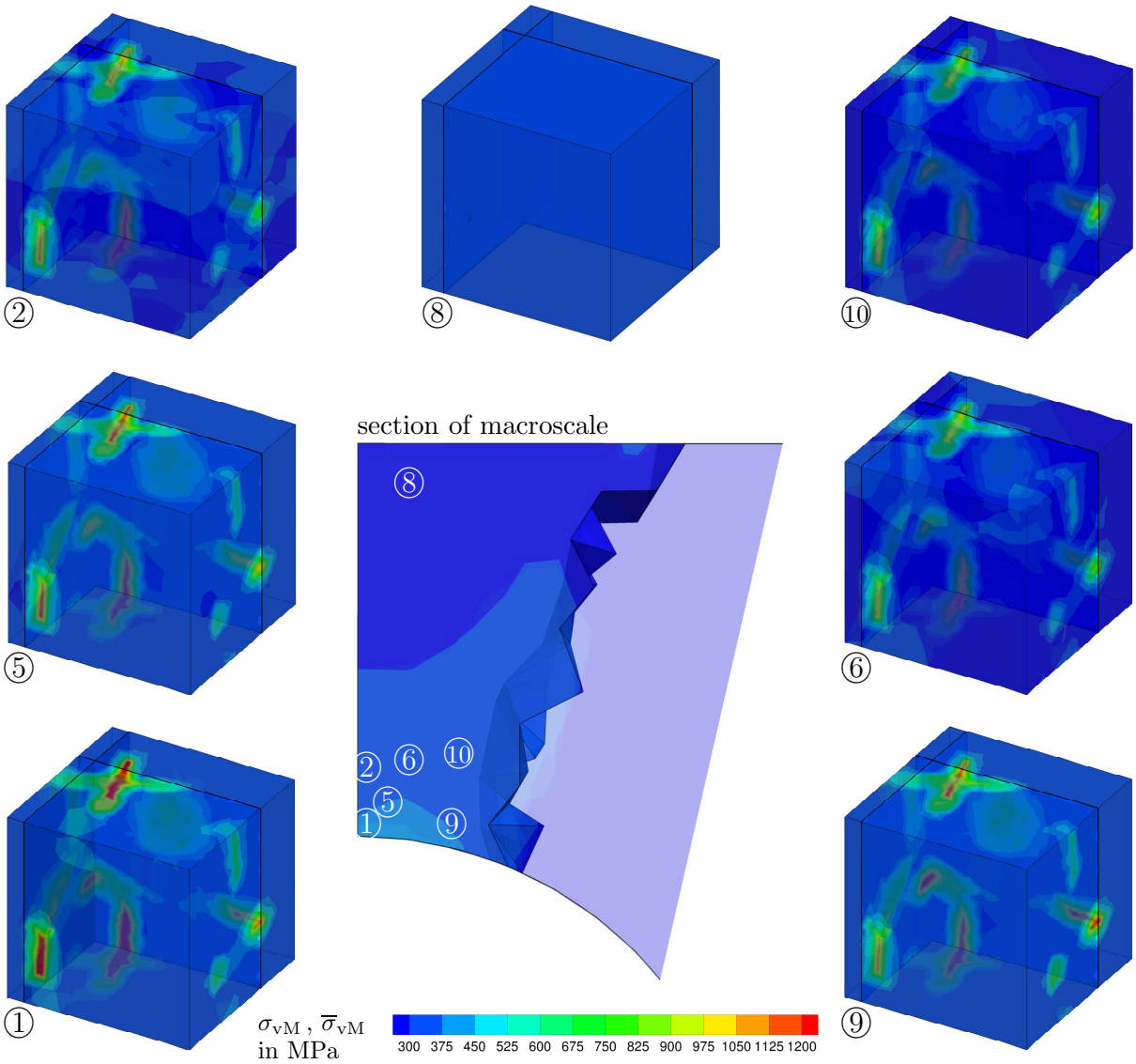

Figure 7.11: Distribution of σ_{vM} on the microscale at different points in the macroscopic problem. The illustration of the macroscopic problem shows the distribution of $\overline{\sigma}_{\mathrm{vM}}$.

Comparing the microscopic stress levels with the macroscopic stress levels, one sees that the maximal microscopic stress is significantly larger than the stress level on the macroscale. This information is especially important in view of further analysis of effects related to high stress magnitudes, such as initiation of damage and failure. Note that in Fig. 7.11, the comparison of stress values is illustrated between the macroscale and the microscale of the FE^2-simulation. However, the purely macroscopic computation leads to even lower maximal stresses in the analyzed region at the perforation as the FE^2-simulation. This leads to the conclusion that the purely macroscopic simulation cannot capture the details in stress deviation on the microscale of the DP steel microstructure and is thus not able to detect the critical regions of high stress. A comparison with an

FE^2-simulation using a real DP steel microstructure in a macroscopically inhomogeneous boundary value problem is expected to show the drastic reduction of computation time when an SSRVE is applied instead. However, this computation could not be carried out due to the cumbersome handling of the enormous amount of data during the computation and limited computational ressources.

Acknowledgment:

The author gratefully acknowledges the computing time granted by the Center for Computational Sciences and Simulation (CCSS) of the Universität Duisburg-Essen and provided on the supercomputer magnitUDE (DFG grants INST 20876/209-1 FUGG, INST 20876/243-1 FUGG) at the Zentrum für Informations- und Mediendienste (ZIM).

8 Macroscopic Yield Surface Based on Polycrystal Simulations

The following section presents results for the computation of macroscopic yield surfaces for textured materials using periodic polycrystalline RVEs. The material under consideration here is a Al-Cu alloy, which consists of a polycrystalline structure with each grain represented by a face centered cubic (fcc) unitcell.

In Section 1, an overview is given on different yield functions which aim at providing a description of the macroscopic yield behavior in a functional form such that the coefficients of the yield function can be obtained from different experiments or analyses of the material. An overview is given in Habraken [49]. However, these experiments are often cumbersome and costly. Darrieulat and Piot [33] presented an analytical description of yield surfaces accounting for shape properties in crystalline material, Kowalczyk and Gambin [75] compare the evolution of a texture-dependent yield surface to classical phenomenological formulations for different loading cases and propose a phenomenological yield function whose parameters evolve with respect to the evolution of a textured material. Bertram et al. [19], see also Böhlke et al. [21], used an RVE to simulate yield surfaces for polycrystalline aggregates for a large strain crystal plasticity formulation.

In the following, 2D macroscopic yield surfaces of textured materials are derived based on the homogenized response of polycrystalline RVEs. Virtual biaxial tests representing different plane stress loading scenarios are computed, wherein the macroscopic deformation state representing the loading scenario is imposed on the RVE and the macroscopic response is obtained from a homogenization of the microscopic quantities by suitable volumetric averages. Fig. 8.1 illustrates the macroscopic loading state, where $\sigma_z = 0$. Different loading ratios σ_x/σ_y are used, namely tensile and compression tests in x- and y-direction, as well as the ratios 0.1, 1 and 2 in each quadrant I, II, III, IV. The RVE is simulated using periodic boundary conditions on its surface, according to Section 5.2.3. The plastic behavior of the single crystals are described by the crystal plasticity material model presented in Section 4.4, where a constant hardening modulus, i.e., $q = 1$ in Eq. (4.27), and the hardening function proposed in Peirce et al. [107], cf. Eq. (4.28), is used. The material parameters, describing an Al-Cu alloy, are listed in Fig. 8.1, for details see Steinmann and Stein [147].

The open source software package *Neper*, cf. Quey et al. [112], is used for the polycrystal generation and meshing. Based on a desired number of grains, a Voronoi tessellation

Table 8.1: Material parameters for Al-Cu alloy, cf. Steinmann and Stein [147]

Lame constant	λ	35,104.88 N/mm^2
shear modulus	μ	23,427.25 N/mm^2
initial slip resistance	τ_0	60.84 N/mm^2
saturation stress	τ_∞	109.51 N/mm^2
initial hardening modulus	h_0	541.48 N/mm^2
material rate sensitivity parameter	p	200
reference slip rate	$\dot{\gamma}_0$	$1 \cdot 10^{-3}$

is created which is conformal with periodicity conditions on the polycrystal. Aspects on the periodic unitcells have been discussed in Section 5.2.3. The Voronoi tesselation is then meshed using the provided meshing tool implemented in *Neper*. Information on the periodically associated faces of the mesh is provided as well. In order to use 10-noded tetrahedral finite elements for the computation, the mesh, as well as the periodic surface information, needs to be modified. Each grain in the polycrystal is modeled as a single crystal of fcc unitcell type with a specific orientation. The material model described in Section 4.4 is used.

8.1 Definition of Isotropic Orientation Distribution

In order to compute the response of a polycrystal, the orientation distribution of the grains in the polycrystal plays an important role. Each grain has be to assigned to a specific orientation, as indicated in Fig. 8.2a. A polycrystal may be isotropically oriented, thus having no distinct overall orientation. A reorientation of the grains can be observed during deformation, while different loading paths lead to specific patterns in the crystalline orientation, see, e.g., Kowalczyk and Gambin [75] and Bertram et al. [19] for examples. The small strain rate dependent crystal plasticity model cannot account for such changes in the orientation of grains. Nevertheless it is necessary to define an orientation distribution for grains in the polycrystal.

In order to obtain an isotropic orientation distribution, the concept of geodesic domes is used, in which the orientation distribution is related to the triangulated surface of a sphere. The architect R. Buckminster Fuller shaped the concept of geodesic domes, wherein he divided a spherical dome into evenly spaced subsurfaces using equilateral congruent triangles. This technology was used for various constructions, such as the "Fuller dome", which was built at the Expo 1967 in Montreal. These dome constructions offer favorable attributes, such as stability and volume to material ratio. Geodesic domes can be obtained using an icosahedron, which is a polytope with 20 equilateral triangles and wherein five

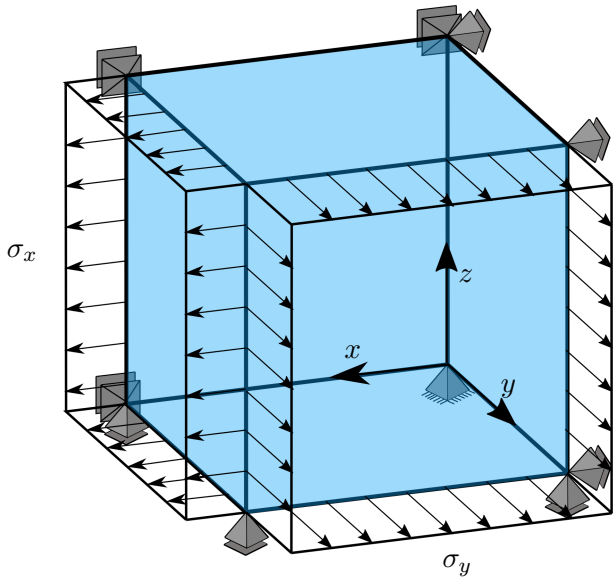

Figure 8.1: Plane stress biaxial loading setup at macroscale.

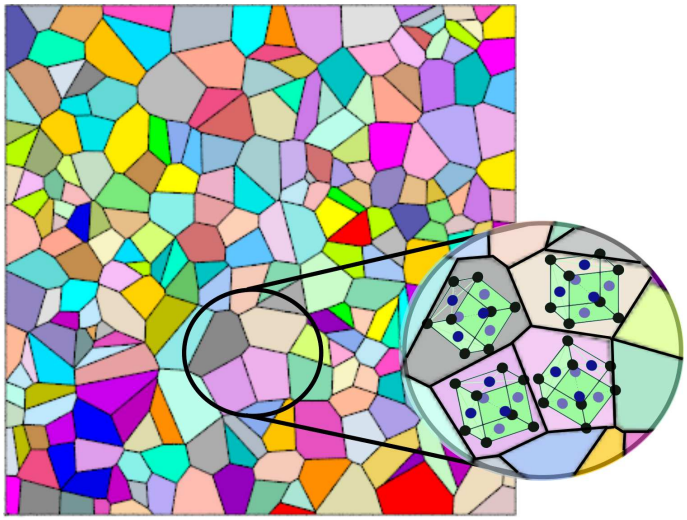

Figure 8.2: Sketch of a polycrystal with indication of different orientation prescribed on each grain.

edges meet at each of the 12 corners. The icosahedron approximates a sphere to some extent already, by subdividing its triangular surfaces, a sphere can be approximated even more closely. After this subdivision of surface triangles, the number of edges meeting in one corner is not always equal to five. The triangle surfaces are divided into smaller triangles, which remain equilateral and congruent. The steps of refinement of the surface are described by frequencies, where a frequency of 2 divides an edge of a triangle into two edges of identical length, thus dividing every triangle into 4 smaller triangles. A frequency of 2 results in 80 triangular faces and 42 corners, a frequency of 3 denotes a polytope with 92 corners. In order to obtain an orientation distribution from geodesic domes, a vector is assumed to point from the center of the dome to the corners of each triangle on the polytope's surface. Fig. 8.3 shows geodesic domes and the resulting orientation distribution for frequencies 2 and 3. Due to the regularity of the surface of the polytope, isotropic orientation distribution functions are obtained. For the description of a body in space, an orientation defined by a triad of three vectors is necessary, which can also be expressed by Euler angles, which have been introduced in Section 6.2.1 in this thesis. The distribution of vectors obtained from the geodesic dome is modified, defining two normal vectors on the given vectors. Finally, a distribution of triads of vectors is obtained for a description of the spatial orientation of grains.

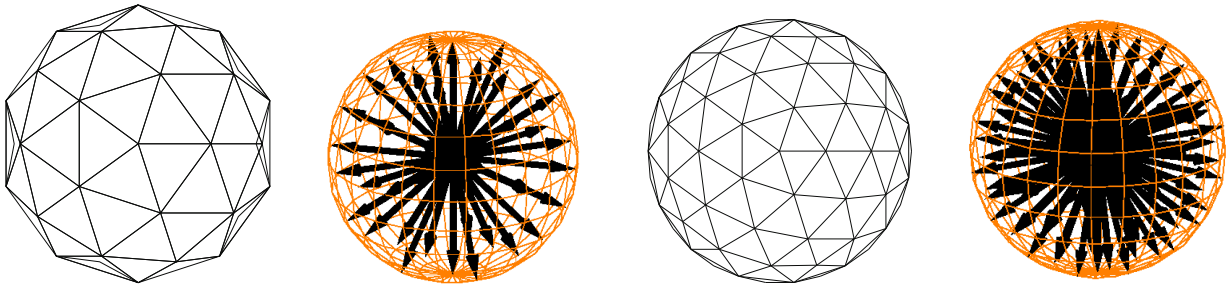

(a) **(b)**

Figure 8.3: Geodesic dome and resulting orientation distribution for (a) frequency 2 and (b) frequency 3, see Kurzhöfer [80].

With these isotropic orientation distributions for different numbers of orientations in hand, one orientation is assigned to every grain in the polycrystal. Depending on the number of grains in the polycrystal, different representations of the geodesic dome with different numbers of triangular surfaces have to be used to obtain an isotropic orientation. The counter-example shows this need: for a polycrystal with only 10 grains, using an orientation distribution with 92 orientations could result in an anisotropic orientation of the polycrystal. Another method to obtain isotropic orientation distributions is the use of evolution algorithms which minimize suitable error functionals, as described in Kurzhöfer [80]. In the case of many orientations, these algorithms lead to large effort for the optimizations. The orientation distribution used here contain 15, 42, 92 or 162 orientations, denoted by n_{orient}. Thereby, $n_{\text{orient}} = 15$ is obtained from an optimization, while the others are constructed using geodesic domes with frequencies 2,3 and 4. The number of grains in a polycrystal are denoted by n_{grain}. We choose an orientation distribution such that $n_{\text{grain}} \leq n_{\text{orient}}$ and assign the orientations in a randomized manner. The identifier for the orientation i_{orient} for each grain is then obtained by

$$\begin{aligned} i_{\text{orient}} &= 1 + \lfloor \text{rand}(i_{\text{grain}}) \rfloor \, (n_{\text{orient}} - 1) \quad \text{if} \quad \text{rand}(i_{\text{grain}}) < 0.5 \,, \\ i_{\text{orient}} &= 1 + \lceil \text{rand}(i_{\text{grain}}) \rceil \, (n_{\text{orient}} - 1) \quad \text{if} \quad \text{rand}(i_{\text{grain}}) \geq 0.5 \,, \end{aligned} \tag{8.1}$$

where rand denotes a list of random numbers between 0 and 1 and i_{grain} denotes the individual grain number with $i_{\text{grain}} = 1 \ldots n_{\text{grain}}$. The square brackets $\lfloor \bullet \rfloor$ and $\lceil \bullet \rceil$ describe the operation of rounding off and rounding up to the nearest integer, respectively. From the list of all orientations, the identifier i_{orient} assigns the according orientation to the grain (with identifier i_{grain}), where $i_{\text{orient}} \in [1, n_{\text{orient}}]$.

8.2 Polycrystalline Periodic RVEs

For a comparison of different periodic polycrystal RVEs, three candidates are constructed using Neper, which contain 15, 45 and 100 grains, respectively. The finite element meshes of the RVEs are shown in Fig. 8.4. The colors distinguish the individual grains. All three finite element meshes are constructed using 10-noded tetrahedral finite elements, with 1122 elements for $n_{\text{grain}} = 15$, 2952 elements for $n_{\text{grain}} = 45$ and 6948 elements for $n_{\text{grain}} = 100$. For each RVE, different loading ratios are evaluated to describe the yield surface. The rate-dependent single crystal plasticity formulation demands for small load steps, which is even amplified by the stress-driven simulation. An automatic time step control is used, leading to a varying step size in the range of $5 \cdot 10^{-2}$ to $5 \cdot 10^{-7}$. All simulations are carried out using FEAP, cf. Taylor [161]. Assigning the orientations based on the procedure described previously, the isotropy of the polycrystalline unitcells can be visualized in a pole figure. Pole figures are commonly used in order to describe the orientation distribution in polycrystalline structures by stereographic projections onto a plane. For an overview, it is referred to Mittermeijer [98]. Fig. 8.5 illustrates the construction of a pole figure with the example of a single grain with fcc unitcell with Euler angles (0, 0, 0). From the orientation of the family of $\{1\,1\,1\}$ lattice planes, four projection points on the xy-plane arise, as shown in Fig. 8.5. The intersection of the normal vectors of the $\{1\,1\,1\}$ family of planes and sphere surface (red dots) are projected onto the xy-plane, where the projection point is the "south pole" of the sphere and the intersections on the "northern hemisphere" are considered in the projection. The pole figures of the polycrystalline RVEs are shown in Fig. 8.6. They show a uniform distribution of orientations and thus the initial isotropic orientation of the polycrystal can be assumed.

In the following, yield surfaces obtained from the polycrystalline RVEs are presented. Therein, similarly to Section 7.2, a yield surface describes elastic stress states, which are located inside the surface, while stress states on the yield surface correspond to material state of equal states of plasticity. This is determined by comparing the volume average of

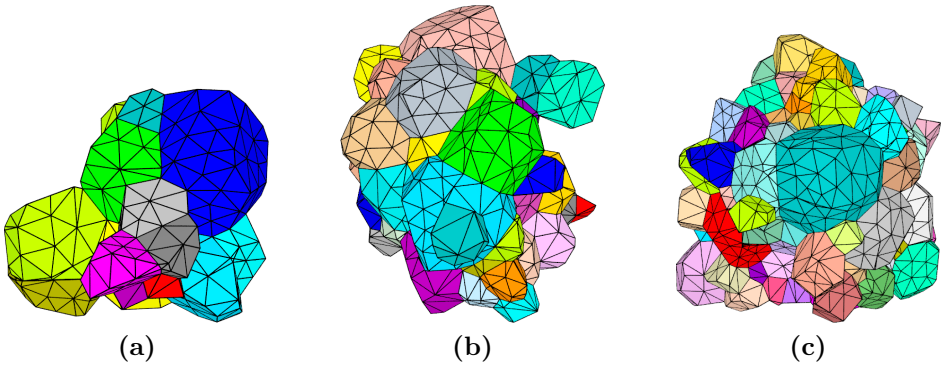

Figure 8.4: Finite element meshes of periodic polycrystalline unitcells with (a) $n_{\text{grain}} = 15$, (b) $n_{\text{grain}} = 45$ and (c) $n_{\text{grain}} = 100$.

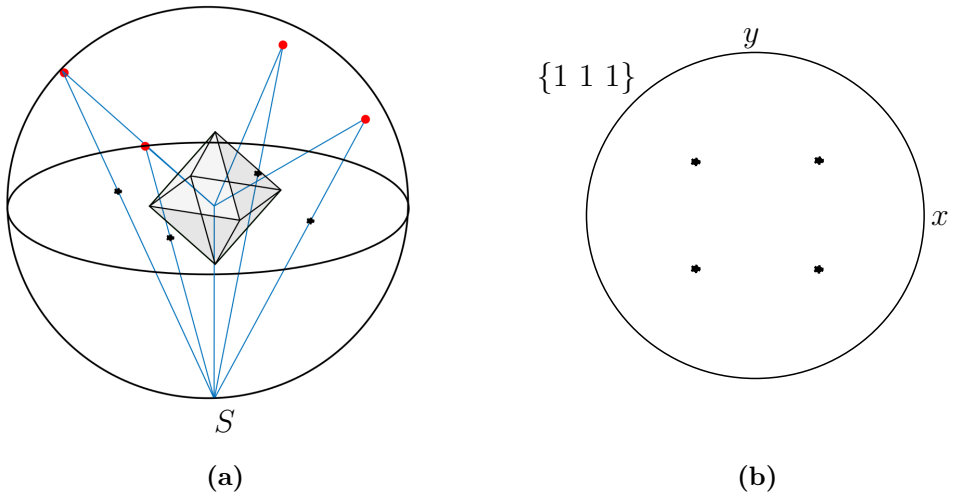

Figure 8.5: (a) Construction of pole figure based on stereographic projection of intersection points of $\{1\,1\,1\}$ family vectors with sphere onto xy-plane. (b) Resulting pole figures for orientation (0,0,0) in Euler angles.

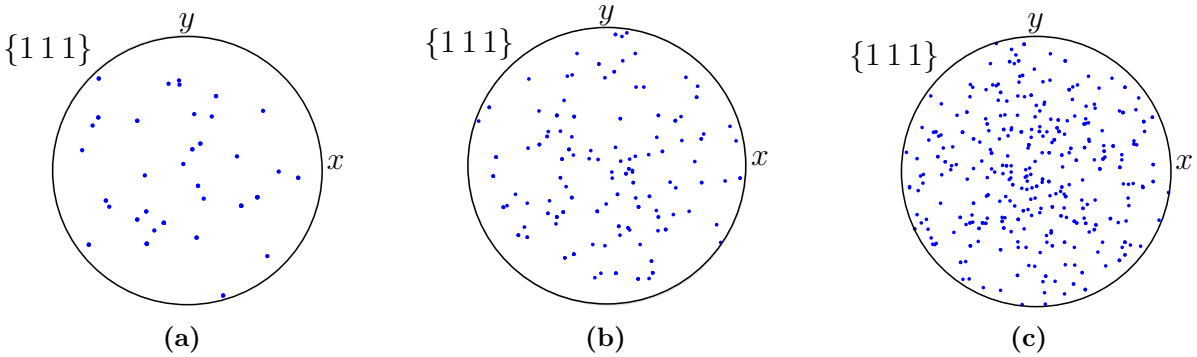

Figure 8.6: Pole figures of $\{1\,1\,1\}$ family of lattice planes projected into xy-plane for (a) $n_{\text{grain}} = 15$, (b) $n_{\text{grain}} = 45$ and (c) $n_{\text{grain}} = 100$.

equivalent plastic strains of the polycrystal. During hardening of the material, the yield surface can evolve and, as shown in BÖHLKE ET AL. [21], change its shape. It is observed that the initial yield surface of a polycrystal tends to be of Tresca type (hexagonal shape), while the yield surface then evolves to a von Mises type surface (ellipsoidal shape). A sketch of 2D von Mises and Tresca type yield surfaces is shown in Fig. 8.7 in the xy-plane.

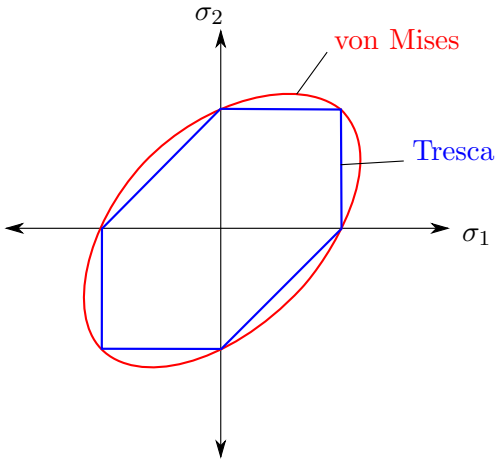

Figure 8.7: Illustration of yield surfaces in 2D of von Mises type and Tresca type.

8.2.1 Initial Macroscopic Yield Surfaces

In the following, the initial yield surface for the three presented polycrystalline structures with 15, 45 and 100 grains are presented. Since the rate-dependent crystal plasticity formulation does not show an explicit point where yielding begins, the initial yield surface is considered here at $\langle \varepsilon_{\mathrm{pl,v}} \rangle = 3.3 \cdot 10^{-8}$. Fig. 8.8 shows the surface of initial yielding for $n_{\mathrm{grain}} = 15$. A total number of 14 biaxial tests are evaluated, the evaluation points are shown as squares on the yield surface. The Tresca type yield surface can be seen with its specific angular shape. For six points on the yield surface, the distribution of equivalent plastic strains on the microscale is shown, related to different loading paths.

The plastic activity in the different grains is compared Fig. 8.8 for different loading ratios. The different levels of plasticity in the grains can be clearly seen: some grains are deformed plastically, while others are still in the elastic regime due to the differences in resolved shear stress on the slip systems in each grain. These result from the differences in orientation of the grains, see, e.g., point ④. Also, different loading paths lead to plastic slip in different grains. For tensile loading in x- and y-direction (⑥), the same state of plastic slip is found in the respective compression loading path (②). Furthermore, it can be seen that in some load cases the plastic activity is concentrated in one grain or activity of multiple grains. Due to the macroscopic loading state, the stress distribution is uniform in the polycrystals at inital yielding. The fact that the distribution of equivalent plastic strains stretches across the borders of the grains in the illustration of the polycrystal, owes from the interpolation procedure used for graphical representation. Here, the value is averaged at each node by considering the values of all elements which are associated to this node. It is not taken into consideration whether all adjacent elements belong to the same grain. This effect is solely due to the postprocessing of the computation for visualization. A

consideration of a distribution per element could be a solution to consider the non-smooth property of the distribution in between the grains more precisely.

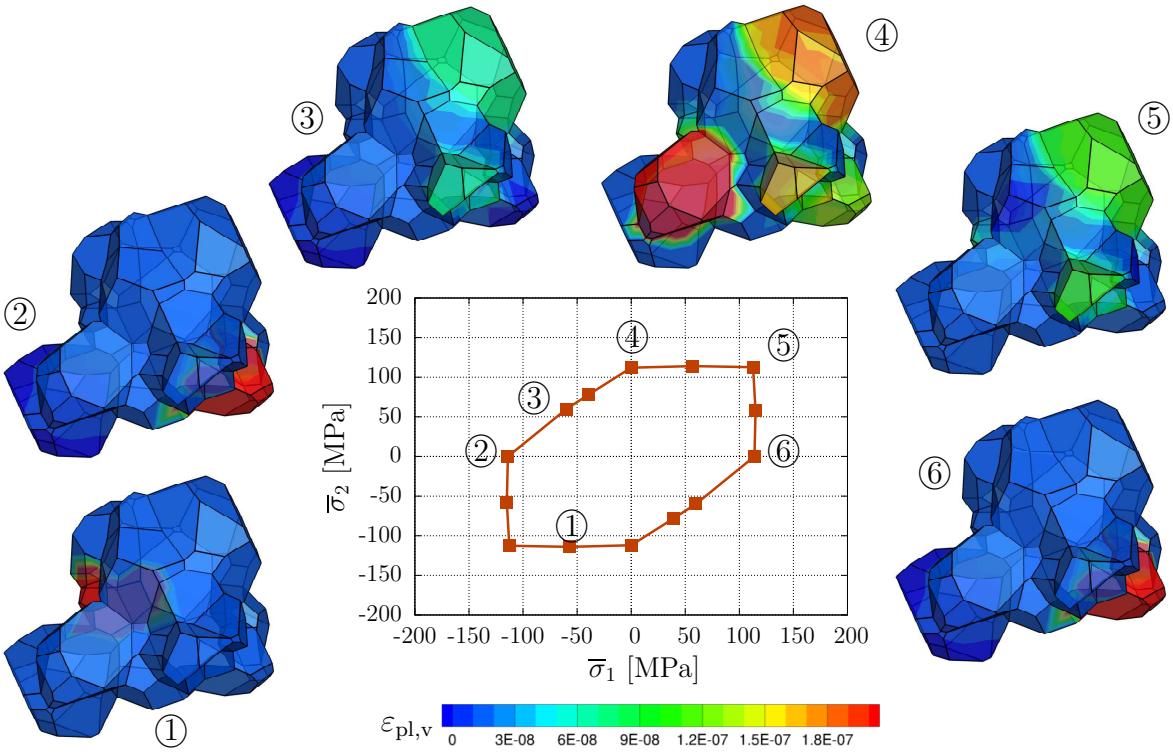

Figure 8.8: Initial yield surface at $\langle \varepsilon_{\mathrm{pl,v}} \rangle = 3.3 \cdot 10^{-8}$ and distribution of $\varepsilon_{\mathrm{pl,v}}$ in the polycrystal for distinct loading paths for $n_{\mathrm{grain}} = 15$.

For the initial yield surface of the polycrystal with 45 grains, 15 load paths are analyzed with initial yield considered at $\langle \varepsilon_{\mathrm{pl,v}} \rangle = 3.3 \cdot 10^{-8}$. The evaluated loading paths are indicated by squares. Fig. 8.9 shows the initial yield surface and the distribution of equivalent plastic strain at the microscale for different load paths, which are indicated by numbers. The same six load paths are evaluated as for $n_{\mathrm{grain}} = 15$. The yield surface is of Tresca type with the same stress values for initial yielding as in the previous example. Again, it can be seen that depending on the loading direction, different grains are deformed plastically. Here, it is also observed that only few grains are show a higher level of plastic slip, while others are still in a range of plastic slip considered as below the initial yielding. Due to the macroscopic loading state, the stress distribution is uniform in the poycrystals at initial yielding.

As before, for the third polycrystal with 100 grains, yielding is considered to initiate at $\langle \varepsilon_{\mathrm{pl,v}} \rangle = 3.3 \cdot 10^{-8}$. Fig. 8.10 shows the yield surface, which is of Tresca type, together with the distribution of equivalent plastic strains at the microscale for different loading paths. 16 loading paths are evaluated to construct the yield surface here, indicated by squares. A similar distribution of equivalent plastic strain in few grains can be seen, while most of the grains are still in the elastic regions for the initiation of yielding. Depending on the loading path, different grains show plastic slip. Again, due to the macroscopic loading state, the stress distribution is uniform in the poycrystals at inital yielding.

From a comparison of the three macroscopic yield surfaces computed using an periodic polycrystalline RVE with a varying number of grains, it can be seen that the number of grains in the RVE does not have an influence on the initial yield surface.

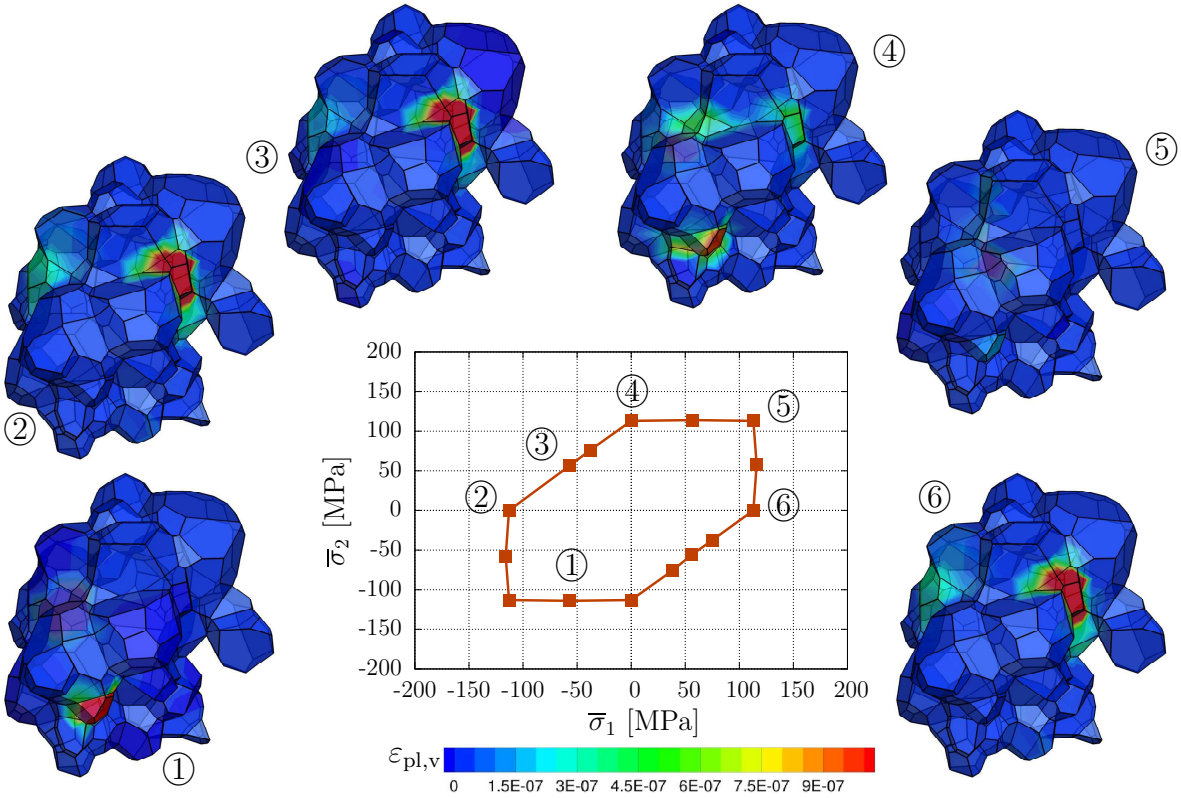

Figure 8.9: Initial yield surface at $\langle \varepsilon_{\mathrm{pl,v}} \rangle = 3.3 \cdot 10^{-8}$ and distribution of $\varepsilon_{\mathrm{pl,v}}$ in the polycrystal for distinct loading paths for $n_{\mathrm{grain}} = 45$.

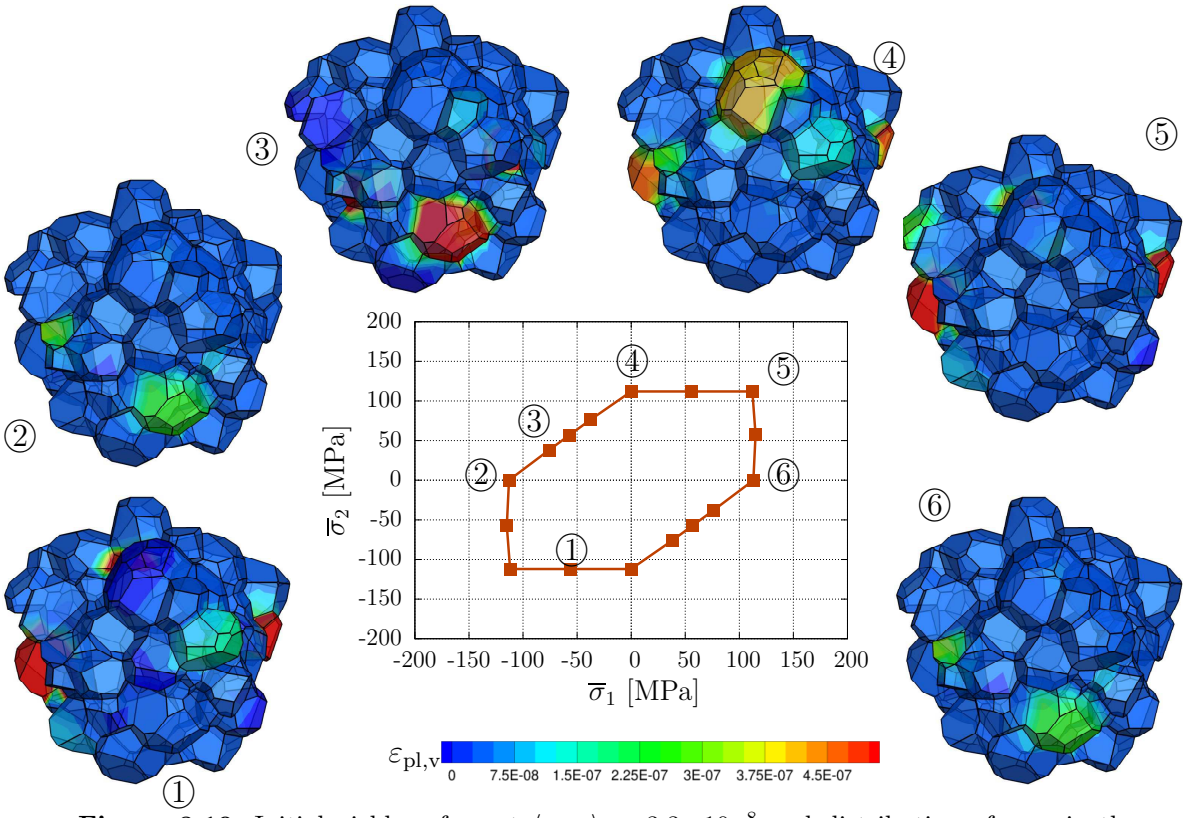

Figure 8.10: Initial yield surface at $\langle \varepsilon_{\mathrm{pl,v}} \rangle = 3.3 \cdot 10^{-8}$ and distribution of $\varepsilon_{\mathrm{pl,v}}$ in the polycrystal for distinct loading paths for $n_{\mathrm{grain}} = 100$.

8.2.2 Evolution of Macroscopic Yield Surface

The evolution of the yield surface during the hardening process is analyzed exemplarily for $n_{\text{grain}} = 15$. Fig. 8.11 shows the yield surface for $\langle \varepsilon_{\text{pl,v}} \rangle = 4.7 \cdot 10^{-4}$ as well as the distribution of equivalent plastic strain on the microscale. At this state, nearly all grains in the polycrystal show plastic activity, which varies from grain to grain and also distributes differently in the different loading paths. The yield surface shows an elliptic shape, which is comparable to a von Mises type yield surface. The difference between the yield surfaces at two different states of plasticization is obvious from comparing Fig. 8.8 and Fig. 8.11 showing an expansion as well as change in shape.

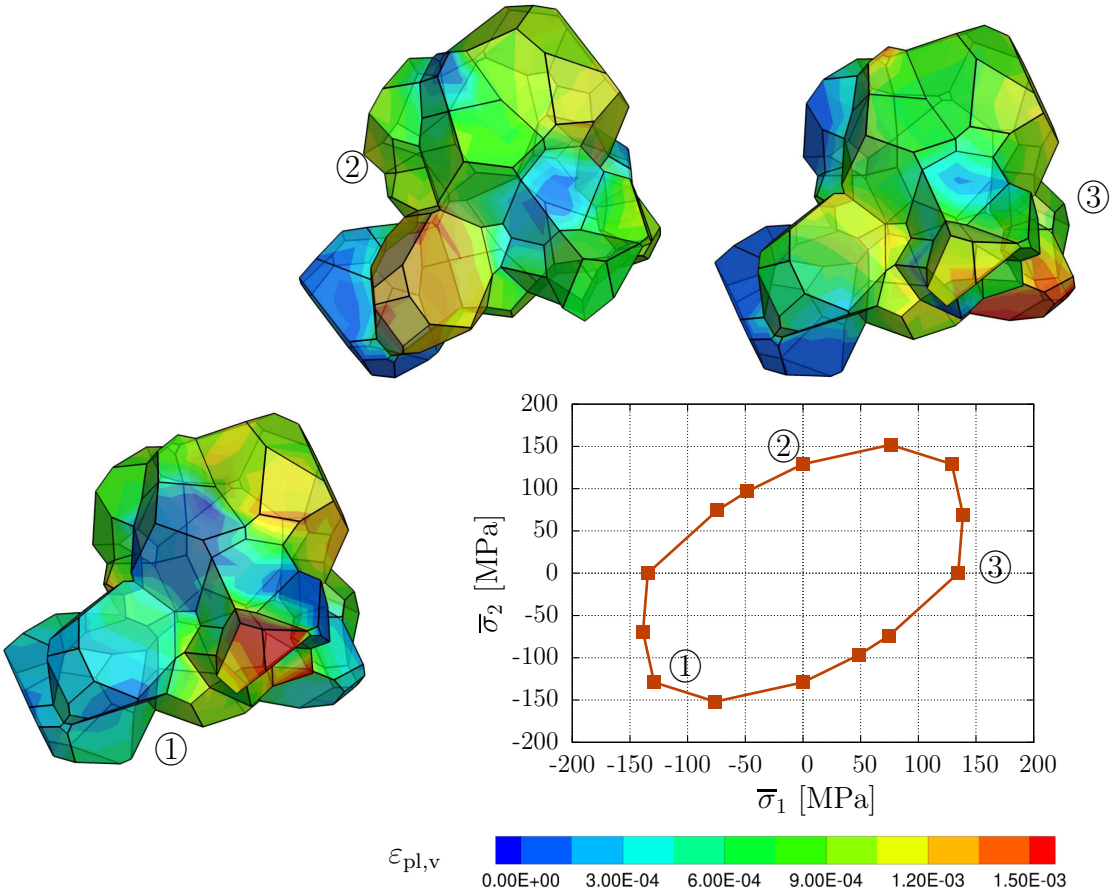

Figure 8.11: Yield surface at $\langle \varepsilon_{\text{pl,v}} \rangle = 4.7 \cdot 10^{-4}$ and distribution of $\varepsilon_{\text{pl,v}}$ in the polycrystal for distinct loading paths for $n_{\text{grain}} = 15$.

8.2.3 Polycrystal Simulation of Tension Test

For an insight into the evolution of stress and equivalent plastic strain, the polycrystal $n_{\text{grain}} = 15$ is analyzed during a virtual tension test in x-direction. Fig. 8.12 shows the resulting stress-strain curve of the simulated tension test. The von Mises stress distribution and equivalent plastic strains are investigated at six different points on this curve, which are defined in Tab. 8.2. Fig. 8.13 shows the von Mises stress in the polycrystal and Fig. 8.14 shows the distribution of equivalent plastic strains.

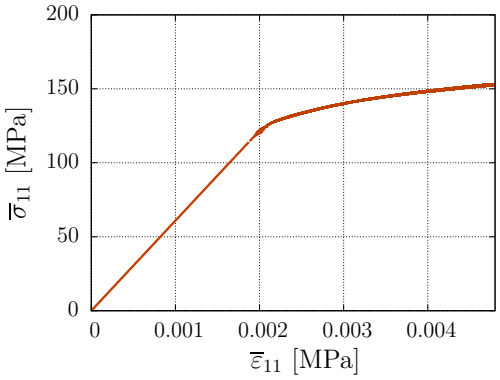

Figure 8.12: Stress-strain curve for $n_{\text{grain}} = 15$ in tension test in x direction.

Table 8.2: Macroscopic stress and strain component $\overline{\sigma}_{11}$ and $\overline{\varepsilon}_{11}$, respectively and volume average of equivalent plastic strain $\langle \varepsilon_{\text{pl,v}} \rangle$ for different states.

	state 1	state 2	state 3	state 4	state 5	state 6
$\overline{\sigma}_{11}$ in MPa	131.06	139.00	144.29	147.44	150.60	152.95
$\overline{\varepsilon}_{11}$	0.0023	0.0029	0.0034	0.0038	0.0044	0.0049
$\langle \varepsilon_{\text{pl,v}} \rangle$	0.00027	0.00079	0.00132	0.00175	0.00229	0.0027

It can be seen that the von Mises stress increases and is non-uniformly distributed in the polycrystal. The increase of plastic strain in the polycrystal is clearly visible in Fig. 8.14. In state 1, almost no plastic activity can be seen in the polycrystal. In the last state a maximal value of equivalent plastic strains is found with $\langle \varepsilon_{\text{pl,v}} \rangle = 0.0047$. It can be seen here that the regions of high magnitudes of von Mises stress do not coincide with the regions of high values of plastic slip. This results from the crystal plasticity formulation considering the Schmid stress on a slip system as relevant for plastic slip. Its magnitude depends not only on the stress state but also on the orientation of the slip systems and the grain.

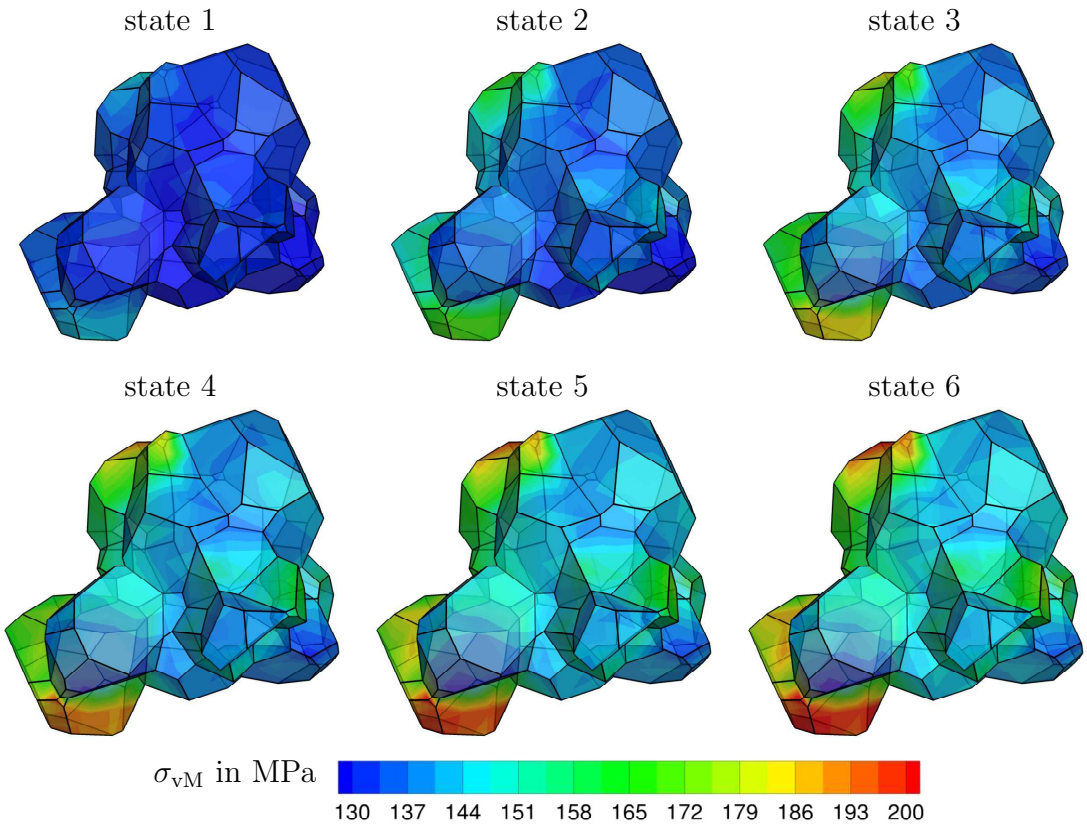

Figure 8.13: Distribution of von Mises stress σ_{vM} at different deformation states for $n_{\mathrm{grain}} = 15$ in tension test in x-direction.

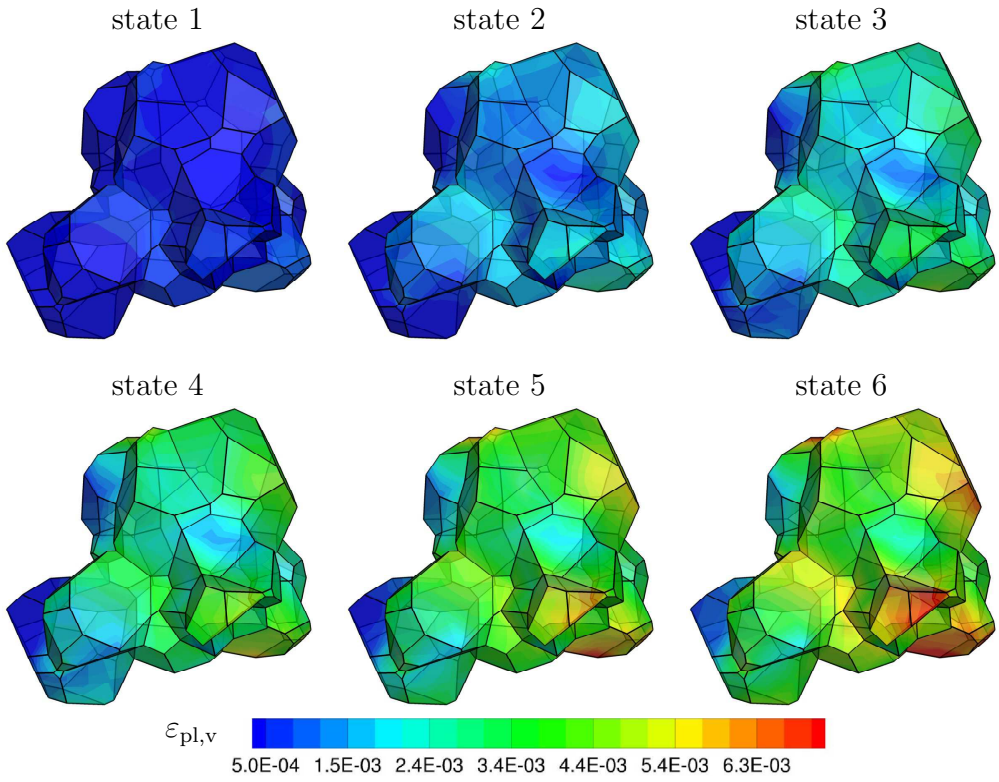

Figure 8.14: Distribution of equivalent plastic strains $\varepsilon_{\mathrm{pl,v}}$ at different deformation states for $n_{\mathrm{grain}} = 15$ in tension test in x-direction.

9 Conclusion and Outlook

This doctoral thesis focuses on the modeling of microheterogeneous materials. An overview on the essential definitions in the framework of continuum mechanics is provided for deformation measures, stress and strain tensors used this work. The balance laws vital for the constitutive framework are revisited, as well as the fundamental principles in material modeling. The finite element method is used for the numerical modeling. Therefore, the variational formulations in the framework of finite deformations are presented, including the weak form as well as its linearization. A focus in the field of modeling microheterogeneous materials is laid upon an efficient description of the mechanical behavior of dual-phase (DP) steel using the FE^2-method. An overview on DP steel's properties, which are important in engineering applications, is given. For a description of the mechanical behavior of the individual phases of DP steel, ferrite and martensite, a finite J_2-plasticity model is revisited. Aiming for a description of textured materials, a framework for small strain rate-dependent single crystal plasticity is presented.

The modeling of microheterogeneous materials demands for the consideration of the morphology of the microstructure, which has a strong influence on the mechanical behavior. In the framework of multiscale modeling, a direct incorporation of the microstructure using suitable representative volume elements (RVEs) may be possible, but often leads to unmanageable computational effort. Therefore, a method for the construction of statistically similar RVEs is proposed in this work. The method aims for a construction of RVEs which are simplified in terms of morphological properties and size compared with a real microstructure. These SSRVEs then provide a statistical equivalent morphological description with respect to the real microstructure as well as a comparable mechanical behavior. The construction of SSRVEs is carried out using an optimization approach, which minimizes least-square functionals comparing selected statistical measures for a real microstructure and the SSRVE.

The statistical measures play a crucial role in the construction of SSRVEs. Among the various possibilities, measures of higher order are analyzed in this thesis. While the lineal-path function and spectral density have been found to be suitable measures for the quantification of morphology two-phase microstructures in the two-dimensional case, the use of statistical measures based on Minkowski functionals is proposed here. They are related to engineering measures, such as the first and second moment of inertia, and offer a powerful tool to characterize a surface's structure. The proposed method for constructing SSRVEs is applied to a DP steel microstructure in this work, whereby combinations of three different sets of statistical measures and four parameterization types are compared. A combination of spectral density and lineal-path function lead to slightly better results compared with SSRVEs based on spectral density and measures based on Minkowski functionals. SSRVEs constructed based on Minkowski functionals however lead to a drastic increase in time efficiency of the optimization algorithm compared with the ones based on the lineal-path function. The effort necessary for the construction of an SSRVE also differs depending on the parameterization: many ellipsoids may lead to a good description of the microstructure morphology, however they increase the number of optimization parameters and thereby the computational costs. Furthermore, they increase the morphological complexity of the resulting SSRVE, which is not always desirable, since it leads to large numbers of elements needed for an appropriate discretization for an application in the finite element method.

The present approach is show to construct satisfying SSRVEs. Nevertheless, it comprises potential for further investigation. In the field of statistical measures, possible further choices are three-point probability functions, which can be efficiently computed combining approximation approaches in the literature based on two-point probability density function. These can themselves be calculated rapidly based on a spectral density using the Wiener-Khinchtin theorem and the application of FFT algorithms. Other statistical measures found in the literature might be beneficial for prospective development. Although the method is used for the construction of SSRVE based on a DP steel microstructure here, it can be applied to other materials and microstructure types, such as polycrystals and can be extended for materials containing more than two phases.

The ability of SSRVEs to describe more complex mechanical behavior is investigated here as well. Therefore, the Bauschinger effect inherent in the real microstructure is compared to the one determined in the SSRVE. The SSRVE is found to describe the kinematic hardening leading to the Bauschinger effect, however a deviation between the computed Bauschinger factors is found. A better description of the effect could be obtained through the incorporation of statistical measures in the SSRVE construction process which describe the specific property leading to the Bauschinger effect in a microstructure. To the authors knowledges, the connection of amount of Bauschinger effect to a specific micromorphological property is however not known.

2D macroscopic yield surfaces are constructed based on the real microstructure and the SSRVE, where the yield surface based on an SSRVE only slightly underestimates the yield surface of the real microstructure. In order to demonstrate the potential of the SSRVE in macroscopically inhomogeneous FE^2-simulations, a comparison with a purely macroscopic simulation of a perforated plate under tension is made. The purely macroscopic computation is based on a description of DP steel as a homogeneous material using a finite J_2-plasticity material model. The FE^2-computation considers the microstructure using the constructed SSRVE in this work on the microscale, wherein ferrite and martensite are modeled using a finite J_2-plasticity material model. Deviations in the stress magnitudes between the two macroscopic computations are found, which could however also be related to the choice of material parameters. Their determination is cumbersome due to large experimental effort needed and additionally different phenomena influencing the mechanical behavior of the phase in a composite and in bulk material. The differences in stress magnitude on the micro- and macroscale are shown, demonstrating the potential of the FE^2-method. Regions of high stress can be identified on the microscale, which are known to be related to failure initialization. Single-scale simulations cannot capture these stress deviations. SSRVEs provide a method to increase the efficiency of FE^2-computations, which would lead to much larger computational costs if a real microstructure were used as an RVE, or might even not be possible.

Lastly, macroscopic yield surfaces based on periodic polycrystalline RVEs are presented, offering the possibility to incorporate information on the texture of materials in multiscale modeling. This provides a vital step to a realistic description of the mechanical behavior of DP steel, where both phases, ferrite and martensite, are governed by texture. The yield surfaces are found show similar behavior as reported in the literature, where initial yield surface is of Tresca type and then evolves to von Mises type through hardening. In

view of the crystal plasticity material model, a realistic description of DP steel texture further demands for an extension of the framework to finite deformations and body centerd cubic unitcells. Their mechanical behavior is governed by more complex effects than the behavior of face centered cubic unitcells, which are used in this thesis. Furthermore, boundary effects between the grains in the polycrystal need to be considered.

A Notation and Calculation rules

This appendix gives information about the mathematical notation used throughout this work. Additionally, some basic calculation rules are revisited.

The calculation rules in this appendix are based on an orthogonal, cartesian base system in three-dimensional euclidean space. The base vectors defined in this space are $\boldsymbol{e}_i$ with $i = \{1, 2, 3\}$ and fulfill the relations $|\boldsymbol{e}_i| = 1$, thus they are unit vectors and their pairwise orthogonality is ensured by $\boldsymbol{e}_i \cdot \boldsymbol{e}_j = \delta_{ij}$. Therein, the kronecker symbol δ_{ij} is defined by

$$\delta_{ij} := \begin{cases} 1 & \text{if} \quad i = j, \\ 0 & \text{if} \quad i \neq j. \end{cases} \tag{A.1}$$

Unless otherwise stated, the summation convention of Einstein applies. The following notation describes scalar, vectorial and tensorial measures

$$\begin{aligned} &\text{Tensor of order 0 (scalar):} && \alpha \\ &\text{Tensor of order 1 (vector):} && \boldsymbol{a} = a^i \, \boldsymbol{e}_i \\ &\text{Tensor of order 2:} && \boldsymbol{B} = B^{ij} \, \boldsymbol{e}_i \otimes \boldsymbol{e}_j \\ &\text{Tensor of order 4:} && \mathbb{C} = C^{ijkl} \, \boldsymbol{e}_i \otimes \boldsymbol{e}_j \otimes \boldsymbol{e}_k \otimes \boldsymbol{e}_l \end{aligned} \tag{A.2}$$

which will be used in this work.

Operations in tensorial and index notation:
Single contraction:
The single contraction is denoted by a single dot and multiplies the innermost base vectors of the involved vectorial or tensorial measures, specifically

$$\begin{aligned} \boldsymbol{a} \cdot \boldsymbol{b} &= (a^i \boldsymbol{e}_i) \cdot (b^j \boldsymbol{e}_j) = a^i b^j \delta_{ij} = a^i b^i, \\ \boldsymbol{A} \cdot \boldsymbol{B} &= (A^{ij} \boldsymbol{e}_i \otimes \boldsymbol{e}_j) \cdot (B^{kl} \boldsymbol{e}_k \otimes \boldsymbol{e}_l) = A^{ij} B^{kl} \delta_{jk} \boldsymbol{e}_i \otimes \boldsymbol{e}_l = A^{ij} B^{jl} \boldsymbol{e}_i \otimes \boldsymbol{e}_l, \end{aligned} \tag{A.3}$$

where the result is scalar, when two vectors are multiplied and a tensor of second order, when two tensors of second order are multiplied. Hence, the order of the result is the sum of the orders of the factors minus two.

Double contraction:
The double contraction is indicated by a colon and is defined as

$$\begin{aligned} \boldsymbol{A} : \boldsymbol{B} &= (A^{ij} \boldsymbol{e}_i \otimes \boldsymbol{e}_j) : (B^{kl} \boldsymbol{e}_k \otimes \boldsymbol{e}_l) = A^{ij} B^{kl} \delta_{ik} \delta_{jl} = A^{ij} B^{ij}, \\ \mathbb{C} : \boldsymbol{D} &= (C^{ijkl} \boldsymbol{e}_i \otimes \boldsymbol{e}_j \otimes \boldsymbol{e}_k \otimes \boldsymbol{e}_l) : (D^{mn} \boldsymbol{e}_m \otimes \boldsymbol{e}_n) \\ &= C^{ijkl} D^{mn} \delta_{km} \delta_{ln} \boldsymbol{e}_i \otimes \boldsymbol{e}_j = C^{ijkl} D^{kl} \boldsymbol{e}_i \otimes \boldsymbol{e}_j, \end{aligned} \tag{A.4}$$

hence the last and the second to last base vectors of both factors are multiplied, respectively. The order of the result is here the sum of the orders of both factors minus four.

Dyadic product:
A dyadic product is denoted by the symbol '$\otimes$' and is defined for vectors and tensors of

second order by

$$\begin{aligned} \boldsymbol{a} \otimes \boldsymbol{b} &= a^i \boldsymbol{e}_i \otimes b^j \boldsymbol{e}_j = a^i\, b^j\, \boldsymbol{e}_i \otimes \boldsymbol{e}_j\,, \\ \boldsymbol{A} \otimes \boldsymbol{B} &= (A^{ij} \boldsymbol{e}_i \otimes \boldsymbol{e}_j) \otimes (B^{kl} \boldsymbol{e}_k \otimes \boldsymbol{e}_l) \;=\; (A^{ij}\, B^{kl}\, \boldsymbol{e}_i \otimes \boldsymbol{e}_j \otimes \boldsymbol{e}_k \otimes \boldsymbol{e}_l). \end{aligned} \tag{A.5}$$

Identity Tensor
The identity tensor used in this work is defined by

$$\boldsymbol{I} := \delta_{ij} \boldsymbol{e}_i \;\otimes\; \boldsymbol{e}_j. \tag{A.6}$$

Permutation Symbol
The permutation symbol is defined by

$$\epsilon_{ijk} := \begin{cases} \quad 0 & \text{for} \quad i = j,\, j = k,\, i = k\,, \\ \quad 1 & \text{for} \quad (i,j,k) \in \{(1,2,3),(2,3,1),(3,1,2)\}\,, \\ -\;\; 1 & \text{for} \quad (i,j,k) \in \{(1,3,2),(2,1,3),(3,2,1)\}\,. \end{cases} \tag{A.7}$$

Gauss' divergence theorem
The divergence theorem states that the outward flux of a vector field $\boldsymbol{a}$ through a close surface $\partial\mathcal{B}$ is equal to the volume integral of the divergence over the volume $\mathcal{B}$ enclosed by the surface, i.e.

$$\int_{\mathcal{B}} \operatorname{div}[\boldsymbol{a}]\, \mathrm{d}V = \int_{\partial\mathcal{B}} \boldsymbol{a} \cdot \boldsymbol{n}\, \mathrm{d}A, \tag{A.8}$$

where $\mathrm{d}A$ in an infinitesimal surface element and $\boldsymbol{n}$ the outward normal vector of the surface. Considering a tensorial field $\boldsymbol{T}$, one obtains

$$\int_{\mathcal{B}} \operatorname{div}[\boldsymbol{T}]\, \mathrm{d}V = \int_{\partial\mathcal{B}} \boldsymbol{T}^{\mathrm{T}} \cdot \boldsymbol{n}\, \mathrm{d}A. \tag{A.9}$$

Spectral decomposition of Second Order Tensors
The eigenvalues of a tensor $\boldsymbol{A}$, denoted by λ, are calculated by

$$\boldsymbol{A} \cdot \boldsymbol{n} = \lambda\, \boldsymbol{n} \qquad \Leftrightarrow \qquad (\boldsymbol{A} \,-\, \lambda \boldsymbol{I}) \cdot \boldsymbol{n} = \boldsymbol{0}. \tag{A.10}$$

For nontrivial vectors $\boldsymbol{n} \neq \boldsymbol{0}$, the above equation can only be fullfilled if

$$\det(\boldsymbol{A} \,-\, \lambda\, \boldsymbol{I}) \;=\; 0 \quad \rightarrow \quad \lambda^3 \,-\, I_{\boldsymbol{A}}\, \lambda^2 \,-\, II_{\boldsymbol{A}}\, \lambda \,-\, III_{\boldsymbol{A}} \;=\; 0, \tag{A.11}$$

where the first second and third invariant are defined by

$$I_{\boldsymbol{A}} := \operatorname{tr}[\boldsymbol{A}]\,, \quad II_{\boldsymbol{A}} := \frac{1}{2}\left((\boldsymbol{A} \,:\, \boldsymbol{A}) \,-\, \operatorname{tr}(\boldsymbol{A})^2\right)\,, \quad III_{\boldsymbol{A}} := \det[\boldsymbol{A}]. \tag{A.12}$$

For symmetric tensors with $\boldsymbol{A} \;=\; \boldsymbol{A}^{\mathrm{T}}$, there exist three real eigenvalues with

$$\lambda_1 \;\geq\; \lambda_2 \;\geq\; \lambda_3 \quad \text{with} \quad \lambda_1,\, \lambda_2,\, \lambda_3 \;\in\; \mathbb{R}. \tag{A.13}$$

The spectral representation form of the tensor then reads

$$\boldsymbol{A} = \sum_{i=1}^{3} \lambda_i\, \boldsymbol{n}_i \otimes \boldsymbol{n}_i, \tag{A.14}$$

with the eigenvectors $\boldsymbol{n}_1$, $\boldsymbol{n}_2$ and $\boldsymbol{n}_3$.

Lie derivative
Considering a spatial tensorial field quantity $\boldsymbol{T} = \boldsymbol{T}(\boldsymbol{x}, t)$, the Lie derivative $\mathcal{L}(\boldsymbol{T})$ is defined by the following steps:

1.) Pull-back operation to reference configuration,

2.) Computation of material time derivative,

3.) Push-forward to current configuration.

For tensors given in orthonormal base systems, where the co- and contravariant base vectors coincide with $\boldsymbol{e}^a = \boldsymbol{e}_a$ and $\boldsymbol{E}^A = \boldsymbol{E}_A$ and thus $T_{ab} = T^{ab}$, the Lie derivative is obtained by

$$\mathcal{L}(\boldsymbol{T}) = \boldsymbol{F}^{\mathrm{T}-1} \cdot \frac{\mathrm{d}}{\mathrm{d}t}\left[\boldsymbol{F}^{\mathrm{T}} \cdot \boldsymbol{T} \cdot \boldsymbol{F}\right] \cdot \boldsymbol{F}^{-1} \;\rightarrow\; F_a{}^A \, \frac{\mathrm{d}}{\mathrm{d}t}\left[F_A{}^a \, T_{ab} \, F^b{}_B\right] \; F^B{}_b. \tag{A.15}$$

Voigt notation
The arrangement of the 4th order elasticity tensor $\mathbb{C}$ in a 9×9 matrix notation with the vector notation for the stresses given by $\bar{\boldsymbol{\sigma}} = [\sigma_{11}\ \sigma_{22}\ \sigma_{33}\ \sigma_{12}\ \sigma_{23}\ \sigma_{13}\ \sigma_{21}\ \sigma_{32}\ \sigma_{31}]$ and the strain vector $\bar{\boldsymbol{\varepsilon}} = [\varepsilon_{11}\ \varepsilon_{22}\ \varepsilon_{33}\ \varepsilon_{12}\ \varepsilon_{23}\ \varepsilon_{13}\ \varepsilon_{21}\ \varepsilon_{32}\ \varepsilon_{31}]$ is given by

$$\mathbb{C}^{9\times 9} = \begin{bmatrix}
\mathbb{C}_{1111} & \mathbb{C}_{1122} & \mathbb{C}_{1133} & \mathbb{C}_{1112} & \mathbb{C}_{1123} & \mathbb{C}_{1113} & \mathbb{C}_{1121} & \mathbb{C}_{1132} & \mathbb{C}_{1131} \\
\mathbb{C}_{2211} & \mathbb{C}_{2222} & \mathbb{C}_{2233} & \mathbb{C}_{2212} & \mathbb{C}_{2223} & \mathbb{C}_{2213} & \mathbb{C}_{2221} & \mathbb{C}_{2232} & \mathbb{C}_{2231} \\
\mathbb{C}_{3311} & \mathbb{C}_{3322} & \mathbb{C}_{3333} & \mathbb{C}_{3312} & \mathbb{C}_{3323} & \mathbb{C}_{3313} & \mathbb{C}_{3321} & \mathbb{C}_{3332} & \mathbb{C}_{3331} \\
\mathbb{C}_{1211} & \mathbb{C}_{1222} & \mathbb{C}_{1233} & \mathbb{C}_{1212} & \mathbb{C}_{1223} & \mathbb{C}_{1213} & \mathbb{C}_{1221} & \mathbb{C}_{1232} & \mathbb{C}_{1231} \\
\mathbb{C}_{2311} & \mathbb{C}_{2322} & \mathbb{C}_{2333} & \mathbb{C}_{2312} & \mathbb{C}_{2323} & \mathbb{C}_{2313} & \mathbb{C}_{2321} & \mathbb{C}_{2332} & \mathbb{C}_{2331} \\
\mathbb{C}_{1311} & \mathbb{C}_{1322} & \mathbb{C}_{1333} & \mathbb{C}_{1312} & \mathbb{C}_{1323} & \mathbb{C}_{1313} & \mathbb{C}_{1321} & \mathbb{C}_{1332} & \mathbb{C}_{1331} \\
\mathbb{C}_{2111} & \mathbb{C}_{2122} & \mathbb{C}_{2133} & \mathbb{C}_{2112} & \mathbb{C}_{2123} & \mathbb{C}_{2113} & \mathbb{C}_{2121} & \mathbb{C}_{2132} & \mathbb{C}_{2131} \\
\mathbb{C}_{3211} & \mathbb{C}_{3222} & \mathbb{C}_{3233} & \mathbb{C}_{3212} & \mathbb{C}_{3223} & \mathbb{C}_{3213} & \mathbb{C}_{3221} & \mathbb{C}_{3232} & \mathbb{C}_{3231} \\
\mathbb{C}_{3111} & \mathbb{C}_{3122} & \mathbb{C}_{3133} & \mathbb{C}_{3112} & \mathbb{C}_{3123} & \mathbb{C}_{3113} & \mathbb{C}_{3121} & \mathbb{C}_{3132} & \mathbb{C}_{3131}
\end{bmatrix}. \tag{A.16}$$

Based on the Voift notation of the stresses $\underline{\boldsymbol{\sigma}} = [\sigma_{11}\ \sigma_{22}\ \sigma_{33}\ \sigma_{12}\ \sigma_{23}\ \sigma_{13}]$ due to symmetry conditions and the strains $\underline{\boldsymbol{\varepsilon}} = [\varepsilon_{11}\ \varepsilon_{22}\ \varepsilon_{33}\ 2\,\varepsilon_{12}\ 2\,\varepsilon_{23}\ 2\,\varepsilon_{13}]$, the 9×9 matix can be written in a 6×6 matrix format

$$\underline{\mathbb{C}}^{6\times 6} = \begin{bmatrix}
\mathbb{C}_{1111} & \mathbb{C}_{1122} & \mathbb{C}_{1133} & \mathbb{C}_{11(12)} & \mathbb{C}_{11(23)} & \mathbb{C}_{11(13)} \\
\mathbb{C}_{2211} & \mathbb{C}_{2222} & \mathbb{C}_{2233} & \mathbb{C}_{22(12)} & \mathbb{C}_{22(23)} & \mathbb{C}_{22(13)} \\
\mathbb{C}_{3311} & \mathbb{C}_{3322} & \mathbb{C}_{3333} & \mathbb{C}_{33(12)} & \mathbb{C}_{33(23)} & \mathbb{C}_{33(13)} \\
\mathbb{C}_{(12)11} & \mathbb{C}_{(12)22} & \mathbb{C}_{(12)33} & \mathbb{C}_{(12)(12)} & \mathbb{C}_{(12)(23)} & \mathbb{C}_{(12)(13)} \\
\mathbb{C}_{(23)11} & \mathbb{C}_{(23)22} & \mathbb{C}_{(23)33} & \mathbb{C}_{(23)(12)} & \mathbb{C}_{(23)(23)} & \mathbb{C}_{(23)(13)} \\
\mathbb{C}_{(13)11} & \mathbb{C}_{(13)22} & \mathbb{C}_{(13)33} & \mathbb{C}_{(13)(12)} & \mathbb{C}_{(13)(23)} & \mathbb{C}_{(13)(13)}
\end{bmatrix}, \tag{A.17}$$

where $\mathbb{C}_{(ij)kl} = \frac{1}{2}(\mathbb{C}_{ijkl} + \mathbb{C}_{jikl})$, $\mathbb{C}_{ij(kl)} = \frac{1}{2}(\mathbb{C}_{ijkl} + \mathbb{C}_{ijlk})$ and $\mathbb{C}_{(ij)(kl)} = \frac{1}{2}(\mathbb{C}_{(ij)kl} + \mathbb{C}_{ij(kl)})$. With the symmetries $\mathbb{C}_{ijkl} = \mathbb{C}_{jikl} = \mathbb{C}_{ijlk} = \mathbb{C}_{klij}$, we obtain the final representation by

$$\underline{\mathbb{C}} = \begin{bmatrix}
\mathbb{C}_{1111} & \mathbb{C}_{1122} & \mathbb{C}_{1133} & \mathbb{C}_{1112} & \mathbb{C}_{1123} & \mathbb{C}_{1113} \\
 & \mathbb{C}_{2222} & \mathbb{C}_{2233} & \mathbb{C}_{2212} & \mathbb{C}_{2223} & \mathbb{C}_{2213} \\
 & & \mathbb{C}_{3333} & \mathbb{C}_{3312} & \mathbb{C}_{3323} & \mathbb{C}_{3313} \\
 & & & \mathbb{C}_{1212} & \mathbb{C}_{1223} & \mathbb{C}_{1213} \\
 & \text{sym.} & & & \mathbb{C}_{2323} & \mathbb{C}_{2313} \\
 & & & & & \mathbb{C}_{1313}
\end{bmatrix}. \tag{A.18}$$

B Convergency Analysis of FE Meshes for SSRVEs

In order to ensure an appropriate element size in the finite element meshes used for the SSRVEs, a convergency study is made. Due to the microheterogeneous structure with two materials, merely choosing finite element meshes with different numbers of elements would not ensure that every mesh approximates the geometry of the inner surfaces in the same way, since high curvatures and sharp corners exist here. Furthermore, a refinement of the mesh could not ensure that the mesh in equally refined in all regions. Therefore, the following procedure is carried out for all SSRVEs presented in Sections. 6.3.1, 6.3.2 and 6.3.3. For a first guess of an appropriate finite element mesh is generated and a virtual tension test in x-direction is computed. The finite element mesh is then refined by dividing every tetrahedral finite element in the original mesh into eight smaller tetrahedrons by subdividing every edge into two edges of equal length. The yield curves in a virtual tensile test in x-direction are then compared with the results from the coarser mesh and the deviation is computed using the method presented in Section 6.2.4. The stress strain curves are shown in Fig. B.1 and the deviation is summarized in Tab. B.1. With none of the refined meshes deviating more than 2.1% from the coarser mesh, the coarser mesh is assumed to have an adequate mesh size for the analyses in this work.

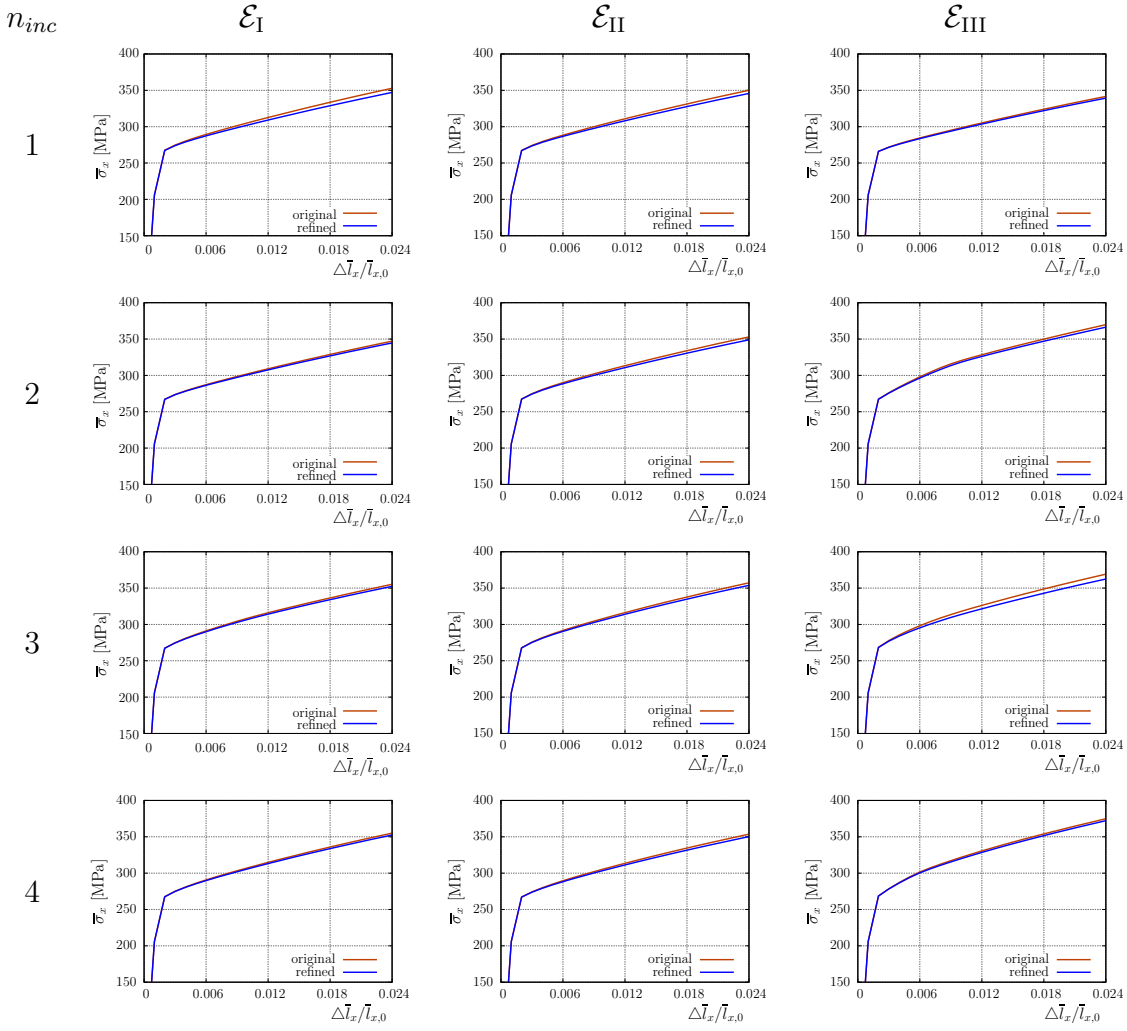

Figure B.1: Comparison of stress-strain curve for SSRVEs in tension test in x-direction.

Table B.1: Overall error $\tilde{r}_{\varnothing}$ in % computed for the comparison of the stress strain curves of original mesh and refined mesh.

n_{inc}	1	2	3	4
$\mathcal{E}_{\mathrm{V,SD,LP}}$	0.8	1.1	2.1	0.7
$\mathcal{E}_{\mathrm{MA,MO}}$	1.4	1.3	1.1	1.1
$\mathcal{E}_{\mathrm{V,SD}}$	1.8	0.6	0.5	0.4

C Slip Systems of Face-Centered Cubic Lattice

Table C.1: Overall error $\tilde{r}_{\varnothing}$ in % computed for the comparison of the stress strain curves of original mesh and refined mesh.

α	$\boldsymbol{s}^{\alpha}$	$\boldsymbol{n}^{\alpha}$	α	$\boldsymbol{s}^{\alpha}$	$\boldsymbol{n}^{\alpha}$	α	$\boldsymbol{s}^{\alpha}$	$\boldsymbol{n}^{\alpha}$
1	[0 1 -1]	(1 1 1)	5	[1 0 1]	(-1 1 1)	9	[-1 -1 0]	(-1 1 -1)
2	[-1 0 1]	(1 1 1)	6	[-1 -1 0]	(-1 1 1)	10	[0 1 1]	(1 1 -1)
3	[1 -1 0]	(1 1 1)	7	[0 1 1]	(-1 1 -1)	11	[1 -1 0]	(1 1 -1)
4	[0 1 -1]	(-1 1 1)	8	[1 0 -1]	(-1 1 -1)	12	[1 0 1]	(1 1 -1)

List of Figures

List of Tables

References

[1] S. Alesker. Description of continuous isometry covariant valuations on convex sets. *Geom. Dedicata*, 74:241–248, 1999.

[2] M. Ambrozinski, K. Bzowski, L. Rauch, and M. Pietrzyk. Application of statistically similar representative volume elements in numerical simulations of crash box stamping. *Archives of Civil and Mechanical Engineering*, 12:126–132, 2012.

[3] P. Armstrong and C. Frederick. A Mathematical Representation of the Multiaxial Bauschinger Effect. CEGB Report RD/B/N731, Berkeley Nuclear Laboratories, 1966.

[4] R. Asaro and J. Rice. Strain localization in ductile single crystals. *Journal of the Mechanics and Physics of Solids*, 25:309–338, 1977.

[5] R. J. Asaro. Crystal plasticity. *Transactions of the ASME*, 50:921–934, 1983.

[6] M. Baiker, D. Helm, and A. Butz. Determination of mechanical properties of polycrystals by using crystal plasticity and numerical homogenization scheme. *Steel Research International*, 85:988–998, 2014.

[7] D. Balzani, J. Schröder, and D. Brands. FE^2-simulation of microheterogeneous steels based on statistically similar RVEs. In *Proceedings of the IUTAM Symposium on Variational Concepts with application to mechanics of materials, September 22-26 2008, Bochum, Germany*, 2009.

[8] D. Balzani, D. Brands, J. Schröder, and C. Carstensen. Sensitivity analysis of statistical measures for the reconstruction of microstructures based on the minimization of generalized least-square functionals. *Technische Mechanik*, 30:297–315, 2010.

[9] D. Balzani, L. Scheunemann, D. Brands, and J. Schröder. Construction of 3D statistically similar RVEs for dual-phase steel microstructures. In E. Oñate, D. Owen, D. Peric, and B. E. Suárez, editors, *XII International Conference on Computational Plasticity. Fundamentals and Applications*, 2013.

[10] D. Balzani, D. Brands, and J. Schröder. Construction of Statistically Similar Representative Volume Elements. In J. Schröder and K. Hackl, editors, *Plasticity and Beyond - Microstructures, Crystal-Plasticity and Phase Transitions (CISM Lecture notes 550)*, pages 355–412. Springer, 2014.

[11] D. Balzani, L. Scheunemann, D. Brands, and J. Schröder. Construction of Two- and Three-Dimensional Statistically Similar RVEs for Coupled Micro-Macro Simulations. *Computational Mechanics*, 54(5):1269–1284, 2014. doi: 10.1007/s00466-014-1057-6.

[12] D. Banabic, H. Aretz, D. Comsa, and L. Paraianu. An improved analytical description of orthotropy in metallic sheets. *International Journal of Plasticity*, 21: 493–512, 2005.

[13] M. Baniassadi, B. Mortazavi, H. A. Hamedani, H. Garmestani, S. Ahzi, M. Fathi-torbaghan, D. Ruch, and M. Khaeel. Three-dimensional reconstruction and homogenization of heterogeneous materials using statistical correlation functions and FEM. *Computational Materials Science*, 51:372379, 2012.

[14] F. Barlat and J. Lian. Plastic behaviour and stretchability of sheet metals. Part I: A yield function for orthotropic sheet under plane stress conditions. *International Journal of Plasticity*, 5:51–61, 1989.

[15] F. Barlat, D. Lege, and J. Brem. A six-component yield function for anisotropic materials. *International Journal of Plasticity*, 7:693–712, 1991.

[16] J. L. Bassani and T.-Y. Wu. Latent materials in single crystals. II. Analytical Characterization and Predictions. *Proc. R. Soc. Lond. A.*, 435:21–41, 1991.

[17] K.-J. Bathe. *Finite-Elemente-Methoden*. Springer, 2 edition, 2002.

[18] J. Bauschinger. Über die Veränderung der Elastizitätsgrenze und der Festigkeit des Eisens und Stahl durch Strecken und Quetschen, durch Erwärmung und Abkühlen und durch oftmals wiederholte Beanspruchung. *Mitteilungen aus dem Mechanisch-Technischem Laboratorium der K. technischen Hochschule, München*, 13:–, 1886.

[19] A. Bertram, T. Boehlke, and M. Kraska. Numerical simulation of texture development of polycrystals undergoing large plastic deformations. In *Proceedings of the Fifth International Conference on computational Plasticity held in Barcelona, Spain, 17.-20. March 1997*, 1997.

[20] J. Bishop and R. Hill. A theory of the plastic distortion of a polycrystalline aggregate under combined stresses. *Philosophical Magazine*, 42(327):414–427, 1951.

[21] T. Böhlke, M. Kraska, and A. Bertram. Simulation der einfachen Scherung einer polykristallinen Aluminiumprobe. *Technische Mechanik*, pages 47–54, 1997.

[22] D. Brands. *Geometrical Modleing and Numerical Simulation of Heterogeneous Materials*. PhD thesis, Institut für Mechanik, Abteilung Bauwissenschaften, Fakultät Ingenieurwissenschaften, Universität Duisburg-Essen, 2012.

[23] D. Brands, D. Balzani, L. Scheunemann, J. Schröder, H. Richter, and D. Raabe. Computational modeling of dual-phase steels based on representative three-dimensional microstructures obtained from EBSD data. *Archive of Applied Mechanics*, 86:575–598, 2016.

[24] J. Bresenham. Algorithm for computer control of a digital plotter. *IBM Systems*, 4:25 – 30, 1965.

[25] B. Budiansky and T. Wu. Theoretical prediction of plastic strains of polycrystals. In *Proc. 4th US Nat. Congr. Appl. Mech.* ASME, New York, 1962.

[26] M. Calcagnotto, D. Ponge, E. Demir, and D. Raabe. Orientation gradients and geometrically necessary dislocations in ultrafine grained dual-phase steels studied in 2d and 3d EBSD. *Mater. Sci, Eng. A*, 527(10-11):2738–2746, 2010.

[27] Y. W. Chang and R. J. Asaro. An experimental study of shear localization in aluminum-copper single crystals. *Acta Metallurgica*, 29:241–257, 1981.

[28] P. Chen and M. Koç. Simulation of springback in forming of advanced high strength steels. *Journal of Materials Processing Technology*, 190:189–198, 2007.

[29] P. Chen, H. Ghassemi-Armaki, S. Kumar, A. Bower, S. Bhat, and S. Sadagopan. Microscale-calibrated modeling of the deformation response of dual-phase steels. *Acta Materialia*, 65:133–149, 2014.

[30] R. M. Christensen. *Mechanics of composite materials.* John Wiley & Sons, New York, 1979.

[31] K. Chung, M. G. Lee, D. Kim, C. Kim, M. Wenner, and F. Barlat. Spring-back evaluation of automotive ssheet based on isotropic-kinematic hardening laws and non-quadratic yield functions, Part I: theory and formulation. *International Journal of Plasticity*, 21:861–882, 2005.

[32] A. M. Cuitiño and M. Ortiz. Computational modelling of single crystals. *Modelling Simul. Mater. Sci. Eng.*, 1:225–263, 1992.

[33] M. Darrieulat and D. Piot. A method of generating analyytical yield surfaces of cryscrystal materials. *International Journal of Plasticity*, 12(5):575–610, 1996.

[34] M. Delincé, Y. Bréchet, J. D. Embury, M. G. D. Geers, P. J. Jacques, and T. Pardoen. Structure-property optimization of ultra.fine-grained dual-phase steels using a microstructure-based strain hardening model. *Acta. Mater.*, 55(7):2337–2350, 2007.

[35] W. J. Drugan and J. R. Willis. A micromechanics-based nonlocal constitutive euation and estimates of representative volume element size for elastic composites. *Journal of Mechanics, Physics and Solids*, 44:497–524, 1996.

[36] A. C. Eringen. *Mechanics of Continua.* John Wiley & Sons, 1967.

[37] J. D. Eshelby. The determination of the elastic field of an ellipsoidal inclusion, and related problems. *Proc. Roy. Soc. Lond. A*, 241:376–396, 1957.

[38] J. D. Eshelby. The elastic field outside an ellipsoidal inclusion. *Proc. Roy Soc. Lond. A*, 252:561–569, 1959.

[39] J. Feng, C. Li, S. Cen, and D. Owen. Statistical reconstruction of two-phase random media. *Computers and Structures*, 137:78–92, 2014.

[40] F. Feyel. Multiscale FE^2 elastoviscolastic analysis of composite structures. *Computational Materials Science*, 16:344–354, 1999.

[41] F. Feyel and J. Chaboche. FE^2 multiscale approach for modelling the elastoviscoplastic behaviour of long fibre SiC/Ti composite materials. *Computer Methods in Applied Mechanics and Engineering*, 183:309–330, 2000.

[42] W. Gan and R. H. Wagoner. Die design method for sheet springback. *International Journal of Mechanical Science*, 46:1097–1113, 2004.

[43] M. Geers, V. Kouznetsova, and W. Brekelmans. Multi-scale first order and second order computational homogenization of microstructures towards ontinua. *International Journal for Numerical Methods in Engineering*, 1:371–386, 2003.

[44] I. M. Gitman, H. Askes, and L. J. Sluys. Representative volume: existence and size determination. *Engineering Fracture Mechanics*, 74:2518–2634, 2007.

[45] R. Glüge. Generalized boundary conditions on representative volume elements and their use in determining the effective material properties. *Computational Materials Science*, 79:408–416, 2013.

[46] H. Goldstein. *Klassische Mechanik*. AULA Verlag, Wiesbaden, 1985.

[47] Q. Grimal, K. Raum, A. Gerisch, and P. Laugier. A determination of the minimum size of representative volume elements for the prediction of cortical bone elastic properties. *Biomechanics and Modeling in Mechanobiology*, 10:925–937, 2011.

[48] D. Gross and T. Seelig. *Fracture Mechanics*. Springer, 2006.

[49] A. Habraken. Modelling the Plastic Anisotropy of Metals. *Archives of Computational Methods in Engineering*, 11:3–96, 2004.

[50] H. Hadwiger. *Vorlesung über Inhalt, Oberfläche und Isoperimetrie*. Springer, 1957.

[51] H. Hadwiger and C. Meier. Studien zur vektoriellen integralgeometrie. *Mathematische Nachrichten*, 56:261 – 268, 1973.

[52] Z. Hashin. Analysis of composite materials - a survey. *Journal of Applied Mechanics*, 50:481–505, 1983.

[53] J. Havelka, A. Kucerova, and J. Sỳkora. Compression and reconstruction of random microstructures using accelerated lineal path function. *Computational Materials Science*, 122:102–117, 2016.

[54] M. Helm. Marching cube algorithm for matlab. Matlab code, 2009. URL `http://null-a.de/homepage/octave/#mc`.

[55] R. Hill. A theory of the yield and plastic flow of anisotropic metals. *Proc. R. Soc. Lond. A.*, 193:281–297, 1948.

[56] R. Hill. Elastic properties of reinforced solids: Some theoretical principles. *Journal of Mechanics, Physics and Solids*, 11:357–372, 1963.

[57] R. Hill. Theory and mechanical properties of fibre-strengthened materials. 3. self-consistent model. *Journal of the Mechanics and Physics of Solids*, 13:189–198, 1965.

[58] R. Hill. Theoretical plasticity of textured aggregates. *Math. Proc. Cambridge Philosophical Soc.*, 85:179–191, 1979.

[59] R. Hill. Constitutive modelling of orthotropic plasticity in sheet metals. *Journal of the Mechanics and Physics of Solids*, 38:405–417, 1990.

[60] R. Hill. A user-friendly theory of orthotropic plasticity in sheet metals. *Int. J. Mech. Sci.*, 35(1):19–25, 1993.

[61] G. A. Holzapfel. *Nonlinear solid mechanics, a continuum approach for engineering.* Wiley, 2000.

[62] T. J. R. Hughes and R. Taylor. Unconditionally stable algorithm for quasi-static elasto/visco-plastic finite element analysis. *Computers and Structures*, 8:169–173, 1978.

[63] J. Hutchinson. Elastic-plastic behaviour of polycrystalline metals and composites. *Proc. Roy. Soc. Lond. A*, 319:247–272, 1970.

[64] J. W. Hutchinson. Bounds and self-consistent estimates for creep of polycrystalline materials. *Proc. R. Soc. Lond. A.*, 348:101–127, 1976.

[65] J. Kadkhodapour, S. Schmauder, D. Raabe, S. Ziaei-Rad, U. Weber, and M. Calcagnotto. Experimental and numerical study on geometrically necessary dislocations and non-homogeneous mechanical properties of the ferrite phase in dual phase steels. *Acta Materialia*, 59:4387–4394, 2011.

[66] T. Kanit, S. Forest, I. Galliet, V. Mounoury, and D. Jeulin. Determination of the size of the representative volume element for random composites: statistical and numerical approach. *International Journal of Solids and Structures*, 40:3647–3679, 2003.

[67] S. Kapfer. *Morphometry and Physics of Particulate and Porous Media.* PhD thesis, Friedrich-Alexander-Universität Erlangen-Nürnberg, 2011.

[68] S. Kapfer, W. Mickel, F. Schaller, M. Spanner, C. Goll, T. Nogawa, N. Ito, K. Mecke, and G. E. Schröder-Turk. Local anisotropy of fluids using Minkowski tensors. *J. Stat. Mech.: Theory and Exp.*, 2010 (11):P11010, 2010.

[69] A. Karafillis and M. Boyce. A general anisotropc yield criterion using bounds and a transformation weighting tensor. *Journal of the Mechanics and Physics of Solids*, 41(12):1859–1886, 1993.

[70] B. Karlsson and B. Sundström. Inhomogeneity in plastic deformation of two-phase steels. *Mater. Sci. Eng.*, 161(1-2):161–168, 1974.

[71] A. Khintchine. Korrelationstheorie der stationären stochastischen Prozesse. *Mathematische Annalen*, 109(1):604–615, 1934.

[72] S. Klinkel. *Theorie und Numerik eines Volume-Schalen-Elementes bei finite elastischen und plastischen Verzerrungen.* PhD thesis, Universität zu Karlsruhe, 2000.

[73] U. F. Kocks. The relation between polycrystalline deformation and single crystal deformation. *Metall. Trans.*, 1:1121–1142, 1970.

[74] J. Konrad, S. Zaefferer, and D. Raabe. Investigation of orientation gradients around a hard laves particle in a warm rolled Fe^3Al-based alloy by a 3d EBSD-FIB technique. *Acta Materialia*, 54:1369–1380, 2006.

[75] K. Kowalczyk and W. Gambin. Model of plastic anisotropy evolution with texture-dependent yield surface. *International Journal of Plasticity*, 20:19–54, 2004.

[76] M. Kraska, M. Doig, D. Tikhomirow, D. Raabe, and F. Roters. Virtual material testing for stamping simulations based on polycrystal plasticity. *Computational Materials Science*, 46:383–392, 2009.

[77] E. Kröner. Berechnung der elastischen Konstanten des Vielkristalls aus den Konstanten eines Einkristalls. *Zeitschrift für Physik*, 151(4):504–518, 1958.

[78] E. Kröner. Allgemeine Kontinuumstheorie der Versetzung und Eigenspannung. *Archive of Rational Mechanics and Analysis*, 4:273–334, 1960.

[79] H. Kumar, C. L. Briant, and W. A. Curtin. Using microstructure reconstruction to model mechanical behavior in complex microstructures. *Mechanics of Materials*, 38:818–832, 2006.

[80] I. Kurzhöfer. *Mehrskalen-Modellierung polykristalliner Ferroelektrika basierend auf diskreten Orientierungsverteilungsfunktionen.* PhD thesis, Universität Duisburg-Essen, Fakultät Ingenieurwissenschaften, Abteilung Bauwissenschaften, Institut für Mechanik, 2006.

[81] E. Lee. Elasto-plastic deformation at finite strains. *Journal of Applied Mechanics*, 36:1–6, 1969.

[82] M. G. Lee, D. Kim, C. Kim, M. Wenner, and K. Chung. Spring-back evaluation of automotive sheet based on isotropic-kinematic hardening laws and non-quadratic yield functions, part iii: applications. *International Journal of Plasticity*, 21:915–953, 2005.

[83] M. G. Lee, D. Kim, C. Kim, M. Wenner, R. H. Wagoner, and K. Chung. Spring-back evaluation of automotive sheet based on isotropic-kinematic hardening laws and non-quadratic yield functions, Part II: characterization of material properties. *International Journal of Plasticity*, 21:883–914, 2005.

[84] X. Ling, M. F. Horstemeyer, and G. P. Potirniche. On the numerical implementation of 3D rate-dependent single crystal plasticity formulations. *IJNME*, 63:548–568, 2005.

[85] B. Lu and S. Torquato. Lineal-path function for random heterogeneous materials. *Physical Reviews A*, 45:922–929, 1992.

[86] K. Madi, S. Forest, D. Jeulin, and M. Boussuge. Estimating RVE sizes for 2D/3D viscoplastic composite materials. Matériaux Proceedings, 2006.

[87] J. Mandel. Plasticité classique et viscoplasticité. In *CISM course Nr. 97*. Springer, 1972.

[88] J. Marsden and J. Hughes. *Mathematical Foundations of Elasticity.* Prentice-Hall, 1983.

[89] M. McKerns, P. Hung, and M. Aivazis. mystic: a simple model-independent inversion framework, 2009.

[90] M. M. McKerns, L. Strand, T. Sullivan, A. Fang, and M. A. G. Aivazis. Building a framework for predictive science. In *Proceedings of the 10th Python in Science Conference*, 2011. URL `http://arxiv.org/pdf/1202.1056`.

[91] C. Miehe. *Kanonische Modelle multiplikativer Elasto-Plastizität. Thermodynamische Formulierung und Numerische Implementierung.* Habilitationsschrift, Universität Hannover, Institut für Baumechanik und Numerische Mechanik, Bericht Nr. F93/1, 1993.

[92] C. Miehe and A. Koch. Computational micro-to-macro transitions of discretized microstructures undergoing small strains. *Archive of Applied Mechanics*, 72(4):300–317, 2002.

[93] C. Miehe and J. Schröder. Computational micro-macro transition and overall moduli in the analysis of polycrystals at large strains. *Computational Materials Science*, 16:372–382, 1999.

[94] C. Miehe and J. Schröder. A comparative study of stress update algorithms for rate independent and rate dependent crystal plasticity. *International Journal for Numerical Methods in Engineering*, 50:273–298, 2001.

[95] C. Miehe and E. Stein. A canonical model of multiplicative elasto-plasticity formulation and aspects of the numerical implementation. *European Journal of Mechanics A / Solids*, 11:25–43, 1992.

[96] C. Miehe, J. Schröder, and J. Schotte. Computational homogenization analysis in finite plasticity. Simulation of texture development on polycrystalline materials. *CMAME*, 171:387–418, 1999.

[97] A. Mikdam, A. Makradi, S. Ahzi, H. Garmestani, D. Li, and Y. Remond. A new approximation for the three-point probability function. *International Journal of Solids and Structures*, 46:3782–3787, 2009.

[98] E. Mittermeijer. *Fundamentals of materials science: the microstructure property relationship using metals as model systems.* Springer, Heidelberg, 2010.

[99] H. Moulinec and P. Suquet. A numerical method for computing the overall response of nonlinear composites with complex microstructure. *Computer Methods in Applied Mechanics and Engineering*, 157:69–94, 1998.

[100] J. M. Moyer and G. S. Ansell. The volume expansion accompanying the martensite transformation in iron-carbon alloys. *Metall. Trans. A*, 6(9):17851791, 1975.

[101] K. Mukherjee, S. S. Hazra, and M. Militzer. Grain refinement in dual-phase steels. *Metall. Mater. Trans. A*, 40(9):2145–2159, 2009.

[102] R. W. Ogden. *Non-linear elastic deformations.* Dover Publications, 1984.

[103] J. Ohser and F. Mücklich. *Statistical analysis of microstructures in materials science.* J. Wiley & Sons, 2000.

[104] M. Ostoja-Starzewski. The use, misuse, and abuse of stochastic random media. In *Proceedings of European Conference on Computational Mechanics*, 2001.

[105] J. Pagenkopf, A. Butz, M. Wenk, and D. Helm. Virtual tesing of dual-phase steels: Effect of martensite morphology on plastic flow behavior. *Materials Science & Engineering A*, 674:672–686, 2016.

[106] S. K. Paul. Real microstructure based micromechanical model to simulate microstructural level deformation behavior and failure initiation in DP 590 steel. *Materials and Design*, 44:397–406, 2013.

[107] D. Peirce, R. J. Asaro, and A. Needleman. An analysis of nonlinear and localized deformation in ductile single crystals. *Acta Metall.*, 30:1087–1119, 1982.

[108] C. Pelissou, J. Baccou, Y. Monerie, and F. Perales. Determination of the size of the representative volume element for random quasi-brittle composites. *International Journal of Solids and Structures*, 46:2842–2855, 2009.

[109] D. Peric, P. Owen, and M. Honnor. A model for finite strain elasto-plasticity based on logarithmic strains: Computational issues. *Computer Methods in Applied Mechanics and Engineering*, 94:35–61, 1992.

[110] A.-P. Pierman, O. Bouaziz, T. Pardoen, P. J. Jacques, and L. Brassart. The influence of microstructure and composition on the plastic behaviour of dual-phase steels. *Acta. Mater.*, 73:298–311, 2014.

[111] G. L. Povirk. Incorporation of microstructural information into models of two-phase materials. *Acta Metall. Mater.*, 43:3199–3206, 1995.

[112] R. Quey, P. R. Dawson, and F. Barbe. Large-scale 3d random polycrystals for the finite element method: Generation, meshing and remeshing. *Computer Methods in Applied Mechanics and Engineering*, 200:1729–1745, 2011.

[113] D. Raabe. Texture simulation for hot rolling of aluminum by use of a Taylor model considering grain interaction. *Acta Materialia*, 43(3):1023–1028, 1995.

[114] A. Ramazani, K. Mukherjee, U. Prahl, and W. Bleck. Modelling the effect of micromechanical banding on the flow curve behaviour of dual-phase (dp) steels. *Computational Materials Science*, 52:46–54, 2012.

[115] V. Randle and O. Engler. *Introduction to Texture Analysis: Macrotexture, Microtexture, and Orientation Mapping*. CRC Press Inc., 2000.

[116] M. Rashid. Dual phase steels. *Annu. Rev. Mater. Sci.*, 11:245:266, 1981.

[117] L. Rauch, M. Pernach, K. Bzowski, and M. Pietrzyk. On application of shape coefficients to creation of the statistically similar representative element of DP steels. *Computer Methods in Materials Science*, 11:531–541, 2011.

[118] L. Rauch, R. Kuziak, and M. Pietrzyk. From High Accuracy to High Efficiency in Simulations of Processing of Dual-Phase Steels. *Metallurgical and Materials transactions B*, 45:497–506, 2014.

[119] J. Rice. Inelastic consitutive relation for solids: an internal-variable theory and its application to metal plasticity. *Journal of the Mechanics and Physics of Solids*, 19: 433–455, 1971.

[120] F. Roters, P. Eisenlohr, T. Biehler, and D. Raabe. *Crystal Plasticity Finite Element Methods in Materials Science and Engineering*. Wiley-VCH, 2010.

[121] F. Roters, P. Eisenlohr, L. Hantcherli, D. D. Tjahjanto, T. R. Bieler, and D. Raabe. Overview of constitutive laws, kinematics, homogenization and multiscale methods in crystal plasticity finite-element modeling: Theory, experiments, applications. *Acta Materialia*, 58:1521211, 2010.

[122] F. Roters, P. Eisenlohr, C. Kords, D. Tjahjanto, M. Diehl, and D. Raabe. Damask: the Düsseldorf Advanced MAterial Simulation Kit for studying crystal plasticity using an fe based or a spectral numerical solver. In *IUTAM Symposium on Linking Scales in Computations: From Microstructure to Macro-scale Properties*, volume 3, pages 3–10. Procedia IUTAM, 2010.

[123] G. Sachs. *Mitteilungen der deutschen Materialprüfungsanstalten*, chapter Zur Ableitung einer Fließ bedingung, pages 94–97. Springer Berlin Heidelberg, 1929.

[124] T. Sakaki, K. Sugimoto, and T. Fukuzato. Role of internal stress for continuous yieyield of dual-phase steels. *Acta Metallurgica*, 31(10):1737–1746, 1983.

[125] D. Saylor, J. Fridy, B. El-Dasher, K.-Y. Jung, and A. Rollet. Statistical representative three-dimensional microstructures based on orthogonal observation sections. *Metallurgical and Materials Transactions A: Physical Metallurgy and Materials Science*, 35A:1969–1979, 2004.

[126] O. Schenk, K. Gartner, and W. Fichtner. Efficient Sparse LU Factorization with Left-right Lokking Strategy on Shared Memory Multiprocessors. *BIT*, 40(1):158–176, 2000.

[127] L. Scheunemann, D. Balzani, D. Brands, and J. Schröder. *Analysis and Computation of Microstructure in Finite Plasticity. Lecture Notes in Applied and Computational Mechanics 78*, chapter Construction of Statistically Similar RVEs, pages 219–256. Springer, 2015.

[128] L. Scheunemann, D. Balzani, D. Brands, and J. Schröder. Design of 3d statistically similar representative volume elements based on minkowski functionals. *Mechanics of Materials*, 90:185–201, 2015. doi: 10.1016/j.mechmat.2015.03.005.

[129] L. Scheunemann, J. Schröder, and D. Brands. Macroscopic yield curves based on statistically similar RVEs for 3D Dual-Phase Steel Microstructures. In A. Zingoni, editor, *Insights and Innovations in Structural Engineering, Mechanics and Computation. Proceedings of the Sixth International Conference on Structural Engineering, Mechanics and Computation (SEMC 2016), 5-7 September 2016, Cape Town, South Africa.*, pages 890–896. Taylor & Francis Group, London, 2016.

[130] J. Schröder. *Homogenisierungsmethoden der nichtlineare Kontinuumsmechanik unter Beachtung von Stabilitätsproblemen*. Habilitation, Lehrstuhl I, Universtät Stuttgart, 2000.

[131] J. Schröder. *Plasticity and Beyond - Microstructures, Crystal-Plasticity and Phase Transitions (CISM Lecture Notes 550, Eds. J. Schröder, K. Hackl)*, chapter A numerical two-scale homogenization scheme: the FE^2-method. Springer, 2014.

[132] J. Schröder, D. Balzani, and D. Brands. Approximation of random microstructures by periodic statistically similar representative volume elements based on lineal-path functions. *Archive of Applied Mechanics*, 81:975–997, 2011.

[133] G. Schröder-Turk, W. Mickel, S. Kapfer, M. Klatt, F. Schaller, M. Hoffmann, N. Kleppmann, P. Armstrong, A. Inayat, D. Hug, M. Reichelsdorfer, W. Peukert, W. Schwieger, and K. Mecke. Minkowski Tensor Shape Analysis of Cellular, Granular and Porous Structures. *Advanced Materials*, 23 (22-23):2535–2553, 2011.

[134] G. E. Schröder-Turk, S. Kapfer, B. Breidenbach, B. C., and K. Mecke. Tensorial minkowski functionals and anisotropy measures for planar patterns. *Journal of Microscopy*, 238:57 – 74, 2010.

[135] G. E. Schröder-Turk, W. Mickel, S. C. Kapfer, F. M. Schaller, B. Breidenbach, D. Hug, and K. Mecke. Minkowski Tensors of Anisotropic Spatial Structure. *New Journal of Physics*, 15:1–17, 2013.

[136] N. A. Seaton and E. D. Glandt. Spatial correlation functions for computer simulations. *The Journal of Chemical Physics*, 85:5262–5268, 1986.

[137] K. Siegert. *Blechumformung - Verfahren, Werkzeuge und Maschinen.* Springer Vieweg, 2015.

[138] J. Simo. A framework for finite strain elastoplasticity based on maximum plastic dissipation and the multiplicative decomposition: Part I. continuum formulation. *Computer Methods in Applied Mechanics and Engineering*, 66:199–219, 1988.

[139] J. Simo. Algorithm for static and dynamic multiplicative plasticity that preserve the classical return mapping sscheme of the infinitesimal theory. *Computer Methods in Applied Mechanics and Engineering*, 99:61–112, 1992.

[140] J. Simo. *Handbook of Numerical Analysis, Vol. VI*, chapter Numerical Analysis and Simulation of Plasticity, pages 183–499. Elsevier B.V., 1998.

[141] J. Simo and T. Hughes. *Computational Inelasticity.* Springer, 1998.

[142] J. Simo and C. Miehe. Associative coupled thermoplasticity at finite strains: Formulation, numerical analysis and implementation. *Computer Methods in Applied Mechanics and Engineering*, 98(1):41–104, 1992.

[143] R. Smit, W. Brekelmans, and H. Meijer. Prediction of the mechanical behaviour of nonlinear heterogeneous systems by multi-level finite element modeling. *Computer Methods in Applied Mechanics and Engineering*, 155:181–192, 1998.

[144] P. A. Smith and S. Torquato. Computer simulation results for the two-point probability function of composite media. *JCP*, 76:176–191, 1988.

[145] S. Sporer, C. Goll, and K. Mecke. Motion by stopping: rectifying brownian motion of nonspherical particles. *Phys. Rev. E*, 78:011917, 2008.

[146] E. Stein and F.-J. Barthold. Elastizitätstheorie. In *Der Ingenieurbau, Grundwissen: Werkstoffe, Elastizittstheorie.* Ernst & Sohn, Berlin, 1996.

[147] P. Steinmann and E. Stein. On the numerical treatment and analysis of finite deformation ductile single crystal plasticity. *Computer Methods in Applied Mechanics and Engineering*, 129:235–254, 1996.

[148] R. F. Stengel. *Stochastic Optimal Control. Theory and Application*. John Wiley & Sons, 1986.

[149] R. Storn. On the usage of differential evolution for function optimization. In *Biennial Conf. of the North American Fuzzy Information Processing Society*, 1996.

[150] R. Storn and K. Price. Differential Evolution- A Simple and Efficient Heuristic for global Optimization over Continuous Spaces. *Journal of Global Optimization*, 11: 341–359, 1997.

[151] M. Stroeven, H. Askes, and L. Sluys. A numerical approach to determine representative volumes for granular materials. In *Fifth World Congress on Computational Mechanics (WCCM V)*. Vienna University of Technology, 2002.

[152] T. Strohmann. Application of multi-objective optimization for the construction of ststatistical similar RVEs (SSRVEs). Technical report, Institut für Mechanik, Report Nr. 133, 2016.

[153] P. Suquet. *Continuum Micromechanics (CISM lecture note)*. Springer, Berlin, 1997.

[154] S. Swaminathan and S. Ghosh. Statistical equivalent representative volume elements for unidirectional composite microstructures: Part ii: with interfacial debonding. *Journal of Composite Materials*, 40(7):605–621, 2006.

[155] S. Swaminathan, S. Ghosh, and N. Pagano. Statistical equivalent representative volume elements for unidirectional composite microstructures: Part i: without damage. *Journal of Composite Materials*, 40(7):583–604, 2006.

[156] K. Tanaka and T. Mori. Note on volume integrals of the elastic field around an ellipsoidal inclusion. *Journal of Elasticity*, 2:199–200, 1972.

[157] C. C. Tasan, M. Diehl, D. Yan, M. Bechtold, F. Roters, L. Schemmann, C. Zheng, N. Peranio, D. Ponge, M. Koyama, K. Tsuzaki, and D. Raabe. An overview of dual-phase steels: Advances in microstructure-oriented processing and micromechanically guided design. *Annu. Rev. Mater. Res.*, 45:391–431, 2015.

[158] G. Taylor. Plastic strains in metals. *Journal of the Institute of Metals*, 62:307–324, 1938.

[159] G. I. Taylor. The mechanism of plastic deformation of crystal. part i: Theoretical. *Proc. Roy. Soc. London A,*, 145:362–387, 1934.

[160] G. I. Taylor. The mechanism of plastic deformation of crystal. part ii: Comparison with observations. *Proc. Roy. Soc. London A,*, 145:388–404, 1934.

[161] R. L. Taylor. *FEAP - - A Finite Element Analysis Program Version 8.2 User Manual*. Department of Civil and Environmental Engineering, University of California at Berkeley, Berkeley, California 94720-1710, March 2008.

[162] K. Terada, M. Hori, T. Kyoyac, and N. Kikuchi. Simulation of the multi-scale convergence in computational homogenization approaches. *International Journal of Solids and Structures*, 37:2285–2311, 2000.

[163] . Thyssen Krupp Steel Europe AG. Produktinformation Dualphasenstähle DP-W und DP-K. Für die Herstellung komplexer hochfester Strukturelemente., 08/2013.

[164] D. Tjahjanto, P. Eisenlohr, and F. Roters. A novel grain-based homogenization scheme. *Model. Simul. Mater. Sci. Eng.*, 18(1):015006, 2010.

[165] S. Torquato. *Random heterogeneous materials. Microstructure and macroscopic properties*. Springer, 2002.

[166] D. Trias, J. Costa, A. Turon, and J. Hurtado. Determination of the critical size of statistical representative volume element (SRVE) for carbon reinforced polymers. *Acta Materialia*, 54:3471–3484, 2006.

[167] C. Truesdell and W. Noll. The nonlinear field theories of mechanics. In *Encyclopedia of physics*, chapter The nonlinear field theories of mechanics. Springer, 1965.

[168] P. Van Houtte, L. Delannay, and I. Samajdar. Quantitative prediction of cold rolling ttexture in low carbon steels by means of the lamel model. *Textures and Microstructures*, 31(3):109–149, 1999.

[169] M. Šilhavý. *The mechanics and thermodynamics of continuous media*. Springer, 1997.

[170] R. Watanabe. Possible slip systems in body centered cubic iron. *Materials Transactions*, 47(8):1886–1889, 2006.

[171] G. Weber and L. Anand. Finite deformation constitutive equations and a time integration porocedure for isotropic, hyperelastic-viscoelastic solids. *Computer Methods in Applied Mechanics and Engineering*, 79:173–202, 1990.

[172] C. R. Weinberger, B. L. Boyce, and C. C. Battaille. Slip planes in bcc transition metals. *International Materials Reviews*, 58(5):296–314, 2013.

[173] N. Wiener. Generalized Harmonic Analysis. *Acta Mathematica*, 55:117–258, 1930.

[174] P. Wriggers. *Nichtlineare Finite-Elemente-Methoden*. Springer, 2001.

[175] T. Yalcinkaya, W. A. M. Brekelmans, and G. M. G. D. BCC single crystal plasticity modeling and its experimental identification. *Modelling Simul. Mater. Sci. Eng.*, 16(8):085007, 2008.

[176] C. L. Y. Yeong and S. Torquato. Reconstructing random media. *Physical Review E*, 57:495–506, 1998.

[177] N. Zaafarani, D. Raabe, R. Singh, F. Roters, and S. Zaefferer. Three-dimensional investigation of the texture and microstructure below a nanoindent in a cu single crystal using 3d EBSD and crystal plasticity finite element simulations. *Acta Materialia*, 54(7):1863–1876, 2006.

[178] S. Zaefferer, S. Wright, and D. Raabe. Three-dimensional orientation microscopy in a focused ion beam-scanning electron microscope: A new dimension of microstructure characterization. *Metallurgical and Materials Transactions A*, 39(2):374–389, 2008.

[179] J. Zeman. *Analysis of composite materials with random microstructure*. PhD thesis, University of Prague, 2003.

[180] M. Zhang, H. ang Diehl, F. Roters, and D. Raabe. A virtual laboratory using high resolution crystal plasticity simulations to determine the initial yield surface for sheet metal forming operations. *International Journal of Plasticity*, 2016. doi: 10.1016/j.ijplas.2016.01.002.

[181] O. Zienkiewicz and R. Taylor. *The finite element method - for solid and structural mechanics*. Elsevier, 6 edition, 2005.

[182] T. Zohdi and P. Wriggers. *Introduction to Computational Micromechanics*. Springer, 2005.

Der Lebenslauf ist in der Online-Version aus Gründen des Datenschutzes nicht enthalten.

In dieser Schriftenreihe bisher erschienene Berichte:

Nr. 1 (2004) *Ein Modell zur Beschreibung finiter anisotroper elastoplastischer Deformationen unter Berücksichtigung diskreter Rissausbreitung*, J. Löblein, Dissertation, 2004.

Nr. 2 (2006) *Polyconvex Anisotropic Energies and Modeling of Damage applied to Arterial Walls*, D. Balzani, Dissertation, 2006.

Nr. 3 (2006) *Kontinuumsmechanische Modellierung ferroelektrischer Materialien im Rahmen der Invariatentheorie*, H. Romanowski, Dissertation, 2006.

Nr. 4 (2007) *Mehrskalen-Modellierung polykristalliner Ferroelektrika basierend auf diskreten Orientierungsverteilungsfunktionen*, I. Kurzhöfer, Dissertation, 2007.

Nr. 5 (2007) *Proceedings of the First Seminar on the Mechanics of Multifunctional Materials*, J. Schröder, D.C. Lupascu, D. Balzani (Ed.), Tagungsband, 2007.

Nr. 6 (2008) *Zur Modellierung und Simulation diskreter Rissausbreitungsvorgänge*, O. Hilgert, Dissertation, 2008.

Nr. 7 (2009) *Least-Squares Mixed Finite Elements for Solid Mechanics*, A. Schwarz, Dissertation, 2009.

Nr. 8 (2010) *Design of Polyconvex Energy Functions for All Anisotropy Classes*, V. Ebbing, Dissertation, 2010.

Nr. 9 (2012) *Modeling of Electro-Mechanically Coupled Materials on Multiple Scales*, M.-A. Keip, Dissertation, 2012.

Nr. 10 (2012) *Geometrical Modeling and Numerical Simulation of Heterogeneous Materials*, D. Brands, Dissertation, 2012.

Nr. 11 (2012) *Modeling and simulation of arterial walls with focus on damage and residual stresses*, S. Brinkhues, Dissertation, 2012.

Nr. 12 (2014) *Proceedings of the Second Seminar on the Mechanics of Multifunctional Materials*, J. Schröder, D.C. Lupascu, M.-A. Keip, D. Brands (Ed.), Tagungsband, 2014.

Nr. 13 (2016) *Mixed least squares finite element methods based on inverse stress-strain relations in hyperelasticity*, B. Müller, Dissertation, 2016.

Nr. 14 (2016) *Electromechanical Modeling and Simulation of Thin Cardiac Tissue Constructs* , R. Frotscher, Dissertation, 2016.

Nr. 15 (2017) *Least-squares mixed finite elements for geometrically nonlinear solid mechanics* , K. Steeger, Dissertation, 2017.